

Copyright
by
Michael David Dickey
2006

**The Dissertation Committee for Michael David Dickey Certifies that this is the
approved version of the following dissertation:**

**Development of Photocurable Pillar Arrays Formed via
Electrohydrodynamic Instabilities**

Committee:

C. Grant Willson, Supervisor

Roger Bonnecaze

John Ekerdt

Lynn Loo

S.V. Sreenivasan

**Development of Photocurable Pillar Arrays Formed via
Electrohydrodynamic Instabilities**

by

Michael David Dickey, B.S.; M.S.

Dissertation

Presented to the Faculty of the Graduate School of

The University of Texas at Austin

in Partial Fulfillment

of the Requirements

for the Degree of

Doctor of Philosophy

The University of Texas at Austin

August 2006

Dedication

To my family.

Acknowledgements

I am extremely grateful to many people who have helped guide my personal and professional development. I will remember my time in Austin as some of the best years of my life largely due to the great friends and colleagues I interacted with daily.

I can clearly remember the first time I met Dr. Willson during recruiting weekend. Dr. Willson was the main reason I came to UT and I have never regretted that decision. I cannot imagine a better advisor. Dr. Willson - your commitment to students is amazing and inspiring. Thank you for being a wonderful mentor, but more importantly, a supportive and understanding friend. I am also thankful to Kathleen Sparks, who does such a wonderful job keeping our group functioning and has become a great friend over the years.

Although it will never appear in any official documentation, I consider Dr. Bonnecaze as a co-mentor. Thank you for going above and beyond the call of duty to help me with my research and career. I am grateful for the friendship we have established during the past four years. You give me inspiration on how to live a balanced life and manage a career.

Thank you to my thesis committee. Your support has made my graduate studies truly enjoyable and your guidance has helped shape me as a researcher. Thank you Dr. Ekerdt and Dr. Sreenivasan for your supervision during our early SFIL work and your

continued support. Dr. Loo - thank you for spending appreciable amounts of time helping me during my job search.

My family is a very important part of my life. Thank you, Kim, for being incredibly supportive of my aspirations. I am also extremely grateful to my parents who give new meaning to the word supportive. I owe everything to them for their steady unconditional love. They are the best role models a son could ask for.

I am fortunate to work in an extremely supportive research group and I would like to thank all Willson group members, both past and present. There are countless examples of fellow students putting aside their work to help me. When I first joined the group, Gerard Schmid, Jason Meiring, Tim Michaelson, Andrew Jamieson, Sean Burns, Nick Stacey, and Ryan Burns were all extremely helpful. In the past few years, Pavlos Tsiartas, Michael Stewart, Frank Palmieri, Elizabeth Collister, and Saul Lee have been very supportive in guiding my research. I also appreciate the chemistry guidance provided by Brian Long, Bill Heath, Ryan Callahan, and Stefan Caparole.

I have had the pleasure of collaborating with several great colleagues. I am particularly thankful to Allen Raines, who is talented and was instrumental in stretching pillars. One of the most rewarding experiences in graduate school was working with Dr. Tom Russell's group at University of Massachusetts at Amherst. Suresh Gupta and Amanda Leach were very welcoming and open in what proved to be a fruitful collaboration and friendship. I also appreciate the assistance of Dr. Bob LeSeur (cyclic voltametry), Dr. Zach Hilt (oxygen measurements), Niraj Kulkarni (carbon nanotubes), Victor Kusama (silver nanowires), Nelson Hu (dielectric measurements), Jamie Kropka (rheology), and Doh Lee (Ge wires).

One of the best experiences of graduate school was working with undergraduate researchers in our laboratory. Keris Allrich, Clint Cooper, Sumarlin Goh, Darren Hipp,

Tom Holcombe, Keith Keitz, Hayley Norris, Justin Shih, and Wyatt Winkenwerder were all a pleasure to work with and each contributed uniquely and significantly to my research. I am very proud of all of them. I am particularly grateful to Tom, who worked with me the longest and was extremely dedicated to our research goals.

I would like to thank a number of professors in the department who have treated me as a colleague and have gone out of their way to help me. Dr. Freeman, Dr. Truskett, Dr. Bonneau, Dr. Loo, Dr. Ekerdt, Dr. Genasan, and Dr. Mullins have all had an open door policy and have been helpful in guiding my career.

I am grateful to the generosity of Dr. Mark Hamilton and Dr. Preston Wilson in the Mechanical Engineering department. They literally gave me a key to their lab and have provided both equipment and expertise in support of the acoustic vibration portion of this work.

Without question the best part of graduate school has been the friends. I would particularly like to thank Christian Green, Brent Bregenzer, Scott Stanley, Shravi Reddy, Ali Ghezelbash, Chris Harrison, Scott Harrison, and April Schricker for being such wonderful friends. I'd also like to recognize Tim Fornes, Jennie Leach, Tom Leach for their continued support and friendship.

Finally, thanks to the NSF, Thrust, and Intel Foundation for fellowship support and the SEMATECH AMRC for project funding.

Development of Photocurable Pillar Arrays Formed via Electrohydrodynamic Instabilities

Publication No. _____

Michael David Dickey, Ph.D.

The University of Texas at Austin, 2006

Supervisor: C. Grant Willson

As photolithography approaches both fundamental and economic barriers, interest in alternative patterning technologies has grown. This thesis focuses on two alternative patterning techniques: nanoimprint lithography (NIL) and electric field assisted assembly.

NIL is a high resolution, yet inexpensive contact patterning process. Step and Flash Imprint Lithography (SFIL) is a type of NIL that involves pressing a topographically patterned template onto a substrate covered with a small volume of liquid. The liquid fills the voids of the template and is hardened by UV irradiation. Low viscosity liquids are ideal for rapid patterning.

An acrylate material formulation was developed to meet the various processing needs of SFIL. Unfortunately, oxygen inhibits the free radical photopolymerization used to cure the acrylate. The effects of oxygen were characterized using a semi-empirical model that relies on rate coefficients measured by real time IR spectroscopy. The model

predicts an inhibition period at the beginning of irradiation as radicals are quenched by oxygen. After the oxygen is consumed, the polymerization proceeds rapidly except at the perimeter of the template, which is subject to oxygen diffusion from the ambient.

Electric field assisted assembly is another attractive patterning technique that is capable of forming polymeric pillar arrays. Pillars form by the amplification of thin-film surface instabilities through the application of an electric field normal to the film.

Work to date on pillars has focused on glassy polymers that are limited by the requirement of heat to modulate the rheological properties. A focus of this thesis is on developing low viscosity materials for the formation of pillars. Low viscosity materials form pillars orders of magnitude faster than high-melt viscosity polymers. The pillars form at room temperature and are hardened by UV irradiation.

In addition to developing and characterizing low viscosity materials, the aspect ratio of the pillars was optimized. The aspect ratio of the pillars was increased by physically stretching the pillars through the development of an active gap tool. Methods to improve long range order were also investigated.

Electric field assisted assembly and imprint lithography are promising photolithographic alternatives that benefit considerably from the use of low viscosity materials.

Table of Contents

| | |
|---|-------------|
| List of Tables | xvi |
| List of Figures..... | xvii |
| Chapter 1: Lithography Introduction..... | 1 |
| 1.1 The Importance of Patterning | 1 |
| 1.2 General Patterning Strategies: “Top-down” vs. “Bottom-up” | 3 |
| 1.3 Photolithography | 4 |
| 1.3.1 Photolithographic Approaches and Limitations..... | 6 |
| 1.4 The Future of Photolithography | 10 |
| 1.4.1 Immersion Lithography | 11 |
| 1.4.2 Extreme Ultraviolet (EUV) Lithography | 12 |
| 1.4.3 Electron-beam (E-beam) Lithography | 12 |
| 1.4.4 Nanoimprint Lithography (NIL) | 13 |
| 1.5 Alternative Lithography | 14 |
| 1.6 Summary | 15 |
| 1.7 References | 16 |
| Chapter 2: Imprint Lithography Background and Materials..... | 22 |
| 2.1 Introduction..... | 22 |
| 2.2 Mold Formation | 25 |
| 2.3 Process Requirements | 28 |
| 2.4 Material Requirements | 29 |
| 2.4.1 Thermal NIL | 29 |
| 2.4.2 Material Requirements: UV-NIL | 30 |
| 2.5 Imprint Capabilities and Limitations | 33 |
| 2.5.1 Resolution | 33 |
| 2.5.2 Residual Layer | 35 |
| 2.5.3 Topography | 37 |
| 2.5.4 Thermal NIL Limitations | 38 |

| | |
|--|------------|
| 2.5.5 UV-NIL Limitations, Requirements, and Advantages | 40 |
| 2.5.6 Defects | 42 |
| 2.6 Summary | 42 |
| 2.7 References | 43 |
| Chapter 3: Imprint Lithography Photopolymerization Kinetics | 55 |
| 3.1 Introduction | 55 |
| 3.2 Materials and methods | 58 |
| 3.3 Kinetics Background and theory | 60 |
| 3.4 Determining Alpha | 66 |
| 3.5 SFIL Kinetics | 69 |
| 3.6 Determining rate coefficients | 73 |
| 3.6.1 Background | 73 |
| 3.6.2 Measurement Strategies | 73 |
| 3.6.3 Determining Rate of Initiation | 76 |
| 3.6.4 Determining k_p and k_t | 82 |
| 3.6.5 Comparison of k_p and k_t with Previous Results | 84 |
| 3.6.6 Modeling k_p and k_t | 85 |
| 3.6.7 Summary of Kinetic Coefficients | 88 |
| 3.7 Modeling | 89 |
| 3.8 Minimizing Oxygen Effects | 93 |
| 3.9 Conclusions | 96 |
| 3.10 References | 96 |
| Chapter 4: Electric Field Assisted Assembly Introduction | 104 |
| 4.1 Introduction | 104 |
| 4.2 Literature Background | 105 |
| 4.3 Theory | 108 |
| 4.3.1 Introduction | 108 |
| 4.3.2 Linear Stability Analysis Derivation | 110 |
| 4.3.3 Linear Stability Analysis Typical Values | 119 |
| 4.3.4 Linear Stability Analysis Discussion | 120 |

| | |
|--|------------|
| 4.3.5 Linear Stability Analysis Assumptions..... | 121 |
| 4.4 Limitation of Work to Date..... | 122 |
| 4.4.1 Time Scale of Formation | 122 |
| 4.4.2 Aspect Ratio..... | 123 |
| 4.5 Experimental Section..... | 123 |
| 4.6 Conclusions..... | 125 |
| 4.7 References..... | 125 |
| Chapter 5: Hierarchical Polymer Structures Formed Via Electric Field Assisted Assembly | 129 |
| 5.1 Introduction..... | 129 |
| 5.2 PMMA / PS / Air Trilayer | 131 |
| 5.2.1 Background..... | 131 |
| 5.2.2 Experimental..... | 133 |
| 5.2.3 Results and Discussion | 135 |
| 5.2.4 Summary of PMMA / PS / Air Trilayer..... | 142 |
| 5.3 PS / PMMA / Air Trilayer | 142 |
| 5.3.1 Background and Theory..... | 142 |
| 5.3.2 Experimental..... | 144 |
| 5.3.3 Results and Discussion | 145 |
| 5.3.4 Summary | 150 |
| 5.4 Conclusions..... | 151 |
| 5.5 References..... | 151 |
| Chapter 6: Low Viscosity Photocurable Pillar Arrays Formed Via Electric Field Assisted Assembly | 154 |
| 6.1 Background..... | 155 |
| 6.2 Materials and Methods..... | 157 |
| 6.3 Experimental Procedure..... | 160 |
| 6.4 Results and Discussion | 162 |
| 6.4.1 Epoxy | 167 |
| 6.4.2 Vinyl Ethers | 168 |
| 6.4.3 Acrylates | 169 |

| | |
|---|------------|
| 6.4.4 Thiol-ene | 169 |
| 6.5 Conclusions..... | 171 |
| 6.6 References..... | 172 |
| Chapter 7: Pillar Growth Mechanisms and Ordering | 175 |
| 7.1 Introduction..... | 175 |
| 7.2 Linear Stability Analysis of Low Viscosity Fluids..... | 176 |
| 7.2.1 Background..... | 178 |
| 7.2.2 Materials | 178 |
| 7.2.3 Methodology | 178 |
| 7.2.4 Experimental Limitations..... | 181 |
| 7.2.5 Results and Discussion | 183 |
| 7.2.6 Theoretical Limitations..... | 186 |
| 7.3 Growth Mechanisms | 188 |
| 7.4 Patterned Electrodes..... | 192 |
| 7.4.1 Background..... | 192 |
| 7.4.2 Methods..... | 192 |
| 7.4.3 Results..... | 194 |
| 7.4.4 Summary | 195 |
| 7.5 Pillars Formed by Alternating Fields..... | 196 |
| 7.6 Vibration Induced Waves | 198 |
| 7.6.1 Results and Discussion | 202 |
| 7.7 Summary | 204 |
| 7.8 References..... | 205 |
| Chapter 8: Pillar Aspect Ratio..... | 208 |
| 8.1 Background..... | 208 |
| 8.2 Theory | 209 |
| 8.3 Tool Design..... | 211 |
| 8.3.1 Mad City Labs Nanopositioner..... | 211 |
| 8.3.2 Active Gap Tool..... | 216 |
| 8.4 Active Gap Tool Stretching Results | 219 |

| | |
|---|------------|
| 8.4.1 Stretching Pillars | 219 |
| 8.4.2 Stretching Limits..... | 221 |
| 8.4.3 Active Gap Tool Capabilities and Limits | 226 |
| 8.5 High aspect ratio polymeric pillars | 227 |
| 8.5.1 Stretching polymeric pillars | 227 |
| 8.5.2 Viscoelastic polymers | 229 |
| 8.6 Conclusions..... | 236 |
| 8.7 References | 237 |
| Chapter 9: Improved ITO Template Surface Treatment | 240 |
| 9.1 Introduction..... | 241 |
| 9.2 Methods and Materials..... | 245 |
| 9.2.1 Materials | 245 |
| 9.2.3 Silylation | 245 |
| 9.2.3 Characterization | 246 |
| 9.3 Results..... | 248 |
| 9.4 Demonstrations | 254 |
| 9.5 Conclusions..... | 255 |
| 9.6 References | 256 |
| Chapter 10: Conclusions and Future Work | 260 |
| 10.1 Nanoimprint Lithography | 260 |
| 10.2 Electric Field Assisted Assembly | 262 |
| 10.3 Future Work | 268 |
| Appendix A: Rotating Sector Method..... | 270 |
| A.1 Derivation..... | 273 |
| A.2 References | 310 |
| Appendix B: Automated Statistical Process Control Experiment | 287 |
| B.1 Background | 287 |
| B.2 Experimental Procedure | 289 |
| B.3 Hazards..... | 290 |
| B.4 Results and Discussion..... | 290 |

| | |
|---|------------|
| B.5 Conclusions | 295 |
| B.5.1 Supplemental Material | 296 |
| B.6 References | 296 |
| Appendix C: Supporting Data | 297 |
| C.1 Materials..... | 297 |
| C.2 Ellipsometry | 298 |
| C.3 Film Thickness | 299 |
| C.4 Electrode Processing | 302 |
| C.5 Electro curing | 304 |
| C.6 DSC Measurements..... | 306 |
| C.7 Scion Software and FFT analysis..... | 308 |
| C.7.1 Scion Procedure..... | 308 |
| C.7.2 FFT Analysis | 309 |
| Appendix D: Academic Genealogy | 316 |
| References | 320 |
| Vita | 351 |

List of Tables

| | |
|---|-----|
| Table 1.1: Photolithography Advantages and Disadvantages..... | 14 |
| Table 3.1: Etch Barrier Composition..... | 59 |
| Table 3.2: Summary of α Values for 4 wt% Dacocur 1173 | 67 |
| Table 3.3: Alpha (α) Using 1 wt% Darocur 1173. | 68 |
| Table 3.4: Parameters for k_t Model..... | 87 |
| Table 3.5: Initial Conditions for Model | 89 |
| Table 5.1: Characteristics of the Polymers Used In This Study | 145 |
| Table 6.1: Advantages of Low-Viscosity Photocurable Materials for Each Processing Step. | 156 |
| Table 6.2: Materials Formulations | 159 |
| Table 6.3: Material Properties..... | 163 |
| Table 7.1: Matrix of Experiments to Study Linear Stability Analysis | 179 |
| Table 9.1: Procedure Purposes..... | 246 |
| Table 9.2: Summary of Results..... | 249 |
| Table 9.3: XPS Results | 253 |
| Table C.1: Key Materials Used in Thesis | 297 |
| Table C.2: Experimentally Determined Cauchy Coefficients | 298 |
| Table C.3: Solution Formulations and Spin Speeds | 299 |

List of Figures

| | | |
|--------------|---|----|
| Figure 1.1: | A 3-D cut away rendering of a transistor..... | 1 |
| Figure 1.2: | Scanning electron micrograph of 80 nm photoresist lines..... | 2 |
| Figure 1.3: | The photolithographic process..... | 5 |
| Figure 1.4: | Photolithography process illustration | 6 |
| Figure 1.5: | Various photolithographic strategies. (a) Contact lithography (b) Proximity printing (c) Projection lithography. | 7 |
| Figure 1.6: | Light diffracts as it exits the mask, degrading the ideal image..... | 9 |
| Figure 1.7: | Moore’s Law..... | 10 |
| Figure 2.1: | Process diagrams for (a) thermal nanoimprint lithography and (b) ultraviolet-assisted NIL (UV-NIL). | 23 |
| Figure 2.2: | Scanning electron micrographs of lines printed using UV-NIL.. | 23 |
| Figure 2.3: | Trade-off between throughput and resolution..... | 25 |
| Figure 2.4: | Template fabrication process. | 26 |
| Figure 2.5: | Potential failure mechanisms for NIL..... | 27 |
| Figure 2.6: | A representative UV-NIL formulation..... | 32 |
| Figure 2.7: | SEM images of sequential imprints. A small defect in the template has been replicated faithfully in each image, illustrating the high resolution of NIL..... | 33 |
| Figure 2.8: | A unique, high resolution mold is formed by selectively etching $\text{Al}_{0.7}\text{Ga}_{0.3}\text{As}$ from the cleaved edge of a multilayer film stack..... | 34 |
| Figure 2.9: | Atomic force microscopy (AFM) images of (a) a carbon nanotube on a flat substrate serving as a ‘mold’. (b) The mold is replicated in a polymerizable liquid (PDMS) multiple times (c), (d)..... | 35 |
| Figure 2.10: | An example “breakthrough” etch process utilized to remove the residual layer between the imprinted features | 36 |
| Figure 2.11: | Planarization strategy for imprinting over topography | 38 |
| Figure 2.12: | Filling issues associated with NIL occur when the mold contains both large and small patterns | 39 |
| Figure 3.1: | The SFIL process. | 56 |
| Figure 3.2: | The effects of oxygen on radical based polymerizations..... | 57 |

| | |
|--|-----|
| Figure 3.3: Oxygen diffuses into the perimeter of the etch barrier under the template..... | 58 |
| Figure 3.4: General free radical reaction mechanism..... | 61 |
| Figure 3.5: Determination of α for a 4 wt% Darocur 1173 system..... | 67 |
| Figure 3.6: Kinetic comparison of individual etch barrier components..... | 70 |
| Figure 3.7: Etch barrier polymerization (31.8 mW/cm ²) | 71 |
| Figure 3.8: Rate of polymerization analysis..... | 72 |
| Figure 3.9: Dark polymerization technique..... | 75 |
| Figure 3.10: Relative intensity spectrum of Hg arc lamp used in prototype SFIL tool. | 78 |
| Figure 3.11: The extinction coefficient (cm ² /mmol) for Darocur 1173 as a function of wavelength | 78 |
| Figure 3.12: k_t and k_p (L/mol·sec) measured for SFIL etch barrier..... | 82 |
| Figure 3.13: k_t data from Figure 3.12 fit with diffusion based model..... | 87 |
| Figure 3.14: Comparison of experimentally determined kinetic data with model..... | 88 |
| Figure 3.15: A cross section of the etch barrier during polymerization..... | 90 |
| Figure 3.16: Time-spatial model of etch barrier polymerizationn. | 91 |
| Figure 3.17: Snapshot of etch barrier polymerization at 10 seconds. | 92 |
| Figure 3.18: Effects of initiation on the diffusion length of oxygen | 94 |
| Figure 4.1: A simple schematic of the pillar formation process..... | 105 |
| Figure 4.2: Patterned upper electrodes results | 107 |
| Figure 4.3: Schematic representation of the capacitor device..... | 110 |
| Figure 4.4: Diagram of voltage drop through film stack..... | 113 |
| Figure 4.5: A non-dimensional plot of S versus K for various values of B. | 118 |
| Figure 4.6: Characteristic formation time (sec) as a function of voltage | 120 |
| Figure 4.7: Experimental configuration used to form pillars.. | 124 |
| Figure 5.1: Illustration of the PMMA / PS / air trilayer system..... | 131 |
| Figure 5.2: PMMA / PS / air trilayer..... | 132 |
| Figure 5.3: Trilayer experimental configuration. | 133 |
| Figure 5.4: SEM image of the trilayer structures. | 135 |

| | |
|---|-----|
| Figure 5.5: SEM image of a single trilayer structure.. | 136 |
| Figure 5.6: SEM image of a single ‘cage’ after cyclohexane rinse..... | 137 |
| Figure 5.7: Cross-sectional SEM image of a cleaved single hollow pillar. | 137 |
| Figure 5.8: Formation mechanism of ‘cage’ structures..... | 138 |
| Figure 5.9: SEM image of PMMA structures obtained with hydrophobic chromium layer and treated with cyclohexane. | 141 |
| Figure 5.10: SEM images of PMMA basins providing evidence of tendrils coarsening. | 142 |
| Figure 5.11: Schematic of trilayer “inversion” with PMMA on top of PS.. | 144 |
| Figure 5.12: Overview of 8 kg/mol PS on 32 kg/mol PMMA..... | 146 |
| Figure 5.13: Acetic acid rinse reveals PS cores and cyclohexane rinse reveals complementary PMMA shell..... | 146 |
| Figure 5.14: Overview of 8 kg/mol PS on 99 kg/mol PMMA shows undulations with several PS breakthroughs. | 148 |
| Figure 5.15: PMMA dewetting determines the regions where pillars form for a sample consisting of 32 kg/mol PMMA on 157kg/mol PS. | 149 |
| Figure 5.16: 32 kg/mol PMMA on 157 kg/mol PS..... | 150 |
| Figure 6.1: Functional materials studied. | 158 |
| Figure 6.2: Active gap tool schematic..... | 161 |
| Figure 6.3: Kinetic profile for each low viscosity material system..... | 164 |
| Figure 6.4: Optical micrograph of thiol-vinyl ether pillars.. | 166 |
| Figure 6.5: SEM close up on cleaved pillar revealing the extremely small residual layer surrounding the pillar. | 167 |
| Figure 6.6: Tilt-view SEM of thiol-vinyl ether pillars. | 170 |
| Figure 7.1: Impact of changing the electrode gap on the pillars | 177 |
| Figure 7.2: Optical micrograph of pillars and an accompanying FFT spectra. | 180 |
| Figure 7.3: Pillar distribution of the array shown in Figure 7.2. | 181 |
| Figure 7.4: Comparison of the measured characteristic wavelength versus the theoretical wavelength for the thiol-ene system. | 184 |
| Figure 7.5: Characteristic wavelength versus e-field in reduced coordinates. | 186 |
| Figure 7.6: Theoretical spacing and time scale of formation versus fill factor. | 187 |
| Figure 7.7: A temporal view of the nucleation growth process | 190 |

| | |
|--|-----|
| Figure 7.8: Images of thiol-ene pillars with corresponding FFT spectra.. | 191 |
| Figure 7.9: Patterned electrodes to dictate the position of pillars. | 192 |
| Figure 7.10: Illustration of the key features on a patterned template..... | 194 |
| Figure 7.11: Thiol-ene pillar arrays formed using a patterned electrode.. | 194 |
| Figure 7.12: Demonstration of the use of a patterned electrode to create structures of arbitrary shape..... | 195 |
| Figure 7.13: Optical micrograph of thiol-ene structures formed by electric field assisted assembly using a pentagon patterned electrode. | 195 |
| Figure 7.14: Micrograph of pillars formed by applying an AC voltage with $V = 200$ Vrms and $f = 100$ Hz.. | 197 |
| Figure 7.15: Micrograph of pillars formed by applying an AC voltage with $V = 40$ Vrms and $f = 2$ MHz..... | 198 |
| Figure 7.16: Example of Faraday waves on a liquid surface..... | 199 |
| Figure 7.17: Photograph of piezo configuration..... | 201 |
| Figure 7.18: Micrographs of pillars formed by applying ultrasonic waves at different burst rates. | 203 |
| Figure 7.19: Flexural modes on a silicon plate at 6.58 MHz. | 204 |
| Figure 8.1: Tilt-view scanning electron micrograph of low viscosity thiol- ene pillars with low aspect ratios. | 208 |
| Figure 8.2: Theoretical aspect ratio versus fill factor..... | 210 |
| Figure 8.3: Photograph of the Mad City Labs nanopositioner | 212 |
| Figure 8.4: Schematic of substrate alignment scheme. | 213 |
| Figure 8.5: A labeled photograph of the substrate alignment scheme. | 213 |
| Figure 8.6: Schematic of the nanopositioner..... | 214 |
| Figure 8.7: Tilt-view photographs of the nanopositioner..... | 215 |
| Figure 8.8: SEM image of thiol-ene pillars formed using the Mad City Labs nanopositioner..... | 215 |
| Figure 8.9: Labeled illustration of the active gap tool..... | 217 |
| Figure 8.10: Schematic of the template and the gap monitoring scheme. | 217 |
| Figure 8.11: Photographs of the active gap tool.. | 219 |
| Figure 8.12: Photograph of a 4 inch wafer illuminated with light..... | 220 |
| Figure 8.13: SEM images of non-stretched pillars | 220 |

| | |
|---|-----|
| Figure 8.14: SEM images of stretched pillars. | 221 |
| Figure 8.15: Liquid bridge stability diagram. | 222 |
| Figure 8.16: High aspect ratio pillar formed using the active gap tool..... | 224 |
| Figure 8.17: SEM images of high aspect ratio thiol-ene fibrils. | 225 |
| Figure 8.18: A longhorn formed via a patterned electrode resolves to a single pillar upon stretching. | 226 |
| Figure 8.19: Small electrode gaps (~560 nm) formed using the active gap tool with a sensing ledge template. | 227 |
| Figure 8.20: PCL pillars stretched during upper electrode removal. | 228 |
| Figure 8.21: SEM images of PLA fibril pillar arrays. | 229 |
| Figure 8.22: PLA pillars formed at 100 °C, 200 V, 2.5 μm gap. | 230 |
| Figure 8.23: SEM images of PMMA pillars at various temperatures..... | 231 |
| Figure 8.24: PLA rheological properties plotted at 0.01 s^{-1} frequency..... | 232 |
| Figure 8.25: PMMA rheological properties plotted at 0.001 s^{-1} frequency | 232 |
| Figure 8.26: PMMA undulations formed at 140°C. | 235 |
| Figure 8.27: SEM images of PLA pillars at different stages of growth. | 235 |
| Figure 9.1: Comparison of the transparency of an ITO film compared to a thin chromium film.. | 242 |
| Figure 9.2: Treated templates (i.e. upper electrode) cleanly release the pillars upon separation. | 242 |
| Figure 9.3: Conventional mechanism for surface silylation reaction..... | 243 |
| Figure 9.4: Photograph of the ITO slides before and after mechanically cleaning.. | 247 |
| Figure 9.5: Peel test illustration..... | 248 |
| Figure 9.6: Water droplet on treated ITO surface using base method (a) pre- durability stress (b) post-durability stress | 250 |
| Figure 9.7: Typical peel force plot | 251 |
| Figure 9.8: Optical micrographs of the ITO template surface..... | 254 |
| Figure 9.9: SEM of pillars formed using a surface treated template..... | 255 |
| Figure 9.10: SEM of pillars formed using an untreated template..... | 255 |
| Figure 10.1: Optical micrographs of pillar arrays..... | 262 |

| | |
|--|-----|
| Figure 10.2: SEM image of thiol-ene pillars with evidence of electrocuring..... | 269 |
| Figure A.1: Radical concentration as a function of time under constant irradiation. | 270 |
| Figure A.2: Illustration of the rotating sector experimental approach..... | 271 |
| Figure A.3: Representative radical concentration as a function of time for various rotating sector frequencies. | 272 |
| Figure A.4: Real time IR data of etch barrier polymerization at various rotating sector frequencies.. | 272 |
| Figure B.1: Process diagram for the mixing system.. | 289 |
| Figure B.2: Typical dye concentration data for the pre-mixer and post-mixer measured spectroscopically.. | 291 |
| Figure B.3: Example SPC charts from the pre-mixer detector during mixing. .. | 292 |
| Figure B.4: Example SPC charts from the post-mixer detector during mixing. . | 293 |
| Figure C.1: Spin curves for thiol-ene (1:1 by weight) in toluene | 301 |
| Figure C.2: Spin curves for thiol-ene (1:1 by weight) in PGMEA | 302 |
| Figure C.3: Top down view of process to from upper electrodes. | 303 |
| Figure C.4: Cyclic voltagram of thiol-ene in MECN. | 304 |
| Figure C.5: Cyclic voltagram of ene in MECN. | 305 |
| Figure C.6: Cyclic voltagram of thiol in MECN. | 305 |
| Figure C.7: Cyclic voltagram of thiol in MECN. | 306 |
| Figure C.8: DSC plots for the polymers utilized in this thesis. | 307 |
| Figure C.9: FFT spectra for an ideally closed-pack array of circles..... | 312 |
| Figure C.10: FFT analysis strategy. | 314 |
| Figure C.11: Typical FFT image.. | 315 |

Chapter 1

Lithography Introduction

1.1 THE IMPORTANCE OF PATTERNING

Electronic technologies have become pervasive in everyday life. Computers, cell phones, digital cameras, and the internet are examples of electronic tools that directly and indirectly improve the quality of life. The rapid progress evident in these technologies can be almost exclusively attributed to advances in the semiconductor industry. Microlithography is the cornerstone technology that has enabled the rapid growth of the semiconductor industry.¹ Microlithography is a process capable of patterning small features on a substrate, which can be utilized to create transistors (Figure 1.1), wires, and other active components required for a functioning chip.

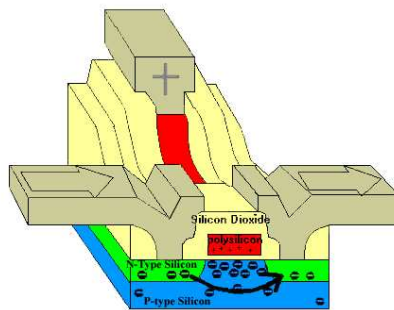


Figure 1.1: A 3-D cut away rendering of a transistor. Electrons flow from the source to the drain when a voltage is applied to the gate. The components in a transistor are typically defined by microlithography.²

Microlithographic progress is defined by the ability to pattern components with ever decreasing size. In electronics, smaller features correspond to faster performance and to a decreased cost on a per transistor (or per function) basis since more of the

smaller components can be patterned in the same amount of processing time. Thus, the ultimate goal of advanced lithography is to generate fields of small features rapidly and economically such that the final devices are fast and inexpensive. State of the art lithography tools are capable of creating features smaller than 100 nm,³ which is approximately 1/1000th the diameter of a human hair. Figure 1.2 is a scanning electron micrograph of 80 nm lines patterned on a substrate with photolithography.

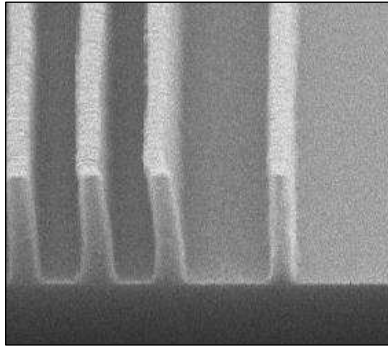


Figure 1.2: Scanning electron micrograph of 80 nm photoresist lines on a substrate.

The most pervasive and economically significant use of lithography is found in the electronics industry. However, the ability to rapidly generate large numbers of nanoscale features with great precision is critical to the advancement of many areas of nanotechnology. Nanostructures (e.g., nanoparticles and nanowires) are garnering significant attention because of the unique properties that arise from their size (generally defined as structures <100 nm).⁴ Nanostructures are being explored as tools for numerous areas, including biological applications (labeling, drug delivery, etc),⁵ solar cells,⁶⁻⁸ and nanocomposites.⁹ Advanced lithography techniques offer promising routes to rapidly produce nanostructures. In addition to nanotechnology, numerous integrated devices rely on patterning techniques to function properly. For example, microlithography is used in the fabrication of micro-electro-mechanical systems

(MEMS), photonic devices, micro-fluidic systems, biosensors, and lab on a chip devices.¹⁰⁻¹⁷

1.2 GENERAL PATTERNING STRATEGIES: “TOP-DOWN” VS. “BOTTOM-UP”

There are numerous lithographic techniques ranging from established industrial techniques to laboratory curiosities.¹⁸⁻²⁰ The two general fabrication strategies are “top-down” and “bottom-up” patterning. Top-down patterning relies on methods to directly write or transfer patterns using external sources (e.g. light, electrons, ions, embossing). Historically, the semiconductor industry has relied almost exclusively on top-down strategies such as photolithography, embossing, and e-beam lithography for fabrication. Although these are extremely effective patterning methods, many traditional top-down nanofabrication techniques (e.g. photolithography and e-beam lithography) are limited by their expense, inaccessibility, and requirement of a planar patterning surface. Furthermore, these traditional methods are restricted to a small class of materials and thus are difficult to adapt to a number of important problems. Imprint lithography has recently garnered significant attention because it is an accessible technology that avoids the use of the expensive projection optics associated with traditional photolithography.²¹ It is also applicable to a wide range of materials and has seemingly unlimited resolution. A significant portion of this thesis will focus on imprint lithography.

The “bottom-up” approach to patterning utilizes the rational design of molecules, colloids, and small particles to create interactions that ultimately result in the assembly of useful structures and patterns.²² This method loosely mimics the way nature forms useful features. Structures formed via bottom-up processing often lack the long range order necessary in many applications. Ultimately, the nanofabrication techniques of the future will likely make use of the best attributes of both top-down and bottom-up approaches

through “directed assembly” or “templated assembly” in which the formation of patterns is guided by external bounds.²³ As the name implies, “templated assembly” uses physical or molecular “templates” to guide product formation. Examples of templated assembly strategies include use of viral cages,²⁴ DNA,²⁵⁻²⁸ and nanostructures.²⁹⁻³² Directed assembly strategies rely on an external driving force to guide the assembly process. Directed assembly strategies include use of electric fields,^{33,34} chemically³⁵⁻³⁷ and topographically³⁸⁻⁴⁰ patterned substrates, and shear forces⁴¹ to improve the long range order of the assembling medium (e.g. block co-polymers⁴²). A significant portion of this thesis will focus on the use of electric fields to direct the formation of structures across a substrate.

The advantages and disadvantages of traditional lithographic techniques (i.e. photolithography) will be discussed to provide context for the alternative lithographies (i.e. imprint lithography and electric field assisted assembly) discussed in this thesis.

1.3 PHOTOLITHOGRAPHY

Photolithography, illustrated in Figure 1.3, is the cornerstone technology responsible for the electronics revolution, as it has enabled the formation of ultra small integrated circuits.^{1,43,44} In photolithography, patterns of light are generated using a mask (also called a reticle) that selectively blocks the passage of light. The image generated by the mask is focused on to a photosensitive film called a photoresist. The photoresist is typically a thin, organic, polymer film deposited on a substrate (e.g. a silicon wafer) by spin casting. Once exposed to light, the solubility of the resist material is altered in a manner that is material specific.

There are two general varieties of photoresists as shown in Figure 1.3. A positive photoresist becomes soluble when exposed to light, whereas a negative resist becomes

insoluble. The soluble regions of the film are subsequently removed using a “developer” solution. The composition of the developer is specific to the photoresist system, some photoresists are soluble in slightly basic aqueous solutions where as others require organic solvents.

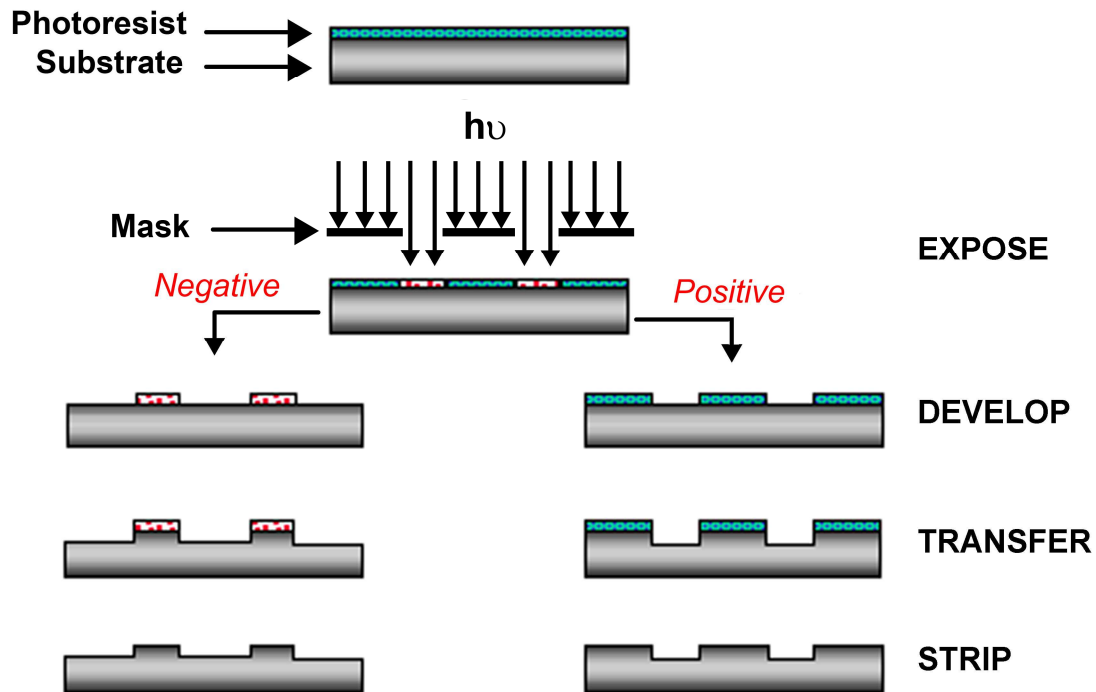


Figure 1.3: The photolithographic process. A substrate is coated with a thin polymeric film called a photoresist. A pattern of light is projected from a mask onto the film, altering the solubility of the exposed regions of the film. Exposed regions of negative resists become insoluble whereas positive resists becomes soluble in a liquid developer solution. The resulting pattern is transferred to the substrate (typically by etching) and the sacrificial resist is removed.

Once the photoresist film is developed the pattern is transferred to the underlying substrate through subsequent etching steps. The term “resist” in the word photoresist refers to the ability of the polymeric film to withstand etching steps utilized to transfer the pattern to the substrate. In addition to etching, other common transfer techniques

include metal deposition (“lift off”) and ion bombardment. In the semiconductor industry, resists serve as a sacrificial material that is removed after transferring the pattern to the substrate. For many nanotechnology applications, creating functional polymeric features may be the ultimate goal, and thus the features would not be sacrificial in nature.

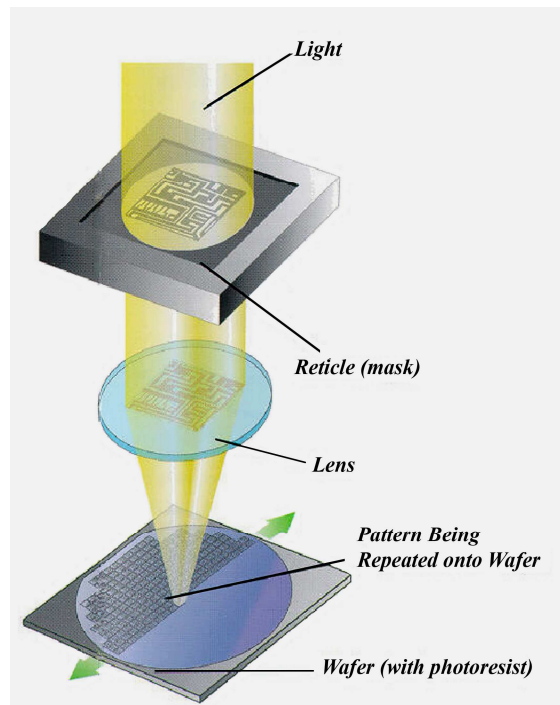


Figure 1.4: Photolithography process illustration. Light passes through a mask that transmits and blocks light in a binary fashion. This projected pattern of light is focused by a series of lenses onto a silicon wafer. The wafer is covered with a photosensitive film called a photoresist that changes solubility upon exposure to the light.⁴⁵

1.3.1 Photolithographic Approaches and Limitations

Photolithographic patterning relies on shining light through a photomask, which defines an aerial light pattern. The photomasks are typically fabricated from quartz or fused silica, materials that are transparent down to ultra-violet wavelengths. The

photomask is patterned with chromium to selectively block the transmission of light. There are three general approaches to the utilization of the photomask. Contact lithography places the mask directly on the photoresist. Proximity lithography leaves a small gap between the mask and the photoresist. Projection lithography utilizes optics to focus the light on the resist after it exits the photomask. These three strategies are shown in Figure 1.5.

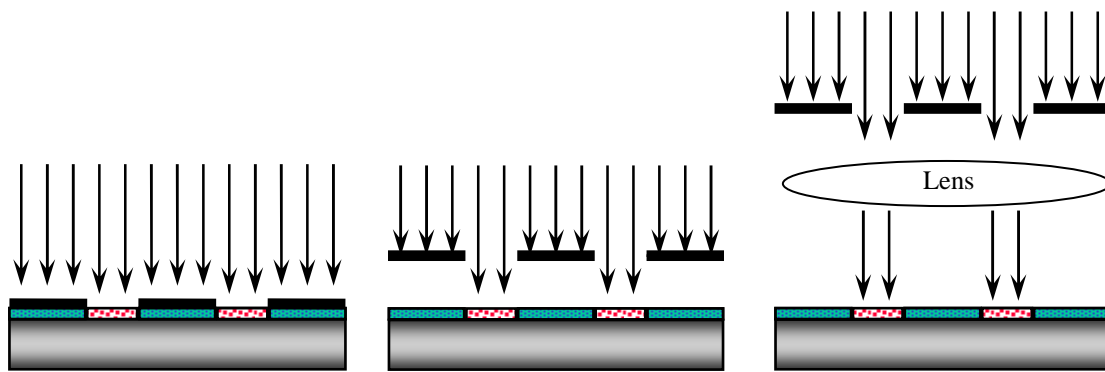


Figure 1.5: Various photolithographic strategies. (a) Contact lithography (b) Proximity printing (c) Projection lithography. The arrows represent light as it passes through a mask and the other symbols are consistent with Figure 1.3.

Contact lithography is the oldest photolithographic technique.¹ One disadvantage of this technique is that the photomask and photoresist come into direct contact, increasing the possibility of defect generation on both surfaces. Proximity printing, which was popular in the early 1970s, avoids this issue by providing a small separation between the mask and resist, at the expense of decreased resolution. Since light diffracts as it exits the mask, the quality of the light pattern degrades with increasing distance from the mask. Projection lithography offers the advantages of proximity printing while maintaining high resolution. The high resolution is accomplished through focusing optics, which capture the diffracted light from the mask and focus it onto the substrate. The use

of focusing optics increases the cost of the lithographic tool, but provides a number of added benefits.

The incorporation of optics allows for feature reduction, resulting in patterns on the substrate that are typically $1/4^{\text{th}}$ the size of those on the mask. This projection process is similar to an overhead projector, but the patterns on the photomask are reduced rather than expanded. The tools used to project the photomask patterns are referred to as steppers or scanners. To achieve high resolution with a reasonably sized lens, a stepper images only a portion of the wafer at one time. The image process is repeated in a step wise manner over the substrate until the entire wafer has been patterned, as shown in Figure 1.4. In contrast, a scanner images only a portion of the mask at any one time while it continuously translates or “scans” both the substrate and the mask (at carefully synchronized rates in opposite directions) until the full mask field is exposed.

The resolution of photolithography is limited by the diffraction of light, as depicted in Figure 1.6. The diffraction optics of photolithography are described by Fourier transform mathematics and the optical resolution limit is described by the Rayleigh criterion,

$$R = k \frac{\lambda}{NA} \quad (1.1)$$

where R represents the minimum feature resolution (i.e. the size of the smallest features which can be patterned) and k can be thought of as scaling factor that in practice varies between 0.3-0.8.⁴⁶ λ is the wavelength of light utilized and NA represents the numerical aperture of the lens. The numerical aperture is proportional to the sine of the maximum half angle at which light can be diffracted and still be captured by the lens system. It is essentially a measure of lens size and thus how much light (i.e. information)

may be captured by the lens. In air the NA can vary from 0 to 1. Currently, first rate steppers operate at NA's larger than 0.8. A well optimized photolithographic tool can print features down to almost half the wavelength of the exposure source. (With alternating phase-shifting masks, the stepper may approach an imaging resolution one quarter of the exposure wavelength.) In general the Rayleigh criterion suggests two routes to improved imaging resolution: 1) wider lenses and 2) lower imaging wavelengths.

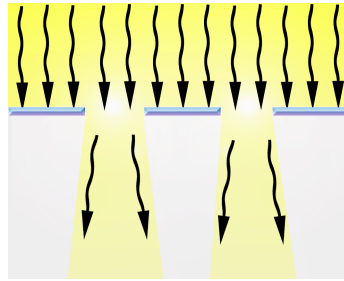


Figure 1.6: Light diffracts as it exits the mask, degrading the ideal image.

Advancements in lithographic resolution have largely been responsible for the exponential improvements in computing technology seen over the past fifty years. In 1965 Gordon Moore, the first CEO of Intel, observed that the number of transistors on a chip had been doubling every 18-24 months.⁴⁷ That prophetic observation has held true for many years and is now referred to as Moore's Law. A plot illustrating Moore's Law is shown in Figure 1.7. Although not based on any laws of physics, this "law" is more of a self-fulfilling prophecy as it guides the pace of technological development necessary to stay afloat in a competitive semiconductor industry. Despite significant technical challenges, Moore's Law is expected to continue to be fulfilled into the foreseeable future based on lithographic advances.^{3,48}

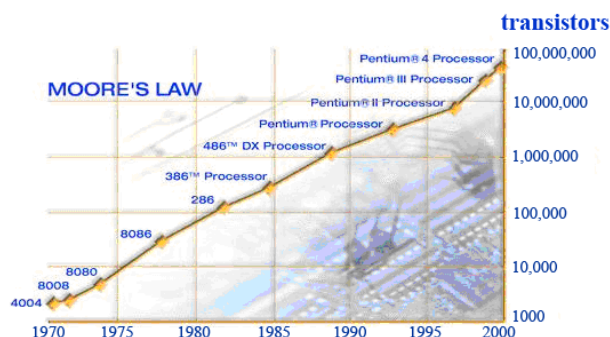


Figure 1.7: Moore's Law. The number of transistors on a chip has doubled every 18-24 months for the past 40 years largely due to advances in lithography.⁴⁹

Since lithography determines the size of the transistor components, there is a constant pressure on lithographers to improve resolution. Resolution is enhanced by making lenses as large as economically feasible and by decreasing the exposure wavelength. Each decrease in wavelength is accompanied by a litany of technical challenges including the generation of new exposure sources, optics, and resist materials. The current state of the art photolithography utilizes 193 nm wavelength light.⁵⁰ Furthermore, low wavelength light (<250 nm) tends to absorb strongly within organic materials, making it difficult to transfer patterns through the depth of the resist. Consequently, great care must be taken to properly design resist materials. Finally, many traditional optical components (e.g. glass) are opaque at sub-200 nm wavelengths. Processing at low wavelengths requires either switching to reflecting optics or using exotic materials (e.g. CaF_2) that make the equipment very expensive.

1.4 THE FUTURE OF PHOTOLITHOGRAPHY

Photolithography has been the technology of choice for the semiconductor industry for over forty years and will continue to be until it is no longer a competitive

technology. Photolithography is a complex process that relies on the ability to merge together a variety of technologies. For example, lowering the irradiation wavelength may require new stepper optics and exposure sources in addition to new photoresists and processing guidelines. As a consequence of these process complexities, the semiconductor industry has developed a unique business model that relies on consensus to guide the development of future technologies utilized in the industry. The semiconductor industry annually publishes a document called the International Technology Roadmap for Semiconductors (ITRS) to guide the research and development performed by the universities and sub-industries that are largely responsible for developing the many technologies (e.g. optics, materials, etc) associated with photolithography.³ The industrial roadmap has identified several technologies as possible replacements for 193 nm lithography, the current state of the art.³ Several of these options are briefly discussed in the following sections.

1.4.1 Immersion Lithography

Immersion lithography is an extension of photolithography that provides improved imaging by placing a fluid between the final lens element and substrate.⁵¹⁻⁵³ If the immersion fluid has an index of refraction higher than air ($n = 1$) at the exposure wavelength, the imaging optics can be designed with numerical aperture (NA in Equation 1.1) larger than 1. With proper design, a system with a higher NA improves imaging resolution. Without redesign of the imaging optics inserting a liquid between final lens and substrate only works to improve depth of focus. The optical properties of the immersion fluid are extremely sensitive to impurities, bubbles, and temperature fluctuations. Immersion lithography appears to be a viable commercial technology,

although challenges still remain in designing non-leaching resists and reliable liquid dispense systems.

1.4.2 Extreme Ultraviolet (EUV) Lithography

EUV lithography^{50,54-62} is, in a sense, an extension of optical lithography, but it is perhaps more closely related to X-ray lithography. In fact EUV has been referred to as “soft X-ray” lithography. EUV lithography relies on 13.4 nm light, an extremely short wavelength that is capable of lowering resolution past the state of the art (193 nm) according to Rayleigh’s criterion (Equation 1.1). There are, however, many challenges to overcome before EUV is a viable patterning option. First, an EUV source that generates a sufficient flux of photons must be developed. Second, the system must operate in ultra-high vacuum since nearly all materials (including air) absorb EUV radiation. Third, reflectance optics must be developed since traditional quartz masks absorb EUV radiation. Finally, resist materials must be developed that are capable of imaging EUV light. The prototype EUV tools are extremely expensive and therefore are only accessible to the largest companies.

1.4.3 Electron-beam (E-beam) Lithography

Patterning by e-beam lithography is achieved by rastering a “beam” of electrons across a photosensitive substrate.⁵⁰ The irradiated electrons induce a chemical change in the resist that corresponds to a solubility switch in the exposed regions of the film. The electrons have a very small wavelength (deBroglie wavelength, <1 nm), allowing for high resolution patterning. In contrast to photolithography, which utilizes masks and lens elements, e-beam lithography uses electric fields to direct and focus the electron beam.

Patterning large areas is a lengthy process since the narrow beam of electrons must be serially rastered across the substrate many times. The exposed regions of the resist require a certain dose of electrons to alter the solubility. The flux of electrons in the beam is limited because individual electrons repel one another, which implies that the beam must be rastered slowly across the surface to achieve the threshold dose, thereby increasing the processing time.

E-beam lithography does not require a mask, an expensive component of photolithography. Consequently, “maskless lithography” has been proposed as a high resolution alternative to photolithography,³ but currently the throughput is too low to be practical. A similar technology called projection e-beam lithography is being investigated in which a flux of electrons is directed through a stencil type mask that determines the pattern.⁵⁰ Again, the flux, and hence the processing speed, is limited by the repulsion of individual electrons.

1.4.4 Nanoimprint Lithography (NIL)

The concept of NIL is to harness the high resolution capabilities of e-beam lithography without the drawback of limited throughput.⁶³ E-beam lithography, a slow, yet high resolution process, is utilized to create a master “mold” with protrusions and recesses. This topographically patterned mold is then pressed into a polymeric material, transferring the high resolution pattern rapidly across the surface. Imprint lithography has been identified as a potential replacement for photolithography³ due to its high resolution and ease of use. Imprint lithography is introduced in more detail in Chapter 2 and discussed in Chapter 3.

1.5 ALTERNATIVE LITHOGRAPHY

The popularity of photolithography can be attributed to its ability to rapidly generate numerous small features over a large area. Although there are many advantages to photolithography, there are some limitations, as listed in Table 1.1. First, the process resolution is limited by the wavelength of light and using wavelengths of light beyond 193 nm (the state of the art) is extremely challenging. Second, the highest resolution processes require very expensive projection optics that are largely inaccessible to most universities and basic research labs. Third, the process is limited to planar substrates as there is only one plane that provides perfect focus of the projected photo-image.

Table 1.1: Photolithography Advantages and Disadvantages

| Advantages | Disadvantages |
|-------------------------------------|---|
| 1. Established processing knowledge | 1. Expensive (~\$25 million for one tool) |
| 2. Established infrastructure | 2. Resolution limited by light wavelength |
| 3. High-throughput | 3. Limited to planar substrate |
| 4. Non-contact / minimum defects | 4. Limited materials set |

The cost and resolution limitations of traditional lithographic techniques have led numerous researchers to explore alternative lithographic strategies.^{18-20,42,50,64} Examples of these techniques include soft lithography,⁶⁴ block copolymer self-assembly,⁴² colloidal lithography,⁶⁵⁻⁶⁷ shadow lithography,⁶⁸ etc.¹⁸⁻²⁰ The ultimate goal is to develop a technique that has all the advantages of photolithography without the drawbacks, a requirement to be relevant to the semiconductor industry. However, there are numerous industries and academic laboratories that do not have the same strict processing

requirements as the semiconductor industry and consequently, would benefit from accessible, low cost patterning technologies. Examples include MEMS, biosensors, photonic devices, membranes, and nanostructured materials. A significant portion of this thesis will be focused on an electric field assisted technique that is capable of spontaneously generating arrays of pillar structures using inexpensive laboratory equipment. This technique is introduced in Chapter 4 and elaborated in Chapters 5-10.

1.6 SUMMARY

The ability to rapidly generate patterns in a controlled manner is critical to the development of semiconductors and nanotechnology, both commercially and academically. Photolithography is an established patterning tool utilized by a number of industries, most notably the semiconductor industry. Photolithography is capable of rapidly producing sub-100 nm features on a substrate through the use of focused patterns of light, but the process limited by a number of factors including cost and resolution. The goal of alternative lithography is to provide patterning options that overcome one or more of the limitations of photolithography. Imprint lithography, as discussed in Chapter 2 and 3, is capable of patterning features with higher resolution than traditional photolithography, at a fraction of the cost. The remainder of the thesis (Chapters 4-10) is focused on electric field assisted lithography, an elegant alternative patterning strategy that is accessible to academic researchers because of its low cost. Although the features created using this technique are larger than current photolithographic standards, the technique is appealing because of its simplicity and accessibility.

1.7 REFERENCES

1. Thompson, L. F.; Willson, C. G.; Bowden, M. J., *Introduction to microlithography*. 2nd ed.; American Chemical Society: Washington, DC, 1994; p xiv, 527.
2. <http://library.thinkquest.org> (May 1, 2006).
3. *International Technology Roadmap for Semiconductors*. Semiconductor Industry Association: San Jose, CA, 2004.
4. Di Ventra, M.; Evoy, S.; Heflin, J. R., *Introduction to nanoscale science and technology*. Kluwer Academic Publishers: Boston, 2004; p xiii, 611.
5. Winters, J. O., *Nanostructures for Cellular Engineering*. Wiley VHC: 2006; Vol. 8.
6. Gur, I.; Fromer, N. A.; Geier, M. L.; Alivisatos, A. P., Air-stable all-inorganic nanocrystal solar cells processed from solution. [Erratum to document cited in CA143:369944]. *Science* **2005**, 310, (5754), 1618.
7. Milliron, D. J.; Hughes, S. M.; Cui, Y.; Manna, L.; Li, J.; Wang, L.-W.; Alivisatos, A. P., Colloidal nanocrystal heterostructures with linear and branched topology. *Nature* **2004**, 430, (6996), 190-195.
8. Huynh, W. U.; Dittmer, J. J.; Alivisatos, A. P., Hybrid nanorod-polymer solar cells. *Science* **2002**, 295, (5564), 2425-2427.
9. Ajayan, P. M.; Schadler, L. S.; Braun, P. V., *Nanocomposite science and technology*. Wiley-VCH: Weinheim, Germany 2003; p ix, 230.
10. Marty, J. D.; Marty, J. D., *Microlithography/molecular imprinting*. 1st ed.; Springer: New York, NY, 2005.
11. Gardner, J. W.; Varadan, V. K.; Awadelkarim, O. O., *Microsensors, MEMS, and smart devices*. J. Wiley: Chichester; New York, 2001; p xvi, 503.
12. Cass, A. E. G., *Biosensors: a practical approach*. IRL Press at Oxford University Press: Oxford [England]; New York, 1990; p xv, 271.
13. Giardi, M. T.; Piletska, E. V., *Biotechnological applications of photosynthetic proteins: biochips, biosensors, and biodevices*. Landes Bioscience;Springer: New York, 2006.

14. Minteer, S. D., *Microfluidic techniques: reviews and protocols*. Humana Press: Totowa, N.J., 2006.
15. Nguyen, N.-T.; Wereley, S. T., *Fundamentals and applications of microfluidics*. Artech House: Boston, MA, 2002; p xiii, 471.
16. Tabeling, P., *Introduction to microfluidics*. Oxford University Press: New York, 2005.
17. Xia, Y.; Gates, B.; Li, Z.-Y., Self-assembly approaches to three-dimensional photonic crystals. *Advanced Materials* **2001**, 13, (6), 409-413.
18. Sotomayor Torres, C. M., *Alternative lithography: unleashing the potentials of nanotechnology*. Kluwer Academic/Plenum: New York, 2003; p xx, 333.
19. Gates, B. D.; Xu, Q.; Love, J. C.; Wolfe, D. B.; Whitesides, G. M., Unconventional nanofabrication. *Annual Review of Materials Research* **2004**, 34, 339-372.
20. Gates, B. D.; Xu, Q.; Stewart, M.; Ryan, D.; Willson, C. G.; Whitesides, G. M., New Approaches to Nanofabrication: Molding, Printing, and Other Techniques. *Chemical Reviews* **2005**, 105, (4), 1171-1196.
21. Guo, L. J., Recent progress in nanoimprint technology and its applications. *Journal of Physics D: Applied Physics* **2004**, 37, (11), R123-R141.
22. Whitesides, G. M.; Grzybowski, B., Self-assembly at all scales. *Science* **2002**, 295, (5564), 2418-2421.
23. Stoykovich, M. P.; Mueller, M.; Kim, S. O.; Solak, H. H.; Edwards, E. W.; de Pablo, J. J.; Nealey, P. F., Directed assembly of block copolymer blends into nonregular device-oriented structures. *Science* **2005**, 308, (5727), 1442-1446.
24. Chen, C.; Daniel, M.-C.; Quinkert, Z. T.; De, M.; Stein, B.; Bowman, V. D.; Chipman, P. R.; Rotello, V. M.; Kao, C. C.; Dragnea, B., Nanoparticle-Templated Assembly of Viral Protein Cages. *Nano Letters* **2006**, 6, (4), 611-615.
25. Stanca, S. E.; Eritja, R.; Fitzmaurice, D., DNA-templated assembly of nanoscale architectures for next-generation electronic devices. *Faraday Discussions* **2006**, 131, 155-165.
26. Ongaro, A.; Griffin, F.; Beecher, P.; Nagle, L.; Iacopino, D.; Quinn, A.; Redmond, G.; Fitzmaurice, D., DNA-templated assembly of conducting gold nanowires between gold electrodes on a silicon oxide substrate. *Chemistry of Materials* **2005**, 17, (8), 1959-1964.

27. Ongaro, A.; Griffin, F.; Nagle, L.; Iacopino, D.; Eritja, R.; Fitzmaurice, D., DNA-Templated assembly of a protein-functionalized nanogap electrode. *Advanced Materials* **2004**, 16, (20), 1799-1803.
28. Braun, E.; Eichen, Y.; Sivan, U.; Ben-Yoseph, G., DNA-templated assembly and electrode attachment of a conducting silver wire. *Nature* **1998**, 391, (6669), 775-778.
29. Meng, G.; Jung, Y. J.; Cao, A.; Vajtai, R.; Ajayan, P. M., Controlled fabrication of hierarchically branched nanopores, nanotubes, and nanowires. *Proceedings of the National Academy of Sciences of the United States of America* **2005**, 102, (20), 7074-7078.
30. Kovtyukhova, N. I.; Mallouk, T. E., Nanowire p-n heterojunction diodes made by templated assembly of multilayer carbon-nanotube/polymer/semiconductor-particle shells around metal nanowires. *Advanced Materials* **2005**, 17, (2), 187-192.
31. Sainsbury, T.; Fitzmaurice, D., Templated Assembly of Semiconductor and Insulator Nanoparticles at the Surface of Covalently Modified Multiwalled Carbon Nanotubes. *Chemistry of Materials* **2004**, 16, (19), 3780-3790.
32. Nagle, L.; Ryan, D.; Cobbe, S.; Fitzmaurice, D., Templated Nanoparticle Assembly on the Surface of a Patterned Nanosphere. *Nano Letters* **2003**, 3, (1), 51-53.
33. Thurn-Albrecht, T.; Schotter, J.; Kastle, G. A.; Emley, N.; Shibauchi, T.; Krusin-Elbaum, L.; Guarini, K.; Black, C. T.; Tuominen, M. T.; Russell, T. P., Ultrahigh-density nanowire arrays grown in self-assembled diblock copolymer templates. *Science* **2000**, 290, (5499), 2126-2129.
34. Morkved, T. L.; Lu, M.; Urbas, A. M.; Ehrichs, E. E.; Jaeger, H. M.; Mansky, P.; Russell, T. P., Local control of microdomain orientation in diblock copolymer thin films with electric fields. *Science* **1996**, 273, (5277), 931-933.
35. Kim Sang, O.; Solak Harun, H.; Stoykovich Mark, P.; Ferrier Nicola, J.; De Pablo Juan, J.; Nealey Paul, F., Epitaxial self-assembly of block copolymers on lithographically defined nanopatterned substrates. *Nature* **2003**, 424, (6947), 411-4.
36. Rockford, L.; Liu, Y.; Mansky, P.; Russell, T. P.; Yoon, M.; Mochrie, S. G. J., Polymers on Nanoperiodic, Heterogeneous Surfaces. *Physical Review Letters* **1999**, 82, (12), 2602-2605.

37. Yang, X. M.; Peters, R. D.; Nealey, P. F.; Solak, H. H.; Cerrina, F., Guided Self-Assembly of Symmetric Diblock Copolymer Films on Chemically Nanopatterned Substrates. *Macromolecules* **2000**, 33, (26), 9575-9582.
38. Segalman, R. A.; Yokoyama, H.; Kramer, E. J., Graphoepitaxy of spherical domain block copolymer films. *Advanced Materials* **2001**, 13, (15), 1152-1155.
39. Cheng, J. Y.; Mayes, A. M.; Ross, C. A., Nanostructure engineering by templated self-assembly of block copolymers. *Nature Materials* **2004**, 3, (11), 823-828.
40. Sundrani, D.; Darling, S. B.; Sibener, S. J., Guiding Polymers to Perfection: Macroscopic Alignment of Nanoscale Domains. *Nano Letters* **2004**, 4, (2), 273-276.
41. Angelescu, D. E.; Waller, J. H.; Adamson, D. H.; Deshpande, P.; Chou, S. Y.; Register, R. A.; Chaikin, P. M., Macroscopic orientation of block copolymer cylinders in single-layer films by shearing. *Advanced Materials* **2004**, 16, (19), 1736-1740.
42. Park, M.; Harrison, C.; Chaikin, P. M.; Register, R. A.; Adamson, D. H., Block copolymer lithography: periodic arrays of ~1011 holes in 1 square centimeter. *Science* **1997**, 276, (5317), 1401-1404.
43. Mack, C. A.; Stevenson, T.; European Optical Society., *Lithography for semiconductor manufacturing: 19-21 May 1999, Edinburgh, Scotland*. SPIE: Bellingham, Wash., USA, 1999; p vii, 262.
44. Mack, C. A.; Stevenson, T.; Society of Photo-optical Instrumentation Engineers.; Scottish Enterprise.; European Optical Society.; Institution of Electrical Engineers., *Lithography for semiconductor manufacturing II: 30 May-1 June, 2001, Edinburgh, UK*. SPIE: Bellingham, Wash., 2001; p vii, 422.
45. <http://www.reed-electronics.com/semiconductor/index.asp>. (May 15, 2006).
46. Mack, C. A., *Field guide to optical lithography*. SPIE Press: Bellingham, Wash., 2006.
47. Moore, G. E., Cramming more components onto integrated circuits. *Electronics* **1965**, 38, (8).
48. Meindl, J. D.; Chen, Q.; Davis, J. A., Limits on silicon nanoelectronics for terascale integration. *Science* **2001**, 293, (5537), 2044-9.
49. <http://www.intel.com/research/silicon/images/MooresLawgraph3.gif>. (May 15, 2006).

50. Wallraff, G. M.; Hinsberg, W. D., Lithographic Imaging Techniques for the Formation of Nanoscopic Features. *Chemical Reviews* **1999**, 99, (7), 1801-1821.
51. Rothschild, M.; Bloomstein, T. M.; Kunz, R. R.; Liberman, V.; Switkes, M.; Palmacci, S. T.; Sedlacek, J. H. C.; Hardy, D.; Grenville, A., Liquid immersion lithography: Why, how, and when? *Journal of Vacuum Science & Technology, B: Microelectronics and Nanometer Structures--Processing, Measurement, and Phenomena* **2004**, 22, (6), 2877-2881.
52. Lin, B. J., Immersion lithography and its impact on semiconductor manufacturing. *Journal of Microlithography, Microfabrication, and Microsystems* **2004**, 3, (3), 377-395.
53. Dammel, R. R.; Houlihan, F. M.; Sakamuri, R.; Rentkiewicz, D.; Romano, A., 193 nm immersion lithography - Taking the plunge. *Journal of Photopolymer Science and Technology* **2004**, 17, (4), 587-602.
54. Okazaki, S., Recent development activities and future plans for EUV lithography in Japan. *Proceedings of SPIE-The International Society for Optical Engineering* **2005**, 5592, (Nanofabrication: Technologies, Devices, and Applications), 27-37.
55. Stamm, U.; Kleinschmidt, J.; Gaebel, K. M.; Birner, H.; Ahmad, I.; Bolshukhin, D.; Brudermann, J.; Chinh, T. D.; Flohrer, F.; Goetze, S.; Hergenhan, G.; Kloepfel, D.; Korobochko, V.; Mader, B.; Mueller, R.; Ringling, J.; Schriever, G.; Ziener, C., High-power sources for EUV lithography: state of the art. *Proceedings of SPIE-The International Society for Optical Engineering* **2004**, 5448, (Pt. 2, High-Power Laser Ablation V), 722-736.
56. Stamm, U.; Kleinschmidt, J.; Gaebel, K.; Birner, H.; Ahmad, I.; Bolshukhin, D.; Brudermann, J.; Chinh, T. D.; Flohrer, F.; Goetze, S.; Hergenhan, G.; Kloepfel, D.; Korobotchko, V.; Mader, B.; Mueller, R.; Ringling, J.; Schriever, G.; Ziener, C., EUV source power and lifetime: the most critical issues for EUV lithography. *Proceedings of SPIE-The International Society for Optical Engineering* **2004**, 5374, (Pt. 1, Emerging Lithographic Technologies VIII), 133-144.
57. Nishiyama, I., EUV lithography. *Optronics* **2003**, 256, 122-127.
58. Cobb, J. L.; Brainard, R. L.; O'Connell, D. J.; Dentinger, P. M., EUV lithography: patterning to the end of the road. *Materials Research Society Symposium Proceedings* **2002**, 705, (Nanopatterning: From Ultralarge-Scale Integration to Biotechnology), 91-100.
59. Kinoshita, H.; Watanabe, T., Current status of EUV lithography. *Journal of Photopolymer Science and Technology* **2000**, 13, (3), 379-384.

60. Okazaki, S., Current status and issues of EUV lithography research. *Optronics* **1999**, 205, 104-110.
61. Hawryluk, A. M.; Ceglio, N. M.; Markle, D. A., EUV lithography. *Solid State Technology* **1997**, 40, (7), 151-152, 154, 156, 159.
62. Kinoshita, H.; Watanabe, T., Present status and future prospects of EUV lithography. *Journal of Photopolymer Science and Technology* **1997**, 10, (3), 369-376.
63. Chou, S. Y.; Krauss, P. R.; Renstrom, P. J., Imprint lithography with 25-nanometer resolution. *Science* **1996**, 272, (5258), 85-7.
64. Xia, Y.; Whitesides, G. M., Soft lithography. *Annual Review of Materials Science* **1998**, 28, 153-184.
65. Yang, S.-M.; Jang, S. G.; Choi, D.-G.; Kim, S.; Yu, H. K., Nanomachining by colloidal lithography. *Small* **2006**, 2, (4), 458-475.
66. Choi, D.-G.; Kim, S.; Jang, S.-G.; Yang, S.-M.; Jeong, J.-R.; Shin, S.-C., Nanopatterned Magnetic Metal via Colloidal Lithography with Reactive Ion Etching. *Chemistry of Materials* **2004**, 16, (22), 4208-4211.
67. Denis, F. A.; Hanarp, P.; Sutherland, D. S.; Dufrene, Y. F., Nanoscale Chemical Patterns Fabricated by Using Colloidal Lithography and Self-Assembled Monolayers. *Langmuir* **2004**, 20, (21), 9335-9339.
68. Chopra, N.; Xu, W.; De Long, L. E.; Hinds, B. J., Incident angle dependence of nanogap size in suspended carbon nanotube shadow lithography. *Nanotechnology* **2005**, 16, (1), 133-136.

Chapter 2

Imprint Lithography Background and Materials

2.1 INTRODUCTION

Nanoimprint lithography (NIL) is a promising low cost, high resolution nano-patterning technique.¹⁻⁴ NIL achieves pattern transfer by pressing a relief mold (also called a template) onto a thin film. There are two general approaches to imprint lithography as depicted in Figure 2.1. Thermal NIL (also called hot embossing) utilizes a thermoplastic polymer film for patterning.¹⁻⁴ The film must be heated above the glass transition temperature of the polymer to soften the material and permit flow. The mold is pressed onto the film and subsequently allowed to cool to harden the polymer structures prior to removing the mold. Ultraviolet-assisted NIL (UV-NIL) utilizes a low viscosity liquid that can be imprinted at room temperature using a transparent mold.⁵ Light is irradiated through the mold to initiate polymerization that ‘locks’ the structures into place. Both thermal NIL and UV-NIL leave a thin residual layer of material that can be removed using a plasma etch.

Thermal NIL and UV-NIL are both capable of producing sub-100 nm features over large areas, as shown in Figure 2.2.¹⁻⁵ NIL is adaptable to patterning various geometries such as lines, posts, holes, and 3-dimensional tiered structures.^{1,6-8} Numerous technologies benefit from NIL including transistors,^{1,9-11} photonic devices,¹²⁻¹⁴ optical components,¹⁴⁻¹⁹ micro fluidic devices,²⁰⁻²² magnetic memory,^{23,24} and sensors.²⁵ NIL is applicable to various biomedical applications²⁶⁻³⁰ and is capable of generating “harvestable” nanostructures³¹ that may find applications in advanced delivery, targeting,

and detection schemes. Imprint lithography has also been demonstrated for hybrid plastic electronics,³² organic thin film transistors,^{33,34} and high resolution organic light emitting diodes.³⁵ The promise of NIL is recognized by MIT's Technology Review, which identified NIL as one of 10 new technologies that are likely to change the world.³⁶

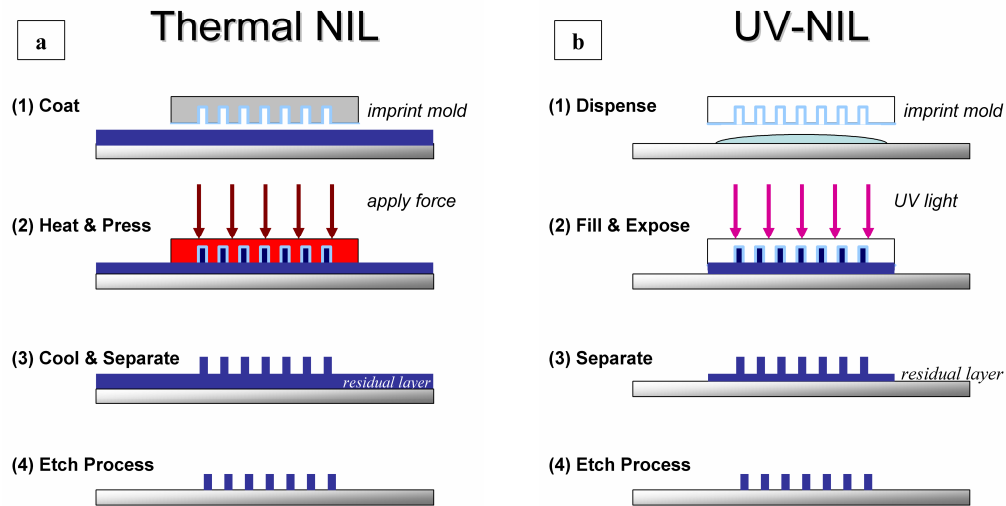


Figure 2.1: Process diagrams for (a) “hot embossing” or thermal nanoimprint lithography and (b) ultraviolet-assisted NIL (UV-NIL). In both processes, a relief mold is pressed onto a soft material to physically transfer the pattern.³⁷

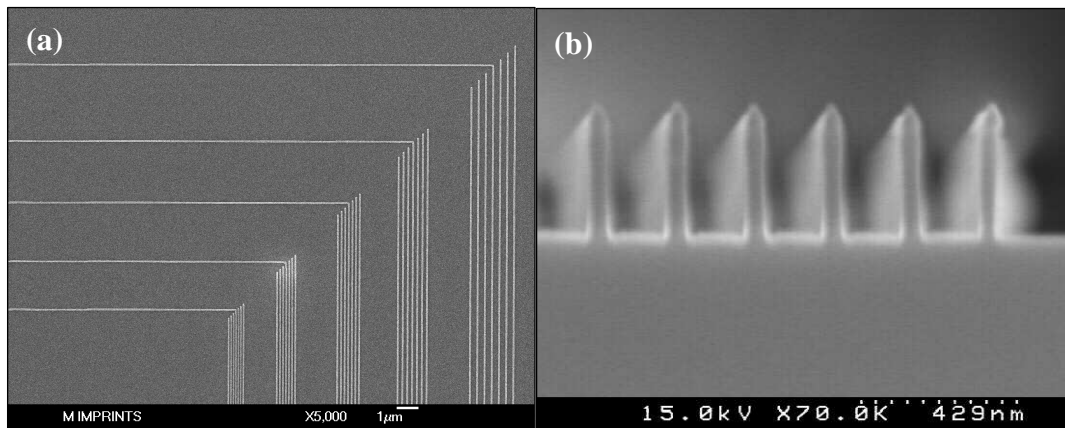


Figure 2.2: Scanning electron micrographs of lines printed using UV-NIL. (a) Top down image. (b) Cross section image showing that the imprinted patterns can be transferred to the silicon substrate by etching.

There are two primary aspects of NIL that make it advantageous compared to conventional photolithography: cost and resolution. In contrast to photolithography, NIL does not require any expensive focusing optics. UV-NIL requires a ‘flood’ exposure of light to initiate the polymerization of the imprinted material, but the light does not have to be focused. The ability of NIL to generate high resolution features is only limited by the ability to make a high resolution template. Templates are typically created using e-beam lithography, a process introduced in Chapter 1. E-beam lithography is a high resolution technique, but is slow due to its serial nature. Creating a high resolution template is a lengthy process that may take hours or even days depending on the size of the imprint area. Upon completion, the template can be used repeatedly to rapidly transfer high resolution patterns over large areas. Thus, NIL has the resolution of e-beam lithography without the limitation of throughput. There has been a historic trade-off between resolution and throughput for various patterning technologies, as shown in Figure 2.3. NIL deviates significantly from this trend, which is the primary appeal of the technology. In addition, NIL is capable of patterning materials that would not be directly compatible with e-beam lithography processing since patterning is accomplished by physical stamping rather than a photo-induced solubility switch.

The concept of NIL borrows from established industrial imprinting technologies. Compact discs and DVDs are created using a similar approach in which a patterned master is pressed against a heated polymer.³⁷ The features patterned with NIL are much smaller than those made using these technologies and thus introduce new processing challenges. This chapter will introduce the various aspects of NIL processing, including material considerations and process limitations. Comprehensive reviews on imprint lithography are available in the literature^{38,39} and in a book titled ‘*Alternative Lithography*’.⁴⁰

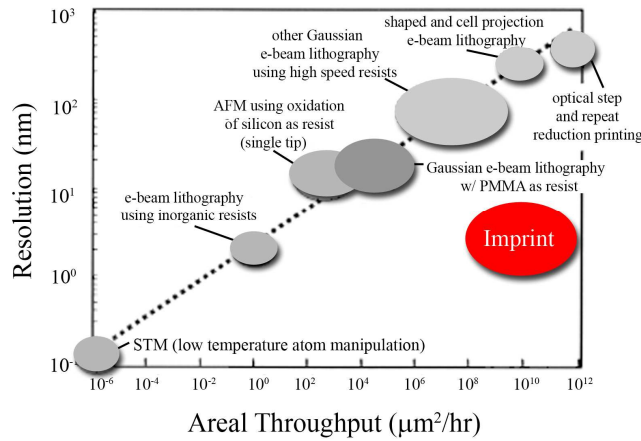


Figure 2.3: Trade-off between throughput and resolution. Adapted from Ref⁴¹ courtesy of Lucent Technologies Bell Labs.

2.2 MOLD FORMATION

The NIL mold is a topographically patterned master used to physically transfer patterns during imprinting. NIL utilizes a hard mold, a requirement to pattern high resolution features. Other contact printing strategies, such as micro-contact printing (μCP),⁴²⁻⁴⁵ use soft elastomeric stamps (e.g. polydimethyl siloxane) that are subject to feature collapse, swelling, and distortion.⁴⁶⁻⁴⁹ Materials such as silicon, silicon dioxide, and some metals (e.g. Ni) are common mold materials, although harder materials such as sapphire, diamond, and SiC have also been investigated.^{1,50-53} An ideal mold material is capable of being patterned using traditional fabrication techniques and is sufficiently rigid (modulus ~100 GPa) for the imprinting process.^{1,54} For UV-NIL the mold must also be transparent to transmit the UV light.

Molds are fabricated by conventional mask making technologies,⁵⁵⁻⁶⁰ such as e-beam lithography, as shown in Figure 2.4a. A chromium coated glass substrate is first

patterned with a polymeric resist film. These features are then transferred into the chromium on the substrate using a chlorine plasma etch. The role of the chromium is two fold: It dissipates charge during the e-beam writing process and acts as a “resist” during the fluorocarbon plasma etch used to transfer the pattern into the glass substrate.⁶¹

Figure 2.4b illustrates a similar mold fabrication process that utilizes an indium tin oxide (ITO) under layer.⁶²⁻⁶⁴ This ITO layer is first deposited on a glass substrate and then coated with a subsequent thin layer of SiO_2 . An e-beam resist is patterned on top of the SiO_2 and the pattern is transferred to the ITO layer via etching. The ITO layer serves as an etch stop during the etching of the silicon dioxide to allow superb control of the etch depth. Additionally, ITO is a transparent, conductive oxide that dissipates charge during the e-beam writing process. The conductivity of the ITO also allows the mold to be inspected by scanning electron microscopy (SEM) to locate defects and imperfections on the mold post-fabrication.⁶⁵⁻⁶⁹

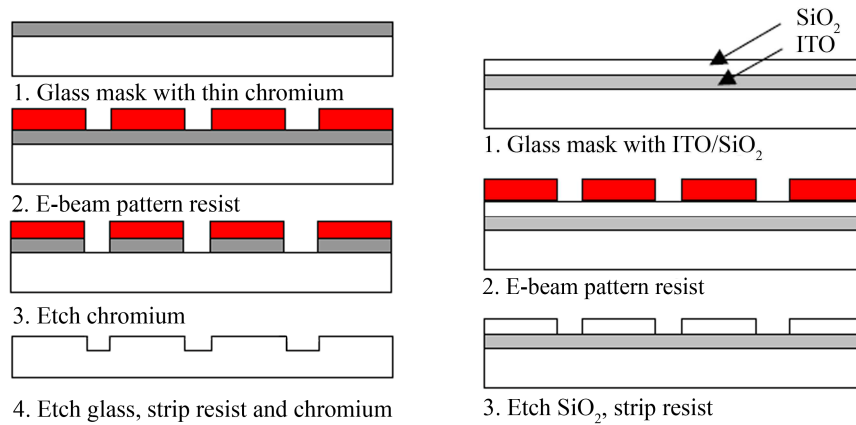


Figure 2.4: Template fabrication process. (a) A thin chrome layer is patterned by e-beam lithography. The chrome acts as a etch mask, allowing the pattern to be transferred to the glass. (b) Indium tin oxide (ITO) is used as an under layer during the generation of the mold. The transparent ITO is conducting, allowing the mold to be inspected by scanning electron microscopy.⁵⁷

The final step of the mold fabrication process is to modify the surface properties. Ideally, imprinted features will adhere selectively to the substrate and release completely from the mold after imprinting. In cases where the mold does not release cleanly from the imprinted material, defects are created on the substrate and the mold is contaminated, as shown in Figure 2.5. Contamination of the mold could result in propagated defects during subsequent imprints. The mechanical integrity of the imprinted features is a particularly important aspect of material design, which has implications that will be elaborated in Chapter 3.

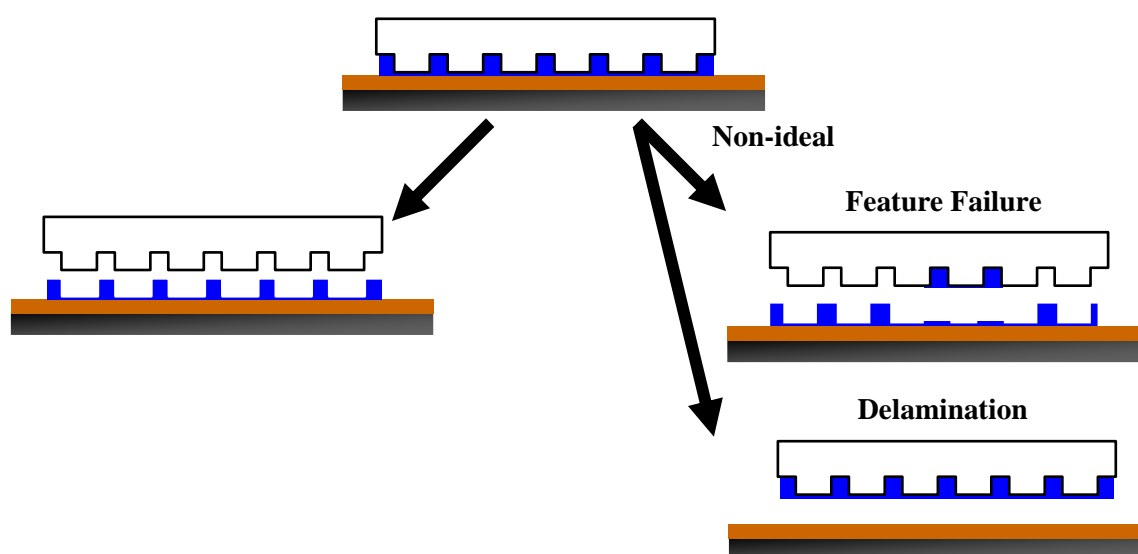


Figure 2.5: Potential failure mechanisms for NIL. Ideally, the template will release cleanly from the features (left). Features can cohesively fail (right, top) or delaminate (right, bottom) if the material properties and template are not properly designed.

To minimize the problems illustrated in Figure 2.5, NIL molds are typically surface treated to improve the release properties of the mold from the imprinted material.⁷⁰ A common strategy is to modify the surface functionality by covalently bonding molecules with fluorinated tails to the surface.⁷¹⁻⁷⁴ For silicon dioxide surfaces,

a silylation reaction is often used to covalently bond a fluorinated chlorosilane molecule (or fluorinated alkyloxysilane). The reaction can be done in either the liquid or gas phase, and with slight modification can be applied to ITO,⁷⁵ as discussed in Chapter 9. Alternatively, the mold surface can be coated via plasma deposition of fluoropolymers,⁷⁶ but this method is less common. The addition of surfactants and fluorinated components to the imprint material is a complementary method to reduce separation forces.^{77,78}

2.3 PROCESS REQUIREMENTS

NIL is a relatively simple process and consequently has a minimal number of processing requirements. The imprint mold must be rigid in order to avoid feature deformation⁴⁹ during imprinting and to facilitate overlay. ‘Soft lithography’ techniques exist that use elastomeric molds (such as poly(dimethyl siloxane)), however, the resolution of these techniques is limited by the flexible nature of the mold.⁴²⁻⁴⁴ NIL requires a planar substrate to provide intimate contact between the mold and the imprint material, although in principle a roll-to-roll type system could be employed.⁷⁹ NIL must be done in a clean environment to avoid trapping particles between the mold and the substrate that would disrupt intimate imprint contact. As discussed previously, NIL benefits from treatment of the template surface with molecules that lower the release force. For commercial applications, the template must be able to be aligned and imprinted multiple times across a substrate.⁸⁰⁻⁸³

2.4 MATERIAL REQUIREMENTS

2.4.1 Thermal NIL

Thermal NIL utilizes a thin thermoplastic film that must meet a number of processing requirements during imprinting.³⁹ First, the substrate must be coated with a uniform thin film (100-300 nm). Second, the material must be able to flow during the imprinting step to fill the recesses of the mold, which is accomplished by heating the film above its glass transition temperature (T_g). The polymer is often heated 40-80 °C above the T_g to permit flow. The material must be chemically stable at these elevated temperatures. After cooling, the material should be mechanically stable at room temperature to preserve the imprinted structures and avoid cohesive failure.

Nearly any thermoplastic material may be imprinted under the right set of conditions. For example, polystyrene, polycarbonate, poly(vinyl alcohol), and poly(ethylene-2,6-naphthalate) have all been demonstrated as viable imprint materials.^{37,39} Conducting polymers such as polyaniline and poly[diphenyl-(4-vinylphenyl-amine)] derivatives have also been patterned using NIL.³⁷ The most thoroughly studied thermal NIL material is poly(methyl methacrylate) (PMMA). PMMA has an accessible glass transition temperature (95-105 °C) that is well above room temperature. PMMA can be coated from a number of common solvents such as chlorobenzene and propylene glycol methyl ether acetate. During imprinting, the film is heated to between 130-180 °C to facilitate flow of the polymer.⁸⁴⁻⁸⁶ Once imprinted and cooled, the resulting structures are mechanically stable.

Use of low T_g polymers allows patterning to occur at lower temperatures, minimizing the imprint cycle time and reducing thermal mismatch between the substrate and the template. Unfortunately, materials with low T_g 's are prone to deform over time.

A number of commercially available photoresists have been patterned with NIL.³⁷ Photoresists are appropriate for applications requiring an etch transfer step since the chemistry of the material has already been optimized for etch processing. The incorporation of photoresists also allows traditional lithography to be simultaneously combined with imprint lithography.

Thermosetting polymers are a promising thermal NIL material.⁸⁷ These polymers harden when heated by the formation of crosslinking bonds. The imprinting temperature must be high enough to allow flow of the polymer, but low enough to minimize crosslinking prior to the displacement of material. The thermally induced crosslinking reaction increases the mechanical strength of the material, eliminating the need for the cooling step in certain cases. Poly(benzene-dicarboxylic diallylestere)s have been reported as imprintable thermosetting polymers.⁸⁸

The concept of thermal NIL has been extended to non-polymeric materials. The direct imprinting of silicon has been demonstrated using intense lasers to locally soften the surface of a silicon substrate.⁸⁹

2.4.2 Material Requirements: UV-NIL

Although UV-NIL has a number of advantages over thermal NIL, there are several unique materials processing constraints.^{90,91} Low viscosity materials facilitate the rapid displacement of fluid during imprinting and lower the necessary imprint pressure.⁹² In principle, spun cast films are compatible with UV-NIL, but many low viscosity materials are too volatile to form stable films. Materials with intermediate viscosities are suitable for this approach (100-300 cPs).³⁷ The space between the mold and substrate can also be filled by capillary action, although this is a less common approach. Typically, the liquid is dispensed as droplets on the imprinting field, which provides several advantages

over the previously discussed techniques. Dispensing multiple droplets lowers the imprint force. Furthermore, both the drop volume and distribution can be controlled to facilitate complete filling of the imprint field that would otherwise be challenging due to feature density variations.⁹³ Most fluid dispensing mechanisms require low viscosity liquids (< 4 cPs) to rapidly create the small droplets of fluid (\sim picoliters) ideal for imprinting.

Imprint materials that photocure rapidly to high conversions are preferable. The throughput of the imprint process is impacted by the cure rate while the mechanical stability of the imprinted features depends both on the extent of polymerization and the degree of crosslinking. To achieve high conversion, the template must be sufficiently transparent at the relevant wavelengths to initiate the reaction and the imprinted material itself must be transparent. Most photocurable systems utilize an absorbing initiator species in low concentrations (0.1-5 wt%) to initiate the polymerization.

When the template is removed, the photocured polymer must adhere entirely to the substrate and maintain its structural integrity. The integrity is generally enhanced through crosslinking. Additionally, cure-induced shrinkage needs to be minimized to limit distortion during the pattern transfer process.^{94,95} Finally, the chemical composition of the final imprinted structures is often critical to meet the needs of the particular patterning application.

To meet the various processing demands of UV-NIL, the imprint material is typically comprised of a multi-component formulation. For example, step and flash imprint lithography (SFIL) has employed a four component material system, shown in Figure 2.6.⁵ The polymerization mechanism of this acrylate based system is free radical initiated. When light strikes the initiator, it forms free radicals that initiate the polymerization of the acrylate double bond. The three acrylate monomers in the

formulation each serve a purpose. The silicon containing monomer provides O₂ etch resistance to the imprinted structures, the crosslinker provides mechanical stability to the resulting structures, and the diluent, a high mobility small molecule, increases the reactivity and lowers the solution viscosity.

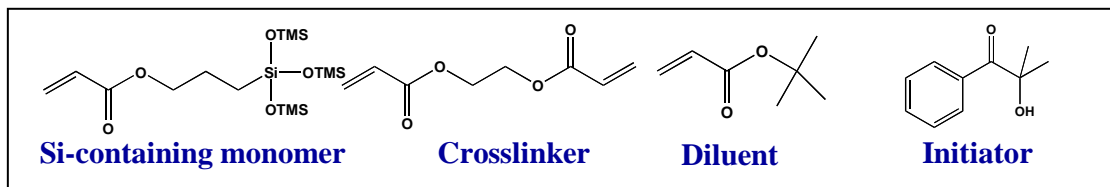


Figure 2.6: A representative UV-NIL formulation. The multi-component formulation provides the various properties required for processing.

There are many other examples of UV-NIL material formulations. Epoxies, vinyl ethers, and acrylates appear to be the most popular materials used for this purpose because of their commercial availability and ability to photocure rapidly.^{78,96,97} In contrast to acrylates, which cure by a radical mechanism, vinyl ethers and epoxies are typically cured by a cationic mechanism. A photo-acid generator (PAG) is used to generate acid molecules that initiate the cationic polymerization. These PAG molecules generate strong acids and some contain heavy metals that render them incompatible with certain applications, including semiconductor devices.

Many of the materials studied for NIL are sacrificial, designed only to transfer patterns to the underlying substrate in a manner similar to photoresists. However, a number of “functional” materials have been imprinted by UV-NIL to provide final imprinted structures that serve a permanent function (e.g. lenses and optical elements). For these materials, an additional constraint of material function must be considered (e.g. conductivity, biocompatibility, etc.). For example, photocurable dielectric materials have been demonstrated as electrical insulators for semiconductor applications.⁹⁸

2.5 IMPRINT CAPABILITIES AND LIMITATIONS

2.5.1 Resolution

The resolution of NIL appears to be only limited by the ability to create high resolution molds. The images of Figure 2.7 show a series of sequential imprints corresponding to the same location on the mold. The lines themselves are quite small (<100 nm) and are replicated faithfully in each field. In each image, a small defect is circled. This corresponds to an exceedingly small defect in the template that successfully transferred in each imprint field. This example illustrates that the imprint process is capable of replicating topographies of the mold that are smaller than the dimensions of the designed features.

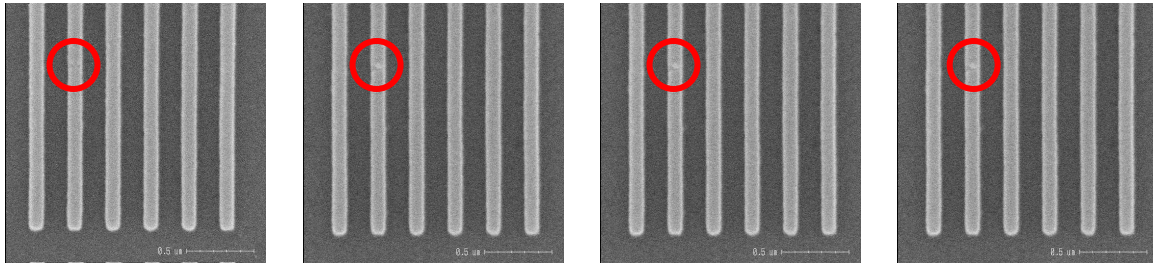


Figure 2.7: A series of scanning electron micrograph images of sequential imprints. A small defect (circled) in the template has been replicated faithfully in each image, illustrating the high resolution of NIL.

A clever demonstration of NIL resolution capabilities was accomplished using a unique mold fabrication technique shown in Figure 2.8.² A mold was created by first depositing alternating layers of GaAs and $\text{Al}_{0.7}\text{Ga}_{0.3}\text{As}$ films on a substrate using molecular beam epitaxy. The $\text{Al}_{0.7}\text{Ga}_{0.3}\text{As}$ was selectively etched away at the cleaved edge of the film stack. The resulting ‘mold’ was pressed into a polymer film and the features were successfully transferred. The advantage of this technique is that the

thickness of each film layer can be controlled with great accuracy (~ 1 nm), whereas e-beam lithography has limited resolution for making template features (~ 10 nm).

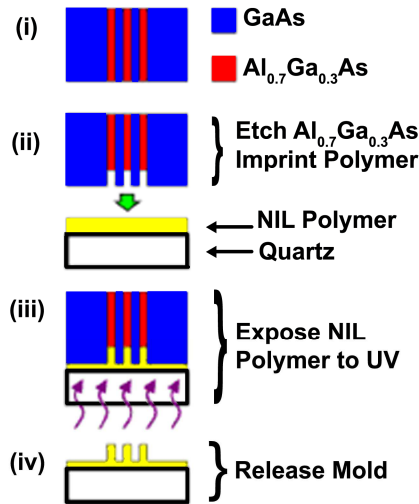


Figure 2.8: A unique, high resolution mold is formed by (i) selectively etching $\text{Al}_{0.7}\text{Ga}_{0.3}\text{As}$ from the cleaved edge of a multilayer film stack. (ii) The mold is pressed into a polymer film. (iii) Light is irradiated, curing the polymer. (iv) The mold is released and the pattern successfully transferred.²

Perhaps the ultimate demonstration of the resolution capabilities of imprint is the work by John Rodgers group at the University of Illinois.⁹⁹ In this work, a carbon nanotube coated substrate was utilized as a “template”. Poly(dimethyl siloxane) (PDMS) was polymerized while in contact with this surface in a process resembling UV-NIL. Once the “template” was removed, there was evidence that the carbon nanotube dimensions were replicated in the PDMS. Figure 2.9 show atomic force microscopy (AFM) images of the PDMS layer after imprinting. The carbon nanotubes used in this work had a diameter of ~ 2 nm. This work suggests that NIL could extend to nearly molecular levels of resolution.

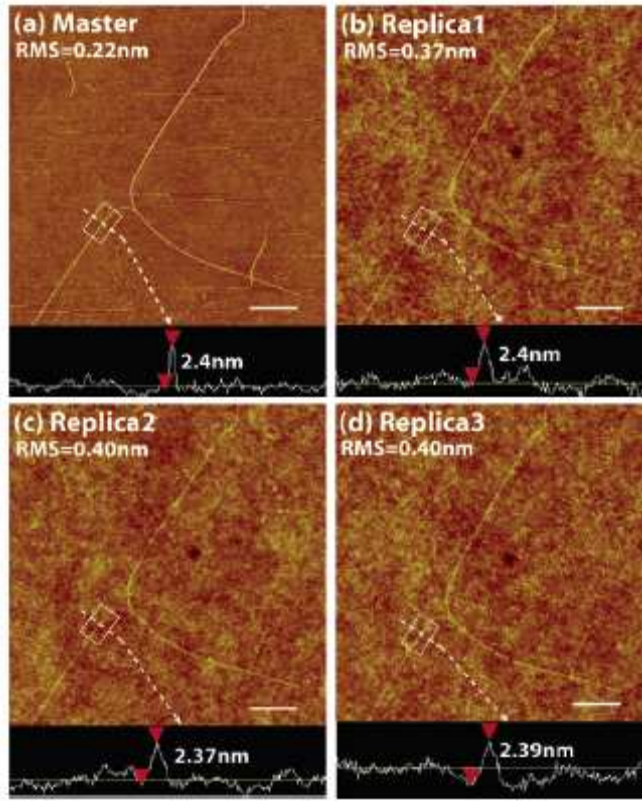


Figure 2.9: Atomic force microscopy (AFM) images of (a) a carbon nanotube on a flat substrate serving as a ‘mold’. (b) The mold is replicated in a polymerizable liquid (PDMS) multiple times (c), (d).⁹⁹

Due to the fidelity of the replication process, the creation of the mold is one of the most important steps in imprint processing. The ability to create commercially relevant, defect free, high resolution molds with processing longevity will continue to be a challenge for NIL.

2.5.2 Residual Layer

As the gap between the template and substrate decreases during imprinting, the viscous forces that resist the displacement of the material become exponentially large. Thus, nearly all forms of NIL leave a thin residual layer of material between imprinted

structures. For pattern transferring purposes, this layer can be removed by a simple plasma etch.¹⁰⁰⁻¹⁰² The etch process must be optimized such that the etch is directionally anisotropic. An ideal etch process will only reduce the vertical dimension of the features. Oxygen plasma is a popular etchant since it rapidly removes carbonaceous materials. SFIL utilizes a two step etch process to achieve high aspect ratio features. As seen in Figure 2.10, a layer of silicon containing material is patterned on top of a thin film of organic polymer. After imprinting, the residual layer is removed by doing a “breakthrough etch” using CF_4 plasma chemistry. The pattern is then transferred to the substrate surface using an oxygen plasma “transfer etch”. The silicon containing imprint material resists the oxygen plasma since it forms SiO_2 , a non-volatile by-product, whereas the carbon containing under layer (the blue film in Figure 2.10) is rapidly converted to volatile by-products (e.g. CO_2). This bi-layer etch process is desirable since it is capable of forming very high aspect ratio features. High aspect ratio features are difficult to directly pattern with imprint lithography due to challenges associated with making high aspect ratio molds. Additionally, high aspect ratio molds have a propensity to induce cohesive failure (Figure 2.5) resulting from the increase in surface area contact between the mold and the imprinted material.

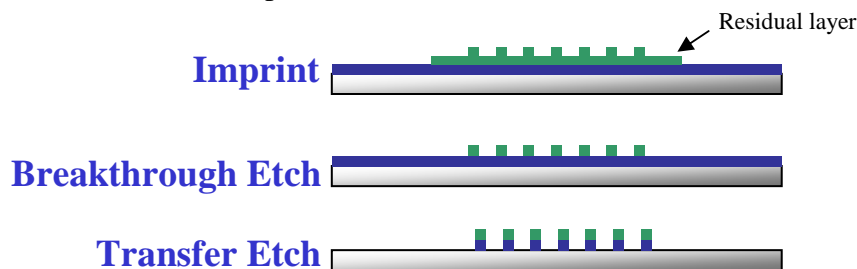


Figure 2.10: An example “breakthrough” etch process utilized to remove the residual layer between the imprinted features. By proper material design, this pattern can subsequently be transferred to the substrate through etch selectivity between the green material and blue material. In SFIL, the breakthrough etch is accomplished with a CF_4 plasma and the transfer etch by an oxygen plasma. The silicon substrate is the bottom layer of the film stack (gray).

The residual layer can reportedly be eliminated through use of a fluorinated template and fluorinated substrate.³¹ This technique is ideal for creating “harvestable” nanostructures since the printed materials are easily removed from the substrate. However, this method is limited to applications in which the substrate can be fluorinated.

2.5.3 Topography

The rigid molds used for imprint lithography are best suited for patterning on planar substrates. This requirement implies that the substrate must be globally flat and the mounting of the substrate must minimize bowing. Although the substrate must be globally flat, many applications require imprinting over surfaces with local topography, as seen in Figure 2.11. In principle, a material could be directly imprinted over topography, but it would be challenging to transfer the imprinted pattern to the substrate, primarily due to the differences in residual layer thickness.

A number of techniques have been proposed or demonstrated to get around the limits imposed by topography. Use of a ‘planarizing’ layer is a common approach to addressing this issue.^{103,104} A planarizing layer is simply a film that is spun cast on top of the features to make the topology more planar. The planarized substrate is amenable to imprinting, as shown in Figure 2.11. If the proper materials are chosen, etch selectivity between the imprinted material and the planarizing layer can enhance aspect ratios using the same approach shown in Figure 2.10.

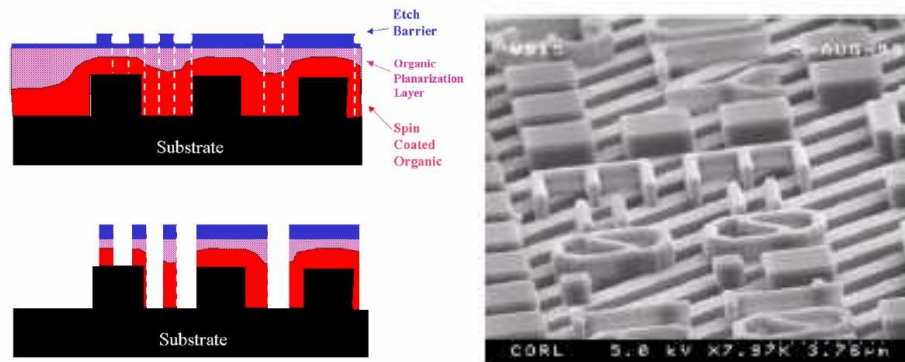


Figure 2.11: Planarization strategy for imprinting over topography. (a) Two films are cast over the initially patterned substrate prior to imprinting. (b) SEM demonstrating the capabilities of this technique.¹⁰⁴

2.5.4 Thermal NIL Limitations

There are a number of challenges associated with thermal NIL that are primarily associated with the high temperatures required for processing. The heating / cooling cycle required for processing could create stresses and deformations due to thermal mismatch of intimately contacted materials. This is particularly relevant to multi-layer patterning, in which the imprinted layer must be aligned with features on the substrate.

The thermoplastics utilized for thermal NIL generally have high viscosities that require large pressures to fill the mold during the imprint step, on the order of 500-5000 kPa. The heating and cooling cycle combined with the time required to fill the mold can extend the imprinting cycle into the tens of minutes. The high viscosity also has ramification in the filling of non-regular features on the mold.^{39,84-86,105} Figure 2.12 illustrates common filling problems that result when large features are placed next to small features, a necessity when patterning the complex features found in the semiconductor industry. Large features cause problems because the viscous polymer must be displaced over longer distances. In general, small features are easier to print

because the material is displaced over shorter lateral distances. Templates with mixed feature sizes may warp due to uneven distribution of forces, as shown in Figure 2.12b.

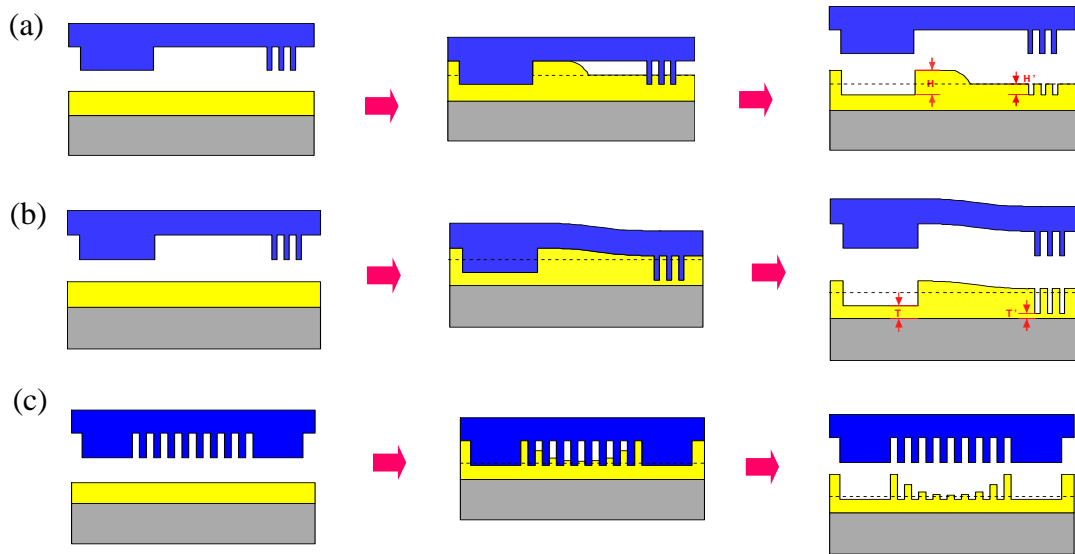


Figure 2.12: Filling issues associated with NIL occur when the mold contains both large and small patterns. The high viscosity prevents total displacement of the polymer under the large size patterns, which affects the neighboring smaller patterns (a) and can create an uneven stress distribution on the mold, leading to deformation (b). Insufficient polymer flow from the large protruding features causes incomplete filling of small neighboring features (c).¹⁰⁵

The low viscosity materials used in UV-NIL mitigates this filling problem. Methods have been proposed to get around the filling issues associated with thermal NIL through the use of a thermally imprintable photosensitive material.¹⁰⁵⁻¹⁰⁷ By using a photocurable material, the large protruding features can be replaced by thin chrome films that block the light and eliminate the need to displace large amounts of material. This process is limited by the complicated template fabrication scheme and by the ability to resolve the photocurable regions of the film.

2.5.5 UV-NIL Limitations, Requirements, and Advantages

UV-NIL overcomes many of the limitations of thermal NIL, but also has several unique requirements. UV-NIL does not require heat or large pressures (< 100 kPa) during imprinting, which reduces the processing cycle time and eliminates the thermal stresses and alignment issues associated with thermal NIL. The lack of a heating and cooling cycle may improve the lifetime of the imprint mold due to reduced thermal stresses. UV-NIL, however, requires a template that is capable of transmitting the appropriate wavelengths of light (typically UV) to initiate the polymerization of the imprint material. Consequently, there is a smaller material set from which molds can be fabricated and common materials like silicon are incompatible due to their opaque nature. As discussed in Section 2.2, the molds must be surface treated to minimize defect formation during separation. Some mold materials, such as ITO, require tailored surface chemistries to create robust treatments, as discussed in Chapter 9.

Acrylates are a popular basis for design of imprint materials utilized for UV-NIL. Acrylates are polymerized via a free radical mechanism. It is well known that this mechanism is strongly inhibited by oxygen.¹⁰⁸ Oxygen manifests itself in two ways during imprinting^{109,110} as discussed in great detail in Chapter 3. Dissolved oxygen in the material creates an inhibition period when the material is initially irradiated, slowing down the throughput. Furthermore, oxygen diffusing from the ambient inhibits a thin layer of material around the perimeter of the template, creating an under-cured ring of tacky material that may contribute to defect generation during subsequent imprints.

The effects of oxygen can be overcome through the use of an inert gas (e.g. nitrogen, helium, etc), through additives (e.g. thiols, amines), or through the use of alternative chemistries. Materials such as vinyl ethers and epoxies have been examined as acrylate alternatives.^{78,96,97} These materials photopolymerize through a cationic

mechanism that is insensitive to oxygen, but require large forces to separate the template from the imprinted material.

In contrast to thermal NIL, which imprints a thin film of thermoplastic polymer, UV-NIL typically imprints droplets of liquid. To be commercially viable, the droplets must be dispensed in the appropriate location with the appropriate volume.¹¹¹ Furthermore, the drops must not evaporate at a significant rate prior to imprinting.¹¹² Dispensing multiple small droplets across the imprint field versus one single large droplet reduces the pressure and spreading time required for imprinting since the material is already partially spread across the surface and does not have to be displaced as far.

There are some disadvantages of dispensing droplets one imprint field at a time. Narrow “streets” are generated between each imprint field that are not covered with material. The imprinted material may be designed to “resist” subsequent etching steps, particularly in electronic applications. The bare “streets” are subject to uneven wear during these post-processing steps. This is a disadvantage of UV-NIL compared with thermal NIL, which starts with a substrate with a uniformly coated polymeric film.

Another concern associated with UV-NIL is feature replication fidelity after polymerization. During polymerization, many materials physically shrink by as much as 20%.⁹⁵ This shrinkage could result in feature deformation and pattern placement error. Initial work has shown that the deformation occurs primarily perpendicular to the substrate.^{40,94,95} The features become shorter, but maintain their width. The lack of lateral deformation is important for maintaining alignment with underlying features on the substrate and for faithful feature replication. The vertical shrinkage can be minimized by using fillers and ring opening polymerizations.

2.5.6 Defects

One of the lingering questions about the capabilities of NIL is how many defect free imprint fields can be consecutively patterned using the same template. As seen in Figure 2.5, the potential for defect formation on the imprinted substrate or contamination of the template are serious issues for most commercial imprint applications. Replacing the template in the imprinting tool can be a lengthy process, reducing the throughput of the process. Contaminated templates can be cleaned, but some imprint materials are more challenging to remove than others. This is particularly true if the composition of the imprinted material is similar to that of the template.

It is extremely difficult to experimentally quantify the longevity of a single template due to the tediousness of the measurements and the challenge of finding defects, which resemble a “needle in a haystack”. Despite this challenge, initial work in this area is extremely promising.^{62,74,113} The imprint process has been shown to be “self-cleaning”,^{74,113} implying that undesirable material on the template is entrained in the polymer and removed during subsequent imprints.

2.6 SUMMARY

Nanoimprint Lithography (NIL) is a high resolution patterning technique that is important for the advancement of nanoscience. NIL is a relatively inexpensive technology that has the resolution of e-beam lithography, without the drawback of throughput. During imprinting, a topographically patterned mold is brought into contact with a soft material on a substrate, physically transferring the pattern into the material. There are two varieties of NIL, thermal NIL and UV-NIL. Both techniques are capable of producing nanoscale features, although each has unique material and processing requirements and limitations. A portion of this thesis is focused on Step and Flash

Imprint Lithography (SFIL), a specific variety of UV-NIL. Chapter 3 will focus on the kinetics of the photopolymerization step of SFIL. The future of NIL is very bright and continues to find applications in new fields despite being initially motivated by electronics applications.

2.7 REFERENCES

1. Chou, S. Y.; Krauss, P. R.; Zhang, W.; Guo, L.; Zhuang, L., Sub-10 nm imprint lithography and applications. *Journal of Vacuum Science & Technology, B: Microelectronics and Nanometer Structures* **1997**, 15, (6), 2897-2904.
2. Austin, M. D.; Zhang, W.; Ge, H.; Wasserman, D.; Lyon, S. A.; Chou, S. Y., 6 nm half-pitch lines and 0.04 mm² static random access memory patterns by nanoimprint lithography. *Nanotechnology* **2005**, 16, (8), 1058-1061.
3. Austin, M. D.; Ge, H.; Wu, W.; Li, M.; Yu, Z.; Wasserman, D.; Lyon, S. A.; Chou, S. Y., Fabrication of 5 nm linewidth and 14 nm pitch features by nanoimprint lithography. *Applied Physics Letters* **2004**, 84, (26), 5299-5301.
4. Chou, S. Y.; Krauss, P. R., Imprint lithography with sub-10nm feature size and high throughput. *Microelectronic Engineering* **1997**, 35, (1-4, Micro- and Nano-Engineering 96), 237-240.
5. Bailey, T. C.; Johnson, S. C.; Sreenivasan, S. V.; Ekerdt, J. G.; Willson, C. G.; Resnick, D. J., Step and flash imprint lithography: an efficient nanoscale printing technology. *Journal of Photopolymer Science and Technology* **2002**, 15, (3), 481-486.
6. Mancini, D. P.; Resnick, D. J.; Sreenivasan, S. V.; Watts, M. P. C., S-FIL for sub-80 nm contact hole patterning. *Solid State Technology* **2004**, 47, (2), 55-56, 58.
7. MacDonald, S.; Hughes, G.; Stewart, M.; Palmieri, F.; Willson, C. G., Design and fabrication of highly complex topographic nano-imprint template for dual Damascene full 3-D imprinting. *Proceedings of SPIE-The International Society for Optical Engineering* **2005**, 5992, 786-794.
8. Miller, M.; Doyle, G.; Stacey, N.; Xu, F.; Sreenivasan, S. V.; Watts, M.; LaBrake, D. L., Fabrication of nanometer sized features on non-flat substrates using a nano-imprint lithography process. *Proceedings of SPIE-The International Society for*

- Optical Engineering* **2005**, 5751, (Pt. 2, Emerging Lithographic Technologies IX), 994-1002.
9. Smith, B. J.; Stacey, N. A.; Donnelly, J. P.; Onsongo, D. M.; Bailey, T. C.; Mackay, C. J.; Resnick, D. J.; Dauksher, W. J.; Mancini, D. P.; Nordquist, K. J.; Sreenivasan, S. V.; Banerjee, S. K.; Ekerdt, J. G.; Willson, G. C., Employing Step-and-Flash imprint lithography for gate-level patterning of a MOSFET device. *Proceedings of SPIE-The International Society for Optical Engineering* **2003**, 5037, 1029-1034.
 10. Zhang, W.; Chou, S. Y., Fabrication of 60-nm transistors on 4-in. wafer using nanoimprint at all lithography levels. *Applied Physics Letters* **2003**, 83, (8), 1632-1634.
 11. Resnick, D. J.; Dauksher, W. J.; Mancini, D.; Nordquist, K. J.; Bailey, T. C.; Johnson, S.; Stacey, N.; Ekerdt, J. G.; Willson, C. G.; Sreenivasan, S. V.; Schumaker, N., Imprint lithography for integrated circuit fabrication. *Journal of Vacuum Science & Technology, B: Microelectronics and Nanometer Structures--Processing, Measurement, and Phenomena* **2003**, 21, (6), 2624-2631.
 12. Kee, C.-S.; Yoon, K. B.; Choi, C.-G.; Kim, J.-T.; Han, S. P.; Park, S.; Schift, H., Nanopatterned Polymer Thin Films. *Journal of Nonlinear Optical Physics & Materials* **2005**, 14, (3), 299-303.
 13. Kee, C.-S.; Han, S.-P.; Yoon, K. B.; Choi, C.-G.; Sung, H. K.; Oh, S. S.; Park, H. Y.; Park, S.; Schift, H., Photonic band gaps and defect modes of polymer photonic crystal slabs. *Applied Physics Letters* **2005**, 86, (5), 051101/1-051101/3.
 14. Huang, Y.; Palocz, G. T.; Poon, J. K. S.; Yariv, A., Bottom-up soft-lithographic fabrication of three-dimensional multilayer polymer integrated optical microdevices. *Applied Physics Letters* **2004**, 85, (15), 3005-3007.
 15. Arakcheeva, E. M.; Tanklevskaya, E. M.; Nesterov, S. I.; Maksimov, M. V.; Gurevich, S. A.; Seekamp, J.; Sotomayor Torres, C. M., Fabrication of Semiconductor- and Polymer-Based Photonic Crystals Using Nanoimprint Lithography. *Technical Physics* **2005**, 50, (8), 1043-1047.
 16. Seekamp, J.; Zankovych, S.; Helfer, A. H.; Maury, P.; Sotomayor Torres, C. M.; Boettger, G.; Liguda, C.; Eich, M.; Heidari, B.; Montelius, L.; Ahopelto, J., Nanoimprinted passive optical devices. *Nanotechnology* **2002**, 13, (5), 581-586.
 17. Hirai, Y.; Harada, S.; Kikuta, H.; Tanaka, Y.; Okano, M.; Isaka, S.; Kobayasi, M., Imprint lithography for curved cross-sectional structure using replicated Ni mold. *Journal of Vacuum Science & Technology, B: Microelectronics and Nanometer Structures* **2002**, 20, (6), 2867-2871.

18. Wang, J.; Schablitsky, S.; Yu, Z.; Wu, W.; Chou, S. Y., Fabrication of a new broadband waveguide polarizer with a double-layer 190 nm period metal-gratings using nanoimprint lithography. *Journal of Vacuum Science & Technology, B: Microelectronics and Nanometer Structures* **1999**, 17, (6), 2957-2960.
19. Cardinale, G. F.; Skinner, J. L.; Talin, A. A.; Brocato, R. W.; Palmer, D. W.; Mancini, D. P.; Dauksher, W. J.; Gehoski, K.; Le, N.; Nordquist, K. J.; Resnick, D. J., Fabrication of a surface acoustic wave-based correlator using step-and-flash imprint lithography. *Journal of Vacuum Science & Technology, B: Microelectronics and Nanometer Structures* **2004**, 22, (6), 3265-3270.
20. Mills, C. A.; Martinez, E.; Bessueille, F.; Villanueva, G.; Bausells, J.; Samitier, J.; Errachid, A., Production of structures for microfluidics using polymer imprint techniques. *Microelectronic Engineering* **2005**, 78-79, 695-700.
21. Cao, H.; Tegenfeldt, J. O.; Austin, R. H.; Chou, S. Y., Gradient nanostructures for interfacing microfluidics and nanofluidics. *Applied Physics Letters* **2002**, 81, (16), 3058-3060.
22. Cao, H.; Yu, Z.; Wang, J.; Tegenfeldt, J. O.; Austin, R. H.; Chen, E.; Wu, W.; Chou, S. Y., Fabrication of 10 nm enclosed nanofluidic channels. *Applied Physics Letters* **2002**, 81, (1), 174-176.
23. Wu, W.; Cui, B.; Sun, X.-y.; Zhang, W.; Zhuang, L.; Kong, L.; Chou, S. Y., Large area high density quantized magnetic disks fabricated using nanoimprint lithography. *Journal of Vacuum Science & Technology, B: Microelectronics and Nanometer Structures* **1998**, 16, (6), 3825-3829.
24. McClelland, G. M.; Hart, M. W.; Rettner, C. T.; Best, M. E.; Carter, K. R.; Terris, B. D., Nanoscale patterning of magnetic islands by imprint lithography using a flexible mold. *Applied Physics Letters* **2002**, 81, (8), 1483-1485.
25. Beck, M.; Persson, F.; Carlberg, P.; Graczyk, M.; Maximov, I.; Ling, T. G. I.; Montelius, L., Nanoelectrochemical transducers for (bio-) chemical sensor applications fabricated by nanoimprint lithography. *Microelectronic Engineering* **2004**, 73-74, 837-842.
26. Mills, C. A.; Escarre, J.; Engel, E.; Martinez, E.; Errachid, A.; Bertomeu, J.; Andreu, J.; Planell, J. A.; Samitier, J., Micro- and nanostructuring of poly(ethylene-2,6-naphthalate) surfaces, for biomedical applications, using polymer replication techniques. *Nanotechnology* **2005**, 16, (4), 369-375.
27. Hoff, J. D.; Cheng, L.-J.; Meyhoefer, E.; Guo, L. J.; Hunt, A. J., Nanoscale Protein Patterning by Imprint Lithography. *Nano Letters* **2004**, 4, (5), 853-857.

28. Reisner, W.; Morton, K. J.; Riehn, R.; Wang, Y. M.; Yu, Z.; Rosen, M.; Sturm, J. C.; Chou, S. Y.; Frey, E.; Austin, R. H., Statics and Dynamics of Single DNA Molecules Confined in Nanochannels. *Physical Review Letters* **2005**, 94, (19), 196101/1-196101/4.
29. Gao, J. X.; Chan-Park, M. B.; Xie, D. Z.; Yan, Y. H.; Zhou, W. X.; Ngoi, B. K. A.; Yue, C. Y., UV Embossing of Sub-micrometer Patterns on Biocompatible Polymeric Films Using a Focused Ion Beam Fabricated TiN Mold. *Chemistry of Materials* **2004**, 16, (6), 956-958.
30. Chan-Park, M. B.; Yan, Y.; Neo, W. K.; Zhou, W.; Zhang, J.; Yue, C. Y., Fabrication of High Aspect Ratio Poly(ethylene glycol)-Containing Microstructures by UV Embossing. *Langmuir* **2003**, 19, (10), 4371-4380.
31. Rolland, J. P.; Maynor, B. W.; Euliss, L. E.; Exner, A. E.; Denison, G. M.; DeSimone, J. M., Direct fabrication and harvesting of monodisperse, shape-specific nanobiomaterials. *Journal of the American Chemical Society* **2005**, 127, (28), 10096-10100.
32. McAlpine, M. C.; Friedman, R. S.; Lieber, C. M., Nanoimprint Lithography for Hybrid Plastic Electronics. *Nano Letters* **2003**, 3, (4), 443-445.
33. Austin, M. D.; Chou, S. Y., Fabrication of 70 nm channel length polymer organic thin-film transistors using nanoimprint lithography. *Applied Physics Letters* **2002**, 81, (23), 4431-4433.
34. Kam, A. P.; Seekamp, J.; Solovyev, V.; Cedeno, C. C.; Goldschmidt, A.; Torres, C. M. S., Nanoimprinted organic field-effect transistors: fabrication, transfer mechanism and solvent effects on device characteristics. *Microelectronic Engineering* **2004**, 73-74, 809-813.
35. Cheng, X.; Hong, Y.; Kanicki, J.; Guo, L. J., High-resolution organic polymer light-emitting pixels fabricated by imprinting technique. *Journal of Vacuum Science & Technology, B: Microelectronics and Nanometer Structures* **2002**, 20, (6), 2877-2880.
36. Report, S., Technology Review. In MIT: 2003; Vol. 106, p 36.
37. Stewart, M. D.; Willson, C. G., Imprint materials for nanoscale devices. *MRS Bulletin* **2005**, 30, (12), 947-952.
38. Gates, B. D.; Xu, Q.; Stewart, M.; Ryan, D.; Willson, C. G.; Whitesides, G. M., New Approaches to Nanofabrication: Molding, Printing, and Other Techniques. *Chemical Reviews* **2005**, 105, (4), 1171-1196.

39. Guo, L. J., Recent progress in nanoimprint technology and its applications. *Journal of Physics D: Applied Physics* **2004**, 37, (11), R123-R141.
40. Sotomayor Torres, C. M., *Alternative lithography: unleashing the potentials of nanotechnology*. Kluwer Academic/Plenum: New York, 2003; p xx, 333.
41. Marrian, C. R. K.; Tennant, D. M., Nanofabrication. *Journal of Vacuum Science & Technology, A: Vacuum, Surfaces, and Films* **2003**, 21, (5, Suppl.), S207-S215.
42. Gates, B. D.; Xu, Q.; Love, J. C.; Wolfe, D. B.; Whitesides, G. M., Unconventional nanofabrication. *Annual Review of Materials Research* **2004**, 34, 339-372.
43. Xia, Y.; Whitesides, G. M., Soft lithography. *Annual Review of Materials Science* **1998**, 28, 153-184.
44. Xia, Y.; Whitesides, G. M., Soft lithography. *Angewandte Chemie, International Edition* **1998**, 37, (5), 550-575.
45. Mancini, D. P.; Gehoski, K. A.; Dauksher, W. J.; Nordquist, K. J.; Resnick, D. J.; Schumaker, P.; McMackin, I., Template fabrication for sub-80-nm contact hole patterning using step and flash imprint lithography. *Proceedings of SPIE-The International Society for Optical Engineering* **2003**, 5256, (Pt. 1, 23rd Annual BACUS Symposium on Photomask Technology, 2003), 122-131.
46. Lee, J. N.; Park, C.; Whitesides, G. M., Solvent Compatibility of Poly(dimethylsiloxane)-Based Microfluidic Devices. *Analytical Chemistry* **2003**, 75, (23), 6544-6554.
47. Rolland, J.; Hagberg, E. C.; Dension, G. M.; Carter, K. R.; De Simone, J. M., Lithography: High-resolution soft lithography: Enabling materials for nanotechnologies. *Angewandte Chemie, International Edition* **2004**, 43, (43), 5796-5799.
48. Odom, T. W.; Love, J. C.; Wolfe, D. B.; Paul, K. E.; Whitesides, G. M., Improved pattern transfer in soft lithography using composite stamps. *Langmuir* **2002**, 18, (13), 5314-5320.
49. Hui, C. Y.; Jagota, A.; Lin, Y. Y.; Kramer, E. J., Constraints on Microcontact Printing Imposed by Stamp Deformation. *Langmuir* **2002**, 18, (4), 1394-1407.
50. Colburn, M.; Johnson, S.; Stewart, M.; Damle, S.; Bailey, T. C.; Choi, B.; Wedlake, M.; Michaelson, T.; Sreenivasan, S. V.; Ekerdt, J.; Willson, C. G., Step and flash imprint lithography: a new approach to high-resolution patterning. *Proceedings of SPIE-The International Society for Optical Engineering* **1999**, 3676, (Pt. 1, Emerging Lithographic Technologies III), 379-389.

51. Taniguchi, J.; Tokano, Y.; Miyamoto, I.; Komuro, M.; Hiroshima, H., Diamond nanoimprint lithography. *Nanotechnology* **2002**, 13, (5), 592-596.
52. Taniguchi, J.; Tokano, Y.; Miyamoto, I.; Komuro, M.; Hiroshima, H.; Kobayashi, K.; Miyazaki, T.; Ohyi, H., Preparation of diamond mold using electron beam lithography for application to nano-imprint lithography. *Japanese Journal of Applied Physics, Part 1: Regular Papers, Short Notes & Review Papers* **2000**, 39, (12B), 7070-7074.
53. Pang, S. W.; Tamamura, T.; Nakao, M.; Ozawa, A.; Masuda, H., Direct nano-printing on Al substrate using a SiC mold. *Journal of Vacuum Science & Technology, B: Microelectronics and Nanometer Structures* **1998**, 16, (3), 1145-1149.
54. Yoo, P. J.; Choi, S.-J.; Kim, J. H.; Suh, D.; Baek, S. J.; Kim, T. W.; Lee, H. H., Unconventional Patterning with A Modulus-Tunable Mold: From Imprinting to Microcontact Printing. *Chemistry of Materials* **2004**, 16, (24), 5000-5005.
55. Resnick, D. J.; Bailey, T. C.; Mancini, D.; Nordquist, K. J.; Dauksher, W. J.; Ainley, E.; Talin, A.; Gehoski, K.; Baker, J. H.; Choi, B. J.; Johnson, S.; Colburn, M.; Meissl, M.; Sreenivasan, S. V.; Ekerdt, J. G.; Willson, C. G., New methods for fabricating step and flash imprint lithography templates. *Proceedings of SPIE-The International Society for Optical Engineering* **2002**, 4608, (Nanostructure Science, Metrology, and Technology), 176-181.
56. Resnick, D. J.; Dauksher, W. J.; Mancini, D.; Nordquist, K. J.; Ainley, E.; Gehoski, K.; Baker, J. H.; Bailey, T. C.; Choi, B. J.; Johnson, S.; Sreenivasan, S. V.; Ekerdt, J. G.; Willson, C. G., High resolution templates for step and flash imprint lithography. *Journal of Microlithography, Microfabrication, and Microsystems* **2002**, 1, (3), 284-289.
57. Resnick, D. J.; Dauksher, W. J.; Mancini, D. P.; Nordquist, K. J.; Ainley, E. S.; Gehoski, K. A.; Baker, J. H.; Bailey, T. C.; Choi, B. J.; Johnson, S.; Sreenivasan, S. V.; Ekerdt, J. G.; Willson, C. G., High-resolution templates for step and flash imprint lithography. *Proceedings of SPIE-The International Society for Optical Engineering* **2002**, 4688, (Pt. 1, Emerging Lithographic Technologies VI), 205-213.
58. Dauksher, W. J.; Mancini, D.; Nordquist, K.; Resnick, D. J.; Hudek, P.; Beyer, D.; Groves, T.; Fortagne, O., Fabrication of step and flash imprint lithography templates using a variable shaped-beam exposure tool. *Microelectronic Engineering* **2004**, 75, (4), 345-351.
59. Bailey, T. C.; Resnick, D. J.; Mancini, D.; Nordquist, K. J.; Dauksher, W. J.; Ainley, E.; Talin, A.; Gehoski, K.; Baker, J. H.; Choi, B. J.; Johnson, S.; Colburn, M.; Meissl, M.; Sreenivasan, S. V.; Ekerdt, J. G.; Willson, C. G., Template

- fabrication schemes for step and flash imprint lithography. *Microelectronic Engineering* **2002**, 61-62, 461-467.
60. Thompson, E.; Rhyins, P. D.; Voisin, R. D.; Sreenivasan, S. V.; Martin, P. M., Fabrication of Step and Flash imprint lithography templates using commercial mask processes. *Proceedings of SPIE-The International Society for Optical Engineering* **2003**, 5037, 1019-1028.
 61. Dauksher, W. J.; Mancini, D. P.; Nordquist, K. J.; Resnick, D. J.; Standfast, D. L.; Convey, D.; Wei, Y., Step and flash imprint lithography template characterization, from an etch perspective. *Journal of Vacuum Science & Technology, B: Microelectronics and Nanometer Structures* **2003**, 21, (6), 2771-2776.
 62. Dauksher, W. J.; Nordquist, K. J.; Mancini, D. P.; Resnick, D. J.; Baker, J. H.; Hooper, A. E.; Talin, A. A.; Bailey, T. C.; Lemonds, A. M.; Sreenivasan, S. V.; Ekerdt, J. G.; Willson, C. G., Characterization of and imprint results using indium tin oxide-based step and flash imprint lithography templates. *Journal of Vacuum Science & Technology, B: Microelectronics and Nanometer Structures* **2002**, 20, (6), 2857-2861.
 63. Gehoski, K. A.; Resnick, D. J.; Dauksher, W. J.; Nordquist, K. J.; Ainley, E.; McCord, M.; Raphaelian, M.; Hess, H., Indium tin oxide template development for step and flash imprint lithography. *Proceedings of SPIE-The International Society for Optical Engineering* **2005**, 5751, (Pt. 2, Emerging Lithographic Technologies IX), 986-993.
 64. Nordquist, K. J.; Ainley, E. S.; Mancini, D. P.; Dauksher, W. J.; Gehoski, K. A.; Baker, J.; Resnick, D. J.; Masnyj, Z.; Mangat, P. J. S., Image placement issues for ITO-based step and flash imprint lithography templates. *Journal of Vacuum Science & Technology, B: Microelectronics and Nanometer Structures--Processing, Measurement, and Phenomena* **2004**, 22, (2), 695-701.
 65. Dauksher, W. J.; Nordquist, K. J.; Le, N. V.; Gehoski, K. A.; Mancini, D. P.; Resnick, D. J.; Casoose, L.; Bozak, R.; White, R.; Csuy, J.; Lee, D., Repair of step and flash imprint lithography templates. *Journal of Vacuum Science & Technology, B: Microelectronics and Nanometer Structures--Processing, Measurement, and Phenomena* **2004**, 22, (6), 3306-3311.
 66. Hess, H. F.; Pettibone, D.; Adler, D.; Bertsche, K.; Nordquist, K. J.; Mancini, D. P.; Dauksher, W. J.; Resnick, D. J., Inspection of templates for imprint lithography. *Journal of Vacuum Science & Technology, B: Microelectronics and Nanometer Structures--Processing, Measurement, and Phenomena* **2004**, 22, (6), 3300-3305.

67. Myron, L. J.; Gershtein, L.; Gottlieb, G.; Burkhardt, B.; Griffiths, A.; Mellenthin, D.; Rentzsch, K.; MacDonald, S.; Hughes, G., Advanced mask metrology enabling characterization of imprint lithography templates. *Proceedings of SPIE-The International Society for Optical Engineering* **2005**, 5752, (Pt. 1, Metrology, Inspection, and Process Control for Microlithography XIX), 384-391.
68. Pettibone, D.; Stokowski, S., Optical inspection of next generation lithography masks. *Journal of Vacuum Science & Technology, B: Microelectronics and Nanometer Structures* **2004**, 22, (6), 3366-3372.
69. Young, S. R.; Daulsher, W. J. Repair of imprint lithography templates prior to relief etching. 2005.
70. Resnick, D. J.; Mancini, D. P.; Sreenivasan, S. V.; Willson, G., Release layers for contact and imprint lithography. *Semiconductor International* **2002**, 25, (6), 71-72,74,76,78,80.
71. Parikh, A. N.; Allara, D. L.; Azouz, I. B.; Rondelez, F., An Intrinsic Relationship between Molecular Structure in Self-Assembled n-Alkylsiloxane Monolayers and Deposition Temperature. *Journal of Physical Chemistry* **1994**, 98, (31), 7577-90.
72. Beck, M.; Graczyk, M.; Maximov, I.; Sarwe, E. L.; Ling, T. G. I.; Keil, M.; Montelius, L., Improving stamps for 10 nm level wafer scale nanoimprint lithography. *Microelectronic Engineering* **2002**, 61-62, 441-448.
73. Ulman, A., *An introduction to ultrathin organic films: from Langmuir-Blodgett to self-assembly*. Academic Press: Boston, 1991; p xxiii, 442.
74. Bailey, T.; Choi, B. J.; Colburn, M.; Meissl, M.; Shaya, S.; Ekerdt, J. G.; Sreenivasan, S. V.; Willson, C. G., Step and flash imprint lithography: Template surface treatment and defect analysis. *Journal of Vacuum Science & Technology, B: Microelectronics and Nanometer Structures* **2000**, 18, (6), 3572-3577.
75. Holcombe, T. W., III; Dickey, M.; Willson, C. G., A New Method for Covalently Bonding Functionality to ITO Films. *Abstracts, 57th Southeast/61st Southwest Joint Regional Meeting of the American Chemical Society, Memphis, TN, United States, November 1-4* **2005**, NOV04-377.
76. Jaszewski, R. W.; Schiff, H.; Schnyder, B.; Schneuwly, A.; Groning, P., The deposition of anti-adhesive ultra-thin Teflon-like films and their interaction with polymers during hot embossing. *Applied Surface Science* **1999**, 143, (1-4), 301-308.
77. Wu, K.; Kim, E. K.; Ekerdt, J. G.; Willson, C. G., Effect of interfacial surfactants on template release in imprint lithography. *Abstracts of Papers, 229th ACS*

- National Meeting, San Diego, CA, United States, March 13-17, 2005* **2005**, COLL-573.
78. Kim, E. K.; Stewart, M. D.; Wu, K.; Palmieri, F. L.; Dickey, M. D.; Ekerdt, J. G.; Willson, C. G., Vinyl ether formulations for step and flash imprint lithography. *Journal of Vacuum Science & Technology, B: Microelectronics and Nanometer Structures* **2005**, 23, (6), 2967-2971.
 79. Tan, H.; Gilbertson, A.; Chou, S. Y., Roller nanoimprint lithography. *Journal of Vacuum Science & Technology, B: Microelectronics and Nanometer Structures* **1998**, 16, (6), 3926-3928.
 80. McMackin, I.; Schumaker, P.; Babbs, D.; Choi, J.; Collison, W.; Sreenivasan, S. V.; Schumaker, N. E.; Watts, M. P. C.; Voisin, R. D., Design and performance of a step and repeat imprinting machine. *Proceedings of SPIE-The International Society for Optical Engineering* **2003**, 5037, (Pt. 1, Emerging Lithographic Technologies VII), 178-186.
 81. McMackin, I.; Choi, J.; Schumaker, P.; Nguyen, V.; Xu, F.; Thompson, E.; Babbs, D.; Sreenivasan, S. V.; Watts, M.; Schumaker, N., Step and Repeat UV nanoimprint lithography tools and processes. *Proceedings of SPIE-The International Society for Optical Engineering* **2004**, 5374, (Pt. 1, Emerging Lithographic Technologies VIII), 222-231.
 82. Moon, E. E.; Mondol, M. K.; Everett, P. N.; Smith, H. I., Dynamic alignment control for fluid-immersion lithographies using interferometric-spatial-phase imaging. *Journal of Vacuum Science & Technology, B: Microelectronics and Nanometer Structures* **2005**, 23, (6), 2607-2610.
 83. Zhang, W.; Chou, S. Y., Multilevel nano-imprint lithography with submicron alignment over 4 in. Si wafers. *Applied Physics Letters* **2001**, 79, (6), 845-847.
 84. Rowland, H. D.; King, W. P.; Sun, A. C.; Schunk, P. R., Simulations of nonuniform embossing: The effect of asymmetric neighbor cavities on polymer flow during nanoimprint lithography. *Journal of Vacuum Science & Technology, B: Microelectronics and Nanometer Structures* **2005**, 23, (6), 2958-2962.
 85. Rowland, H. D.; Sun, A. C.; Schunk, P. R.; King, W. P., Impact of polymer film thickness and cavity size on polymer flow during embossing: Toward process design rules for nanoimprint lithography. *Journal of Micromechanics and Microengineering* **2005**, 15, (12), 2414-2425.
 86. King, W. P.; Rowland, H. D., Understanding polymer flow during micro- and nano-embossing. *PMSE Preprints* **2006**, 94, 732.

87. Haisma, J.; Verheijen, M.; van den Heuvel, K.; van den Berg, J., Mold-assisted nanolithography: A process for reliable pattern replication. *Journal of Vacuum Science & Technology, B: Microelectronics and Nanometer Structures* **1996**, 14, (6), 4124-4128.
88. Schulz, H.; Scheer, H. C.; Hoffmann, T.; Sotomayor Torres, C. M.; Pfeiffer, K.; Bleidiessel, G.; Grutzner, G.; Cardinaud, C.; Gaboriau, F.; Peignon, M. C.; Ahopelto, J.; Heidari, B., New polymer materials for nanoimprinting. *Journal of Vacuum Science & Technology, B: Microelectronics and Nanometer Structures* **2000**, 18, (4), 1861-1865.
89. Chou, S. Y.; Keimel, C.; Gu, J., Ultrafast and direct imprint of nanostructures in silicon. *Nature* **2002**, 417, (6891), 835-837.
90. Dickey, M. D.; Collister, E.; Kim, E. K.; Willson, C. G., Tailoring photopolymerization materials for nanotechnology. *Abstracts of Papers, 228th ACS National Meeting, Philadelphia, PA, United States, August 22-26, 2004* **2004**, POLY-337.
91. Xu, F.; Stacey, N. A.; Watts, M.; Truskett, V.; McMackin, I.; Choi, J.; Schumaker, P.; Thompson, E.; Babbs, D.; Sreenivasan, S. V.; Willson, C. G.; Schumaker, N., Development of imprint materials for the Step and Flash Imprint Lithography process. *Proceedings of SPIE-The International Society for Optical Engineering* **2004**, 5374, (Pt. 1, Emerging Lithographic Technologies VIII), 232-241.
92. Reddy, S.; Bonnacaze, R. T., Simulation of fluid flow in the step and flash imprint lithography process. *Microelectronic Engineering* **2005**, 82, (1), 60-70.
93. Colburn, M.; Choi, B. J.; Sreenivasan, S. V.; Bonnacaze, R. T.; Willson, C. G., Ramifications of lubrication theory on imprint lithography. *Microelectronic Engineering* **2004**, 75, (3), 321-329.
94. Johnson, S.; Burns, R.; Kim, E. K.; Dickey, M.; Schmid, G.; Meiring, J.; Burns, S.; Willson, C. G.; Convey, D.; Wei, Y.; Fejes, P.; Gehoski, K.; Mancini, D.; Nordquist, K.; Dauksher, W. J.; Resnick, D. J., Effects of etch barrier densification on step and flash imprint lithography. *Journal of Vacuum Science & Technology, B: Microelectronics and Nanometer Structures--Processing, Measurement, and Phenomena* **2005**, 23, (6), 2553-2556.
95. Colburn, M.; Suez, I.; Choi, B. J.; Meissl, M.; Bailey, T.; Sreenivasan, S. V.; Ekerdt, J. G.; Willson, C. G., Characterization and modeling of volumetric and mechanical properties for step and flash imprint lithography photopolymers. *Journal of Vacuum Science & Technology, B: Microelectronics and Nanometer Structures* **2001**, 19, (6), 2685-2689.

96. Cheng, X.; Guo, L. J.; Fu, P.-F., Room-temperature, low-pressure nanoimprinting based on cationic photopolymerization of novel epoxysilicone monomers. *Advanced Materials* **2005**, 17, (11), 1419-1424.
97. Kim, E. K.; Stacey, N. A.; Smith, B. J.; Dickey, M. D.; Johnson, S. C.; Trinque, B. C.; Willson, C. G., Vinyl ethers in ultraviolet curable formulations for step and flash imprint lithography. *Journal of Vacuum Science & Technology, B: Microelectronics and Nanometer Structures--Processing, Measurement, and Phenomena* **2004**, 22, (1), 131-135.
98. Stewart, M. D.; Wetzel, J. T.; Schmid, G. M.; Palmieri, F.; Thompson, E.; Kim, E. K.; Wang, D.; Sotodeh, K.; Jen, K.; Johnson, S. C.; Hao, J.; Dickey, M. D.; Nishimura, Y.; Laine, R. M.; Resnick, D. J.; Willson, C. G., Direct imprinting of dielectric materials for dual damascene processing. *Proceedings of SPIE-The International Society for Optical Engineering* **2005**, 5751, (Pt. 1, Emerging Lithographic Technologies IX), 210-218.
99. Hua, F.; Sun, Y.; Gaur, A.; Meitl, M. A.; Bilhaut, L.; Rotkina, L.; Wang, J.; Geil, P.; Shim, M.; Rogers, J. A.; Shim, A., Polymer Imprint Lithography with Molecular-Scale Resolution. *Nano Letters* **2004**, 4, (12), 2467-2471.
100. Le, N. V.; Dauksher, W. J.; Gehoski, K. A.; Resnick, D. J.; Hooper, A. E.; Johnson, S.; Willson, G., Selective dry etch process for step and flash imprint lithography. *Microelectronic Engineering* **2005**, 78-79, 464-473.
101. Le, N. V.; Gehoski, K. A.; Dauksher, W. J.; Baker, J. H.; Resnick, D. J.; Dues, L., Development of an etch-definable lift-off process for use with step and flash imprint lithography. *Proceedings of SPIE-The International Society for Optical Engineering* **2005**, 5751, (Pt. 1, Emerging Lithographic Technologies IX), 219-226.
102. Weisbrod, E. J.; Dauksher, W. J.; Zhang, D.; Rauf, S.; Mangat, P. J. S.; Ventzek, P. L. G.; Smith, K. H.; Clemens, S. B.; Martin, C. J.; Engelstad, R. L., Thermal modeling of extreme ultraviolet and step and flash imprint lithography substrates during dry etch. *Journal of Vacuum Science & Technology, B: Microelectronics and Nanometer Structures* **2002**, 20, (6), 3047-3052.
103. Sun, X.; Zhuang, L.; Zhang, W.; Chou, S. Y., Multilayer resist methods for nanoimprint lithography on nonflat surfaces. *Journal of Vacuum Science & Technology, B: Microelectronics and Nanometer Structures* **1998**, 16, (6), 3922-3925.
104. Colburn, M.; Grot, A.; Amistoso, M. N.; Choi, B. J.; Bailey, T. C.; Ekerdt, J. G.; Sreenivasan, S. V.; Hollenhorst, J.; Willson, C. G., Step and flash imprint lithography for sub-100-nm patterning. *Proceedings of SPIE-The International*

- Society for Optical Engineering* **2000**, 3997, (Emerging Lithographic Technologies IV), 453-457.
105. Cheng, X.; Guo, L. J., One-step lithography for various size patterns with a hybrid mask-mold. *Microelectronic Engineering* **2004**, 71, (3-4), 288-293.
 106. Cheng, X.; Chang, M.-H.; Guo, L. J., Combined nanoimprint- and photolithography technique with a hybrid mold. *Proceedings of SPIE-The International Society for Optical Engineering* **2004**, 5374, (Pt. 1, Emerging Lithographic Technologies VIII), 337-347.
 107. Cheng, X.; Guo, L. J., A combined-nanoimprint-and-photolithography patterning technique. *Microelectronic Engineering* **2004**, 71, (3-4), 277-282.
 108. Decker, C.; Jenkins, A. D., Kinetic approach of oxygen inhibition in ultraviolet- and laser-induced polymerizations. *Macromolecules* **1985**, 18, (6), 1241-4.
 109. Dickey, M. D.; Burns, R. L.; Kim, E. K.; Johnson, S. C.; Stacey, N. A.; Willson, C. G., Study of the kinetics of Step and Flash imprint lithography photopolymerization. *AIChE Journal* **2005**, 51, (9), 2547-2555.
 110. Dickey, M. D.; Willson, C. G., Effects of oxygen on step and flash imprint lithography photopolymerization kinetics. *PMSE Preprints* **2004**, 90, 24-25.
 111. Abdo, A.; Schuetter, S.; Nellis, G.; Wei, A.; Engelstad, R.; Truskett, V., Predicting the fluid behavior during the dispensing process for step-and-flash imprint lithography. *Journal of Vacuum Science & Technology, B: Microelectronics and Nanometer Structures* **2004**, 22, (6), 3279-3282.
 112. Kim, E. K.; Ekerdt, J. G.; Willson, C. G., Importance of evaporation in the design of materials for step and flash imprint lithography. *Journal of Vacuum Science & Technology, B: Microelectronics and Nanometer Structures--Processing, Measurement, and Phenomena* **2005**, 23, (4), 1515-1520.
 113. Bailey, T.; Smith, B.; Choi, B. J.; Colburn, M.; Meissl, M.; Sreenivasan, S. V.; Ekerdt, J. G.; Willson, C. G., Step and flash imprint lithography: Defect analysis. *Journal of Vacuum Science & Technology, B: Microelectronics and Nanometer Structures* **2001**, 19, (6), 2806-2810.

Chapter 3

Imprint Lithography Photopolymerization Kinetics

This chapter presents a semi-empirical kinetic model that captures the effects of oxygen on SFIL. Kinetic rate coefficients used in the model were measured using real time IR techniques. Dissolved oxygen causes an inhibition period at the onset of exposure that extends the required exposure time. Oxygen inhibition also results in a thin perimeter of under-cured material surrounding the template due to oxygen diffusion from the ambient during polymerization. The model allows the impact of oxygen on SFIL to be studied as a function of various formulation and exposure variables. Methods of limiting the impact of oxygen are presented, such as alternative chemistries and inerting techniques.

3.1 INTRODUCTION

Imprint lithography offers a high resolution, yet low cost alternative to conventional lithography by avoiding the use of expensive projection optics.^{1,2} Several variations of imprint lithography have been investigated, as introduced in Chapter 1.³⁻⁵ Step and Flash Imprint Lithography (SFIL), depicted in Figure 3.1, is distinguished by its use of UV curable materials that allow pattern replication at room temperature and low pressure.^{6,7}

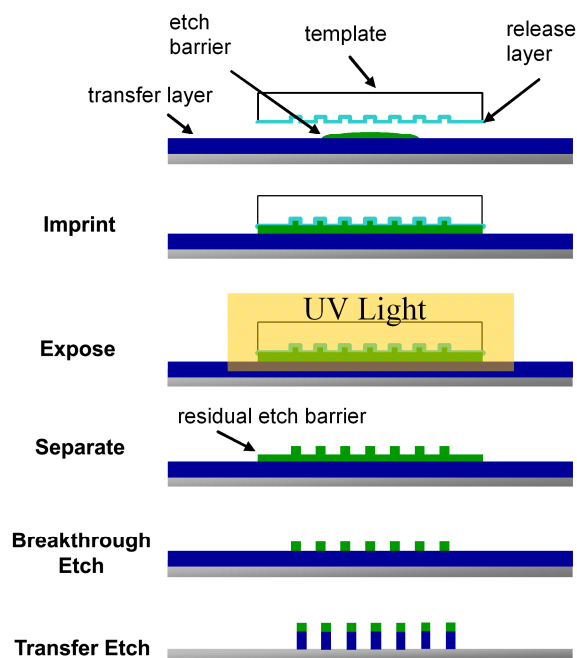


Figure 3.1: The SFIL process. A photocurable acrylate-based material is dispensed onto a substrate. The material is pressed into a molded template and irradiated through the template by UV light. The template is removed, leaving behind a replica of the mold. A series of selective etch steps results in high aspect ratio patterned features.

SFIL utilizes an acrylate-based, free radical photopolymerization of the sort found in many industrial applications, such as coatings. Acrylate systems are attractive due to their high reactivity and commercial availability. Unfortunately, oxygen strongly inhibits free radical polymerizations⁸ due to its triplet di-radical electronic ground state, which is highly reactive toward carbon based radicals.⁹ In SFIL, photoinitiated radicals react with oxygen to form peroxy radicals that do not promote acrylate chain growth. Radicals react preferentially with oxygen over monomer, which implies that essentially all dissolved oxygen must be consumed before the system begins to polymerize.⁸ Decker provides an excellent summary of the effects of oxygen on acrylate polymerizations.¹⁰ Several studies

have been performed on oxygen inhibition, but the effects of oxygen are still being investigated due to the importance of free radical polymerizations.¹¹⁻¹⁸

Since acrylates are often used for coatings, oxygen inhibition has primarily been studied in thin films.^{10,12} When thin films are photo cured in an ambient atmosphere, the polymerization in the top few microns of the film is inhibited by diffusing oxygen. This inhibition can alter certain physical properties of the film, such as the modulus at the film's surface.¹² In the SFIL process, the top surface of the film is protected from oxygen diffusion by the quartz template. Despite this protection, oxygen inhibition still presents problems for the SFIL process, as shown in Figure 3.2.^{17,18}

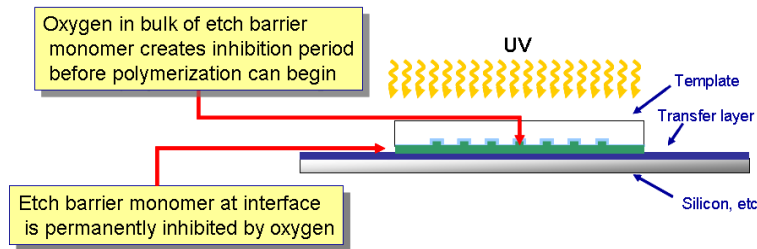


Figure 3.2: The effects of oxygen on radical based polymerizations. Dissolved oxygen quenches photogenerated radicals and polymerization will not proceed until nearly all the oxygen is consumed. Oxygen from the periphery diffuses into the material at the edge of the template, creating a rim of undercured material around the edge of the template.

Oxygen dissolved in the etch barrier produces an initial inhibition period during irradiation, which ultimately lowers process throughput. In addition, oxygen can diffuse into the etch barrier from the template edge during curing. As a result, a thin layer of under-cured etch barrier surrounds the edges of the imprint, as shown in Figure 3.3. This under-cured material may potentially foul the template and contribute to defect generation during subsequent imprints. The potential deleterious effects of oxygen on the SFIL process are a focus of this chapter. Both kinetic measurements and a kinetic-based model of the SFIL are presented.

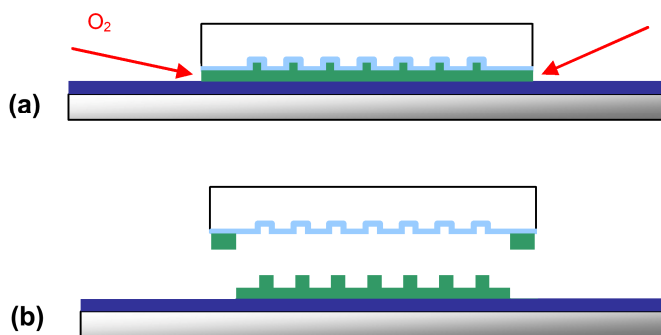


Figure 3.3: (a) Oxygen diffuses into the perimeter of the etch barrier under the template. (b) Under-cured material remains on template, potentially affecting subsequent imprints.

3.2 MATERIALS AND METHODS

The formulation of the etch barrier was carefully chosen to meet all SFIL processing requirements. For example, the etch barrier must adhere to the transfer layer, but release from the template.¹⁹ Furthermore, the etch barrier must provide sufficient etch resistance and selectivity for the transfer etch.¹ To achieve this end, the etch barrier must contain a minimum of 12 wt% silicon to provide resistance to an anisotropic oxygen etch.²⁰ The etch barrier must also have a sufficiently low viscosity to rapidly achieve a thin residual layer during imprinting. The formulation of the etch barrier used in this study is a mixture made of four different components¹, as seen in Table 3.1. The total density of the etch barrier solution is 0.92 g/mL at room temperature, which provides 5.3 mol/L of reactive acrylate groups and 0.061 mol/L initiator (for 1 wt% initiator) in the etch barrier formulation.

Acrylate monomers are typically used with a benzoin photoinitiator, which undergoes a rapid homolytic cleavage upon UV exposure, according to a Norrish-type I mechanism, to generate free radicals that initiate the polymerization.¹⁰ Darocur 1173 (2,2-dimethyl-2-hydroxyacetophenone, CIBA) was chosen as the free radical initiator

because it is a commercially available liquid initiator that is both highly efficient²¹ and UV sensitive at 365 nm.

Table 3.1: Etch Barrier Composition

| Component | Structure | Purpose | Weight Percent |
|-----------------------------------|---|---|----------------|
| Gelest SIA-0210 (SIA) | $\begin{array}{c} \text{O}-\text{SiMe}_3 \\ \\ \text{Me}_3\text{Si}-\text{O}-\text{Si}-(\text{CH}_2)_3-\text{O}-\text{C}(=\text{O})-\text{CH}=\text{CH}_2 \\ \\ \text{O}-\text{SiMe}_3 \end{array}$ | Silicon containing monoacrylate for etch resistance | 44 |
| Ethylene Glycol Diacrylate (EGDA) | $\text{H}_2\text{C}=\text{CH}-\text{C}(=\text{O})-\text{O}-\text{CH}_2-\text{CH}_2-\text{O}-\text{C}(=\text{O})-\text{CH}=\text{CH}_2$ | Crosslinker for mechanical stability | 15 |
| t-Butyl Acrylate (TBA) | $\begin{array}{c} \text{O} \\ \\ \text{t-BuO}-\text{C}-\text{CH}=\text{CH}_2 \end{array}$ | Reactive diluent to maintain low viscosity | 37 |
| Darocur 1173 | $\begin{array}{c} \text{O} \quad \text{OH} \\ \quad \\ \text{Ph}-\text{C}-\text{C}-\text{Me} \\ \\ \text{Me} \end{array}$ | Photoinitiator | 1-4 |

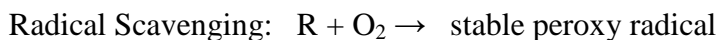
Real Time – Fourier Transform Infrared (RTIR) Spectroscopy was used to monitor the polymerization. RTIR utilizes *in situ* IR measurements to track the disappearance of acrylate double bonds during photo curing.¹⁰ A Nicolet Magna-IR 550 was used at 8 cm⁻¹ resolution, which allowed for measurements every 0.07 seconds. Samples were prepared by placing a drop of etch barrier solution on a double polished silicon wafer. The drop was covered with a sodium chloride disk (Wilmad). The salt disk forced the drop to form a thin film and provided a barrier to prevent oxygen diffusion during curing. Dissolved oxygen was not removed from the etch barrier. Monomer was used as received: TBA (98%, Aldrich 327182), EGDA (96%, Aldrich 409995), and SIA (Gelest SIA 0210.0). Each monomer contains a low concentration of MEHQ (Hydroquinone monomethyl ether) that is added by the manufacturer to provide stability

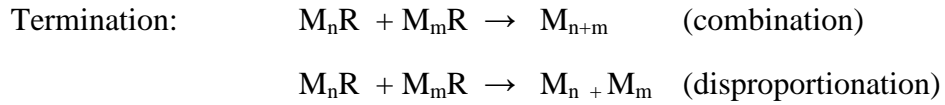
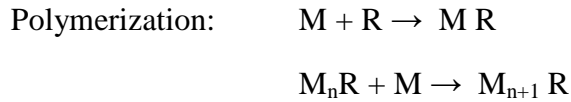
during shipping. It was experimentally determined that removing the MEHQ inhibitor resulted in no observable difference in the kinetics. To prove this claim, the inhibitor was removed from each component using commercially available inhibitor removal columns (Aldrich 306312). The polymerizations were irradiated with a mercury lamp (Novacure EFOS) at 31.8 mW/cm^2 , unless otherwise noted. The polymerizations were all performed under normal, ambient atmospheric conditions.

The properties of oxygen in the etch barrier are critical to the kinetic model. The initial concentration of dissolved oxygen in the etch barrier was $2.8 \times 10^{-4} \text{ mol/L}$, as measured using a dissolved oxygen probe (YSI-5100). Generally, acrylate systems are assumed to contain 10^{-3} mol/L oxygen²², but this appears to be a literature estimate rather than a measured value. The diffusion coefficient of oxygen in the etch barrier was measured as $5.5 \times 10^{-6} \text{ cm}^2/\text{s}$. The diffusivity of oxygen in the monomer solution was measured using chronoamperometry,²³ a method that relies on measuring both the transient and steady state current resulting from oxidation of diffusing oxygen to an electrode of known diameter (25 μm , platinum) submerged in solution.

3.3 KINETICS BACKGROUND AND THEORY

Classical free radical polymerization kinetics²⁴ were assumed to give a first-order approximation of the effects of oxygen. This model consists of four important reaction steps: initiation, propagation, termination, and radical scavenging, as shown below.





I, R, O₂, M, and M_nR represent, respectively, initiator, radicals, oxygen, acrylate monomer, and radical chains of length n. M_{n+m} represents the polymer that results from termination. These reaction steps are interrelated, as shown in Figure 3.4.

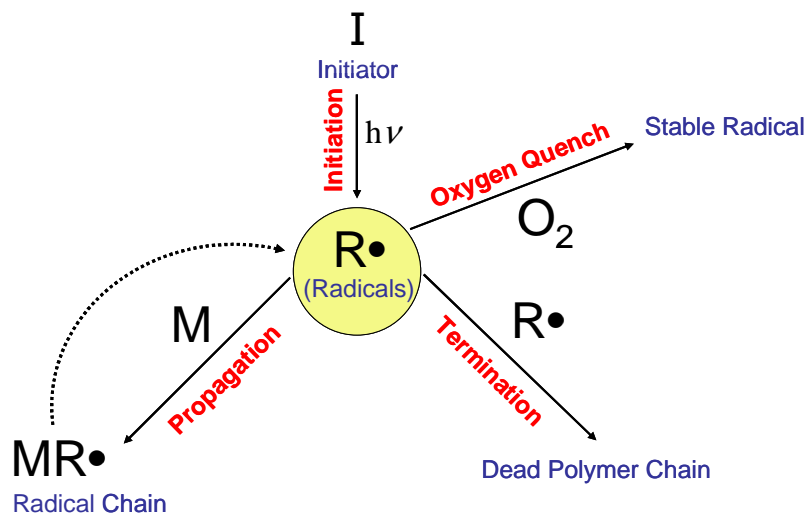


Figure 3.4: General free radical reaction mechanism.

The initiation step shown in Figure 3.4 involves an initiating species absorbing UV light, $h\nu$, and splitting into two radicals. Generated radicals rapidly react with oxygen to form peroxy species that are non-reactive towards the acrylate double bond, but once the oxygen is depleted, the radicals react with monomer to form a growing polymer chain. It has been shown experimentally that the concentration of dissolved oxygen must be lowered by at least two orders of magnitude before polymerization begins due to the

high reactivity of oxygen with radicals.⁸ The polymer chain continues to propagate until it encounters a radical end of another chain at which point the two radical ends terminate by either combination or disproportionation.

The critical rate equations for the model include the rate of initiation, radical scavenging, polymerization, and termination. The expression for rate of initiation is shown below in Equation 3.1. In Equations 3.1-3.4, the brackets ([...]) denote concentration (mol/L).

$$\text{Rate of Initiation: } R_i = 2 \Phi k_I [I] \quad (3.1)$$

R_i is the rate of initiation and k_I is the reaction coefficient for initiation (s^{-1}), which represents the amount of light absorbed per mol of initiator. Equation 3.1 has a coefficient of 2 due to two radicals formed for each initiator broken down. Quantum yield, Φ , is defined as the product of two terms, $\Phi = \Phi' f$, where f is the initiator efficiency (fraction of radicals produced that initiate propagating chains) and Φ' is the number of initiator molecules dissociated per photon absorbed.^{8,25} The notation of Equation 3.1 was chosen such that the effects of initiator absorbance and irradiation intensity can be wrapped into one term, k_I , which is useful when modeling the effects of initiation on the polymerization. Following the initiation step, radicals that react with oxygen form relatively stable peroxy radicals. The kinetic rate expression is shown in Equation 3.2.

$$\text{Rate of Scavenging: } R_{O_2} = -k_o [O_2][R] \quad (3.2)$$

Here k_o is the rate coefficient of oxygen consumption (L/mol·s). Based on previous studies, the value of k_o was assumed to be 1×10^9 (L/mol·s).^{8,26,27} This value is several orders of magnitude higher than any other reaction coefficients in the polymerization. Due to the large difference in reactivity, essentially no polymerization occurs in the presence of oxygen. Equation 3.2 implies that one radical consumes one oxygen molecule. In certain reaction systems, a single radical is often capable of consuming multiple oxygen molecules since the peroxy radical can generate new radicals via hydrogen abstraction.¹³ However, the SFIL acrylate formulation does not contain any easily abstractable hydrogens. Once the concentration of oxygen is sufficiently reduced, the radicals begin to react with monomer to form polymer. The kinetic expression for polymerization is shown in Equation 3.3.

$$\text{Rate of Polymerization: } R_p = -k_p [M][R] \quad (3.3)$$

R_p is the rate of polymerization and k_p is the rate coefficient of polymerization (L/mol·s). By definition, the rate of polymerization is the rate at which monomer is consumed. Individual radical chains continue to propagate until they are terminated by another radical. The kinetics of the termination process is shown in Equation 3.4.

$$\text{Rate of Termination: } R_t = -2 k_t [R][R] \quad (3.4)$$

Here k_t represents the termination coefficient (L/mol·s), which generically represents the combined effects of combination and disproportionation. The factor of 2 accounts for two radical chains destroyed per termination event. It should be noted that $[R]$ represents the concentration of all radicals, regardless of chain length (i.e. M_nR).

This is a classic assumption that simplifies the modeling tremendously. This assumption is generally justified by considering the rate coefficients k_p and k_t to represent the net effect of polymerization and termination processes. Furthermore, k_p and k_t are coefficients, not constants, and subsequently change as the reaction proceeds. This approach helps to account for chain length dependent reactions^{28,29} and changes in the reaction medium due to polymerization.

A species balance based on Equations 3.1-3.4 gives the basis for the following kinetic expressions:

$$\text{Initiator: } \frac{d[I]}{dt} = -\Phi' k_I [I] \quad (3.5)$$

$$\text{Radicals: } \frac{d[R]}{dt} = 2 \Phi k_I [I] - k_O [O_2][R] - 2 k_t [R]^2 \quad (3.6)$$

$$\text{Oxygen: } \frac{d[O_2]}{dt} = D_{O_2} \frac{\partial^2 [O_2]}{\partial x^2} - k_O [O_2][R] \quad (3.7)$$

$$\text{Monomer: } \frac{d[M]}{dt} = -k_p [M][R] \quad (3.8)$$

Equation 3.7 contains the oxygen diffusion coefficient, D (cm^2/s). This expression for diffusion, based on Fick's second law, accounts for diffusion of oxygen from the perimeter of the template. It should be further noted that the etch barrier is a ternary system, so the reaction coefficients are overall coefficients representing the net effect of the system. The values of the reaction coefficients will be discussed in Section 3.6.¹⁸

Equation 3.8, which is the expression for the rate of polymerization, is in terms of both monomer and radical concentration. Radical concentration is very difficult to

measure experimentally, thus it is common practice to utilize an alternative expression for radicals. A more convenient expression for the rate of polymerization can be obtained by applying the well known quasi steady-state approximation (QSSA), which assumes the rate of initiation is equal to the rate of termination.²⁴ The QSSA is reasonable when the radical lifetimes are small compared to the time scales of initiator consumption and monomer conversion. Making the QSSA gives the following expression for the rate of polymerization, as seen in Equation 3.9. This expression is experimentally useful since all terms in Equation 3.9 are measurable.

$$\frac{d[M]}{dt} = -k_p [M] \left(\frac{R_i}{2k_t} \right)^{0.5} \quad (3.9)$$

The power of 0.5 in Equation 3.9 is highly dependent on the termination mechanism. This coefficient is referred to as alpha (α), and is exactly 0.5 when the radicals terminate entirely by the classical bimolecular mechanism. When primary radical termination (PRT) occurs, α drops below 0.5.³⁰ PRT is a termination process whereby primary radicals scavenge growing radicals chains rather than reacting with monomer to form a polymer chain. Primary radicals are either initiated radicals or short chain radicals that have high mobility compared to long radical chains. Equation 3.9 holds well for most systems since PRT usually only occurs when there is a large concentration of radicals compared to monomer groups.³¹ Similarly, unimolecular termination has the effect of raising α above 0.5. Unimolecular termination results when radical chains become trapped within the polymer matrix and are unable to terminate in a bimolecular reaction. Therefore, α is expected to increase with conversion as unimolecular termination becomes more prominent due to gelation. This is especially

true in multifunctional systems where crosslinking limits mobility. For instance, α has been shown to be ~ 0.85 in a multifunctional acrylate system, implying unimolecular termination.³² In order to use classical kinetic modeling, α must be ~ 0.5 . Thus, we set out to determine α for the SFIL etch barrier system to learn more about the termination mechanisms at play and to determine the applicability of Equation 3.9 for further kinetic analysis.

3.4 DETERMINING ALPHA

An established method was used to determine α for the etch barrier acrylate system.³⁰ Etch barrier with 4 wt% initiator loading was exposed at various intensities and RTIR was used to track the disappearance of monomer. The value of α is equivalent to the slope of a plot of $\log(t')$ versus $\log(\text{intensity}, I_0)$. The t' represents the time to reach a given conversion minus the inhibition time due to inherent oxygen, which does not factor into the analysis. By performing this analysis at various points of conversion, the variation of α with conversion can be determined. The data from this method are shown in Figure 3.5 and the results summarized in Table 3.2. The methodology behind the α measurement is partly flawed since changing light intensity can change the radical concentration, and thus increase the likelihood of primary radical termination. However, the linear fit of the results and the consistency of the data suggest that the reaction environment is a more important factor than light intensity in determining α . The value of α appears to increase with conversion from ~ 0.3 to ~ 0.4 in the etch barrier with a 4 wt% initiator etch barrier system. The increase of α with conversion is consistent with theory since the on-set of gelation limits the mobility of small radicals. Generally, free radical formulations use initiator concentrations between 0.5-5 wt% initiator. It is not surprising

that the high end of this scale results in some primary radical termination due to the high concentration of initiator.

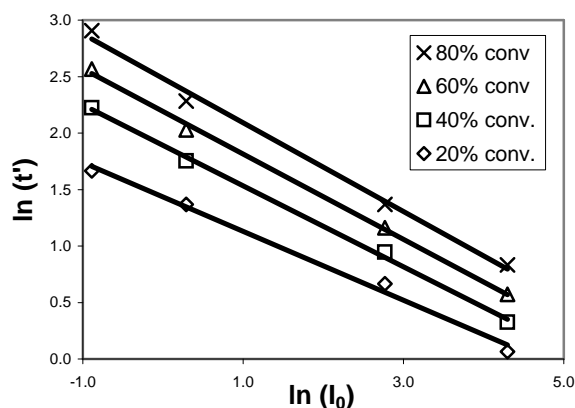


Figure 3.5: Determination of α for a 4 wt% Darocur 1173 system. The slope is equivalent to Alpha, as measured at various conversions.

Table 3.2: Summary of α Values for 4 wt% Dacocur 1173 Taken from Figure 3.5. (R^2 is the correlation coefficient from the linear fit of the data.)

| Percent Conversion | Alpha | R^2 |
|--------------------|-------|-------|
| 20 | 0.31 | 0.993 |
| 40 | 0.36 | 0.998 |
| 60 | 0.38 | 0.998 |
| 80 | 0.39 | 0.994 |

Alpha for a 1 wt% initiator etch barrier formulation was also measured, while keeping the proportions of the other components constant relative to each other. Table 3.3 shows that α is 0.46 when using 1 wt% Darocur 1173 in the etch barrier formulation, which is very close to the 0.5 value for pure bimolecular termination using the steady

state approximation. The value of α is essentially constant, within experimental error, over the range of conversions studied.

Table 3.3: Alpha (α) Using 1 wt% Darocur 1173.

| Percent Conversion | Alpha | R ² |
|--------------------|-------|----------------|
| 10 | 0.46 | 0.993 |
| 20 | 0.44 | 0.977 |
| 30 | 0.43 | 0.979 |
| 40 | 0.43 | 0.976 |
| 50 | 0.45 | 0.967 |
| 60 | 0.46 | 0.936 |
| 70 | 0.52 | 0.997 |

The value of α was also determined using a separate analysis technique.¹⁰ An estimation for α can be made by comparing R_p for polymerizations at different irradiation intensities. The principle behind this method stems from the fact that R_p is proportional to irradiation intensity raised to the power of α . Using this method, α was found to be 0.58 +/- 0.08 from 10-50% conversion, with no apparent trend in the data. This slightly larger value of α is likely due to the error associated with determining R_p . These methods each have their limitations, but the results are consistent with the use of the theoretical value of α (0.5) as a first order approximation in the kinetic modeling.

Of course, the value of α represents the net effect of the termination mechanisms involved in the polymerization. Therefore, in theory a α value of 0.5 could represent a combination of unimolecular, primary radical, and bimolecular termination. To prove that bimolecular termination is the dominant termination mechanism in a system with a α of ~0.5, the absence of either PRT or unimolecular termination must be verified. Previously, the presence of unimolecular termination has been observed in polymer

samples by heating crosslinked samples post-photocuring. This heating mobilizes trapped radicals and results in additional observable conversion.^{33,34} When cured etch barrier samples were heated, this effect was not observed experimentally, so it was concluded that unimolecular termination is insignificant. It is likely that the termination mechanism is primarily bimolecular since α is close to 0.5 and there are no signs of significant unimolecular termination. Therefore, the use of Equation 3.9 is justified in both the kinetic analysis and modeling.

3.5 SFIL KINETICS

Before analyzing the kinetics of the etch barrier mixture, kinetic profiles of the individual components in the etch barrier were obtained by performing three separate homopolymerizations. As shown in Figure 3.6, each component has a unique kinetic profile. (Note that the data was taken at 1 mW/cm² in order to accentuate the unique aspects of the curing profiles of the components.) The t-butyl acrylate component displays autoacceleration, which can be seen as the polymerization rate increases from 10% conversion to 40% conversion. Autoacceleration is a well-known phenomenon that is characterized by an increasing rate of polymerization with conversion. As the polymerization proceeds, the reaction environment grows more viscous and cross-linked, which limits the mobility of radical chains. This causes the radical termination rate to drop and consequently the polymerization rate increases. The t-butyl acrylate reaction goes to nearly complete conversion, which indicates that the monomer maintains high mobility up to high conversions, as expected. EGDA cures rapidly at low conversions due its difunctionality, which increases the reactive acrylate group concentration and also results in crosslinking that contributes to autoacceleration at very low conversions. In contrast to t-butyl acrylate, EGDA only partially cures due to cross-linking. Due to its

difunctionality, the EGDA monomer can be incorporated into the polymer while still maintaining an unreacted functional group. SIA also reacts rapidly at low conversions, possibly due to the viscosity of the bulk material (~ 3.83 cp), which would limit chain mobility and thus lower the rate of termination. The mono-functional SIA goes to nearly complete conversion, which indicates that the monomer maintains high mobility up to high conversions.

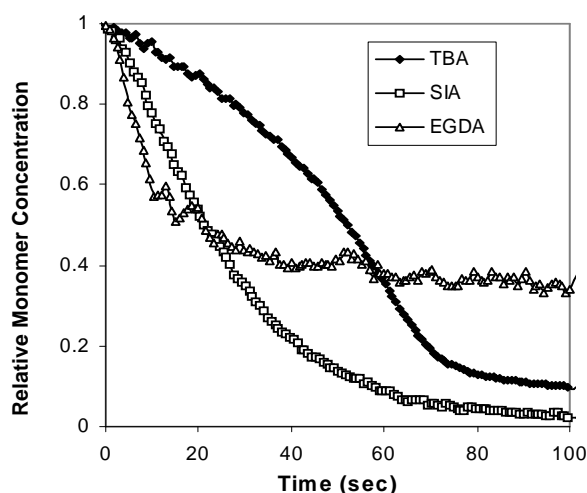


Figure 3.6: Comparison of individual components (1.0 mW/cm², 4 wt% Darocur 1173, no oxygen).

The kinetic profile of the etch barrier is shown in Figure 3.7 at two initiator concentrations. The inhibition period is four times as long for 1 wt% initiator as for 4 wt%, which is in perfect agreement with theory (0.61 seconds for 4 wt% and 2.64 sec for 1 wt%, based on the time to reach 1% conversion). Thus, higher initiator concentration provides added benefit for SFIL by reducing the inhibition period, which has literature precedent.²¹ There are tradeoffs to increasing the initiator concentration though, such as increasing the optical opacity of the film, which could lead to under cured regions in extreme cases. Furthermore, raising the initiator concentration increases the likelihood of

primary radical termination, which lowers the efficiency of the reaction. In systems containing monofunctional monomer, the average polymer chain length is shortened with increased initiator concentration, which would be detrimental to the mechanical properties of the polymer. Although typical initiator concentrations range from 0.5 to 5 wt%, an analysis of mechanical properties as a function of initiator concentration was outside the scope of this study.

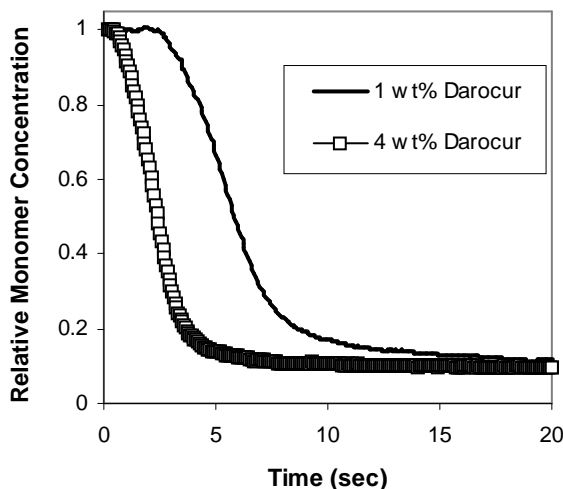


Figure 3.7: Etch barrier polymerization (31.8 mW/cm^2).

The data from Figure 3.7 were analyzed further by finding the relative rate of polymerization (R_p/M_0) as a function of conversion by determining the slope, as shown in Figure 3.8. The rate of polymerization displays the typical characteristics of bulk free radical polymerizations. There is an initial rapid increase in polymerization rate, followed by a more gradual rate increase (autoacceleration), reaching a maximum at ~40% conversion. Many multifunctional polymerization systems reach max R_p at 10-30% conversion.¹⁰ The SFIL etch barrier contains only 15 wt% crosslinker (EGDA), so it is not surprising that R_p reaches a maximum at slightly higher conversions.

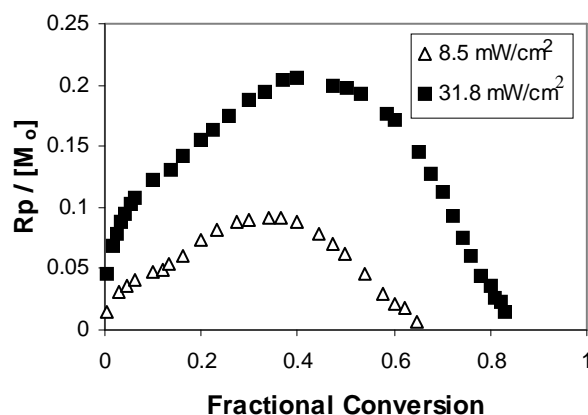


Figure 3.8: Rate of polymerization analysis for a 1 wt% Darocur 1173 system at 8.5 and 31.8 mW/cm². R_p/M_0 is the rate of polymerization divided by the initial monomer concentration.

In Figure 3.8, the higher intensity exposure (31.8 mW/cm²) has a higher rate of polymerization than the lower intensity (8.5 mW/cm²), as expected. However, the maximum rate of polymerization occurs at a higher fractional conversion. This is consistent with a theory related to delayed volume shrinkage, which occurs during intense illumination.³⁵ The principle of this theory is that higher polymerization rates allow less time for volume relaxation, and thus the reactive components maintain greater mobility up to a higher conversion. Therefore, all studies for the rate coefficients were performed at the same intensity, which was chosen to mimic the exposure source on our SFIL tool.³⁶ Figure 3.8 also displays a well-known trend: high light intensities lead to higher final conversion. Again, this is likely due to a temporary excess free volume, which occurs due to the volume shrinkage rate lagging behind the reaction rate.^{34,37} Of course, the final conversion is normally found to be less than 100% due to diffusional constraints.³⁷

3.6 DETERMINING RATE COEFFICIENTS

3.6.1 Background

The focus of this section is on determining the kinetic parameters in Equations 3.5-3.8 that are required for modeling (k_i , k_p , k_t). The reaction coefficient for initiation, k_i , represents the amount of light absorbed per mole of initiator. The coefficient of polymerization, k_p , and the rate coefficient of termination, k_t , are two critical rate coefficients that define the kinetics of acrylate-based systems. Note that these coefficients are not rate “constants” because they are highly dependent on conversion.³⁸ Consequently, effects such as autoacceleration and autodeceleration can be accounted for by measuring these coefficients as functions of conversion.^{38,39}

3.6.2 Measurement Strategies

Determining the explicit values of the individual rate coefficients k_p and k_t is not a trivial task.⁴⁰ In fact, an IUPAC committee has been working for the last 15 years to address the most appropriate way to measure rate coefficients.³⁸ The committee recommends using a combination of the Pulsed-Laser Polymerization (PLP) method to find k_p and a single pulse-pulsed laser polymerization (SP-PLP) to find k_t .³⁸ In these pulsed-laser based methods, the molecular weight distribution of the photo-generated polymer is measured after irradiating a sample of monomer with several pulses of light. The molecular weight distribution is a function of the time between the pulses and the reaction coefficients. PLP typically determines k_p only at low conversions, and then extends those values over all conversions since propagation is chemically controlled.^{41,42} The PLP method has proven to be very reliable, but unfortunately is not applicable to the etch barrier system due to the presence of cross-linker (EGDA), which prevents the use

of Size-Exclusion Chromatography (SEC) necessary for the analysis.⁴³ In addition, the PLP method has proven to be difficult to apply to acrylates,^{44,45} partly due to the skew in molecular weight distribution caused by chain transfer.⁴⁶

Considerable effort was invested in measuring the reaction coefficients using the “rotating sector” method (Boston Electronics 300 CD optical chopper, Scitec). A general explanation of the rotating sector method and a derivation of the equations used for the analysis is shown in detail in Appendix A. Unfortunately, this method proved to have several limitations, including its tedious nature. The rotating sector method has problems with unjustified assumptions, primarily due to the fact that the reaction environment is not necessarily constant from experiment to experiment.^{38,45,47} An alternative kinetic analysis technique is Electron Spin Resonance (ESR), which directly measures radical concentration but it also has many challenges and difficulties associated with it.⁴⁰

After evaluating several kinetic measurement techniques, the individual coefficients k_p and k_t were determined using an established two step procedure. The ratio $k_p/k_t^{0.5}$ can be obtained from the slope of a RTIR polymerization profile (e.g. Figure 3.7) using a quasi steady state approximation.⁴⁸ A second expression for k_p and k_t was then obtained using the dark polymerization method, which has literature precedence for both mono-functional^{11,21,39,49-51} and multifunctional (*i.e.* cross-linked) systems.^{11,21,35,39,49,52-55} This non-steady state method involves halting the UV exposure at a certain point in the polymerization. The radicals that remain active after the light is turned off continue to contribute to polymerization until they are terminated. The resulting “dark” polymerization can be tracked by RTIR. The concept behind the dark polymerization technique is shown in Figure 3.9, along with some representative data.

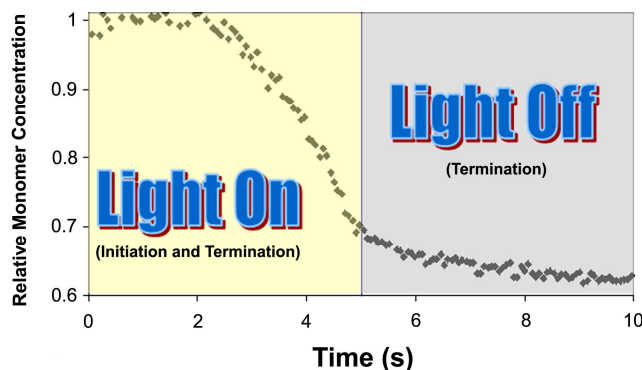


Figure 3.9: Dark polymerization technique. At a certain point, the reaction medium ceases to be irradiated, yet radicals continue to contribute to polymerization in the “dark”. During this dark period, there is no initiation and thus the kinetics are altered.

The analysis of the resulting dark polymerization data gives a second expression for the reaction coefficients, k_p/k_t . The individual coefficients k_p and k_t are calculated by combining the measured ratios, k_p/k_t and $k_p/k_t^{0.5}$. The mathematical derivation for this method is explained by Decker.¹¹ Numerous runs were performed using this method, each time turning off the light source at a new point in the polymerization to allow for the measurement of the coefficients as a function of conversion. By taking measurements at various conversions, effects such as autoacceleration and autodeceleration can be accounted for in the model by establishing the relationship between k_p and k_t and conversion.³¹ Fortunately, k_p and k_t do not change significantly during an individual dark polymerization measurement since the extent of conversion during a measurement is quite small (2-4%). The low extent of conversion during dark polymerization is due to the rapid rate of radical termination associated with acrylates. Radicals terminate most rapidly at low levels of overall conversion, where they have relatively high mobility. As a result, the contribution of RTIR noise to experimental error is largest when using the

dark polymerization method at the beginning of the reaction since the duration of the dark polymerization is relatively short.

The dark polymerization method requires assumption of the applicability of classical free radical kinetics. The use of traditional kinetics is often justified by considering polymerization to consist of three main steps (initiation, polymerization, termination) where k_p and k_t are composite values that represent processes contributing to propagation and termination, which change with conversion to account for changes in reaction environment.⁵⁶ Section 3.4 established that the etch barrier rate of polymerization is proportional to $(R_i/k_t)^{0.5}$, which is also a requisite of classical free radical kinetics. (R_i represents the rate of initiation, as defined in Equation 3.5.)

In order to perform the dark polymerization analysis, the rate of initiation must be known. Therefore, a portion of this work is dedicated to characterizing the initiation properties of the SFIL system.

3.6.3 Determining Rate of Initiation

Understanding the rate of initiation, as shown below in Equation 3.10, involves determining two terms, Φ and k_I . The reaction coefficient k_I depends solely on the amount of light absorbed by the initiator. Only a fraction of the absorbed photons result in propagating radical chains, as described by the quantum yield, Φ .

k_I is derived in Equations 3.10-3.12 using a thin film approximation of Beer's Law. The thin film approximation is justified since the etch barrier thickness is only on the order of several hundred nanometers.

$$\text{Rate of Initiation} = 2 \Phi k_I [I] = 2 \Phi I_{\text{abs}} \quad (3.10)$$

I_{abs} represents the moles of absorbed light per unit volume, which is defined by the thin film approximation of Beer's Law, as seen in Equation 3.11. Equation 3.11 is a modified form of Beer's Law since both sides of the equation have been normalized by film thickness, b . This approach makes the model insensitive to the thickness of the etch barrier.

$$I_{abs} = I_0(2.3\epsilon[I]) \quad (3.11)$$

I_0 is the incident light intensity upon the etch barrier film (mol of incident light/cm²) and ϵ is the film's extinction coefficient (L/mol-cm). The factor of 2.3 derives from the conversion between log base 10 and natural log during linearization. Equation 3.10 and 3.11 can be combined to give k_I .

$$k_I = I_0(2.3\epsilon) \quad (3.12)$$

Determining k_I is not trivial since both I_0 and ϵ are dependent on wavelength. Thus the absorbance spectrum of Darocur 1173 and the light intensity spectrum for the exposure source must be convolved.⁵⁷ The lamp used in our prototype SFIL imprinting tool is a medium pressure Mercury lamp, with the relative intensity spectrum shown in Figure 3.10. The extinction coefficient as a function of wavelength for Darocur 1173 initiator is shown in Figure 3.11.

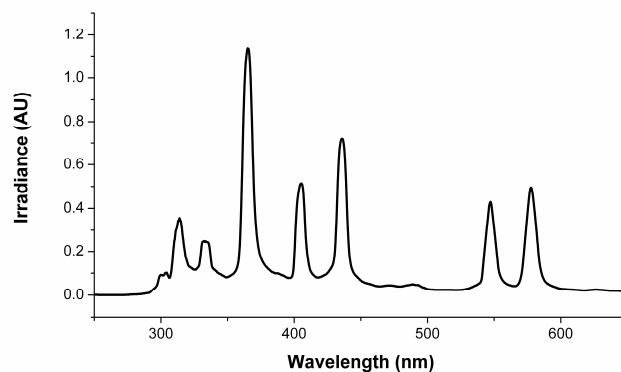


Figure 3.10: Relative intensity spectrum of Hg arc lamp used in prototype SFIL tool.

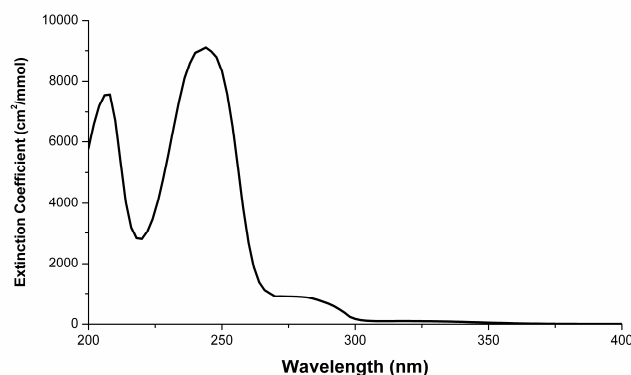


Figure 3.11: The extinction coefficient (cm^2/mmol) for Darocur 1173 as a function of wavelength

The extinction coefficient was calculated after measuring the absorbance of a 0.054 wt% solution of Darocur 1173 in acetonitrile using UV-Vis spectrometry. Since Darocur is highly absorbing below 300 nm, two different measurements were taken. A cuvette with a 0.1 cm path length was used to measure absorbance below 300 nm and a cuvette cell with a path length of 1 cm was used to measure absorbance above 300 nm. The experimental values in Figure 3.11 agree with advertised values given by CIBA, the manufacturer of Darocur 1173.

Convolving the extinction coefficients from Figure 3.11 with the spectrum from Figure 3.10 gives the absorbed light intensity for Darocur 1173, I_{abs} . Normalizing this value to thickness and initiator concentration, which is justified by the Beer's Law thin film approximation, gives a k_I value of 6.7×10^{-3} (mol-photon/mol-I sec, where I represents initiator). It should be noted that this value is for a 32 mW/cm^2 exposure dose using a mercury lamp. However, this value scales linearly with intensity. The benefit of using the k_I format is that the value is independent of initiator concentration and film thickness as long as the thin film approximation holds. In addition, the k_I format is convenient for modeling the effects of varying light intensity and initiator absorbance on the polymerization with a single parameter, k_I . The value of k_I does not change drastically with conversion, however efficiency does change.³⁸

The second parameter necessary for modeling the initiation process, Φ , is generally very difficult to measure and the few values that are reported in literature are system specific.⁵⁸ In fact, direct measurements of initiator efficiencies are nearly non-existent.⁵⁹ There are several possible measurement methods, but none of these methods are applicable for the SFIL etch barrier (e.g. end-group analysis, C^{13} NMR, deduction from emulsion studies using bulk data, RT-UV, etc).^{40,60} An unknown quantum yield is often addressed by putting data in terms of a relative radical concentration.⁴⁴ This has also been done by lumping efficiency with k_p .³⁵ Unfortunately, to effectively model the effects of oxygen on SFIL, the value of Φ must be known explicitly.

An estimation method was used to determine Φ for the SFIL etch barrier. The method requires measuring both the inhibition period at the beginning of the polymerization due to oxygen and the dissolved oxygen concentration. The inhibition period is due to the high reactivity of oxygen with free radicals ($k_{\text{O}_2} \sim 10^9 \text{ L/mol}\cdot\text{s}$).^{8,48} As radicals are generated by irradiation, they are immediately quenched in the presence of

oxygen. Thus, an estimate of Φ can be determined by measuring the amount of time necessary to consume the oxygen (*i.e.* the inhibition period). This method requires removing any inhibitor shipped with the monomers that would lengthen the inhibition period. This was done using a commercially available inhibitor remover (Aldrich 306312-1EA). Once purified and formulated, the etch barrier polymerization reaction was tracked using RTIR. The duration of the inhibition period was estimated as the time necessary to reach 1% conversion. If it is assumed that all active radicals are instantaneously consumed by oxygen, the initial concentration of oxygen divided by inhibition time gives the rate of initiation, as seen in Equation 3.13. This of course assumes that the initiator concentration remains constant, which is a reasonable assumption for the rates of initiation used in this process (changes ~2 % during the inhibition period).

$$\frac{d[O_2]}{dt} = 2 \Phi k_i [I] = \frac{[O_2]_0}{\text{Inhibition Time}} \quad (3.13)$$

The initial concentration of oxygen was 2.8×10^{-4} mol/L at room temperature, as measured using a dissolved oxygen probe (YSI-5100, YSI Environmental). The average inhibition time was 2.2 seconds for an incident intensity of 31.8 mW/cm^2 , initiator concentration of 0.061 mol/L (~1 wt%), and k_i equal to $6.7 \times 10^{-3} \text{ s}^{-1}$. Therefore, Φ is approximately 0.15 for the etch barrier formulation. Note that there was no significant difference in inhibition time for systems with removed inhibitor versus those with inhibitor. This is consistent with literature results, which show that the induction period is overwhelmingly due to depletion of oxygen rather than MEHQ inhibitor (~500 ppm).⁶¹

Thus, for the SFIL system there is no need to make an extra effort to remove inherent inhibitor.

Although Φ is highly dependent on reaction environment, a literature survey of Φ values in similar free radical systems provides a valuable point of reference. The quantum yield of Darocur 1173 in benzene was reported to be 0.163 for 313 nm light.⁶² Fouassier reports the quantum yield of Darocur 1173 to be 0.2 under practical conditions of bulk polymerization based on time-resolved laser-spectroscopy.⁶³ Another study⁶⁴ reports a quantum yield of 0.25 for Darocur 1173, which is the value used in a study of butyl acrylates.^{64,65} Irgacure 651 (dimethoxyphenylacetophenone, DMPA) is similarly structured to Darocur 1173. One study, using a fluorescence probe technique, showed that the quantum efficiency of Darocur 1173 is 0.73-0.88 times the quantum efficiency of Irgacure 651.⁶⁶ Thus, it may also be instructive to list several values of efficiency for Irgacure 651. Irgacure 651 has been shown to have quantum yields of 0.1, 0.4, 0.24, and 0.7 for various systems.^{8,21,65,67,68} Based on these separate findings, our measured quantum yield (0.15) of Darocur 1173 in etch barrier is in the range of previously reported values.

It is well known that efficiency decreases with conversion.³⁷ As the network becomes more cross-linked and viscous, the cleaved radicals are more likely to recombine than diffuse apart to form new radical chains.⁶⁹ However, a study on butyl acrylate showed that $k_p \times \Phi$ is constant well into the intermediate-conversion range, suggesting that Φ is independent of conversion over this range since k_p is known to be relatively constant.⁴⁰ For simplicity, we assume that the measured quantum efficiency of 0.15 is constant over the course of the polymerization. This assumption should only introduce significant error towards the final stages of conversion, where efficiency is known to drop rapidly. To compensate for this effect, the model allows the quantum

efficiency to drop rapidly at high conversions to reflect the limited conversion observed experimentally (80-90% conversion).

3.6.4 Determining k_p and k_t

Establishing the initiation properties for the etch barrier system allows for the measurement of the reaction coefficients k_t and k_p using the dark polymerization method. The resulting values of these coefficients as a function of conversion are displayed in Figure 3.12.

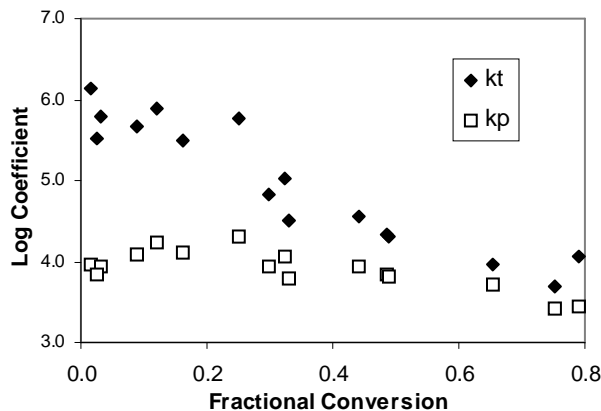


Figure 3.12: k_t and k_p (L/mol·sec) measured for SFIL etch barrier (1 wt% Darocur 1173 , 31.8 mW/cm²)

Figure 3.12 displays several trends typical of polymerization reactions. As expected, the value of k_p is relatively constant since the mobility of the monomer remains unhindered up to high levels of conversion (*i.e.* polymerization is a chemically controlled process^{41,70}). In contrast, k_t decreases by several orders of magnitude with increasing conversion due to the reduced mobility of macro-radicals caused by changes in the reaction environment (*i.e.* termination is a diffusion-controlled process⁵⁵).

The initial plateau in k_t from 0 to 30% conversion is due to the high mobility of macro-radicals at low conversion.⁵⁵ As the polymerization proceeds and the reaction environment becomes more viscous, translational diffusion (diffusion of the center-of-mass of the polymer) begins to control the termination process, causing the k_t value to decrease dramatically, as seen between 30 and 40 % conversion. The value of k_t is known to drop dramatically around the region where polymerization is most rapid.⁵⁵ After approximately 40% conversion, the value of k_t levels off, indicating a transition from translational diffusion to reaction diffusion.⁴⁶ The reaction diffusion concept was first introduced by Schulz⁷¹ and is explained thoroughly elsewhere.^{35,52} Reaction diffusion occurs when the chain mobility is reduced to the point where termination primarily occurs by radical chains propagating towards each other via reaction with mobile monomer units. Since the termination reaction occurs via propagation, the respective rate coefficients become proportional. Thus, the reaction diffusion region is characterized by a plateau in the ratio k_t/k_p ,⁵² which appears to occur around 40% in the SFIL etch barrier system. As a basis for comparison, reaction diffusion has been observed at conversions as low as 5% in multifunctional systems, but typically occurs at ~50% conversion in linear systems.⁵² Thus, the trends of Figure 3.12 are consistent for a system containing 15 wt% cross-linker. Furthermore, the k_t of typical cross-linked systems decrease drastically from 20-40% and then level out until about 80% conversion, at which point it is expected to decrease again.³⁸ Our data does not show a dramatic decrease at high conversion, but the error associated with determining rate coefficients at high conversion using the dark polymerization method is large when the slope (i.e. rate of polymerization) is nearly zero.

3.6.5 Comparison of k_p and k_t with Previous Results

It might be misleading to compare the k_p and k_t values in Figure 3.12 with those in the literature because the reported coefficients are overall rate coefficients specific to the SFIL etch barrier formulation. However, all of the components in the etch barrier are acrylates and k_p values of acrylates tend to show a family-type behavior.⁷⁰ Butyl acrylate is a commonly studied homopolymer reaction system. Although k_p is generally regarded as a chemically controlled process, it would be reasonable to expect the etch barrier k_p values to be slightly lower than a pure butyl acrylate system due to reduced mobility of the larger monomers in the etch barrier. In addition, the presence of the EGDA cross-linker causes the system to vitrify more rapidly than a mono-functional system. With that in mind, the PLP measurement method recommended by IUPAC found the k_p of butyl acrylate to be $\sim 14,000$ (L/mol·sec) at 20 °C.⁴⁶ This is slightly higher than the k_p of the etch barrier, which hovers just below 10,000 (L/mol·sec), as seen in Figure 3.12. The k_p for multiacrylates are typically on the order of 10,000 (L/mol·sec)^{10,55}, which is consistent with the values in Figure 3.12.

In contrast to k_p values, the k_t values in acrylates do not show a family-type behavior.⁷⁰ Termination is a diffusion controlled process so it is reasonable to expect that the k_t value for the etch barrier will be between that of butyl acrylate, a highly mobile molecule, and that of a multifunctional, highly cross-linked system. The value of k_t for butyl acrylate is estimated to be between 10^7 and 10^8 (L/mol·sec) at low conversions.⁴⁴ Typically, k_t is on the order of 10^7 (L/mol·sec) for monoacrylate monomers at the beginning of reaction.³⁹ These values serve as a point of reference to understand the magnitude of k_t for small, mono-functional acrylates. As a point of contrast, k_t is reported to be on the order of 10^5 (L/mol·sec) for multiacrylates.¹⁰ Thus, it is expected that the etch barrier's k_t value should be between 10^5 (L/mol·sec), which is the value for

multiacrylates, and 10^7 (L/mol·sec) for a highly mobile mono-functional acrylate. This is indeed the case at the beginning of the reaction, where k_t appears to be on the order of 10^6 (L/mol·sec), but decreases rapidly with conversion due to gelation. This is clearly the case in the etch barrier polymerization, with k_t going from 10^6 at low conversions and decreasing to 10^4 (L/mol·sec) after 40% conversion. Thus it appears the results of Figure 3.12 are within the bounds of literature precedent.

3.6.6 Modeling k_p and k_t

A goal of this modeling work was to develop an expression for k_p and k_t as a function of conversion for use in the kinetic model (Equations 3.1-3.4).⁴⁸ The value of k_p is not expected to vary significantly until high conversion (~80%) since it is a chemically controlled process⁴², however, little experimental evidence is available for high conversion k_p values.⁴⁶ The k_p values in the etch barrier are very consistent over the entire range of measured conversion, showing only a slight decrease at higher conversions. This trend is captured using Equation 3.14, where U is fractional conversion.⁴⁶ Equation 3.14 leads to almost a constant value of k_p until high conversions. The constants k_{p0} and b were found to be 10.1 and 1.8, respectively, using a least squares fit.

$$k_p = \frac{k_{p0}}{(1 + e^{bU})} \quad (3.14)$$

Although k_p is relatively constant with conversion, k_t varies dramatically due to the extreme changes in reaction medium over the course of the polymerization.³⁸ The k_t data from Figure 3.12 can be fit with a model based on diffusion limited termination, as seen in Figure 3.13.⁷² The model for k_t is based on a summation of the two dominant

mechanisms that control termination, diffusion ($k_{t,D}$) and reaction diffusion ($k_{t,RD}$), as seen in Equation 3.15. The relative value of these two terms as a function of conversion reflects the dominant termination mechanism. The maximum rate of polymerization can be thought of as the point where a shift occurs from $k_{t,D} \gg k_{t,RD}$ to $k_{t,RD} \gg k_{t,D}$.⁵⁵

$$k_t = k_{t,D} + k_{t,RD} \quad (3.15)$$

The diffusion component is a combination of segmental diffusion (k_{SD}), which is a constant, and translational diffusion (k_{TD}), which is inversely proportional to relative viscosity.

$$\frac{1}{k_{t,D}} = \frac{1}{k_{SD}} + \frac{1}{k_{TD}} \quad (3.16)$$

The reaction diffusion term is proportional to k_p , since reaction diffusion by definition involves propagating chain growth. C_{RD} is a reaction diffusion parameter and U is conversion.

$$k_{t,RD} = C_{RD} \cdot k_p \cdot (1 - U) \quad (3.17)$$

The model in Equation 3.15 was fit to the experimental data using a least-squares regression method. The parameters are shown in Table 3.4 and the resulting fit is shown in Figure 3.13, which captures the trends of the data well.

Table 3.4: Parameters for k_t Model

| Parameter | Value | Units |
|--------------------|-------------------|-----------|
| $\ln(n_r)$ | $28 \cdot U$ | ----- |
| k_{TD}^0 | 2.6×10^8 | L/mol·sec |
| $C_{RD} \cdot k_p$ | 3.6×10^4 | L/mol·sec |
| k_{SD} | 5.5×10^5 | L/mol·sec |

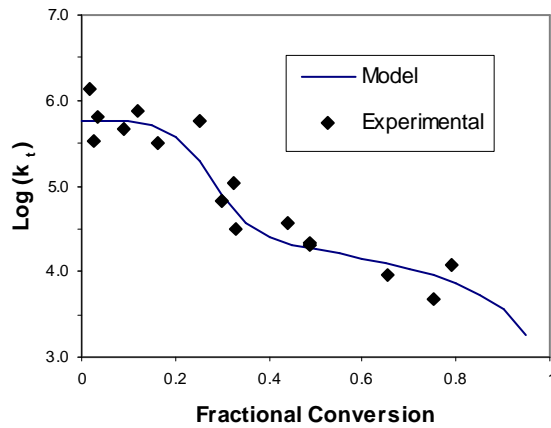


Figure 3.13: k_t data from Figure 3.12 fit with diffusion based model

3.6.7 Testing Validity of Measurements

The ultimate test of the validity of the experimental measurements and the kinetic model is to incorporate the parameters into the model and compare the results with experimental observation. The result of this exercise is a fit in agreement with experimental data⁴⁸, as shown in Figure 3.14. This one-dimensional model does not incorporate the diffusivity of oxygen. The initiator efficiency was assumed constant through 80% conversions, at which point it was forced to decay exponentially to reflect the limiting effects of vitrification on conversion observed experimentally. The largest

deviation occurs at the beginning of the polymerization (up to 20% conversion), where rate coefficients are difficult to measure due to the rapid rate of termination.

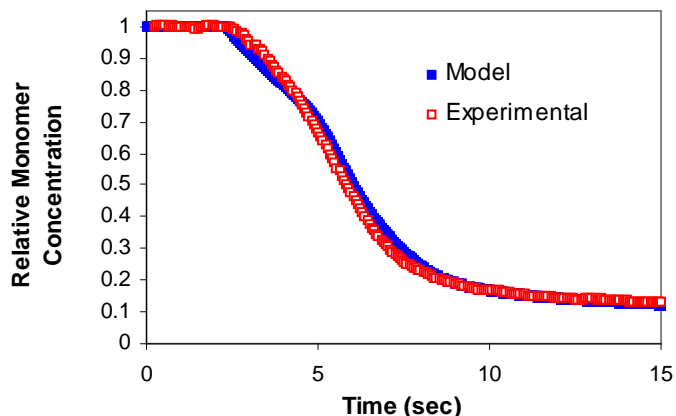


Figure 3.14: Comparison of experimentally determined kinetic data with model

3.6.7 Summary of Kinetic Coefficients

Values of the reaction parameters k_i , k_t , k_p , and Φ that are required to effectively model the effects of oxygen on the SFIL polymerization have been established. The rate coefficient for initiation, k_i , was determined experimentally by measuring the absorbance of the initiator (Darocur 1173) and convolving it with the emission spectrum of the irradiation source. The quantum efficiency, Φ , was found to be 0.15 using an estimation method based on the measurement of the initial oxygen inhibition period. The MEHQ inhibitor shipped with the commercial monomers makes no observable differences in the polymerization kinetics. The reaction coefficients k_p and k_t were measured using the dark polymerization method. The experimental values of both parameters were mathematically modeled to extract the changes in the values as a function of conversion, which helps account for effects such as autoacceleration. The reaction parameters were shown to be consistent with literature precedent.

3.7 MODELING

Once the kinetic coefficients were established, Equations 3.5-3.8 were used to model the effects of oxygen during the SFIL photopolymerization.¹⁷ These differential equations require knowledge of the initial conditions, which are listed in Table 3.5.

Table 3.5: Initial Conditions for Model

| Component | Initial Condition (mol/L) |
|-----------|------------------------------|
| Monomer | 5.3 |
| Initiator | 6.0×10^{-2} |
| Radicals | 0 |
| Oxygen | 2.80×10^{-4} |

Two boundary conditions are required to account for the effects of oxygen diffusion in the model. Boundary conditions were applied at the edge of the template and in the middle of the template. Oxygen was assumed to remain saturated at the edge of the template. Similarly, the oxygen concentration was assumed not to have a gradient under the middle of the template due to symmetry.

Of the four components tracked in the model (monomer, initiator, radicals, and oxygen), oxygen was the only component assumed to have significant diffusion. There are no gradients in the initiator concentration since the irradiation is uniform across the film. Radicals are assumed to not diffuse significantly compared to oxygen because of their reactivity with monomer and other radicals.⁷³ Once the inherent dissolved oxygen is consumed in the initial stages of the reaction, there become essentially two “regions” under the template, as shown in Figure 3.15: An interior region devoid of significant

oxygen, which polymerizes rapidly, and a perimeter region containing oxygen diffusing from the ambient, which essentially does not polymerize due to the reactivity of oxygen with free radicals. In the polymer-containing region, diffusion is likely to be very slow due to high viscosity and chain entanglements. In the oxygen-containing perimeter, there is essentially no monomer gradient because no polymerization takes place due to oxygen inhibition. Assuming a constant diffusivity for oxygen provides a worse case scenario since there is likely to be some polymerization in the perimeter region. Oxygen diffusivity has been shown to be at least two orders of magnitude lower in a polymer matrix, which is an approximation based on oxygen induced scavenging.⁷³

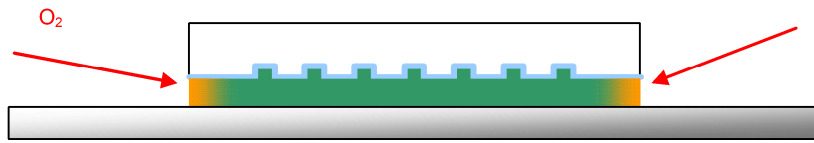


Figure 3.15: A cross section of the etch barrier during polymerization. The interior of the etch barrier (green) rapidly forms polymer once the dissolved oxygen is consumed. The perimeter of the etch barrier (orange) remains uncured as oxygen diffuses from the ambient. Diffusion between these regions is assumed negligible since the materials have very different viscosities. Note: Not to scale.

The results of the model that incorporates oxygen diffusion are shown in Figure 3.16. The axis labeled time represents the duration of UV irradiation, with time zero indicating the beginning of irradiation. The axis labeled distance represents the distance into the etch barrier with respect to the edge of the template. A distance of zero marks the edge of the etch barrier, which is exposed to ambient oxygen. Only the outer 80 microns of the etch barrier are shown in this model because diffusing oxygen only affects the perimeter of the etch barrier. The polymerization in the interior, which is immune to the diffusional effects of oxygen, is represented by the profile of a planar cross-section at

80 microns. This profile is identical to the results of Figure 3.14, where diffusional effects were neglected.

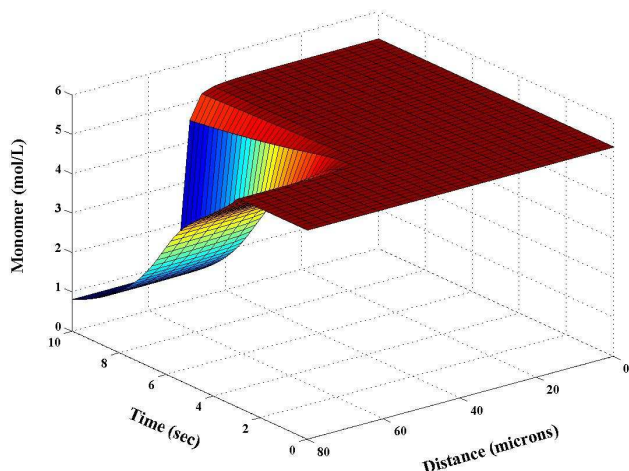


Figure 3.16: Time-spatial model of etch barrier polymerization including the effects of diffusing oxygen (1 wt% initiator, 31.8 mW/cm^2).

Two distinct effects of oxygen are revealed and quantified in Figure 3.16. First, the inhibition period due to dissolved oxygen is shown during the first few seconds of irradiation. Essentially no polymerization takes place in the presence of oxygen, which demonstrates the inhibitory strength of the oxygen. This is best illustrated in Figure 3.14, where the inhibition period is shown to be 2.3 seconds for the formulation and exposure conditions. The second distinct feature of Figure 3.16 is the effect of diffusing oxygen, which inhibits polymerization on the perimeter of the etch barrier. A snapshot of the monomer profile after 10 seconds of irradiation best illustrates this phenomenon, as shown in Figure 3.17.

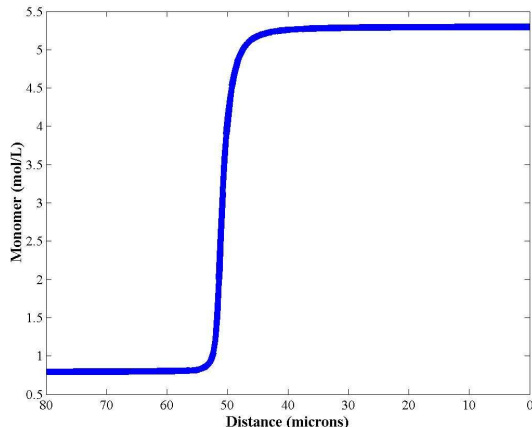


Figure 3.17: Snapshot of etch barrier polymerization at 10 seconds (1 wt% initiator, 31.8 mW/cm²).

Based on the model, oxygen diffusion results in an under-cured layer of about 50 μm around the etch barrier perimeter for typical reaction conditions, as seen in Figure 3.17. This phenomenon has been observed experimentally, but is difficult to quantify. A crude calculation using a diffusion coefficient between 10^{-5} and $10^{-6}\text{cm}^2/\text{s}$ of oxygen in monomer gives a diffusion length estimated to be 2-140 μm based on diffusion theory, assuming a 10 second reaction time.¹² The diffusion length calculated from the model is in the middle of this range, which shows that the value is reasonable. The steepness of the monomer profile in Figure 3.17 is due to the magnitude of the oxygen reaction coefficient. The implication is that in the presence of even a small amount of oxygen, no polymerization occurs, but in the absence of oxygen, polymerization proceeds rapidly. This is consistent with the “two region” scenario suggested by Figure 3.15. The model provides a worst-case scenario for the width of the under-cured boundary because it assumes constant oxygen diffusivity throughout the polymerization. The effects of oxygen are retarded by increases in viscosity and can be extremely restricted in the vitrified state.⁵⁵ However, due to the high reactivity of oxygen with radicals, it is unlikely

that any significant polymerization occurs in the presence of oxygen, so the assumption of constant diffusivity is reasonable.

3.8 MINIMIZING OXYGEN EFFECTS

The rate of initiation is an easily adjustable system parameter that can be tuned to reduce the deleterious effects of oxygen.¹⁰ The rate of initiation is directly proportional to light intensity and initiator absorbance, concentration, and efficiency. The effects of adjusting any of these parameters can be captured by plotting the oxygen diffusion length versus k_i , as seen in Figure 3.18. The rate of initiation is directly proportional to all these factors (e.g. doubling the light intensity has an equivalent effect as doubling k_i). The polymerization conditions modeled in Figure 3.16-3.17 are identified on Figure 3.18 as a point of reference. By increasing the initiator concentration to 4 wt % and using a more intense mercury lamp (43 mW/cm^2), the under-cured layer is reduced to $\sim 22 \text{ }\mu\text{m}$ according to the model. The inhibition time from would also be reduced from 2.3 seconds to approximately 480 msec. The diffusion length in Figure 3.18 asymptotes to $\sim 10 \text{ }\mu\text{m}$ at large values of k_i . This asymptote suggests that even at very high initiation rates, the perimeter of the etch barrier maintains a thin rim of under-cured material due to the high reaction rate of oxygen with radicals.

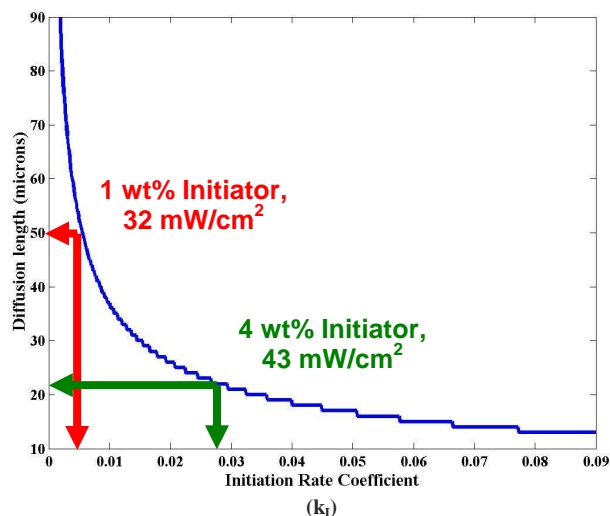


Figure 3.18: Effects of initiation on the diffusion length of oxygen during photopolymerization.

In practice, the rate of polymerization can actually reach a maximum at extreme light intensities, which is called the saturation point. This has been reported to occur at $\sim 100 \text{ mW/cm}^2$.^{21,74} It is theorized that this maximization is due to the on-set of primary radical termination, which negates the benefits of creating additional radicals. This could explain why Figure 3.18 does not asymptote towards zero. In addition to increasing the irradiation intensity, the product $\Phi \cdot k_I$ can be increased by considering alternative initiators. For example, Irgacure 369 has been shown to reduce the effects of oxygen, presumably due to its high efficiency.¹⁴

Increasing k_I is one of several options available to reduce the effects of oxygen. One obvious option is to remove the dissolved oxygen prior to polymerization. A 10-minute nitrogen flush has proven sufficient to get rid of oxygen.³⁵ For short degassing periods, helium was found to be more effective than nitrogen, due to the relative size of the molecules.⁷⁵ An inert gas flush is not an ideal option for SFIL because it would likely

change the composition of the etch barrier due to differences in component volatility. As an alternative, the dissolved oxygen could be removed by a pump / freeze / thaw method, but this is also an inefficient alternative for this application. Even if oxygen was removed from the etch barrier prior to polymerization, oxygen would also have to be removed from the imprinting area by an inert blanket to eliminate diffusion effects. Carbon dioxide is an advantageous inert blanket since it is heavier than air, which results in a pooling effect.^{10,13,14} A blanketing system would inevitably increase operating costs.

Several additives have been proposed to overcome the effects of oxygen, such as amines and thiols. Amines bind oxygen, while yielding radicals capable of contributing to the polymerization.¹² For instance, cyclic N-vinylamides were used to increase the rate of polymerization in systems exposed to air, although the mechanism is still unclear.⁹ Aromatic thiols have been shown to aid polymerization by rejuvenating peroxy radicals.²² However, none of these systems have proven to be robust, and furthermore thiols are not a feasible option for the material sensitive semiconductor industry and amines are particularly troublesome to the base sensitive imaging processes used in the microelectronics industry.

There are several alternative polymerization chemistries, such as the polyene - thiol systems, which are insensitive to oxygen but obviously contain a thiol component.¹⁰ Similarly, cationic polymerizations are not inhibited by oxygen.⁷⁶ Cationic polymerizations benefit from a post-polymerization period in the dark, low shrinkage, high mechanical performance, and good adhesion. Results of this chapter have led to studies of cationic polymerization etch barrier systems and preliminary results are very promising.⁷⁷

3.9 CONCLUSIONS

A model has been developed to quantify the inhibitory effects of oxygen on the SFIL etch barrier polymerization. An analysis of the kinetics verified the validity of equations used in the model and illustrated that the termination mechanism is primarily bimolecular by showing α to be ~ 0.5 . A significant inhibition period was shown to result from dissolved oxygen in the etch barrier depending on the irradiation intensity and initiator concentration. The etch barrier perimeter, which is exposed to ambient oxygen, is inhibited by diffusing oxygen. This results in a ring of under-cured etch barrier around the perimeter of the template for reasonable exposure conditions (4 wt% initiator with 43 mW/cm²). A predictive model was presented that shows the effects of changing the initiation conditions on oxygen diffusion length. Methods are available to reduce or even overcome the effects of oxygen and they are being pursued in our group.

3.10 REFERENCES

1. Johnson, S. C.; Bailey, T. C.; Dickey, M. D.; Smith, B. J.; Kim, E. K.; Jamieson, A. T.; Stacey, N. A.; Ekerdt, J. G.; Willson, C. G.; Mancini, D. P.; Dauksher, W. J.; Nordquist, K. J.; Resnick, D. J., Advances in Step and Flash imprint lithography. *Proceedings of SPIE-The International Society for Optical Engineering* **2003**, 5037, (Pt. 1, Emerging Lithographic Technologies VII), 197-202.
2. *International Technology Roadmap for Semiconductors*. Semiconductor Industry Association: San Jose, CA, 2003.
3. Colburn, M.; Johnson, S.; Stewart, M.; Damle, S.; Bailey, T. C.; Choi, B.; Wedlake, M.; Michaelson, T.; Sreenivasan, S. V.; Ekerdt, J.; Willson, C. G., Step and flash imprint lithography: a new approach to high-resolution patterning. *Proceedings of SPIE-The International Society for Optical Engineering* **1999**, 3676, (Pt. 1, Emerging Lithographic Technologies III), 379-389.

4. Chou, S. Y.; Krauss, P. R.; Zhang, W.; Guo, L.; Zhuang, L., Sub-10 nm imprint lithography and applications. *Journal of Vacuum Science & Technology, B: Microelectronics and Nanometer Structures* **1997**, 15, (6), 2897-2904.
5. Whidden, T. K.; Ferry, D. K.; Kozicki, M. N.; Kim, E.; Kumar, A.; Wilbur, J.; Whitesides, G. M., Pattern transfer to silicon by microcontact printing and RIE. *Nanotechnology* **1996**, 7, (4), 447-451.
6. Bailey, T. C.; Johnson, S. C.; Sreenivasan, S. V.; Ekerdt, J. G.; Willson, C. G.; Resnick, D. J., Step and flash imprint lithography: an efficient nanoscale printing technology. *Journal of Photopolymer Science and Technology* **2002**, 15, (3), 481-486.
7. Bailey, T.; Smith, B.; Choi, B. J.; Colburn, M.; Meissl, M.; Sreenivasan, S. V.; Ekerdt, J. G.; Willson, C. G., Step and flash imprint lithography: Defect analysis. *Journal of Vacuum Science & Technology, B: Microelectronics and Nanometer Structures* **2001**, 19, (6), 2806-2810.
8. Decker, C.; Jenkins, A. D., Kinetic approach of oxygen inhibition in ultraviolet- and laser-induced polymerizations. *Macromolecules* **1985**, 18, (6), 1241-4.
9. Miller, C. W.; Hoyle, C. E.; Jonsson, S.; Nason, C.; Lee, T. Y.; Kuang, W. F.; Viswanathan, K., N-vinylamides and reduction of oxygen inhibition in photopolymerization of simple acrylate formulations. *ACS Symposium Series* **2003**, 847, (Photoinitiated Polymerization), 2-14.
10. Decker, C., Kinetic study and new applications of UV radiation curing. *Macromolecular Rapid Communications* **2002**, 23, (18), 1067-1093.
11. Decker, C., The use of UV irradiation in polymerization. *Polymer International* **1998**, 45, (2), 133-141.
12. Cao, H.; Currie, E.; Tilley, M.; Jean, Y. C., Oxygen inhibition effect on surface properties of UV-curable acrylate coatings. *ACS Symposium Series* **2003**, 847, (Photoinitiated Polymerization), 152-164.
13. Studer, K.; Decker, C.; Beck, E.; Schwalm, R., Overcoming oxygen inhibition in UV-curing of acrylate coatings by carbon dioxide inerting, Part I. *Progress in Organic Coatings* **2003**, 48, (1), 92-100.
14. Studer, K.; Decker, C.; Beck, E.; Schwalm, R., Overcoming oxygen inhibition in UV-curing of acrylate coatings by carbon dioxide inerting: Part II. *Progress in Organic Coatings* **2003**, 48, (1), 101-111.

15. O'Brien, A. K.; Bowman, C. N., Modeling the effect of oxygen on photopolymerization kinetics. *Macromolecular Theory and Simulations* **2006**, 15, (2), 176-182.
16. O'Brien, A. K.; Bowman, C. N., Impact of Oxygen on Photopolymerization Kinetics and Polymer Structure. *Macromolecules* **2006**, 39, (7), 2501-2506.
17. Dickey, M. D.; Burns, R. L.; Kim, E. K.; Johnson, S. C.; Stacey, N. A.; Willson, C. G., Study of the kinetics of Step and Flash imprint lithography photopolymerization. *AIChE Journal* **2005**, 51, (9), 2547-2555.
18. Dickey, M. D.; Willson, C. G., Kinetic parameters for step and flash imprint lithography photopolymerization. *AIChE Journal* **2006**, 52, (2), 777-784.
19. Bailey, T.; Choi, B. J.; Colburn, M.; Meissl, M.; Shaya, S.; Ekerdt, J. G.; Sreenivasan, S. V.; Willson, C. G., Step and flash imprint lithography: Template surface treatment and defect analysis. *Journal of Vacuum Science & Technology, B: Microelectronics and Nanometer Structures* **2000**, 18, (6), 3572-3577.
20. Colburn, M.; Grot, A.; Amistoso, M. N.; Choi, B. J.; Bailey, T. C.; Ekerdt, J. G.; Sreenivasan, S. V.; Hollenhorst, J.; Willson, C. G., Step and flash imprint lithography for sub-100-nm patterning. *Proceedings of SPIE-The International Society for Optical Engineering* **2000**, 3997, (Emerging Lithographic Technologies IV), 453-457.
21. Decker, C.; Moussa, K., Kinetic investigation of photopolymerizations induced by laser beams. *Makromolekulare Chemie* **1990**, 191, (4), 963-79.
22. Krongauz, V. V.; Chawla, C. P., Oxygen and radical photopolymerization in films. *Abstracts of Papers, 222nd ACS National Meeting, Chicago, IL, United States, August 26-30, 2001* **2001**, POLY-376.
23. Bard, A. J.; Faulkner, L. R., *Electrochemical methods: fundamentals and applications*. 2nd ed.; Wiley: New York, 2001; p xxi, 833.
24. Odian, G. G., *Principles of polymerization*. 3rd ed.; Wiley: New York, 1991; p xxii, 768.
25. Kurdikar, D. L.; Peppas, N. A., Kinetics of photopolymerizations of multifunctional monomers. *Polymeric Materials Science and Engineering* **1993**, 69, 174-5.
26. Fouassier, J. P.; Merlin, A., Laser investigation of Norrish type I photolysis in the photoinitiator Irgacure (2,2-dimethoxy-2-phenylacetophenone). *Journal of Photochemistry* **1980**, 12, (1), 17-23.

27. Neta, P.; Huie, R. E.; Ross, A. B., Rate constants for reactions of peroxy radicals in fluid solutions. *Journal of Physical and Chemical Reference Data* **1990**, 19, (2), 413-513.
28. Berchtold, K. A.; Lovell, L. G.; Nie, J.; Hacıoglu, B.; Bowman, C. N., The significance of chain length dependent termination in cross-linking polymerizations. *Polymer* **2001**, 42, (11), 4925-4929.
29. Hacıoglu, B.; Berchtold, K. A.; Lovell, L. G.; Nie, J.; Bowman, C. N., Polymerization kinetics of HEMA/DEGDMA: using changes in initiation and chain transfer rates to explore the effects of chain-length-dependent termination. *Biomaterials* **2002**, 23, (20), 4057-4064.
30. Bajdala, J.; Mueller, U.; Wartewig, S.; Winkler, K., Photoinitiated crosslinking of silicones. 10. Photoinitiated crosslinking of silicone acrylates as studied by Fourier transform infrared spectroscopy. *Makromolekulare Chemie* **1993**, 194, (11), 3093-105.
31. Goodner, M. D.; Bowman, C. N., Modeling primary radical termination and its effects on autoacceleration in photopolymerization kinetics. *Macromolecules* **1999**, 32, (20), 6552-6559.
32. Decker, C., Laser-induced polymerization. *ACS Symposium Series* **1984**, 266, (Mater. Microlithogr.), 207-23.
33. Decker, C.; Moussa, K., Radical trapping in photopolymerized acrylic networks. *Journal of Polymer Science, Part A: Polymer Chemistry* **1987**, 25, (2), 739-42.
34. Kloosterboer, J. G.; Van de Hei, G. M. M.; Gossink, R. G.; Dortant, G. C. M., The effects of volume relaxation and thermal mobilization of trapped radicals on the final conversion of photopolymerized diacrylates. *Polymer Communications* **1984**, 25, (11), 322-5.
35. Anseth, K. S.; Wang, C. M.; Bowman, C. N., Reaction behavior and kinetic constants for photopolymerizations of multi(meth)acrylate monomers. *Polymer* **1994**, 35, (15), 3243-50.
36. Choi, B. J.; Johnson, S. C.; Sreenivasan, S. V.; Colburn, M.; Bailey, T. C.; Willson, C. G. In *Partially Constrained Compliant Stages for High Resolution Imprint Lithography*, Proc. ASME DETC2000, 2000; 2000; p 861.
37. Kurdikar, D. L.; Peppas, N. A., Investigation of diffusion-controlled homopolymerization of bifunctional monomers. *Vysokomolekulyarnye Soedineniya, Seriya A i Seriya B* **1994**, 36, (11), 1852-61.

38. Buback, M.; Egorov, M.; Gilbert, R. G.; Kaminsky, V.; Olaj, O. F.; Russell, G. T.; Vana, P.; Zifferer, G., Critically evaluated termination rate coefficients for free-radical polymerization, 1: The current situation. *Macromolecular Chemistry and Physics* **2002**, 203, (18), 2570-2582.
39. Decker, C.; Elzaouk, B.; Decker, D., Kinetic study of ultrafast photopolymerization reactions. *Journal of Macromolecular Science, Pure and Applied Chemistry* **1996**, A33, (2), 173-90.
40. Buback, M.; Gilbert, R. G.; Russell, G. T.; Hill, D. J. T.; Moad, G.; O'Driscoll, K. F.; Shen, J.; Winnik, M. A., Consistent values of rate parameters in free radical polymerization systems. II. Outstanding dilemmas and recommendations. *Journal of Polymer Science, Part A: Polymer Chemistry* **1992**, 30, (5), 851-63.
41. Buback, M., Initiation, propagation and termination in fluid phase free-radical polymerization. *Macromolecular Symposia* **2001**, 174, (Polymerization Processes and Polymer Materials I), 213-227.
42. Fischer, J. P.; Schulz, G. V., Effect of solvent on the Arrhenius parameters of chain-growth and chain-breaking in the radical polymerization of methyl methacrylate. *Berichte der Bunsen-Gesellschaft* **1970**, 74, (10), 1077-82.
43. Lyons, R. A.; Hutovic, J.; Piton, M. C.; Christie, D. I.; Clay, P. A.; Manders, B. G.; Kable, S. H.; Gilbert, R. G., Pulsed-Laser Polymerization Measurements of the Propagation Rate Coefficient for Butyl Acrylate. *Macromolecules* **1996**, 29, (6), 1918-27.
44. Beuermann, S.; Paquet, D. A., Jr.; McMinn, J. H.; Hutchinson, R. A., Determination of free-radical propagation rate coefficients of butyl, 2-ethylhexyl, and dodecyl acrylates by pulsed-laser polymerization. *Macromolecules* **1996**, 29, (12), 4206-4215.
45. Van Herk, A. M., Pulsed initiation polymerization as a means of obtaining propagation rate coefficients in free-radical polymerizations. II Review up to 2000. *Macromolecular Theory and Simulations* **2000**, 9, (8), 433-441.
46. Beuermann, S.; Buback, M., Rate coefficients of free-radical polymerization deduced from pulsed laser experiments. *Progress in Polymer Science* **2002**, 27, (2), 191-254.
47. Hutchinson, R. A.; Aronson, M. T.; Richards, J. R., Analysis of pulsed-laser-generated molecular weight distributions for the determination of propagation rate coefficients. *Macromolecules* **1993**, 26, (24), 6410-15.

48. Dickey, M. D.; Burns, R. L.; Kim, E. K.; Johnson, S. C.; Stacey, N. A.; Willson, C. G., A Study of the Kinetics of Step and Flash Imprint Lithography Photopolymerization. *AIChE Journal* **2005**, 51, (9), 2547-2555.
49. Decker, C.; Elzaouk, B., Photopolymerization of functional monomers. VII. Evaluation of the rate constants of propagation and termination. *European Polymer Journal* **1995**, 31, (12), 1155-63.
50. Williams, R. M.; Khudyakov, I. V.; Purvis, M. B.; Overton, B. J.; Turro, N. J., Direct and sensitized photolysis of phosphine oxide polymerization photoinitiators in the presence and absence of a model acrylate Monomer: A time resolved EPR, cure monitor, and photoDSC study. *Journal of Physical Chemistry B* **2000**, 104, (44), 10437-10443.
51. Tryson, G. R.; Shultz, A. R., A calorimetric study of acrylate photopolymerization. *Journal of Polymer Science, Polymer Physics Edition* **1979**, 17, (12), 2059-75.
52. Anseth, K. S.; Wang, C. M.; Bowman, C. N., Kinetic evidence of reaction diffusion during the polymerization of multi(meth)acrylate monomers. *Macromolecules* **1994**, 27, (3), 650-5.
53. Anseth, K. S.; Bowman, C. N.; Peppas, N. A., Polymerization kinetics and volume relaxation behavior of photopolymerized multifunctional monomers producing highly crosslinked networks. *Journal of Polymer Science, Part A: Polymer Chemistry* **1994**, 32, (1), 139-47.
54. Decker, C.; Moussa, K., Photopolymerization of polyfunctional monomers. III. Kinetic analysis by real-time IR spectroscopy. *European Polymer Journal* **1990**, 26, (4), 393-401.
55. Andrzejewska, E., Photopolymerization kinetics of multifunctional monomers. *Progress in Polymer Science* **2001**, 26, (4), 605-665.
56. Khudyakov, I. V.; Purvis, M. B.; Turro, N. J., Kinetics of photopolymerization of acrylate coatings. *ACS Symposium Series* **2003**, 847, (Photoinitiated Polymerization), 113-126.
57. Mack, C. A., Absorption and exposure in positive photoresist. *Applied Optics* **1988**, 27, (23), 4913-19.
58. Scherzer, T.; Decker, U., Kinetic investigations on UV-induced photopolymerization reactions by real-time FTIR-ATR spectroscopy: the efficiency of photoinitiators at 313 and 222 nm. *Nuclear Instruments & Methods in Physics Research, Section B: Beam Interactions with Materials and Atoms* **1999**, 151, (1-4), 306-312.

59. Buback, M.; Huckestein, B.; Kuchta, F.-D.; Russell, G. T.; Schmid, E., Initiator efficiencies in 2,2'-azoisobutyronitrile-initiated free-radical polymerizations of styrene. *Macromolecular Chemistry and Physics* **1994**, 195, (6), 2117-40.
60. Buback, M.; Garcia-Rubio, L. H.; Gilbert, R. G.; Napper, D. H.; Guillot, J.; Hamielec, A. E.; Hill, D.; O'Driscoll, K. F.; Olaj, O. F.; et al., Consistent values of rate parameters in free radical polymerization systems. *Journal of Polymer Science, Part C: Polymer Letters* **1988**, 26, (7), 293-7.
61. Wight, F. R., Oxygen inhibition of acrylic photopolymerization. *Journal of Polymer Science, Polymer Letters Edition* **1978**, 16, (3), 121-7.
62. Lewis, F. D.; Magyar, J. G., Photoreduction and α . cleavage of aryl alkyl ketones. *Journal of Organic Chemistry* **1972**, 37, (13), 2102-7.
63. Fouassier, J. P., Polymerization photoinitiators: excited state processes and kinetic aspects. *Progress in Organic Coatings* **1990**, 18, (3), 229-52.
64. Eichler, J.; Herz, C. P.; Naito, I.; Schnabel, W., Laser flash photolysis investigation of primary processes in the sensitized polymerization of vinyl monomers. IV. Experiments with hydroxy alkylphenones. *Journal of Photochemistry* **1980**, 12, (3), 225-34.
65. Buback, M.; Degener, B., Rate coefficients for free-radical polymerization of butyl acrylate to high conversion. *Makromolekulare Chemie* **1993**, 194, (10), 2875-83.
66. Hu, S.; Popielarz, R.; Neckers, D. C., Fluorescence Probe Techniques (FPT) for Measuring the Relative Efficiencies of Free-Radical Photoinitiators. *Macromolecules* **1998**, 31, (13), 4107-4113.
67. Mateo, J. L.; Serrano, J.; Bosch, P., Photopolymerization of Di- and Tetrafunctional Methacrylic Monomers in a Polymeric Medium: Kinetics and Evidence of Reaction Diffusion during an All Photopolymerization Reaction. *Macromolecules* **1997**, 30, (5), 1285-1288.
68. Groenenboom, C. J.; Hageman, H. J.; Overeem, T.; Weber, A. J. M., Photoinitiators and photoinitiation. 3. Comparison of the photodecompositions of α -methoxy- and α , α -dimethoxydeoxybenzoin in 1,1-diphenylethylene as model substrate. *Makromolekulare Chemie* **1982**, 183, (2), 281-92.
69. Decker, C., Real-time monitoring of polymerization quantum yields. *Macromolecules* **1990**, 23, (25), 5217-20.

70. Buback, M., Initiation and termination rates associated with free-radical polymerization in extended ranges of temperature and pressure. *ACS Symposium Series* **2000**, 768, (Controlled/Living Radical Polymerization), 39-56.
71. Schulz, G. V., Polymerization kinetics in highly concentrated systems. Kinetics of the Trommsdorf effect on methyl methacrylate. *Zeitschrift fuer Physikalische Chemie* **1956**, 8, 290-317.
72. Buback, M.; Huckestein, B.; Russell, G. T., Modeling of termination in intermediate and high conversion free radical polymerizations. *Macromolecular Chemistry and Physics* **1994**, 195, (2), 539-54.
73. Krongauz, V. V.; Schmelzer, E. R.; Yohannan, R. M., Kinetics of anisotropic photopolymerization in polymer matrix. *Polymer* **1991**, 32, (9), 1654-62.
74. Okamura, S.; Manabe, T., Radiation polymerization in solution. III. Effect of primary radicals in the termination reaction. *Polymer* **1961**, 2, 83-94.
75. Krongauz, V. V.; Chawla, C. P.; Dupre, J., Oxygen and radical photopolymerization in films. *ACS Symposium Series* **2003**, 847, (Photoinitiated Polymerization), 165-175.
76. Decker, C., Light-induced crosslinking polymerization. *Polymer International* **2002**, 51, (11), 1141-1150.
77. Kim, E. K.; Stacey, N. A.; Smith, B. J.; Dickey, M. D.; Johnson, S. C.; Trinquet, B. C.; Willson, C. G., Vinyl ethers in ultraviolet curable formulations for step and flash imprint lithography. *Journal of Vacuum Science & Technology, B: Microelectronics and Nanometer Structures* **2004**, 22, (1), 131-135.

Chapter 4

Electric Field Assisted Assembly Introduction

This chapter introduces the concept of pillar arrays formed via electric field assisted assembly. Pillar arrays form across a narrow gap when thin film destabilizing forces overcome the stabilizing effects of surface tension. The mechanism behind this phenomenon has been understood for years, but has only recently been harnessed for patterning applications. Pillars were first demonstrated through a serendipitous discovery that occurred during a failed imprint experiment. Thus, this chapter is a natural transition from the imprint work described in Chapters 2-3. Furthermore, the formation of pillars benefits considerably from the use of low viscosity materials (Chapter 6) in a manner similar to nanoimprint lithography (Chapter 2).

4.1 INTRODUCTION

As photolithography approaches fundamental physical barriers, interest in alternative patterning techniques has grown. In particular, directed-assembly patterning techniques are appealing because of their ability to harness natural phenomena to form useful structures. Examples of directed assembly include block copolymers on functionalized surfaces¹ and DNA origami.² Recently, a directed-assembly technique has emerged that is capable of forming polymeric pillar arrays.³⁻⁷ These arrays may find application in technologies such as micro-electro-mechanical systems (MEMS), micro-fluidic devices, patterned magnetic media, optical interconnects (“sea of polymer pillars”,

SoPP), super-hydrophobic surfaces, DNA manipulation devices, and photonic bandgap materials.⁸⁻¹²

The physical basis for the formation of the pillars is the amplification of film undulations by a destabilizing force, such as an electric field.¹³ Experimentally, this is achieved by positioning an electrode above a thin film on a grounded substrate, a structure which resembles a parallel plate capacitor. Pillar formation occurs when the destabilizing electrostatic force overcomes the stabilizing effects of surface tension acting at the film-air interface. This force imbalance amplifies film fluctuations until they span the capacitor gap, as shown in Figure 4.1. In addition to electric fields, other destabilizing forces, such as thermal flux, have proven to be sufficient to form pillars.³ At extremely small air gaps (~ 100 nm), pillars have been observed to form spontaneously without an applied field, presumably due to an induced electrostatic force.^{14,15}

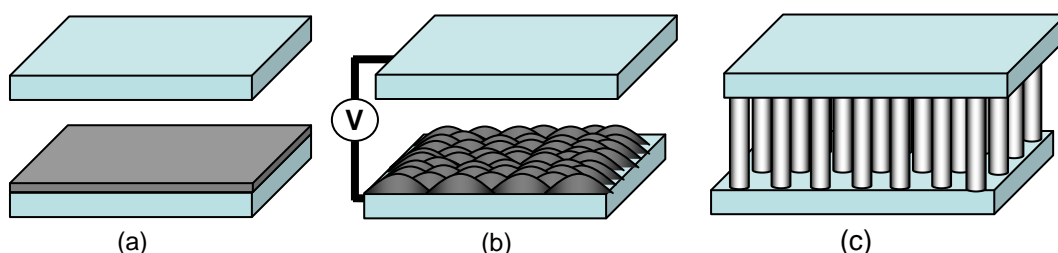


Figure 4.1: A simple schematic of the pillar formation process. (a) A thin film is placed between two planar, electrically conductive surfaces, thus forming a capacitor. (b) Application of a voltage amplifies undulations in the film due to electrohydrodynamic instabilities. (c) The force imbalance amplifies these film undulations until they span the capacitor space.

4.2 LITERATURE BACKGROUND

The study of the stability of thin films is critical for numerous technological applications, such as coatings and lithography. Numerous forces are capable of inducing a thin film instability including van der Waals forces,¹⁶⁻¹⁸ temperature gradients,¹⁹

mechanical stresses,^{20,21} substrate chemical heterogeneities,^{22,23} and electric fields.⁴ Electric fields are attractive because they are simple to control externally and the wavelength of the instability can be tuned with the field strength.

The theoretical concepts of electrohydrodynamics and the effects of electric fields on fluid-fluid interfacial stability have been known for years.^{15,24,25} Electrohydrodynamics have been harnessed for micromixing,²⁶ patterning with surfactants,²⁷ and organizing colloids.²⁸ Recently, electric fields have been used to destabilize thin films to form pillar arrays for patterning applications.³ Pillars were initially observed during a failed nanoimprint experiment (Chapters 2-3) when an inadvertent particle prevented the template from contacting the polymer film. The resulting air gap proved ideal for pillar formation. The formation of pillars under these conditions is remarkable considering no electric field was applied across the gap. These results are generally explained by an “induced electrostatic force” at the film interface, although the theoretical forces using this argument are not nearly large enough to form pillars.^{4,5} Subsequent work by other research groups showed that pillars only form when an external force is applied, such as an electric field or thermal gradient.⁸

Recent literature work has primarily focused on studying pillar array formation using various homopolymer films, such as polystyrene (PS), poly(methyl methacrylate) (PMMA), polyisoprene (PI), and brominated polystyrene (Br-PS).³ Each of these polymers responds slightly differently to electrostatic fields due to the differences in dielectric constant, surface tension, and melt viscosity. These material properties ultimately impact the characteristic spacing and the rate of pillar formation.

Other recent studies have focused on varying the process configuration, producing remarkable and potentially useful results. For example, the use of a patterned upper electrode (“template”) has been shown to induce pattern replication.³ Protruding features

on the template have a higher localized electric field due to their proximity to the underlying film. Thus, the pillars preferentially form under the features, allowing pattern replication with high fidelity, as shown in Figure 4.2. Features as small as 100 nm have been patterned in PMMA using this technique.³ This technique is explored further in Chapter 7.

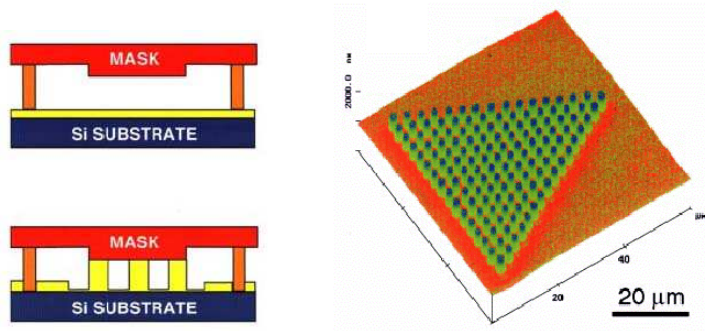


Figure 4.2: Patterned upper electrodes result in direct assembly of the pillars^{3,29}

In Figure 4.2, the features on the mask are replicated with arrays of pillars. The mask features can be fully replicated (e.g. formation of a solid triangle in Figure 4.2) by simply changing the surface properties of the template. Chou et al. refers to these two techniques as lithographically induced self-assembly (LISA) and lithographically induced self-construction (LISC), respectively.³⁰ Recent modeling suggests that the replication of features (i.e. features replicated with pillar arrays vs. fully replicated structures) is only a function of the fill fraction, defined as the ratio of film height to capacitor gap.³¹

Variations on the pillar formation process have been explored, demonstrating the versatility of this technique. For example, the air layer above the polymeric film has been replaced by poly(dimethyl siloxane) (PDMS), which lowers the interfacial energy and reduces the characteristic spacing of the pillars.³¹⁻³³ Bi-layer film systems have also been explored, such as PS on PMMA (note: these are often referred to as tri-layer

systems because the dielectric fluid stack consists of air-PS-PMMA).³⁴ Tri-layer polymeric systems will be discussed in Chapter 5.

The pillar formation process has also been demonstrated on block copolymers.^{4,8,35} In a macroscopic sense, the pillars form as usual. However, a cross-section of the pillar shows domains of aligned columns within the pillars due to phase separation.

In summary, the work to date demonstrates the versatility of the pillar formation process. Preliminary studies on homopolymers, bi-layer systems, patterned electrodes, and block copolymers have all shown interesting results that justify further exploration. The remainder of this chapter discusses the theory behind pillar formation, providing the context for understanding the work described in Chapters 5-10. This chapter concludes with a description of the experimental techniques used in Chapters 5-10.

4.3 THEORY

4.3.1 Introduction

The dynamics of pillar formation are often modeled using linear stability analysis, which predicts a characteristic spacing for the pillars.^{4-6,8,30,31,35-38} This analysis accounts for the forces acting on the film / air interface to determine the fastest mode of growth. During pillar formation, the two dominant forces at the film-air interface are surface tension, a restoring force, and electrostatics, a destabilizing force. Large destabilizing forces and small restoring forces favor the formation of structures with small wavelengths, and vice versa.

Although linear stability analysis only predicts what happens during the initial stages of undulation growth, it has proven to be an accurate model for predicting the final

characteristic wavelength, defined as the center-to-center spacing of the pillars.³⁰ The implication of this model is that the initial spacing of surface undulations projects to the upper electrode as pillars. The appropriateness of linear stability analysis for describing pillar formation has been further verified by 3-D non-linear simulations.³⁶ Thus, linear stability analysis provides a useful tool for predictably tuning the characteristic spacing of the pillars as a function of physical parameters such as interfacial energy, dielectric constant, and electric field. The characteristic spacing of nearly all polymeric pillars can be described by linear stability analysis and falls within two regimes: perfect insulator and leaky dielectric.³⁹ Leaky dielectrics tend to reduce the characteristic spacing due to uncompensated charge that accumulates at the film interface during pillar formation.³⁷

The absolute rate of pillar formation cannot be predicted by linear stability analysis since it only accounts for early stage undulation development. However, the relative rate of pillar formation can be predicted and the analysis reveals that the time scale of pillar formation is proportional to viscosity. These predictions have been verified experimentally in the early stage of undulation growth.³⁶ The analysis predicts that the viscosity only affects the rate of formation and does not impact the characteristic spacing. Thus, theory suggests that low viscosity materials will increase the rate of pillar formation, without any drawbacks. This approach is explored in Chapter 6 through the rational development of photocurable material systems. Chapter 7 characterizes the growth mechanisms, characteristic spacing, and ordering of these low viscosity systems.

In summary, linear stability analysis provides a useful tool for designing experiments and predicting the spacing and relative growth rates of the pillars. Linear stability analysis is derived in the following section and will be referred to throughout this thesis.

4.3.2 Linear Stability Analysis Derivation

The first step in the linear stability analysis is to define the geometry of the system. As shown in Figure 4.3, d is the distance between the two plates and h is the film thickness. The potential on the top plate is defined as V_2 and the field on the bottom plate as V_1 . The direction of the applied field is inconsequential to the dynamics of the film's response.

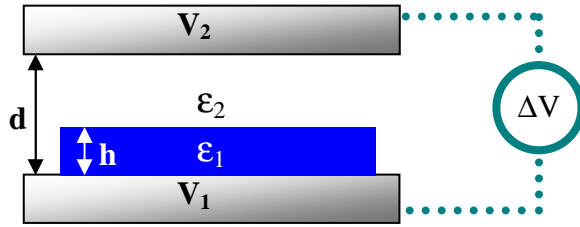


Figure 4.3: Schematic representation of the capacitor device. V is voltage, d is the capacitor gap, h is the film height, and ϵ is dielectric constant.

The potential in the film is defined as Φ_1 and the potential in the space between the film and the top plate as Φ_2 . The change of potential with distance can be described generically by the following linear equations:

$$\Phi_1 = Ay + B \quad (4.1)$$

$$\Phi_2 = A'y + B' \quad (4.2)$$

These equations are subject to the following boundary conditions, where ϵ_1 is the permittivity of the film and ϵ_2 is the permittivity of the space between the film and the top

plate. The point $y = 0$ corresponds to the substrate–film interface and the y -coordinate is normal to the substrate.

$$\Phi_1 = V_1 \quad @ \ y = 0$$

$$\Phi_2 = V_2 \quad @ \ y = d$$

$$\epsilon_1 \frac{\partial \Phi_1}{\partial y} = \epsilon_2 \frac{\partial \Phi_2}{\partial y} \quad @ \ y = h$$

$$\Phi_1 = \Phi_2 \quad @ \ y = h$$

Using these four boundary conditions, the four unknown coefficients A , B , A' , and B' can be determined. For example, A' is shown in Equation 4.3

$$A' = \frac{V_2 - V_1}{\left(d + \frac{\epsilon_2 - \epsilon_1}{\epsilon_1} h \right)} \quad (4.3)$$

The coefficient A' is particularly relevant in this analysis since the pressure in the film at the interface is given by,

$$P|_h = \frac{1}{2} \epsilon_1 E_1^2 - \frac{1}{2} \epsilon_2 E_2^2 = \frac{1}{2} E_2^2 \left(\frac{\epsilon_2^2}{\epsilon_1} - \epsilon_1 \right) \quad (4.4)$$

and E_2 , which is the electric field, is defined in terms of A' .

$$E_2 = -\left. \frac{\partial \Phi_2}{\partial y} \right|_h = -A' \quad (4.5)$$

Equation 4.4 is derived from the Maxwell stress tensor, taken only in the y direction. Combining Equations 4.3, 4.4, and 4.5 results in an expression for pressure as a function of film height, as seen in Equation 4.6.

$$P|_h = \frac{1}{2} \left(\frac{V_2 - V_1}{d + \frac{\epsilon_2 - \epsilon_1}{\epsilon_1} h} \right)^2 \left(\frac{\epsilon_2^2}{\epsilon_1} - \epsilon_2 \right) \quad (4.6)$$

The pressure at the interface can be understood as a consequence of the disconnect in the slope of the potential (i.e. the electric field strength) at the film–air interface, as shown in Figure 4.4. The film stack is rotated clockwise ninety degrees from that shown in Figure 4.3 to illustrate the concept of voltage drop as a function of position in the film stack. The medium with the lower dielectric constant has a larger electric field strength, which is responsible for the pressure at the interface. The pressure can also be thought of in terms of uncompensated dielectric “charge” at the interface.

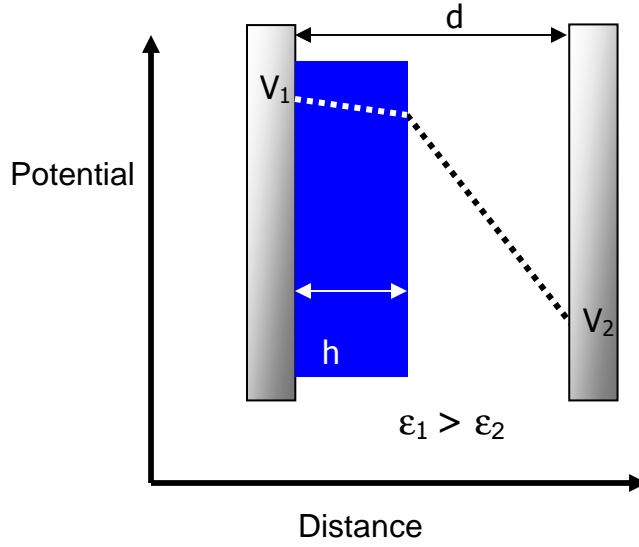


Figure 4.4: Diagram of voltage drop through film stack. The differences in dielectric constant between the air and film results in a disconnect between the slopes of the potential (i.e. electric field strength) at the film interface. Note that the film stack is turned 90 degrees from Figure 4.2.

Equation 4.6 relates the way in which the applied potential and the geometry of the system relate to the interfacial pressure. The change in this pressure with respect to the horizontal axis is expressed in Equation 4.7.

$$\frac{\partial p}{\partial x} = - \frac{(V_2 - V_1)^2}{\left(d + \frac{\epsilon_2 - \epsilon_1}{\epsilon_1} h\right)^3} \left(\frac{\epsilon_2^2}{\epsilon_1} - \epsilon_2 \right) \left(\frac{\epsilon_2 - \epsilon_1}{\epsilon_1} \right) \frac{\partial h}{\partial x} \quad (4.7)$$

An expression is required to describe the rheological response of the film under the applied electrostatic forces. The general thin-film equation, derived from the continuity equation, is a common approach to handling thin film flow.

$$\frac{\partial h}{\partial t} = \frac{1}{3\mu} \nabla \cdot (h^3 \nabla P) \quad (4.8)$$

Here t represents time, μ represents viscosity, and P represents interfacial pressure. The pressure term in Equation 4.8 is a summation of the atmospheric pressure, gravity, curvature, and electric field effects, as shown below.

$$P|_h = P_{\text{atm}} + \rho g(h - y) - \gamma \nabla^2 n + \frac{1}{2} \left(\frac{V_2 - V_1}{d + \frac{\epsilon_2 - \epsilon_1}{\epsilon_1} h} \right)^2 \left(\frac{\epsilon_2^2}{\epsilon_1} - \epsilon_2 \right) \quad (4.9)$$

In Equation 4.9, γ is surface tension, ρ is density, g is gravity, and n is the unit vector normal to the surface.

Next, Equation 4.9 is plugged into Equation 4.8. For simplification, the gradient terms in Equations 4.8 will be taken only in the x -direction, parallel to the substrate. Also, the lubrication theory is assumed to hold true ($\frac{\partial h}{\partial x} \ll 1$).

$$\nabla P = \frac{\partial P}{\partial x} = \rho g \left(\frac{\partial h}{\partial x} \right) - \gamma \frac{\partial^3 h}{\partial x^3} - \epsilon_2 \frac{(V_2 - V_1)^2}{\left(d + \frac{\epsilon_2 - \epsilon_1}{\epsilon_1} h \right)^3} \left(\frac{\epsilon_2 - \epsilon_1}{\epsilon_1} \right)^2 \frac{\partial h}{\partial x} \quad (4.10)$$

Combining Equations 4.8 and 4.10, while neglecting gravitational effects due to the thin nature of the film, results in Equation 4.11:

$$\frac{\partial h}{\partial t} = \frac{1}{3\mu} \frac{\partial}{\partial x} \left[-\gamma h^3 \frac{\partial^3 h}{\partial x^3} - h^3 \epsilon_2 \frac{(V_2 - V_1)^2}{\left(d + \frac{\epsilon_2 - \epsilon_1}{\epsilon_1} h\right)^3} \left(\frac{\epsilon_2 - \epsilon_1}{\epsilon_1}\right)^2 \frac{\partial h}{\partial x} \right] \quad (4.11)$$

The analysis of this equation is simplified using a linearization, which is justified due to the thin nature of the film. Assuming a small disturbance, η , is applied to the undisturbed film height, h_0 , the film height can be expressed as:

$$h = h_0 + \eta \quad \text{and} \quad \eta \ll h_0$$

Using these assumptions, Equation 4.11 can be simplified to Equation 4.12.

$$\frac{\partial \eta}{\partial t} = \frac{1}{3\mu} \left[-\gamma h_0^3 \frac{\partial^4 \eta}{\partial x^4} - h_0^3 \epsilon_2 \frac{(V_2 - V_1)^2}{\left(d + \frac{\epsilon_2 - \epsilon_1}{\epsilon_1} h_0\right)^3} \left(\frac{\epsilon_2 - \epsilon_1}{\epsilon_1}\right)^2 \frac{\partial^2 \eta}{\partial x^2} \right] \quad (4.12)$$

Furthermore, we will assume the film disturbance takes the following form:

$$\eta = \hat{\eta} e^{st+ikx} \quad (4.13)$$

Plugging Equation 4.13 into 4.12, results in an expression for s , the characteristic disturbance growth rate (i.e. inversely proportional to time scale of formation).

$$s = \frac{1}{3\mu} \left[-\gamma h_0^3 k^4 + h_0^3 \epsilon_2 \frac{(V_2 - V_1)^2}{\left(d + \frac{\epsilon_2 - \epsilon_1}{\epsilon_1} h_0\right)^3} \left(\frac{\epsilon_2 - \epsilon_1}{\epsilon_1}\right)^2 k^2 \right] \quad (4.14)$$

Equation 4.14 is used to determine the stability properties of the film under an electric field. For $s > 0$, the film is unstable and $s < 0$, the film is stable.

Thus, the film is unstable under the following criteria:

$$k < \left[\epsilon_2 \frac{(V_2 - V_1)^2}{\gamma \left(d + \frac{\epsilon_2 - \epsilon_1}{\epsilon_1} h_0\right)^3} \left(\frac{\epsilon_2 - \epsilon_1}{\epsilon_1}\right)^2 \right]^{\frac{1}{2}} \quad (4.15)$$

And the film is unstable when:

$$k > \left[\epsilon_2 \frac{(V_2 - V_1)^2}{\gamma \left(d + \frac{\epsilon_2 - \epsilon_1}{\epsilon_1} h_0\right)^3} \left(\frac{\epsilon_2 - \epsilon_1}{\epsilon_1}\right)^2 \right]^{\frac{1}{2}} \quad (4.16)$$

Since k is defined as $2\pi/\lambda$, in which λ is wavelength, Equation 4.15 can be rewritten as:

$$\lambda > \left[4\pi^2 \epsilon_2 \frac{(V_2 - V_1)^2}{\gamma \left(d + \frac{\epsilon_2 - \epsilon_1}{\epsilon_1} h_0 \right)^3} \left(\frac{\epsilon_2 - \epsilon_1}{\epsilon_1} \right)^2 \right]^{\frac{1}{2}} \quad (4.17)$$

From Equation 4.14, it follows that the system will have the fastest growing mode when:

$$k = \left[\epsilon_2 \frac{(V_2 - V_1)^2}{2\gamma \left(d + \frac{\epsilon_2 - \epsilon_1}{\epsilon_1} h_0 \right)^3} \left(\frac{\epsilon_2 - \epsilon_1}{\epsilon_1} \right)^2 \right]^{\frac{1}{2}} \quad (4.18)$$

In order to plot s vs. k , Equation 4.14 was converted into a non-dimensional form (Equation 4.19), where the dimensionless variables are defined below:

$$\bar{S} = \frac{s}{s_c} \quad \bar{K} = k \cdot h_0 \quad s_c = \frac{\gamma}{3\mu h_0}$$

$$\bar{S} = [-\bar{K}^4 + B\bar{K}^2] \quad (4.19)$$

where:
$$B = \frac{h_0 \epsilon_2}{3\mu s_c} \frac{(V_2 - V_1)^2}{\left(d + \frac{\epsilon_2 - \epsilon_1}{\epsilon_1} h_0 \right)^3} \left(\frac{\epsilon_2 - \epsilon_1}{\epsilon_1} \right)^2$$

Plotting the non-dimensional variables S vs K in Equation 4.19, results in the Figure 4.5, plotted for various values of B . Pillars only occur when S is positive (ie.

when the film is unstable). The fastest growth mode occurs when S is maximized. The value of K where this maximum occurs defines the characteristic spacing of the pillars. The characteristic spacing decreases (i.e. larger K values, smaller wavelengths) and the range of positive growth modes increases with larger values of B . B is maximized by increasing the electrostatic forces (destabilizing) and minimizing the surface tension (restoring forces).

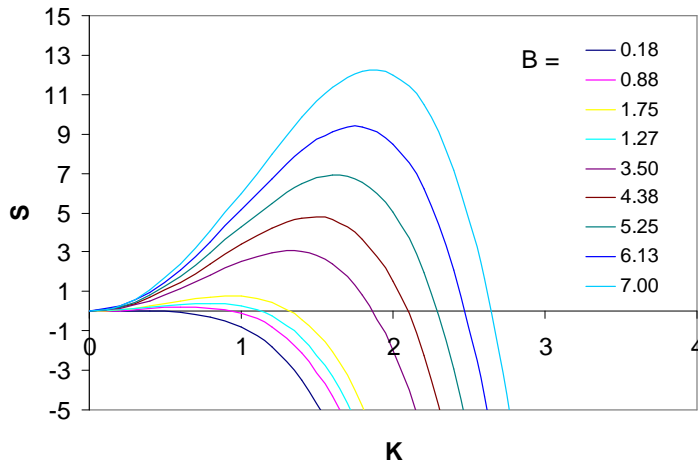


Figure 4.5: A non-dimensional plot of S versus K for various values of B .

The fastest growing mode can be determined analytically at the point where there first derivative of S vs. K (Equation 4.19) is zero, as shown in Equations 4.20-4.21.

$$\bar{S}_{\max} \text{ occurs @ } \bar{K} = \sqrt{\frac{B}{2}} \quad (4.20)$$

$$\bar{S}_{\max} = \frac{B^2}{4} \quad (4.21)$$

The rate of pillar formation and the characteristic spacing can be altered by changing the physical properties that define B. For example, increasing the voltage between the plates increases B by the voltage squared. Therefore, doubling the voltage results in (1) the span of unstable disturbance frequencies doubling, (2) the spacing of the fastest growing mode decreasing by a factor of 2, and (3) the rate of growth of the fastest growing mode increasing by a factor of 16. B can also be modified by varying the geometry of the system and changing the properties of the film.

4.3.3 Linear Stability Analysis Typical Values

To illustrate the dynamics of a representative system, the physical constants of brominated polystyrene are listed below and plugged into the linear stability model.

| | |
|------------------------------|--|
| $\mu = 10000 \text{ kg/ms}$ | $\epsilon_1 = 5 \cdot \epsilon_0$ |
| $\gamma = 30 \text{ mJ/m}^2$ | $\epsilon_2 = \epsilon_0 \text{ (air)}$ |
| $h_0 = 50 \text{ nm}$ | $\epsilon_0 = 8.854 \times 10^{-12} \text{ C}^2/\text{Jm}$ |
| $d = 200 \text{ nm}$ | $\Delta V = 10 \text{ V}$ |

Using these values (in which k is in nm^{-1}),

$$s = -1.25 \times 10^8 k^4 + 5.76 \times 10^2 k^2$$

$$s_{\max} = 6.65 \times 10^{-4} \text{ sec}^{-1} \quad @ \quad k = 1.56 \times 10^{-3} \text{ nm}^{-1}$$

Figure 4.6 is a plot of s^{-1} versus ΔV for these representative values, which illustrates the nature of the time scale for a given potential difference. Figure 4.6 is plotted with s^{-1} (seconds) on a log scale. The inverse of s_{\max} for brominated polystyrene results in approximately half an hour for the characteristic time scale at 10 V.

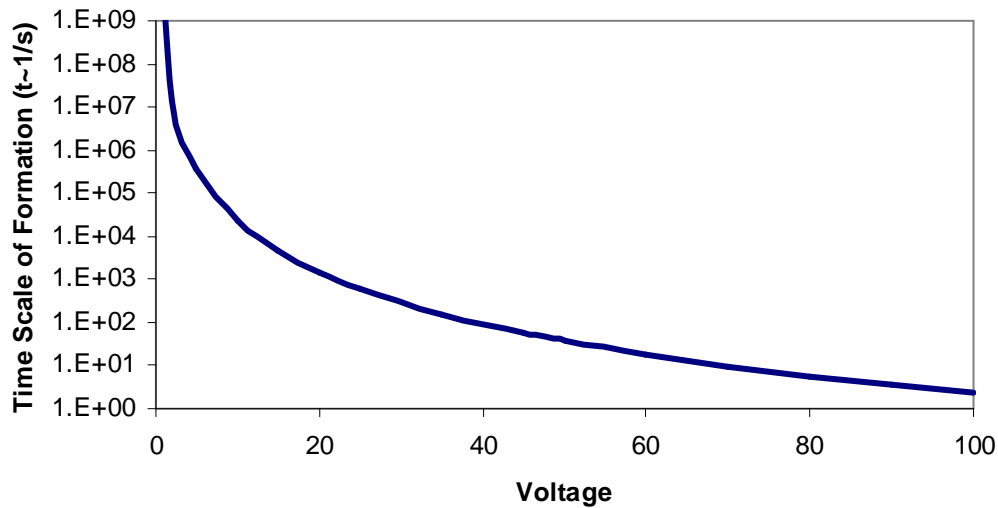


Figure 4.6: Characteristic formation time (sec) as a function of applied voltage. For these conditions, the dielectric breakdown of the capacitor occurs at >15 V.

4.3.4 Linear Stability Analysis Discussion

The origin of the film instability can be understood by considering the forces that act on the film-air interface. Surface tension is a stabilizing force that acts to reduce surface undulations. In contrast, the applied electric field creates a destabilizing force at the surface that amplifies film undulations. Local perturbations of the film thickness creates a pressure gradient in the film that is dependent on the electrostatic and surface forces. Depending on the wavelength of this perturbation, the disturbance will either grow or decay, as shown in Figure 4.5. For a film of given thickness and permittivity, the range of unstable frequencies can be widened by increasing the voltage between the plates or by decreasing the distance between the plates. Both adjustments effectively increase the strength of the applied electric field. In general, pillars form at a faster rate when the electric forces are maximized and the surface forces are minimized.

Although theory predicts that there are no limits to the characteristic spacing, there are some practical limits. The longest wavelengths are associated with impossibly long time scales of formation. The shortest wavelengths are accomplished using unrealistic electrode gaps, film thicknesses, and electric fields. The dielectric breakdown of air serves as the ultimate limit on the applied electric field. Larger electric fields result in less macroscopic ordering and a larger distribution of pillar diameters due to the increase in favorable growth modes (Figure 4.5). These limits will be discussed in more detail in Chapter 7.

4.3.5 Linear Stability Analysis Assumptions

Linear stability analysis ignores the effects of van der Waals forces because of their relative insignificance compared to the electrostatic forces. In the absence of an electric field, thin films with the appropriate Hamaker constant are capable of forming instabilities. According to the literature, significantly longer annealing times are required for van der Waals (dispersive force) induced instabilities and the resulting film morphology is more stochastic compared to electric field induced structures.^{4,5} Furthermore, van der Waals forces only become significant below ~ 100 nm and the experiments reported in this thesis use film thicknesses > 100 nm (generally ~ 1 μm). For a typical polymeric system, if the applied field is ~ 10 V/ μm and Hamaker constants are assumed to be $\sim 10^{20}$ J for a 100 nm film, the electric forces are three orders of magnitude larger than the van der Waal forces.

In summary, the linear stability analysis assumes: (1) the system utilizes a thin film, (2) the lubrication approximation applies, (3) the fluid is incompressible, (4) linearized equations are applicable, (5) gravity can be neglected, and (6) van der Waals forces can be neglected.

4.4 LIMITATION OF WORK TO DATE

4.4.1 Time Scale of Formation

All of the work reported in literature on the pillar formation process has been on polymers. Unfortunately, polymers generally require long processing times for several reasons. The polymer film must first be heated above its glass transition temperature (T_g), such that the polymer has sufficient mobility to allow amplification of surface undulations. Once pillars are formed, the polymer must be cooled below the T_g to preserve the columnar structures. This heating and cooling cycle can be quite lengthy, especially for high T_g polymers. In addition to this lengthy cycle, the time scale of pillar formation can be extremely long due to the high viscosity of polymer melts. Equation 4.14, derived from the linear stability analysis, predicts the time scale of formation to be proportional to viscosity. For most polymers, the time scale of formation (both theoretical and actual) is on the order of hours.³⁶ Replacing polymeric films with photocurable liquids drastically reduces the time scale of pillar formation due to the large difference in viscosities between these materials.⁴⁰ Furthermore, using photocurable liquids eliminates the heating-cooling cycle associated with polymer films since liquid films form pillars at room temperature. Once pillars are formed, the structures are locked into place using a photocuring step, resulting in polymeric columns. The use of low viscosity, photocurable materials is discussed in detail in Chapter 6. The growth mechanisms, characteristic spacing, and ordering of the low viscosity pillars are discussed in Chapter 7.

4.4.2 Aspect Ratio

The aspect ratio of the pillars is defined as the height of the columnar structure (i.e. the capacitor gap) divided by the diameter of the pillar. A literature survey shows that the aspect ratio for pillars typically ranges from 0.05-0.2, implying that the pillars are more like discs than columns. Large aspect ratio pillars are desirable for patterning because of their ability to withstand vertical feature degradation during etching. In addition, high aspect ratio pillars (and consequently higher surface area to volume ratio) may enable this technology to find more uses and applications, such as cylindrically shaped additives for composite materials.

The development of a tool designed to stretch pillars in an attempt to increase the aspect ratio will be discussed in Chapter 8.

4.5 EXPERIMENTAL SECTION

Unless otherwise stated, the following techniques were used in Chapters 5-10. Pillars were formed using a simple experimental configuration. Typically, aluminum backed polished silicon wafers were used as substrates. The doped wafers provide a uniform ground in the capacitor device, while the aluminum provides a robust electrical contact. Films were spin coated onto the substrate. The film thickness was measured using ellipsometry (J.A. Woollam WVASE32) and profilometry (Tencor Alpha-Step 200). Typically, the processing conditions (spin speed, solvent dilution, etc.) were tailored to produce films ~1 μm thick.

The top surface (i.e. template) in the capacitor device was a glass slide. Recesses were etched into the slide using a hydrogen fluoride etch to create spacers between the top electrode and the film, as seen in Figure 4.7. Typical gaps were 1-5 μm deep, as measured by profilometry. The top electrode was created by coating the recess with a 4-

10 nm chromium film via thermal evaporation. A 4-10 nm chromium film is semi-transparent, allowing for visual observation of the pillar formation process *in-situ* and for photo-curing as necessary. Indium tin oxide (ITO) was also used as an electrode because it is both transparent and conductive. The ITO was deposited by e-beam evaporation and annealed for several hours at 350°C.

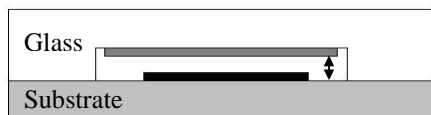


Figure 4.7: A side view of the experimental configuration used to form pillars. A recess, as shown by the arrow, is etched into the glass slide using HF. The recess is coated with a thin layer of chromium to form an electrode, as shown in dark gray. The polymeric film is depicted by the black rectangle located on the substrate.

An electric field (0.1-50 V/ μm) was applied across the resulting gap by connecting a positive lead to the chromium electrode on the template and grounding the aluminum coated substrate. For photocurable samples, the pillars were irradiated through the template by a UV exposure tool (Novacure 2000) to polymerize the pillars. A typical exposure time was 100 seconds at $\sim 12 \text{ mW/cm}^2$. While a shorter exposure time would likely be sufficient, longer times were used to ensure thorough curing. After pillar formation, the upper template was removed to analyze the pillars on the substrate. The resulting structures were characterized by scanning electron microscopy (SEM) and optical microscopy. For polymeric films, the procedure was identical except the samples were heated with either a hot plate or oven.

4.6 CONCLUSIONS

Electric field assisted assembly is a simple, inexpensive technique that offers a promising route to spontaneously generate arrays of pillars. Linear stability analysis is commonly used to model the pillar formation process, in which the destabilizing electrostatic forces amplify thin film undulations against the restoring forces of surface tension. Most of the work to date on pillars has been done with polymers, which slowly form pillars because of their large melt viscosities. The remaining chapters discuss novel processing and materials development for the electric field assisted assembly process. Goals include understanding the dynamics of tri-layer film stacks (Chapter 5), increasing the rate of pillar formation through rational material design (Chapter 6), characterizing the order of the structures and studying ways to improve order (Chapter 7), and increasing the structural aspect ratio (Chapter 8).

4.7 REFERENCES

1. Stoykovich, M. P.; Mueller, M.; Kim, S. O.; Solak, H. H.; Edwards, E. W.; de Pablo, J. J.; Nealey, P. F., Directed assembly of block copolymer blends into nonregular device-oriented structures. *Science* **2005**, 308, (5727), 1442-1446.
2. Rothmund, P. W. K., Folding DNA to create nanoscale shapes and patterns. *Nature* **2006**, 440, (7082), 297-302.
3. Chou, S. Y.; Zhuang, L., Lithographically induced self-assembly of periodic polymer micropillar arrays. *Journal of Vacuum Science & Technology, B: Microelectronics and Nanometer Structures* **1999**, 17, (6), 3197-3202.
4. Schaffer, E.; Thurn-Albrecht, T.; Russell, T. P.; Steiner, U., Electrically induced structure formation and pattern transfer. *Nature* **2000**, 403, (6772), 874-877.
5. Schaffer, E.; Thurn-Albrecht, T.; Russell, T. P.; Steiner, U., Electrohydrodynamic instabilities in polymer films. *Europhysics Letters* **2001**, 53, (4), 518-524.

6. Lin, Z.; Kerle, T.; Baker, S. M.; Hoagland, D. A.; Schaffer, E.; Steiner, U.; Russell, T. P., Electric field induced instabilities at liquid/liquid interfaces. *Journal of Chemical Physics* **2001**, 114, (5), 2377-2381.
7. Chou, S. Y.; Zhuang, L.; Deshpande, P.; Chen, L.; Sun, X., Lithographically-induced self-assembly of periodic micro-pillar arrays in a single homopolymer film. *Polymer Preprints (American Chemical Society, Division of Polymer Chemistry)* **2000**, 41, (1), 78.
8. Pease, L. F.; Russel, W. B., Electrostatically induced submicron patterning of thin perfect and leaky dielectric films: A generalized linear stability analysis. *Journal of Chemical Physics* **2003**, 118, (8), 3790-3803.
9. Yan, X.; Liu, G.; Dickey, M.; Willson, C. G., Preparation of porous polymer membranes using nano- or micro-pillar arrays as templates. *Polymer* **2004**, 45, (25), 8469-8474.
10. Bakir, M. S.; Villalaz, R. A.; Ogunsola, O. O.; Gaylord, T. K.; Kohl, P. A.; Martin, K. P.; Meindl, J. D., Sea of polymer pillars: Dual-mode electrical-optical Input/Output interconnections. *Proceedings of the IEEE International Interconnect Technology Conference, 6th, San Francisco, CA, United States, June 2-4, 2003* **2003**, 77-79.
11. Yang, M.-C.; Shieh, J.; Hsu, C.-C.; Cheng, T.-C., Well-Aligned Silicon Nanograss Fabricated by Hydrogen Plasma Dry Etching. *Electrochemical and Solid-State Letters* **2005**, 8, (10), C131-C133.
12. Cao, H.; Tegenfeldt, J. O.; Austin, R. H.; Chou, S. Y., Gradient nanostructures for interfacing microfluidics and nanofluidics. *Applied Physics Letters* **2002**, 81, (16), 3058-3060.
13. Schaffer, E.; Harkema, S.; Roerdink, M.; Blossey, R.; Steiner, U., Thermomechanical lithography: pattern replication using a temperature gradient driven instability. *Advanced Materials* **2003**, 15, (6), 514-517.
14. Landau, L. D.; Lifshitz, E. M., *Electrodynamics of continuous media*. Pergamon Press: Oxford, New York, 1960; p 417.
15. Melcher, J. R., *Field-coupled surface waves, a comparative study of surface-coupled electrohydrodynamic and magnetohydrodynamic systems*. M.I.T. Press: Cambridge, Mass., 1963; p xiv, 190.
16. Sharma, A.; Ruckenstein, E., An analytical nonlinear theory of thin film rupture and its application to wetting films. *Journal of Colloid and Interface Science* **1986**, 113, (2), 456-79.

17. Ruckenstein, E.; Jain, R. K., Spontaneous rupture of thin liquid films. *Journal of the Chemical Society, Faraday Transactions 2: Molecular and Chemical Physics* **1974**, 70, (1), 132-47.
18. Zhang, W. W.; Lister, J. R., Similarity solutions for van der waals rupture of a thin film on a solid substrate. *Physics of Fluids* **1999**, 11, (9), 2454-2462.
19. Oron, A., Nonlinear dynamics of three-dimensional long-wave Marangoni instability in thin liquid films. *Physics of Fluids* **2000**, 12, (7), 1633-1645.
20. Monch, W.; Herminghaus, S., Elastic instability of rubber films between solid bodies. *Europhysics Letters* **2001**, 53, (4), 525-531.
21. Ghatak, A.; Chaudhury, M. K.; Shenoy, V.; Sharma, A., Meniscus Instability in a Thin Elastic Film. *Physical Review Letters* **2000**, 85, (20), 4329-4332.
22. Kargupta, K.; Sharma, A., Templating of Thin Films Induced by Dewetting on Patterned Surfaces. *Physical Review Letters* **2001**, 86, (20), 4536-4539.
23. Zope, M.; Kargupta, K.; Sharma, A., Self-organized structures in thin liquid films on chemically heterogeneous substrates: Effect of antagonistic short and long range interactions. *Journal of Chemical Physics* **2001**, 114, (16), 7211-7221.
24. Taylor, G. I.; McEwan, A. D., The stability of a horizontal fluid interface in a vertical electric field. *Journal of Fluid Mechanics* **1965**, 22, (1), 1-15.
25. Saville, D. A., Electrohydrodynamics: the Taylor-Melcher leaky-dielectric model. *Annual Review of Fluid Mechanics* **1997**, 29, (27).
26. Oddy, M. H.; Santiago, J. G.; Mikkelsen, J. C., Electrokinetic instability micromixing. *Analytical Chemistry* **2001**, 73, (24), 5822-5832.
27. Warner, M. R. E.; Craster, R. V.; Matar, O. K., Pattern formation in thin liquid films with charged surfactants. *Journal of Colloid and Interface Science* **2003**, 268, (2), 448-463.
28. Ristenpart, W. D.; Aksay, I. A.; Saville, D. A., Assembly of colloidal aggregates by electrohydrodynamic flow: kinetic experiments and scaling analysis. *Physical Review E: Statistical, Nonlinear, and Soft Matter Physics* **2004**, 69, (2-1), 021405/1-021405/8.
29. Chou, S. Y.; Zhuang, L.; Guo, L., Lithographically induced self-construction of polymer microstructures for resistless patterning. *Applied Physics Letters* **1999**, 75, (7), 1004-1006.

30. Verma, R.; Sharma, A.; Kargupta, K.; Bhaumik, J., Electric Field Induced Instability and Pattern Formation in Thin Liquid Films. *Langmuir* **2005**, 21, (8), 3710-3721.
31. Lin, Z.; Kerle, T.; Russell, T. P.; Schaeffer, E.; Steiner, U., Structure Formation at the Interface of Liquid/Liquid Bilayer in Electric Field. *Macromolecules* **2002**, 35, (10), 3971-3976.
32. Lin, Z.; Kerle, T.; Russell, T. P.; Schaeffer, E.; Steiner, U., Electric Field Induced Dewetting at Polymer/Polymer Interfaces. *Macromolecules* **2002**, 35, (16), 6255-6262.
33. Morariu, M. D.; Voicu, N. E.; Schaeffer, E.; Lin, Z.; Russell, T. P.; Steiner, U., Hierarchical structure formation and pattern replication induced by an electric field. *Nature Materials* **2003**, 2, (1), 48-52.
34. Xiang, H.; Lin, Y.; Russell, T. P., Electrically Induced Patterning in Block Copolymer Films. *Macromolecules* **2004**, 37, (14), 5358-5363.
35. Herminghaus, S., Dynamical Instability of Thin Liquid Films Between Conducting Media. *Physical Review Letters* **1999**, 83, (12), 2359-2361.
36. Pease, L. F., III; Russel, W. B., Limitations on Length Scales for Electrostatically Induced Submicrometer Pillars and Holes. *Langmuir* **2004**, 20, (3), 795-804.
37. Pease, L. F.; Russel, W. B., Linear stability analysis of thin leaky dielectric films subjected to electric fields. *Journal of Non-Newtonian Fluid Mechanics* **2002**, 102, (2), 233-250.
38. Craster, R. V.; Matar, O. K., Electrically induced pattern formation in thin leaky dielectric films. *Physics of Fluids* **2005**, 17, (3), 032104/1-032104/17.
39. Leach, K. A.; Lin, Z.; Russell, T. P., Early Stages in the Growth of Electric Field-Induced Surface Fluctuations. *Macromolecules* **2005**, 38, (11), 4868-4873.
40. Dickey, M. D.; Collister, E.; Raines, A.; Tsiartas, P.; Holcombe, T.; Sreenivasan, S. V.; Bonnacaze, R. T.; Willson, C. G., Photocurable Pillar Arrays Formed via Electrohydrodynamic Instabilities. *Chemistry of Materials* **2006**, 18, (8), 2043-2049.

Chapter 5

Hierarchical Polymer Structures Formed Via Electric Field Assisted Assembly

Polystyrene (PS) and poly(methyl methacrylate) (PMMA) were the first homopolymers demonstrated to form pillars.¹ Although these polymers form pillars slowly due to their large melt viscosities, multi-layer film stacks of these polymers form remarkable hierarchical structures via electric field assisted assembly.²⁻⁴ These three-dimensional structures arise from the immiscibility of the polymers and the differences in their dielectric constants. Such structures are quite difficult to produce using traditional fabrication steps. This chapter discusses the various mechanisms that are responsible for the formation of these structures with a focus on the role of the wetting properties of the electrodes in dictating the final morphology of the structures.

5.1 INTRODUCTION

Electrohydrodynamic instabilities are an attractive method for forming pillar arrays since the size scale of the pattern can be controlled by adjusting the strength of the electric field. The process of pattern generation with an electric field gradient can easily be coupled with the wetting and dewetting of thin polymer films to generate novel structures. The dewetting of thin polymer films is driven by van der Waals forces. Dewetting occurs when fluctuations at the free polymer surface are amplified in an effort to lower the overall energy of the system.⁵ In an electric field, the instability is produced by the stresses at the interface between two dielectric fluids due to uncompensated

displacement charges. This imbalance makes the system unstable to fluctuations of a specific wavelength and patterns are generated with a wavelength determined by the interfacial energy and the electric field gradient at the fluid-fluid interface. In this chapter, the combined effects of electric field gradients and dewetting surfaces are studied in multi-layer polymer systems.

Structure formation at polymer/air (single layer),⁶ polymer/polymer (bilayer)⁷ and polymer/polymer/air (trilayer)² interfaces have been studied. Multi-layered polymer film systems are interesting because (1) the interfacial energy is low between the polymer layers, favoring smaller characteristic wavelengths, (2) the polymers are immiscible, resulting in hierarchical structures, and (3) the different wetting properties of the polymers at the electrodes contribute to the final geometry of the induced structures.

In this chapter, two variations of the trilayer experiment are discussed. First, a PMMA / PS / air system is studied in which the wetting characteristics of the upper electrode are varied. Second, a PS / PMMA / air system is evaluated. This system is interesting because (1) PS does not wet the native oxide on the silicon substrate whereas PMMA does and (2) PMMA has a higher dielectric constant than both air and PS, resulting in a pressure at both interfaces (i.e. PMMA/air, PMMA/PS) that favors movement of the interface towards the respective electrodes (i.e. the PMMA is being pulled in opposite directions). Altering the wetting properties of the substrate as well as the molecular weight of the polymers impacts the electrohydrodynamics. These trilayer systems are capable of forming both encapsulated and cage-type structures that would be difficult to produce otherwise.

5.2 PMMA / PS / AIR TRILAYER

5.2.1 Background

There has only been one trilayer system reported in the literature, PMMA covered by PS with an overlying air gap. Lin et al.⁸ and Morariu et al.² showed that electrostatic forces applied to the PMMA / PS / air trilayer generate fluctuations first at the PS / air interface, with the PMMA film remaining relatively unperturbed. In those experiments, the wavelength of the fastest-growing fluctuation amplified by the electric field defined the characteristic spacing of a well-ordered array of PS columns, spanning the electrodes. This concept is illustrated in Figure 5.1.

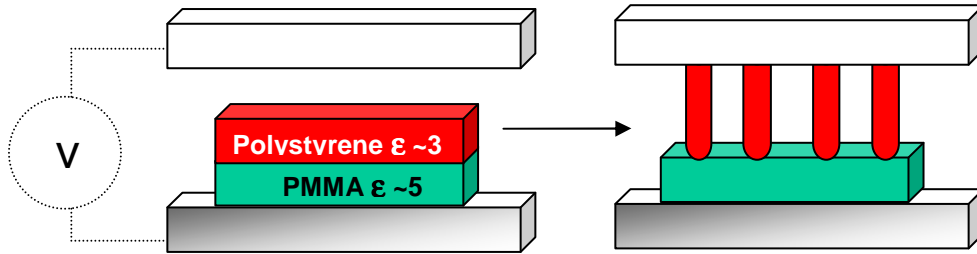


Figure 5.1: Illustration of the PMMA / PS / air trilayer system. The PS forms pillars first because there is less viscous resistance at the PS / air interface.

Although the electric field creates a destabilizing force at both the PS / air interface and the PMMA / PS interface, the time scale of pillar formation is much faster at the PS / air interface. This is largely due to the low viscous resistance at the air interface, combined with the tendency of PS to dewet PMMA, allowing for interfacial slip. Qu et al.⁹ used measurements of dewetting velocities to confirm quantitatively the theoretical predictions about liquid/liquid bilayers made by Brochard-Wyart and coworkers.¹⁰ These studies suggest that, for liquid/liquid dewetting where $\eta_A/\theta_E < \eta_B$ (η_A

and η_B are the viscosities of the upper and lower layer respectively, and θ_E is the equilibrium contact angle between the two liquids), the upper layer dictates dewetting dynamics and morphology, while the lower layer displays solid-like behavior, similar to the situation observed for the PMMA/PS/air trilayers. However, for $\eta_A/\theta_E > \eta_B$, Brochard-Wyart et al.¹⁰ predict a crossover to a regime in which viscous dissipation occurs mostly in the lower layer, which controls dewetting dynamics (Note: This scenario is observed for PS/PMMA/air trilayers).

The formation of PS pillars in the PMMA / PS / air trilayer was accompanied by a small deformation in the PMMA film, resulting in a rim at the PS / PMMA contact line at the base of the pillars. Given sufficient time, this PMMA rim is drawn up around the PS pillar surface, parallel to the overall electric field. Eventually, the flow of PMMA results in a concentric sheath. This approach to layered, hierarchically ordered structures has the advantage that it results in significantly reduced feature sizes in the pattern after the PS component is removed with a selective solvent. These results were replicated in our lab, as shown in Figure 5.2.

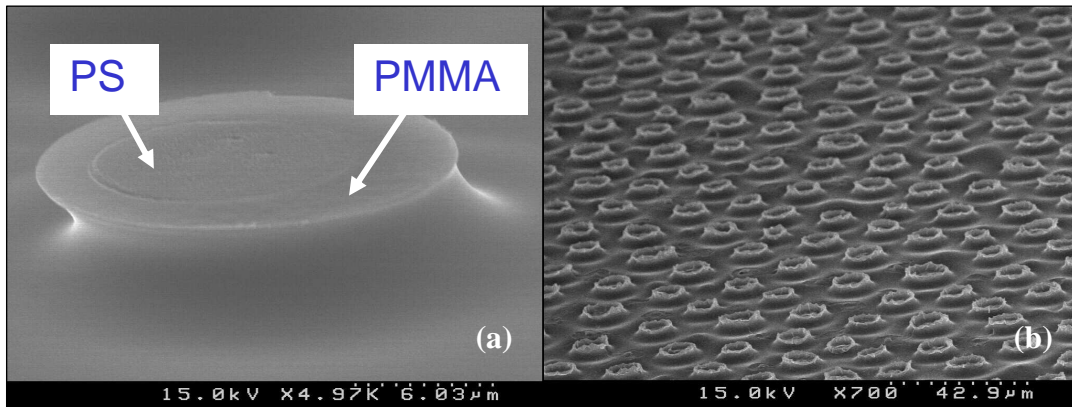


Figure 5.2: PMMA / PS / air trilayer: (a) A pillar with a PS core and PMMA sheath. (b) The PS cores are selectively removed by cyclohexane, resulting in an array of hollow structures.

A slight variation on this process results in significantly different structures. First, by changing the wetting properties of the upper electrode, the PMMA sheath can encapsulate the PS core. Second, the sheath of PMMA that grows up the side of the PS core can break into secondary undulations under certain conditions, resulting in cage structures. These two effects are discussed in the following section.

5.2.2 Experimental

A schematic diagram of the experimental geometry is shown in Figure 5.3 (for more details, see Chapter 4). The glass slide had a $3.5 \mu\text{m}$ rectangular recess in the center with an area of $\sim 1 \text{ cm}^2$. A $\sim 50 \text{ nm}$ chromium layer was thermally evaporated on the recess to create the upper electrode.

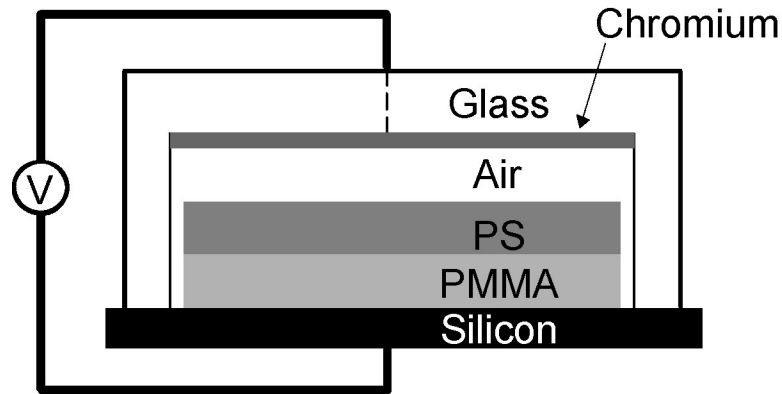


Figure 5.3: N-doped, backside aluminum coated silicon wafer serves as the substrate and chromium deposited on glass serve as the upper electrode. The setup is heated on a hotplate.

The surface properties of the chromium surface were modified by a coating of fluoropolymer (3M HFE 7100), which makes the surface hydrophobic. The coating was applied by dipping the chromium layer in the fluoropolymer solution. Experiments were done with both the fluoropolymer-coated and uncoated chromium layer. A $\sim 1 \mu\text{m}$ thick PMMA (Polysciences, catalog 04554, avg MW 25,000) film was spin coated onto a

silicon wafer from 10% solution in chlorobenzene. A $\sim 0.7\ \mu\text{m}$ thick PS (Aldrich, catalog 33,164-1, avg MW 200,000 and 4,000) film was spin coated from 12.5% solution in toluene on top of the PMMA. Both PMMA and PS were prepared by free radical polymerization, therefore are atactic and have broad molecular weight distribution. The glass transition temperature of PMMA is $105\ ^\circ\text{C}$ and of PS is $100\ ^\circ\text{C}$ as determined by differential scanning calorimetry (TA instruments). The films were heated to $90\ ^\circ\text{C}$ for 1 minute after each step to remove residual solvent. The edges of the polymer film were removed with solvent and the two electrodes were clamped together, such that the layered polymer films were entirely under the recess. The resulting air gap was $\sim 5\ \mu\text{m}$, as determined by measurement of the height of the structures formed after removal of the upper electrode. The system was heated to $120\ ^\circ\text{C}$ on a hotplate and 200 V DC was applied across the two electrodes. This led to a destabilization of the layered polymer films, causing the initially transparent polymer bilayer to become translucent. This macroscopic change indicates the formation of microscopic structures on a size scale that scatters visible light and would typically take ~ 45 minutes to occur. The temperature was then raised to $190\ ^\circ\text{C}$ for 45 minutes, with the voltage being maintained. The system was then cooled to room temperature before removing the electric field. The polarities of the electrodes do not affect the results. The silicon wafer was removed and divided into two parts. Electrode separation was facilitated by using a chromium etch solution to remove the evaporated chromium layer from both the treated and untreated chromium surfaces. This prevented the fracture of structures while removing the wafer from the glass slide. A section of the sample was imaged by SEM, while another section was imaged after selectively removing the PS with cyclohexane, a non-solvent for PMMA.

5.2.3 Results and Discussion

Figure 5.4 shows the structures formed in the case where the chromium surface was not treated. These structures are similar to those obtained by electrohydrodynamic instabilities in a single layer of polymer. Columns of polymer are seen with concave walls and flat tops. From this image no distinction can be made between the different components, PS and PMMA. It is evident that these columnar structures are uniformly distributed over the surface and that the lateral size of the structures ($\sim 15\text{ }\mu\text{m}$ diameter) is uniform.

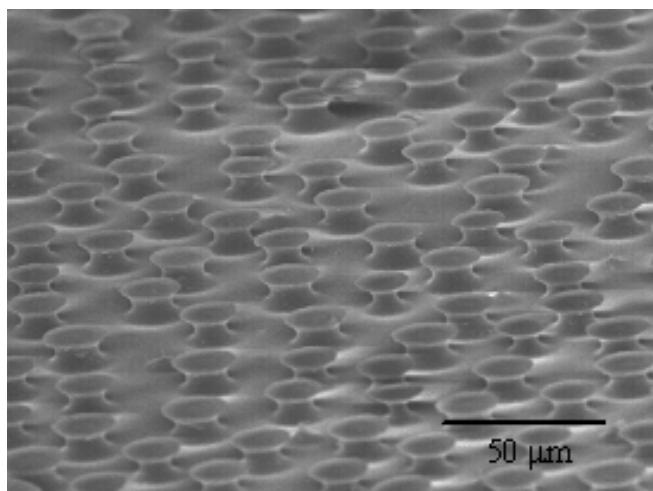


Figure 5.4: SEM image of the structures obtained after removing the upper electrode and without further treatment.

Magnifying a single pillar reveals the hour-glass shape of the structures, as shown in Figure 5.5. Exposure of the multi-component structure to an electron beam in the SEM degrades the PMMA without altering the PS. There is a recess on the top of the column, a distinct rim on the side wall at the top, and, what appear to be channels running vertically up the walls of the column. The complement to this image was obtained by

selectively removing the PS with cyclohexane. Figure 5.6 reveals a very unique cage-type structure made by the PMMA. Strands of PMMA spanned between the bottom PMMA film and a disk of PMMA that formed on the upper electrode. Note that the surface of this disk or ceiling was smooth since it was adjacent to the upper electrode. In addition, around the ring of PMMA strands, there was an elevated rim of PMMA that corresponded to the diameter of the columns formed by the PS / PMMA bilayer. A cross-sectional SEM image of a cleaved cage-type structure is shown in Figure 5.7 where the diameter of the cage is $\sim 16.5\text{ }\mu\text{m}$ with a height of $4\text{ }\mu\text{m}$, the separation distance between the electrodes and the ceiling thickness is $1.2\text{ }\mu\text{m}$.

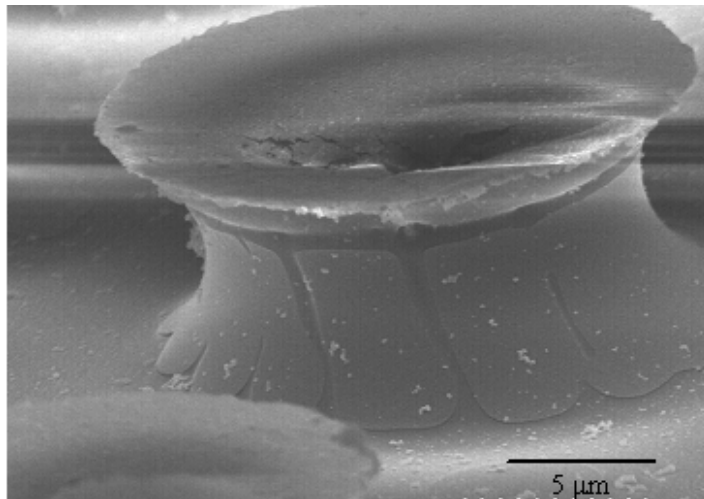


Figure 5.5: SEM image of a single structure. The dark recesses along the height of the pillar are due to PMMA that has been degraded because of e-beam exposure in the SEM.

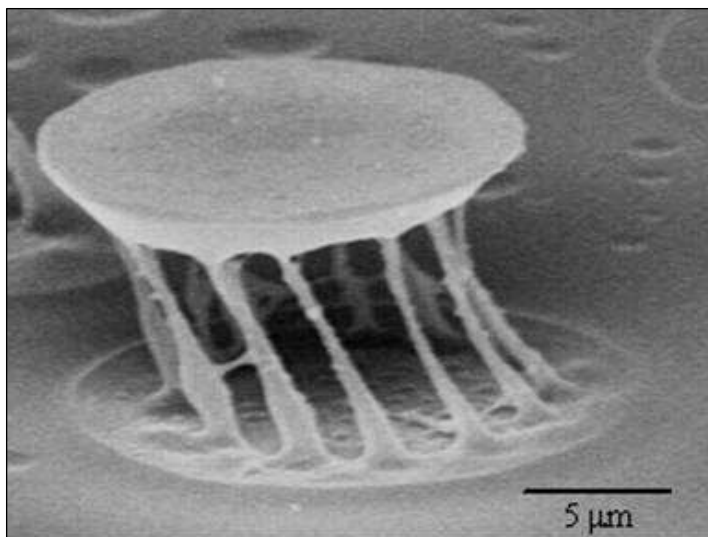


Figure 5.6: SEM image of a single 'cage'. Sample was cyclohexane washed to remove PS and close cell structure made of PMMA was obtained.

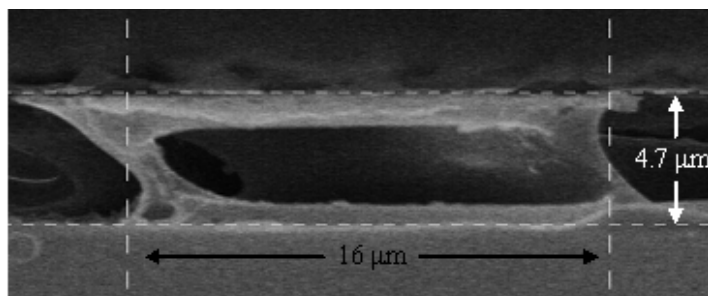


Figure 5.7: Cross-sectional SEM image of a cleaved single hollow pillar. The dimensions of a single close cell structure are shown.

The structures in Figures 5.5-5.7 can be understood in the context of electrohydrodynamic instabilities. As shown previously,² the upper PS layer forms columnar structures on the lower layer of PMMA. The PMMA film acts like a substrate despite being above its glass transition temperature. This can be easily understood by comparing the short characteristic times required to initiate instabilities at the PS-air interface to the much longer characteristic times for instabilities to grow at the PMMA-PS interface. Instabilities at the PS-PMMA interface require viscous flow in both layers,

and therefore the time required to amplify fluctuations is large. After the growth of the PS structures, the contact line at PS / PMMA interface is locally deformed, forming a rim on the PMMA surface as shown in Figure 5.8b. The Neuman construction¹⁰ can be used to determine the direction of surface forces at the contact line, and the uncompensated normal component of the surface tension leads to contact line deformation. In addition to surface tension, viscous stresses due to lateral movement of the contact line during growth of the PS structures, lead to a deformation of the contact line.

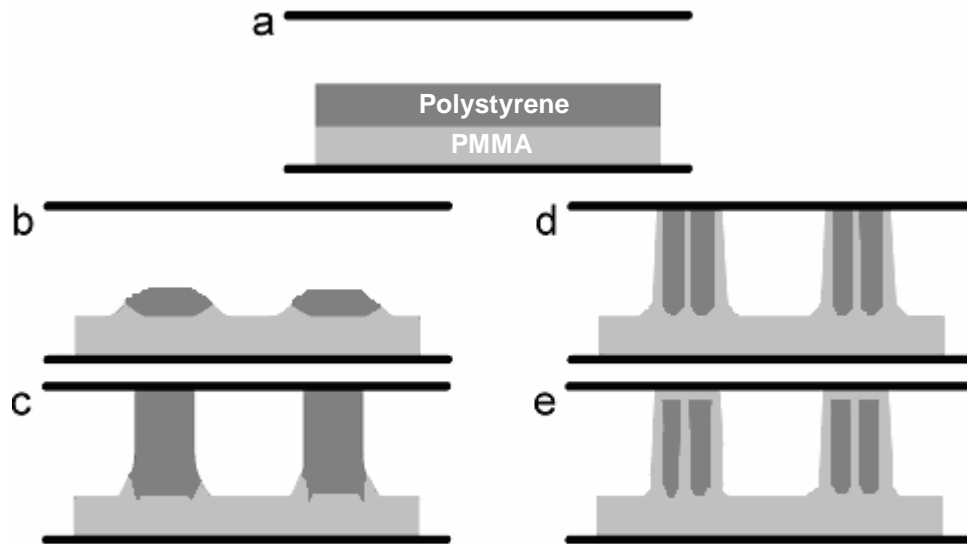


Figure 5.8: Schematic of the mechanism of the formation of 'cage' structures. (a) Initial smooth films. (b) PS dewets the PMMA surface and form structures while conserving mass. (c) These structures grow under electric field and touch the top electrode. (d) PMMA 'fingers' climb up along the pillar under electric field and touch the top electrode. (e) PMMA displaces PS from the top electrode and exerts downward pressure on PS due to electric field. There remains an observable residual film of PMMA between the structures. Note: (a)-(c) are cut-away depictions, whereas (d)-(e) are side views of the structures, illustrating the formation of fingers on the side of the structures.

The electric field strength at the top of the rim was enhanced by the curvature of the structures. This led to the initiation of an instability and the rim was pulled upwards. Morariu et al.² observed that the rim was pulled up uniformly by the electric field, forming a sheath of PMMA around the PS column. In contrast, we observed the growth of a fingering instability along the circumference of the rim. This fingering instability arose from the flow of the thin film of PMMA on the PS pillar under the influence of electric field stresses. Since PMMA has a small contact angle ($\sim 23^\circ$) with PS,¹¹ flow of PMMA induced an instability and led to the formation of fingers perpendicular to the direction of flow as shown in Figure 5.8d.¹² The wavelength of the instability is characteristic of the film thickness and the capillary number (Ca), and is given by, $\lambda \sim h(\text{Ca})^{-1/3} = h(3\eta V/\sigma)^{-1/3}$ where h is film thickness, η is the viscosity, V is the velocity of the flow front and σ is the surface tension of PMMA.¹² For the fingering instabilities to occur, the film should flow over a distance on the order of λ . Since the separation distance between electrodes is about one order more than that used by Morariu et al., they did not observe this fingering instability. Once the fingering instability forms, the electric field amplifies the instability, causing the formation of strands around the circumference of the existing PS columns. There is some experimental evidence that these strands eventually merge to form a sheath, although determining this experimentally is extremely challenging (e.g. see Figures 5.9-5.10).

There are small bumps in the base of the structure in Figure 5.6. The small characteristic wavelength between these structures is attributed to the low surface tension at the PS / PMMA interface. These undulations are amplified at a slower rate than those on the periphery of the structure due to higher viscous resistance to flow on the interior of the structure. The PMMA structures on the perimeter of the structure also experience a

slightly larger electric force due to the existence of the PMMA rim around the basin of the PS pillar, bringing the strands closer to the upper electrode.

Once the strands of PMMA reached the top electrode, PMMA wetted the chromium surface displacing the PS, as shown in Figure 5.8e. This was experimentally confirmed by coating a film of PMMA on top of a PS film on a chromium surface. After annealing the films in the absence of an electric field, PMMA was observed on the chromium surface after removing the PS with cyclohexane. This is consistent with the observations of Harris et al.¹¹ in which PS/PMMA bilayers on silicon oxide were studied. The energetic gain of replacing the PS / chromium interface with the more favorable PMMA / chromium interface caused the formation of a thin PMMA film between the PS and chromium. This thin PMMA film was the ceiling in the cage-like structure. The formation of this thin film requires that the strands of PMMA act like channels for the flow of PMMA from the lower layer to the upper electrode surface. The reduction in interfacial energy not only promoted the formation of the ceiling but, once formed, the higher dielectric constant of PMMA versus that of PS produced an electrostatic pressure that pulled the PMMA/PS interface in the ceiling down to the lower electrode. This, in turn, caused the thickness of the ceiling to increase to $\sim 1.2 \mu\text{m}$.

This mechanism was further verified by using the surface treated chromium electrode. Figure 5.9 shows SEM image of the structures formed by keeping the same film thickness and electric field strength as in the previous experiment, but fluorinating the chromium layer. The sample was treated with cyclohexane to remove PS selectively before imaging. It can be seen that the PMMA formed a sheath around the PS pillar but had not encased the PS completely. Since the chromium was coated with a fluoropolymer, PMMA did not preferentially wet the surface and could not displace the PS from the electrode, and therefore, it does not form a ceiling in the structures. This

demonstrates that when the inherent surface interactions of the polymer are coupled with electric fields, novel 3D structures are formed.

Evidence suggests that the hollow structures shown in Figure 5.9 form by the coarsening of tendrils, as shown in Figure 5.10. Although it is difficult to prove coarsening conclusively through experimentation, Figure 5.10 shows images of tendrils that are just forming (a) and that have merged (b). The images in Figure 5.10 were observed on the same sample as those on Figure 5.9. The difference in the structures could be attributed to either a slightly wedged capacitor geometry or to differences in the rate of instability growth, consistent with observations of “stochastic growth” discussed in the Chapter 6 and 7.

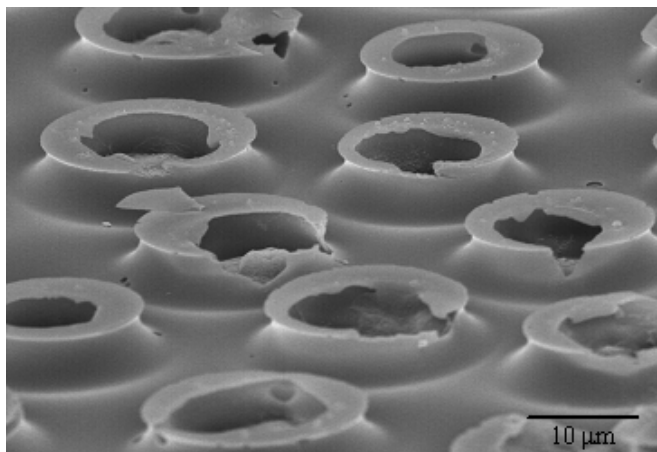


Figure 5.9: SEM image of PMMA structures obtained with hydrophobic chromium layer and treated with cyclohexane. The structures are hollow and do not have a cap or ceiling.

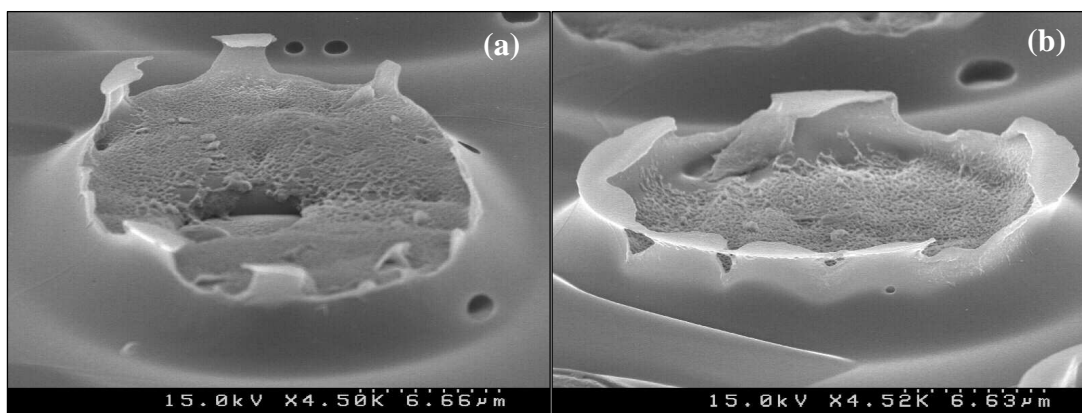


Figure 5.10: SEM images of PMMA basins providing evidence of tendrils coarsening to form the hollow concentric type structures shown in Figure 5.9.

5.2.4 Summary of PMMA / PS / Air Trilayer

In summary, a route to fabricate three-dimensional microscopic structures in thin films has been shown by coupling electrohydrodynamic instabilities with preferential wetting. When PMMA wets the upper electrode, the PMMA completely encapsulates the PS core. Cage-like structures were produced by instabilities enhanced by the applied electric field. The structures form when the growing PMMA sheath breaks into fingering instabilities. This methodology has the potential of producing arrays of unique closed-cell structures that cannot be produced using traditional fabrication techniques.

5.3 PS / PMMA / AIR TRILAYER

5.3.1 Background and Theory

One might expect the dynamics of the PS / PMMA / air trilayer system to mimic the PMMA / PS / air system, with PMMA forming an array of pillars on top of the underlying PS, followed by concentric growth of PS around the PMMA pillars. Despite this intuitive expectation, the inverted system (i.e. PS/PMMA/air) structures surprisingly

resemble those formed by the non-inverted system (i.e. PMMA/PS/air). Despite the resemblance in the final structure, the mechanism by which the pillars form is completely different due to changes in interfacial forces resulting from the inverted configuration.

The most significant change in system dynamics resulting from placement of PMMA in the middle of the trilayer is a *downward* electrostatic force at the PMMA/PS interface. At the PMMA/air interface, there is an upward force (i.e. toward the upper electrode) since PMMA has a higher dielectric constant than air. This is akin to the force acting on the PS layer in the non-inverted system. The downward electrostatic force at the PMMA/PS interface is due to PMMA having a larger dielectric constant than PS, which is a rational, yet non-obvious, result that has a significant impact on the system dynamics.

In addition to altering the electrostatic forces, the inverted trilayer system creates new dewetting interfaces. The previously studied PMMA / PS / air trilayer has one dewetting interface, PS / PMMA. In contrast, the inverted system of PS / PMMA / air has two interfaces that energetically favor dewetting; PS / PMMA and PS / silicon substrate (with 2 nm thick native oxide). Thus, the dewetting of the bottom PS layer is highly favored. Although the films are relatively thick (~500 nm), dewetting can be initiated by electric-field amplified surface undulations. Thus, the electrostatic forces and the interfacial energies work in tandem to dewet the underlying PS layer, as shown schematically in Figure 5.11, which ultimately affects the final structure morphology.

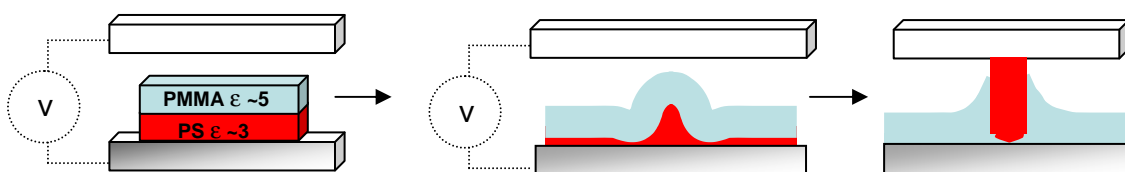


Figure 5.11: Schematic of trilayer “inversion” with PMMA on top of PS. The dielectric constant of PMMA is larger than PS, creating a downward electrostatic force at the PMMA/PS interface. The tendency of PS to dewet both the substrate and PMMA accelerates the structures formation. The PMMA displaces the PS and the PS emerges towards the upper electrode.

The aim of this section is to provide insights into the complex concerted effects of dewetting and electrostatic pressure acting at the polymer/polymer and polymer/air interfaces in the PS / PMMA / air system. The degree to which viscosity affects the final structure will also be discussed. Larger viscosity films have slower dewetting and electrohydrodynamic time scales. The combined effects of varying polymer mobility and polymer-electrode surface interactions strongly impact the dynamics of structure formation.

5.3.2 Experimental

Films of PS and PMMA, having the molecular weights shown in Table 5.1, were spin coated onto polished silicon substrates from toluene solutions. Acetic acid was used to deposit the PMMA upper layer in cases where a selective solvent was required. Prior to spin coating, the silicon substrates were cleaned in concentrated sulfuric acid mixed with inorganic oxidizers. All of the polymer films were uniformly smooth (± 1 nm over the 1×1 cm² sample area) and had thicknesses of 500 nm (± 10 nm), measured by spectral interferometry. Trilayer systems were assembled using the silicon substrate as one electrode and a soda-lime glass slide coated with chromium for the other, as described in Chapter 4. Using a polymer mask at the edges of the slide, a rectangular well was etched by immersion in buffered hydrofluoric acid. The electrode spacing was varied between

experiments by varying the etching time to control the depth of the well, which was measured using a contact probe profilometer (Veeco Dektak 3). The voltage was applied and the films heated to 170°C for 1.5 to 3 hours. Following each experiment, the upper electrode was removed and the film on the silicon substrate was broken into three sections for selective solvent washing. One section was rinsed with acetic acid to remove the PMMA component, another was rinsed with cyclohexane to remove the PS component, and the third was not rinsed. Finally, the structures were imaged using SEM and comparisons were made between each set of three images to determine the overall morphology.

Table 5.1: Characteristics of the Polymers Used In This Study

| Polymer | M _w (g/mol) | M _w /M _n | Viscosity (Pa s) at 170°C * | Dielectric Constant |
|---------|---------------------------|--------------------------------|--------------------------------|------------------------|
| PS | 8,000 | 1.09 | 24 | 2.95 |
| PS | 157,000 | 1.04 | 7.3 x 10 ⁴ | 2.95 |
| PMMA | 32,000 | 1.61 | 2.3 x 10 ⁵ | 5.24 |
| PMMA | 99,000 | 1.04 | 9.2 x 10 ⁵ | 5.24 |

* PS viscosities calculated from reference,¹³ PMMA viscosities measured using a TA Instruments AR2000 Rheometer.

5.3.3 Results and Discussion

Figures 5.12a-b show SEM images of the pattern of structures formed when the electric field was applied across the PS / PMMA / air trilayer. PS with 8 kg/mol molecular weight and PMMA with 32 kg/mol molecular weight were used for these experiments and the film thickness for each layer was 0.5 µm. The air gap was ~ 5 µm

and 136 volts were applied across the two electrodes. The spacing between the structures is observed to be $\sim 20 \mu\text{m}$ from the image. Figure 5.13a shows the structures after removing the PMMA with acetic acid (which does not remove PS), while Figure 5.13b shows a structure after selectively removing the PS with a cyclohexane rinse. These images show that the PS has formed the core of the structures while PMMA forms the sheath.

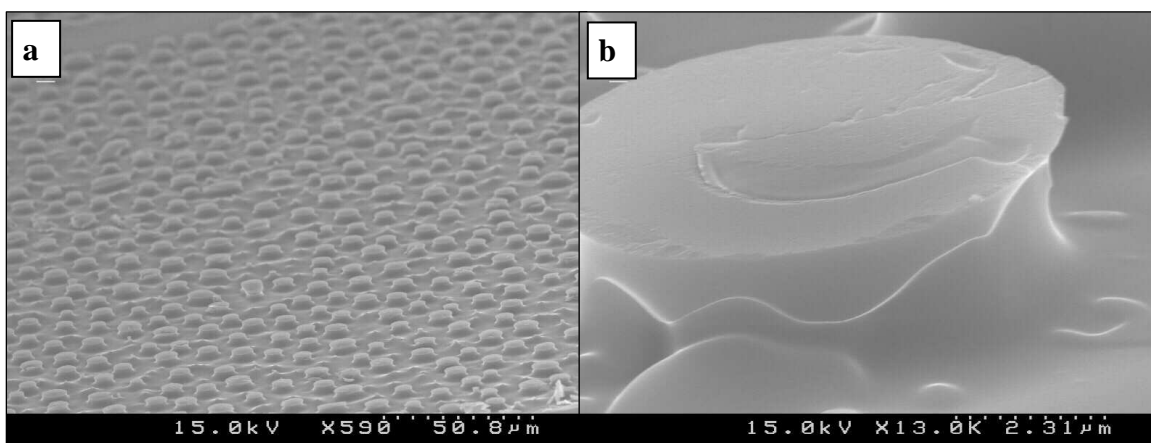


Figure 5.12: (a) Overview of 8 kg/mol PS on 32 kg/mol PMMA. (b) PS core surrounded by PMMA sheath.

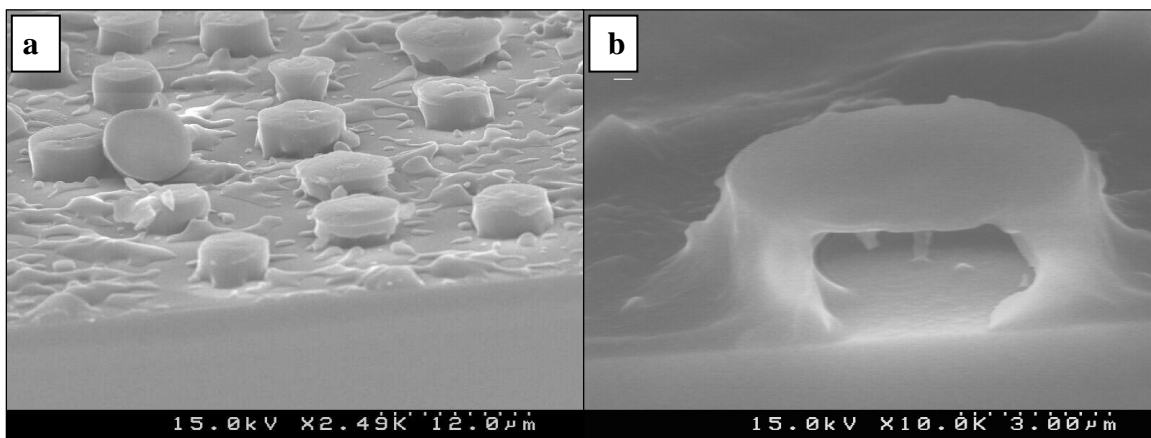


Figure 5.13: (a) Acetic acid rinse reveals PS cores. (b) Cyclohexane rinse reveals complementary PMMA shell.

These observations can be explained by the dynamics at the PMMA/PS, PMMA/air and PS/substrate interfaces. When an electric field is applied across two dielectric layers, a Maxwell stress, T_{ij} , is produced and is given by Equation 5.1.

$$T_{ij} = \frac{1}{4\pi} \left[\epsilon E_i E_j - \frac{1}{2} \epsilon E^2 \delta_{ij} \right] \quad (5.1)$$

E_i is the component of the electric field, ϵ is the dielectric constant of the medium with respect to the environment and δ is the kronecker delta. When a low dielectric material is placed next to a high dielectric material under an electric field, the interface is pushed towards the lower dielectric material. Since PMMA has a higher dielectric constant than both PS and air, the PMMA/air interface is pulled towards the glass electrode and the PS/PMMA interface is pulled towards the substrate. At the fluid/fluid interface, the Maxwell stress destabilizes the smooth interface and leads to the growth of electrohydrodynamic instabilities.¹⁴⁻¹⁶ In addition, the dispersion forces at the PS/PMMA interface and PS/substrate interface are repulsive which leads to dewetting of the fluids at these interfaces.

The Maxwell stress at the PMMA/air interface is higher than at the PMMA/PS interface because of the larger mismatch in dielectric constant between air and PMMA than between PMMA and PS; therefore the characteristic time for the instability to grow at PMMA/air interface should be smaller. The characteristic time is furthermore dependent upon the viscosities of the fluids,¹⁴ which should make it smaller for the PMMA/air interface than the PMMA/PS interface because of the negligible viscosity of air. However, we find the PS/PMMA interface becomes unstable initially, allowing PS to push through the PMMA film. The negative disjoining pressure at the PS/substrate interface accelerates the dewetting of the PS nucleated by the electrohydrodynamic

instability. The relatively low viscosity of the PS allows the lower layer to be highly mobile. This is well represented in Figure 5.14a, which shows an SEM image of the undulations on a polymer film at an early time period, i.e. before the structures could span the air gap. The molecular weight of PMMA was increased to 99 kg/mol to slow down the kinetics of the instability. It can be observed that the PS/PMMA interface has undulations and some of them are fully grown. Figure 5.14b shows an image of a cleaved edge, which illustrates that the PS forms a cone while the film thickness of PMMA has not changed noticeably; consequently the PS/PMMA interface is destabilized first. At later time scales, these undulations develop into pillars that have a PS core and a sheath of PMMA, similar to the structures formed by a PMMA/PS/air trilayer. The formation of a PS core is facilitated by both PS dewetting as well as the Maxwell pressure exerted at the PS/PMMA interface. From Figure 5.13a, it is observed that the PS has dewetted the silicon substrate and is only present in the cores of the pillars, while Figure 5.13b suggests the PMMA film is continuous and also covers the pillars, as expected because of favorable interactions between PMMA with the silicon substrate

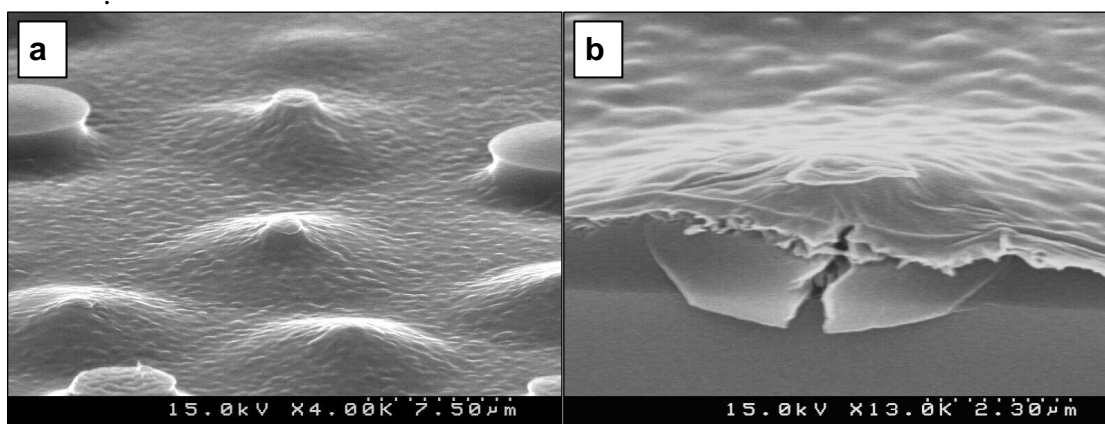


Figure 5.14: (a) Overview of 8 kg/mol PS on 99 kg/mol PMMA shows undulations with several PS breakthroughs. (b) Cleaved edge of sample. PS film has dewetted and filled the void created by undulations. The PMMA film blankets this cone shape.

When the molecular weight of polystyrene was changed to 157 kg/mol, increasing the viscosity by several orders of magnitude, while keeping the molecular weight of the PMMA at 32 kg/mol, the kinetics of dewetting of PS on the silicon surface under the electric field was retarded. Figure 5.15 shows an SEM image of the film surface where circular rings are observed with some structures within them, while no structures are present outside these rings. These rings result from the PMMA dewetting from the PS. The circular dewetting ring pattern is reminiscent of nucleation and growth dewetting. During dewetting, the PMMA receding layer has a thicker rim as can be seen in the image and, hence, magnifies the electric field due to the height and curvature associated with the front. This amplifies the instability at PS/PMMA interface which nucleates the dewetting of PS from the silicon wafer and give structures as observed in Figure 5.16a. The PMMA rim continues to recede and the structures are generated along the way, hence no structures are formed outside the rings. The PMMA forms a wetting layer on the exposed silicon wafer after the PS has dewetted thus forming mounds around the PS pillars as seen in Figure 5.16b.

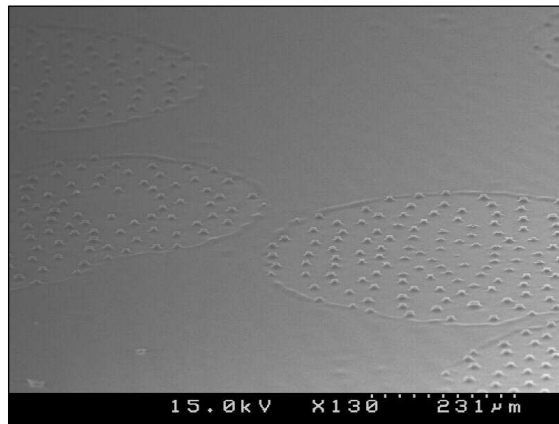


Figure 5.15: PMMA dewetting determines the regions where pillars form for a sample consisting of 32 kg/mol PMMA on 157kg/mol PS.

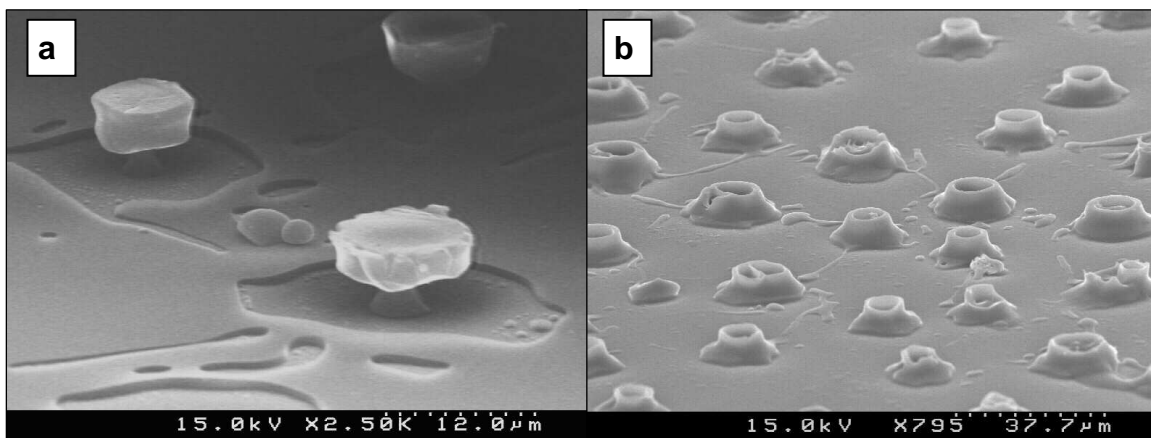


Figure 5.16: 32 kg/mol PMMA on 157 kg/mol PS. (a) Acetic acid rinse reveals PS cores and a residual PS film. (b) Cyclohexane rinse reveals complementary PMMA bases with no residual layer.

The importance of the PS dewetting in determining the final structure was proven by first coating the substrate with gold, a wetting surface for PS. Under identical processing conditions as those described within this section, the PMMA formed pillars on top of the underlying PS film. Thus, when the substrate is wetting, the formation mechanism is similar to that proposed in Figure 5.1 (although with the materials reversed), but when the underlying film can rapidly dewet, the mechanism is consistent with that shown in Figure 5.12.

5.3.4 Summary

Electrohydrodynamic instabilities in polymer thin films were studied in which a higher dielectric constant polymer film was sandwiched between two lower dielectric constant fluids. Along with the electrostatic forces, the dewetting forces at two of the interfaces played a major role in the type of structures obtained. The size and spacing of the structures are controlled by the electrostatic forces while the dewetting kinetics

dictated the interface at which the instabilities were grown. When a low molecular weight PS was used, the PS/PMMA interface was destabilized, leading to the formation of novel structures. Pillars were formed, spanning the air gap, with a PS core and a PMMA sheath. By selectively removing the PS core, hollow structures can be obtained that are difficult to produce by other existing techniques.

5.4 CONCLUSIONS

This chapter illustrated the importance of the order of the PS / PMMA film stack as well as the wetting properties of the electrodes in determining the final morphology of the electrohydrodynamically induced structures. In the PMMA / PS / air trilayer, a sheath of PMMA grows up around a core of PS. If the upper electrode is wetting to the PMMA, the PMMA will encapsulate the PS core. Cage like structures are formed when the PMMA sheath breaks into fingering instabilities. In the case of the PS / PMMA / air trilayer, the final structures have a PS core with a PMMA shell. These methods offer a simple route to forming hierarchical structures that would be challenging to produce by traditional fabrication methods.

5.5 REFERENCES

1. Schaffer, E.; Thurn-Albrecht, T.; Russell, T. P.; Steiner, U., Electrohydrodynamic instabilities in polymer films. *Europhysics Letters* **2001**, 53, (4), 518-524.
2. Morariu, M. D.; Voicu, N. E.; Schaeffer, E.; Lin, Z.; Russell, T. P.; Steiner, U., Hierarchical structure formation and pattern replication induced by an electric field. *Nature Materials* **2003**, 2, (1), 48-52.
3. Leach, K. A.; Gupta, S.; Dickey, M. D.; Willson, C. G.; Russell, T. P., Electric field and dewetting induced hierarchical structure formation in polymer/polymer/air trilayers. *Chaos* **2005**, 15, (4), 047506/1-047506/5.

4. Dickey, M. D.; Gupta, S.; Leach, K. A.; Collister, E.; Willson, C. G.; Russell, T. P., Novel 3-D Structures in Polymer Films by Coupling External and Internal Fields. *Langmuir* **2006**, 22, (9), 4315-4318.
5. Reiter, G., Dewetting of Thin Polymer-Films. *Physical Review Letters* **1992**, 68, (1), 75-78.
6. Schaffer, E.; Thurn-Albrecht, T.; Russell, T. P.; Steiner, U., Electrically induced structure formation and pattern transfer. *Nature* **2000**, 403, (6772), 874-877.
7. Lin, Z. Q.; Kerle, T.; Russell, T. P.; Schaffer, E.; Steiner, U., Structure formation at the interface of liquid liquid bilayer in electric field. *Macromolecules* **2002**, 35, (10), 3971-3976.
8. Lin, Z. Q.; Kerle, T.; Russell, T. P.; Schaffer, E.; Steiner, U., Electric field induced dewetting at polymer/polymer interfaces. *Macromolecules* **2002**, 35, (16), 6255-6262.
9. Qu, S.; Clarke, C. J.; Liu, Y.; Rafailovich, M. H.; Sokolov, J.; Phelan, K. C.; Krausch, G., Dewetting dynamics at a polymer-polymer interface. *Macromolecules* **1997**, 30, (12), 3640-3645.
10. Wyart, F. B.; Martin, P.; Redon, C., Liquid-Liquid Dewetting. *Langmuir* **1993**, 9, (12), 3682-3690.
11. Harris, M.; Appel, G.; Ade, H., Surface morphology of annealed polystyrene and poly(methyl methacrylate) thin film blends and bilayers. *Macromolecules* **2003**, 36, (9), 3307-3314.
12. Troian, S. M.; Herbolzheimer, E.; Safran, S. A.; Joanny, J. F., Fingering Instabilities of Driven Spreading Films. *Europhysics Letters* **1989**, 10, (1), 25-30.
13. Fox, T. G.; Flory, P. J., 2nd-Order Transition Temperatures and Related Properties of Polystyrene.1. Influence of Molecular Weight. *Journal of Applied Physics* **1950**, 21, (6), 581-591.
14. Lin, Z. Q.; Kerle, T.; Baker, S. M.; Hoagland, D. A.; Schaffer, E.; Steiner, U.; Russell, T. P., Electric field induced instabilities at liquid/liquid interfaces. *Journal of Chemical Physics* **2001**, 114, (5), 2377-2381.
15. Pease, L. F.; Russel, W. B., Linear stability analysis of thin leaky dielectric films subjected to electric fields. *Journal of Non-Newtonian Fluid Mechanics* **2002**, 102, (2), 233-250.

16. Verma, R.; Sharma, A.; Kargupta, K.; Bhaumik, J., Electric field induced instability and pattern formation in thin liquid films. *Langmuir* **2005**, 21, (8), 3710-3721.

Chapter 6

Low Viscosity Photocurable Pillar Arrays Formed Via Electric Field Assisted Assembly

Low viscosity, photocurable liquids are demonstrated as ideal materials for the formation of pillar arrays generated spontaneously by electric field-assisted assembly. Conventional polymer films form pillars slowly due to their relatively large viscosities and are often process limited by a requirement of heat to modulate rheological properties. In contrast, low viscosity liquids require no heat and form pillars orders of magnitude faster, as predicted by theory. The resulting structures are preserved by photopolymerization, eliminating the lengthy heating-cooling cycle necessary to process most polymers. The combination of nearly instantaneous formation and rapid photocuring at room temperature is ideal for patterning. Epoxy, vinyl ether, acrylate, and thiol-ene systems were evaluated for pillar formation. Relevant material properties were characterized (viscosity, dielectric constant, interfacial energy, kinetics) to explain the phenomenological behavior of each system during electrohydrodynamic patterning. The thiol-ene system formed pillar arrays nearly instantaneously and cured rapidly under ambient conditions, ideal characteristics for pillar formation. This work has been published.¹

6.1 BACKGROUND

Electrohydrodynamic patterning requires a fluid material during pillar formation and a mechanism to lock the structures into place post-formation. In prior work, pillars have only been formed with polymer films, such as polystyrene, poly(methyl methacrylate), and polyisoprene.²⁻¹⁰ With polymeric materials, structure formation is accomplished using heat to modulate the rheological properties of the material. The polymer must be first heated above the T_g to allow the polymer to flow and subsequently cooled to preserve the electric field induced structures. The time scale of formation can be lengthy due to high melt-viscosities and the accompanying heating-cooling cycle. Heating also limits the ability to predictably control the characteristic spacing due to distortion of geometry and thermal flux.^{11,12} Linear stability analysis, introduced in Chapter 4, predicts that replacing polymeric films with liquids reduces the time scale of pillar formation by several orders of magnitude, due to the substantial decrease in viscosity. Even when heated, many of the polymers studied to date have viscosities two to six orders of magnitude higher than the materials reported in this work.^{10,13}

Photocurable liquids eliminate the heating-cooling cycle since the structures are fixed by photocuring. The photocuring process produces mechanically stable cross-linked polymeric columns. In many patterning applications, it is desirable to leave no residual material between patterned features. In contrast to polymeric pillars⁶, photocurable liquids generally leave very little residual material between the pillars (for example, see Figure 6.5). This is likely due to a combination of viscous and surface effects, both of which factor into surface wetting dynamics. The advantages of photocurable pillars are summarized in Table 6.1.

Table 6.1: Advantages of Low-Viscosity Photocurable Materials for Each Processing Step.

| Processing Step | Polymeric Pillars | Photocurable Pillars |
|---------------------|---------------------------------------|---------------------------------------|
| Sample preparation | Heat film above T _g | Room temperature |
| Apply e-field | High viscosity, slow pillar formation | Low viscosity, rapid pillar formation |
| Solidify structures | Cool sample below T _g | Rapid photopolymerization |
| Processing time | Hours | Seconds |
| Final Structures | Residual material between pillars | No residual material between pillars |

In this chapter, the behavior of various photopolymerizable systems under electrohydrodynamic conditions is investigated. Initial material selection criteria were based upon several processing requirements. The material must form a film that remains stable for the duration of the experiment, but form pillars rapidly when exposed to the electric field. Thus, the material should be non-volatile, yet have a relatively low viscosity (~ 1 Pa's). The material must photo-polymerize rapidly, requiring highly reactive molecules with high mobility. Molecules with multi-functionality were favored to ensure mechanical stability of the columnar structures upon curing. Preference was given to commercially available materials because of their accessibility. A variety of photocurable reaction mechanisms and functional groups were auditioned. These materials were chosen to represent a range of physical properties such as surface energy, viscosity, and dielectric constant. This study provides a basis for future rational material selection for photocurable electrohydrodynamic patterning.

6.2 MATERIALS AND METHODS

The materials studied are illustrated in Figure 6.1. Acryloxy terminated polydimethylsiloxane (“DMS”) was purchased from Gelest (Morrisville, PA). Tris [4-(vinylloxy)butyl] trimellitate (“Vinyl Ether”), Pentaerythritol tetrakis(3-mercaptopropionate) (“Thiol”), Di(trimethylolpropane) tetraacrylate (“Acrylate”), and 3,4-Epoxy cyclohexylmethyl 3,4-epoxycyclohexanecarboxylate (“CHO Epoxy”) were purchased from Aldrich (Milwaukee, WI). Bisphenol A diglycidyl ether (“Epon Epoxy”, Epon 828) was purchased from Polysciences (Warrington, PA). The following materials were generously donated by their manufacturers: Darocur 4265 initiator (CIBA, Basel, Switzerland) and Cyacure Photoinitiator UVI-6992 (Dow / Union Carbide, Houston, TX).

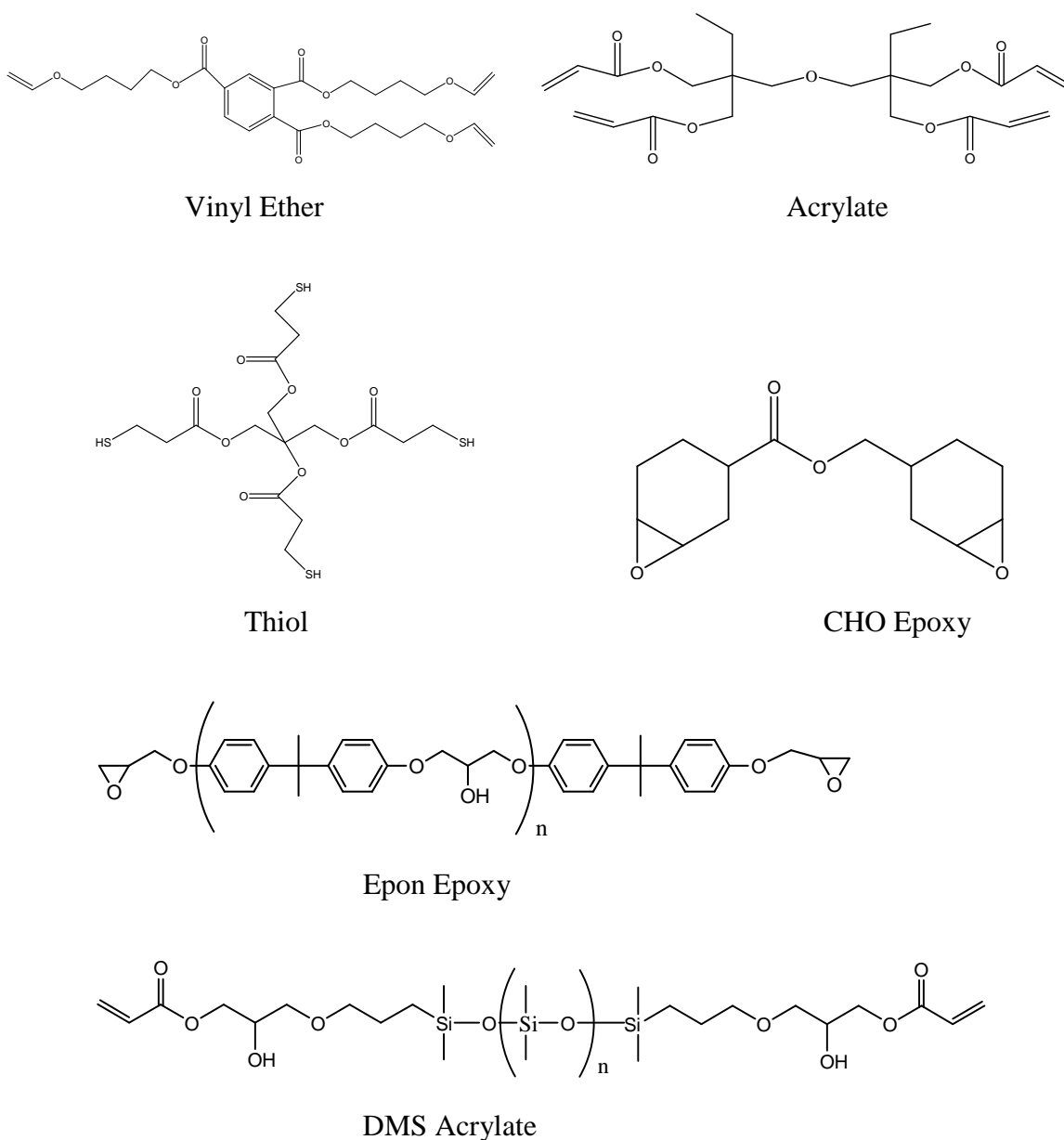


Figure 6.1: Functional materials studied.

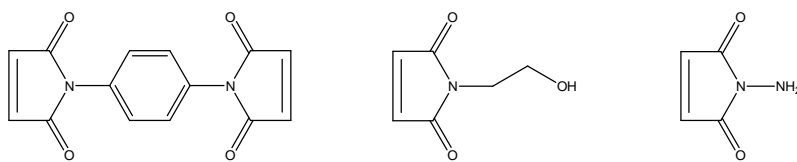
Solutions were formulated to produce a ~800 nm film under reasonable spin casting conditions (2000-3500 rpm). Film thicknesses were measured by ellipsometry (Woollam WVASE32) and profilometry (Tencor Alpha-Step 200). A list of the material classes studied and the formulations for each class are shown in Table 6.2.

Table 6.2: Materials Formulations (wt%)

| Material Class | Component 1 | Component 2 | Initiator | Reaction Mechanism |
|-------------------|-----------------|-------------------|----------------|--------------------------|
| Thiol-Vinyl Ether | 17.5% Thiol | 17.5% Vinyl Ether | --- | Step Radical |
| Vinyl Ether | 30% Vinyl Ether | --- | 5% Cyracure | Cationic |
| Thiol-Acrylate | 17.5% Thiol | 17.5% Acrylate | --- | Step Radical |
| Acrylate (DMS) | 25% DMS* | ---- | 5% Darocur | Radical |
| Epoxy | 17.5% Epon | 17.5% CHO | 5% Cyracure | Ring Opening Cationic |

* The DMS was formulated in toluene, all others in PGMEA casting solvent

In addition to the material classes listed in Table 6.2, other photocurable materials were considered. Derivatives of cinnamic acid are known to undergo [2+2] photodimerization, an appealing reaction because of its reversibility and insensitivity to ambient oxygen. A difunctional cinnamate was synthesized by reacting 4,8-Bis(hydroxymethyl) tricyclo[5.2.1.0.2.6] decane with an excess of cinnamoyl chloride. Unfortunately the time to sufficiently crosslink the material was found to be on the order of an hour, consistent with other studies on polymers with pendant cinnamate groups.^{14,15} This increase in processing time off-set one of the biggest advantages of using photocurable materials and thus cinnamates were removed from consideration. Maleimides, another common photocurable material, were also preliminarily investigated. Maleimides can act both as photoinitiators and as comonomers with various donor monomers including vinyl ethers. Various monofunctional and difunctional maleimides were synthesized, but were found to be solids that were insoluble in the vinyl ether comonomers and thus inappropriate for this study. Representative maleimide structures are shown on the following page.



Surface energies were measured using a Rame-Hart Goniometer in pendant drop mode. The images from this instrument were analyzed using FTA2000, a software package donated by First Ten Ångströms. The dielectric constant was measured at room temperature using a Hewlett-Packard Impedance Analyzer (HP 4192A) with a Hewlett-Packard dielectric test fixture (HP 16451B) over three capacitor gaps. The viscosity was measured using a cone and plate rheometer (Physica MCR 300, 1° cone Anton Paar part #79040) at room temperature, calibrated with an oil of known viscosity.

The kinetics of polymerization were measured for each materials system using real time – Fourier transform infrared spectroscopy (RTIR, Nicolet Magna-IR 550). RTIR utilizes *in situ* IR measurements to track the disappearance of functional groups during photo curing.¹⁶ The IR was operated at 4 cm⁻¹ resolution and 4 scans per spectrum with a collection time of 1.5 seconds per spectrum. Samples were prepared by spin casting films on aluminum backed, double polished silicon wafers. The films were irradiated with a mercury lamp (EFOS Novacure) at 3.5 mW/cm², an intentionally low intensity such that differences in the kinetics could easily be contrasted. The relative functional group concentration was determined by measuring peak height as a function of time.

6.3 EXPERIMENTAL PROCEDURE

Pillars were formed using a custom built machine designed for studying electrohydrodynamic instabilities, henceforth referred to as the active gap tool. A

schematic of the active gap tool is shown in Figure 6.2. This tool, which will be described in greater detail in Chapter 8, utilizes servo motors to position an optically flat quartz template parallel to a silicon wafer that is held stationary by a grounded vacuum chuck. White light interferometry was used to measure and control the air gap between the wafer and the quartz template. The interferometer also measures the film thickness, providing a valuable tool for measuring the approximate time scale of pillar formation. The quartz template was coated with a thin layer of indium-tin-oxide by e-beam evaporation to provide a transparent, conducting surface. The templates were surface treated by silylation (Chapter 9) to aid release of the pillars from the upper electrode after curing. Load cells in the tool were used to measure the pillar-electrode release force.

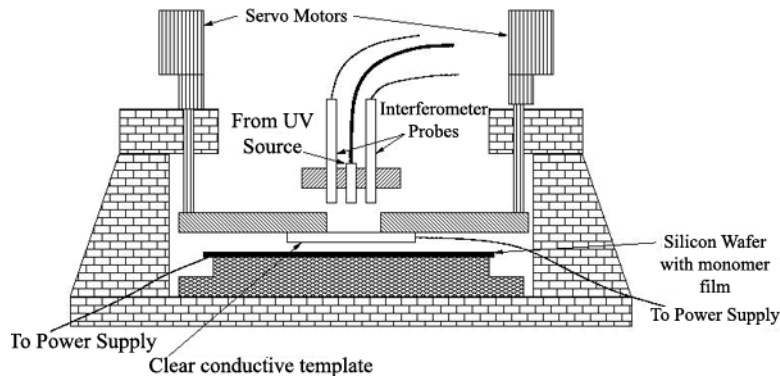


Figure 6.2: Active gap tool schematic. Three interferometer probes are used to non-invasively measure the gap between the template and substrate. Servo motors actively position the template until planarity is achieved using feedback from the probes.

Doped silicon wafers were used as substrates for the films and the total substrate to upper electrode gap was set to $\sim 3 \mu\text{m}$. The gaps, measured by interferometry in real-time, were verified by measuring the final pillar heights using scanning electron microscopy (SEM) analysis. Once the gap was set using the active gap tool, pillars were

formed by applying 40 V across the electrodes for two minutes before curing the sample by exposure with a mercury lamp (EFOS Novacure) for two minutes.

In addition to the aforementioned tool, the technique described in Chapter 4 was also utilized to study pillar formation, an approach used by many other groups who study electrohydrodynamic instabilities.^{2,3,6-8} This method relies on a physical spacer to create the capacitor gap. Spacers were created by etching a recess into a glass slide and depositing a thin layer of metal to create the electrode. The disadvantage of this method is that the spacer contacts the film, disrupting an otherwise smooth surface. Despite this disadvantage, this method was used for monitoring the formation of pillars *in-situ* using optical microscopy, an option unavailable on the active gap tool due to geometry restrictions.

6.4 RESULTS AND DISCUSSION

The properties of the primary materials studied are summarized in Table 6.3. The viscosity spans an order of magnitude and the surface energy varies by a factor of two across the materials, as does the dielectric constant. Most of the materials have a relatively high dielectric constant, a trait that is favorable for pillar formation since it increases the destabilizing electrostatic force. The relatively low viscosity of the materials is also favorable for pillar formation since the time scale of formation is proportional to viscosity.

Table 6.3: Material Properties

| Material | Viscosity (Pa's) | Surface Energy (dyn/cm) | Dielectric Constant |
|-------------------|---------------------|----------------------------|------------------------|
| Thiol-Vinyl Ether | 0.471 | 40.0 | 8.55 |
| Vinyl Ether | 0.286 | 39.5 | 7.92 |
| Thiol-Acrylate | 0.593 | 34.8 | 9.89 |
| DMS Acrylate | 0.101 | 20.8 | 3.91 |
| Epoxy | 1.786 | 45.2 | 10.41 |

Polymerization kinetics for each material are shown in Figure 6.3. As expected, the DMS has extremely slow cure kinetics since the radical mechanism by which it cures is strongly inhibited by oxygen.^{17,18} Pillars have a high surface area to volume ratio, making them particularly susceptible to inhibition by oxygen diffusion during irradiation well after the initial dissolved oxygen is consumed. The epoxy system also cured slowly. Although epoxies are generally very reactive, the high viscosity of the epoxy formulation limits the kinetic rate. In highly viscous systems, it is difficult for reactive centers to find unreacted functional groups to propagate the polymerization.

The vinyl ether polymerizes via a cationic mechanism and has the fastest polymerization kinetics of all the materials studied. The low viscosity of the material combined with the relatively large functional group concentration results in a rapid polymerization. The thiol-vinyl ether and thiol-acrylate polymerization proceed at a very similar rate, as seen in Figure 6.3. The reaction proceeds via a free-radical step growth mechanism, in which a thiyl radical first inserts into the ene, followed by hydrogen abstraction from another thiol to generate a new thiyl radical.¹⁹ The presence of the thiol acts like a chain transfer agent and reduces the deleterious effects of oxygen seen in traditional radical systems. The thiol does not proceed to the same extent of conversion as the acrylate or vinyl, implying that the enes homopolymerize. Although virtually any

ene will participate in the free radical reaction with thiol, vinyl ethers and acrylates were chosen because of their commercial availability, viscosity, and relatively high reactivity. These systems are particularly interesting because they do not require an initiator, resulting in a simplified formulation.²⁰⁻²²

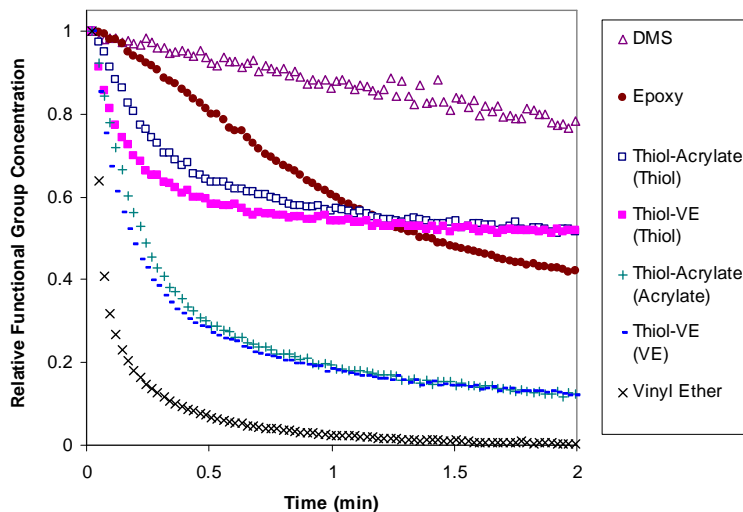


Figure 6.3: RTIR kinetic profile for each material system, representing the consumption of each respective functional group with time due to polymerization. (3.5 mW/cm²)

As expected, all of the materials studied formed pillars rapidly under the influence of the electric field. The thiol-vinyl ether exhibited the best characteristics for pillar formation. An example top-down optical micrograph of thiol-vinyl ether pillars is shown in Figure 6.4. The average pillar diameter was 17.8 μm as determined using Scion[®] image analysis software. The characteristic spacing was found to be $\sim 30 \mu\text{m}$ using 2-dimensional fast Fourier Transform. Linear stability analysis predicts the characteristic spacing of the fastest growing mode to be $\sim 40 \mu\text{m}$ for these conditions (gap 2.5 μm). Although the difference between experimental and theoretical values is within

experimental error, the smaller experimental value could be indicative of a leaky dielectric.^{5,10}

Based on *in-situ* growth observations, pillars formed either instantaneously or within seconds, with the exception being the epoxy which took 30-60 seconds to form. The center-to-center spacing of the resulting structures closely matched the spacing of the initial undulations induced by the electric field. However, pillar growth was somewhat stochastic as fluctuations did not grow into columns simultaneously, consistent with observations by Leach et al.²³ In addition to the observed spinodal instabilities, there was also evidence of nucleated growth. This observation is consistent with experiments and modeling done by other groups on polymeric systems.^{2,3,6-8,24} In nucleated growth, a pillar initially forms at a nucleation site, followed by growth of concentric rings of pillars. In a similar type of phenomenon, growth fronts were observed initiating near edges. Sharp spatial gradients in the electrostatic force at the electrode edge cause this nucleation, as predicted by modeling.²⁴ These fronts typically propagate toward the center of the sample until they impinge another growth region. As a result, there were regions with local hexagonal close-packed order, but no long range order. The lack of long range order in photocurable systems is consistent with published images of polymeric pillars.^{2-4,6-8,23,25,26} In agreement with theory²⁴, local ordering was best towards the electrode edges, as shown in Figure 6.4b. It appears that packing occurs due to the rings of depleted material surrounding each pillar and by the nature of the spinodal instability.

Although low viscosity films form uniform pillars rapidly, the resulting structures are only in a local energy minima. The overall energy of the system can be lowered by pillars merging. A few merged pillars (less than 1%) can be seen in Figure 6.4. This tendency is minimized by the use of thiol-vinyl ether, and was worst with DMS due to its

low viscosity and surface energy. Obviously, the merging of pillars can be minimized by reducing the lag time between pillar formation and photocuring. Modeling has shown that pillar coalescence is largely a function of the air gap to film thickness ratio, where values greater than 3 form quasi-stable columns.²⁴ This ratio was ~ 4 in all of the experiments performed in this study, thus coalescence was not favored. Despite this favorable configuration, a number of factors could lead to pillar agglomeration: heterogeneities on the electrode surface, liquid bridges between structures resulting from residual material, pillar to pillar contact due to upper electrode wetting, and distortions of the electric field resulting from structure formation. In the case of a wedged capacitor geometry, the pillars could move to minimize interfacial energy. This was ruled out as a possibility based on real-time monitoring of pillar formation since the pillars did not move in concert in any one direction.

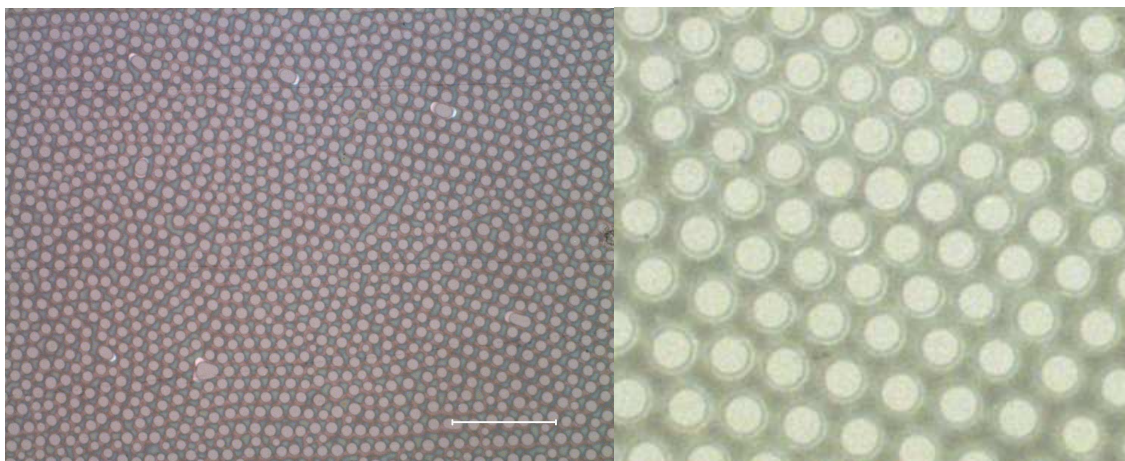


Figure 6.4: Optical micrograph of thiol-vinyl ether pillars. (a) Overview of pillars shows local order, but lacks long range order (scale bar 200 μm). (b) Enlarged view of local order near electrode edge (width of image $\sim 250 \mu\text{m}$).

The presence of residual material between pillar structures can be seen via optical microscopy and via cross-section SEM. All of the materials studied left little to no

residual material. Figure 6.5 shows the cleaved edge of a silicon substrate and the edge of a pillar can be seen in the upper left corner. No residual layer exists surrounding the base of the pillar, a trait that is highly favorable for transferring patterns to the underlying substrate. The epoxy was the only material that left a significant residual layer between structures. The exact reasons for this are unclear, although the larger resistance to flow at the silicon-film interface due to the higher viscosity of the epoxy is likely a factor.

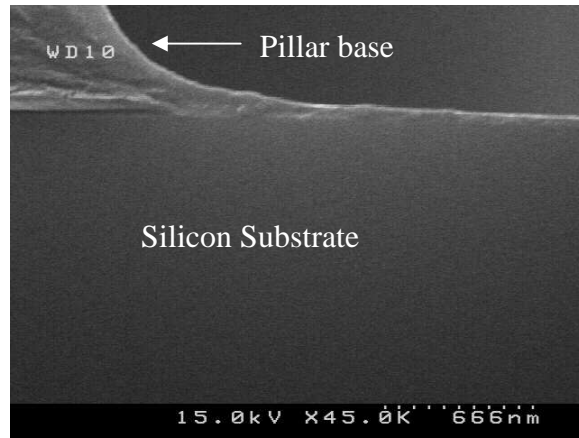


Figure 6.5: SEM close up on cleaved pillar on top of a cleaved silicon substrate, which reveals the extremely small residual layer surrounding the pillar.

In the following section, the advantages and disadvantages of each materials class will be discussed, with a particular focus on the effects of material properties on pillar formation.

6.4.1 Epoxy

The epoxy had the most processing limitations of all the materials studied. The high viscosity caused the pillars to form slowly (30-60 seconds) and cure slowly as seen in Figure 6.3. The epoxy only cures using sub-300 nm UV-light due to the absorbance characteristics of the photoacid generator (PAG), adding additional requirements to the

exposure source and UV transparent template. As previously discussed, the epoxy pillars had an unusually large amount of residual material between structures. The epoxies also displayed the largest separation force required to release the pillars from the upper electrode (~30 lbs versus ~12 lbs for the other materials). This was not surprising since epoxies are often used as adhesives.

6.4.2 Vinyl Ethers

Vinyl ethers are appealing because they photocure rapidly and the cationic polymerization mechanism is insensitive to oxygen.²⁷ However, they can be inhibited by ambient species such as moisture and base. Unfortunately, most commercially available vinyl ethers are volatile, and therefore do not form stable films.¹⁶ The few vinyl ethers that are capable of forming stable films tend to have limited ability to dissolve PAGs necessary for initiating the cationic mechanism. Over ten different PAGs, including common PAGs such as Triphenylsulfonium SbF₆ and bis-p-t-butyl phenyl iodonium triflate, were screened for compatibility and none were readily soluble in the vinyl ether. The Cyacure initiator used in this system is a liquid, formed by dissolving a PAG into a solvent. Therefore, the possibility of the PAG coming out of solution during spin casting exists, but did not appear to be a problem since the spin cast films were smooth. However, there was evidence of instability over a period of a few days,

The vinyl ether films formed pillars very rapidly (~5 seconds). During separation, the pillars underwent cohesive failure rather than adhesive failure, resulting in rough and distorted features. Residue remained on the template (both ITO and Cr electrodes) despite surface treatment. This residue could not be removed by UV-ozone treatment or oxygen plasma, ultimately destroying the templates. The residue on the template affected subsequent experiments, causing pillars to migrate due to

heterogeneities of the surface energy. X-ray photoelectron spectroscopy analysis of the contaminated surface revealed the presence of atomic species from the PAG.

6.4.3 Acrylates

As expected, the acrylates formed pillars very rapidly (< 1 second) due to the low viscosity of the DMS material. The acrylate pillars also had the largest variation of pillar diameter, largely due to their tendency to migrate and merge after forming. The combination of low viscosity and low surface energy allowed the DMS to have high mobility prior to curing. The result is an array of pillars with many different diameter (i.e. polydisperse). *In-situ* growth observation confirmed that the PDMS pillars form with a uniform diameter, but rapidly merge to form larger pillar agglomerates.

The biggest disadvantage of using an acrylate system is that the radical polymerization mechanism is oxygen sensitive.^{17,18} Curing the structures requires either inerting or an intense irradiation dose. These multiple processing constraints make acrylates unappealing for processing.

6.4.4 Thiol-ene

Thiol-ene systems are desirable because they are insensitive to base and oxygen. The addition of a thiol to an ene (acrylate, vinyl ether, etc.) reduces the sensitivity to oxygen by acting as a chain transfer agent. Thus, the reaction mechanism for thiol-ene systems involves a step reaction using free radicals generated by irradiation, although the system does not require initiator.²⁰⁻²² Thiol-ene systems have been studied for many years,²⁸⁻³⁰ but there has been a recent surge of interest in these materials due to their many desirable properties.³¹ Both the thiol-acrylate and thiol-vinyl ether materials

performed well during pillar formation. They formed pillars rapidly (<5 seconds) and cured rapidly. One disadvantage of the thiol-acrylate system is that thin films require sub-300 nm irradiation to cure. Bulk thiol-acrylate cures rapidly with light above 300 nm, however thin films only cure when protected from the ambient air by a cover slip. The implication is that when >300 nm light is used for photocuring, radicals are generated at an insufficient rate to keep up with inhibition by diffusing oxygen. Cramer et al. demonstrated that thiol-ene photopolymerizations proceed more readily at sub-300 nm wavelengths and undergo a wavelength dependent initiation process.^{21,22} This wavelength restriction can be avoided by adding a radical initiator (e.g. Darocur 4265), which detracts from the elegance of the initiator-less system. It should be noted that adding initiator (~ 5 wt%) to either of the thiol-ene systems dramatically increases the rate of polymerization (~ 6 seconds to reach 80% conversion versus ~ 45 seconds in the initiator-less system).

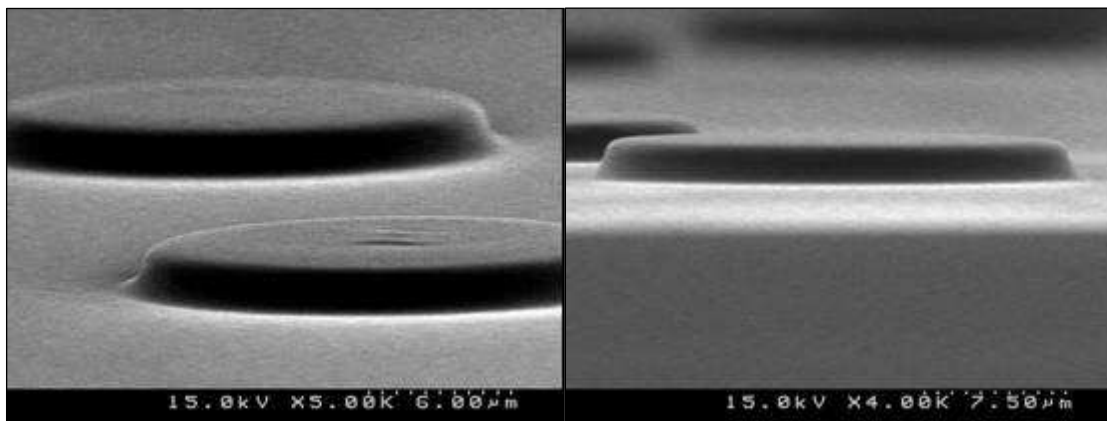


Figure 6.6: Tilt-view SEMs of thiol-vinyl ether pillars.

Figure 6.6 is an SEM image of the thiol-vinyl ether pillars, in which the pillars measure approximately $2.5\ \mu\text{m}$ tall with a diameter of $17\ \mu\text{m}$. Again, a residual layer is undetectable, implying that all the material gets drawn into the columns. In general, the

thiol-vinyl ether displayed the most ideal properties for pillar formation of all the materials studied. The thiol-vinyl ether cured at both sub-300 nm and >300 nm light, implying it is less sensitive to oxygen, which is consistent with vinyl ethers being one of the most reactive ene species in thiol-ene systems.³¹ In addition to rapid pillar formation and curing, the thiol-vinyl ether system showed almost no pillar merging tendencies under any conditions. This is rather remarkable considering the material properties of the thiol-vinyl ether do not differ greatly from the other materials studied. Electrochemistry might be playing a roll in the curing process, ultimately reducing the mobility of the thiol-vinyl ether by inducing polymerization when the material spans the electrodes. A small current ($\sim 25 \text{ uA/cm}^2$) was detected during pillar formation, but this was not unique to the thiol-vinyl ethers. However, the thiol-vinyl ether pillars did cure in the absence of light when applied to a 40 V potential for five minutes. None of the other materials displayed this property. The mechanism is unclear, but preliminary cyclic voltametry studies show that the thiol rapidly forms disulfide bonds at low voltages ($<1 \text{ V}$), which points to a potential source of electrically generated radicals. This inadvertent, yet fortuitous property of the thiol-vinyl ether allows the pillars to be cured in the absence of light and minimizes the post-formation coalescence.

The only observed drawback of the thiol-ene system is that the solutions are unstable. They oligomerize in the absence of light on the time scale of days. To keep consistent performance, fresh solutions must be made frequently or an inhibitor must be added to the casting solutions.

6.5 CONCLUSIONS

The ability to form arrays of pillars using photocurable materials was demonstrated. The pillars form at room temperature and the time scale of formation is

orders of magnitude faster than high T_g polymers (seconds vs. hours). A number of photopolymerizable materials with a variety of material properties were investigated. The thiol-vinyl ether displayed many desirable properties for pillar formation. It forms pillars nearly instantaneously with minimal coalescence, cures rapidly without an initiator, and is insensitive to ambient species.

6.6 REFERENCES

1. Dickey, M. D.; Collister, E.; Raines, A.; Tsiartas, P.; Holcombe, T.; Sreenivasan, S. V.; Bonnecaze, R. T.; Willson, C. G., Photocurable Pillar Arrays Formed via Electrohydrodynamic Instabilities. *Chemistry of Materials* **2006**, 18, (8), 2043-2049.
2. Schaffer, E.; Thurn-Albrecht, T.; Russell, T. P.; Steiner, U., Electrohydrodynamic instabilities in polymer films. *Europhysics Letters* **2001**, 53, (4), 518-524.
3. Lin, Z.; Kerle, T.; Baker, S. M.; Hoagland, D. A.; Schaffer, E.; Steiner, U.; Russell, T. P., Electric field induced instabilities at liquid/liquid interfaces. *Journal of Chemical Physics* **2001**, 114, (5), 2377-2381.
4. Lin, Z.; Kerle, T.; Russell, T. P.; Schaeffer, E.; Steiner, U., Structure Formation at the Interface of Liquid/Liquid Bilayer in Electric Field. *Macromolecules* **2002**, 35, (10), 3971-3976.
5. Pease, L. F.; Russel, W. B., Linear stability analysis of thin leaky dielectric films subjected to electric fields. *Journal of Non-Newtonian Fluid Mechanics* **2002**, 102, (2), 233-250.
6. Schaffer, E.; Thurn-Albrecht, T.; Russell, T. P.; Steiner, U., Electrically induced structure formation and pattern transfer. *Nature* **2000**, 403, (6772), 874-877.
7. Chou, S. Y.; Zhuang, L., Lithographically induced self-assembly of periodic polymer micropillar arrays. *Journal of Vacuum Science & Technology, B: Microelectronics and Nanometer Structures* **1999**, 17, (6), 3197-3202.
8. Chou, S. Y.; Zhuang, L.; Deshpande, P.; Chen, L.; Sun, X., Lithographically-induced self-assembly of periodic micro-pillar arrays in a single homopolymer film. *Polymer Preprints (American Chemical Society, Division of Polymer Chemistry)* **2000**, 41, (1), 78.
9. Pease, L. F.; Russel, W. B., Electrostatically induced submicron patterning of thin perfect and leaky dielectric films: A generalized linear stability analysis. *Journal of Chemical Physics* **2003**, 118, (8), 3790-3803.

10. Pease, L. F., III; Russel, W. B., Limitations on Length Scales for Electrostatically Induced Submicrometer Pillars and Holes. *Langmuir* **2004**, 20, (3), 795-804.
11. Schaffer, E.; Harkema, S.; Roerdink, M.; Blossey, R.; Steiner, U., Thermomechanical lithography: pattern replication using a temperature gradient driven instability. *Advanced Materials* **2003**, 15, (6), 514-517.
12. Schaffer, E.; Harkema, S.; Blossey, R.; Steiner, U., Temperature-gradient-induced instability in polymer films. *Europhysics Letters* **2002**, 60, (2), 255-261.
13. Leach, K. A.; Gupta, S.; Dickey, M. D.; Willson, C. G.; Russell, T. P., Electric field and dewetting induced hierarchical structure formation in polymer/polymer/air trilayers. *Chaos* **2005**, 15, (4), 047506/1-047506/5.
14. Lendlein, A.; Jiang, H.; Juenger, O.; Langer, R., Light-induced shape-memory polymers. *Nature* **2005**, 434, (7035), 879-882.
15. Ali, A. H.; Srinivasan, K. S. V., Photoresponsive functionalized vinyl cinnamate polymers: synthesis and characterization. *Polymer International* **1997**, 43, (4), 310-316.
16. Decker, C., Kinetic study and new applications of UV radiation curing. *Macromolecular Rapid Communications* **2002**, 23, (18), 1067-1093.
17. Decker, C.; Jenkins, A. D., Kinetic approach of oxygen inhibition in ultraviolet- and laser-induced polymerizations. *Macromolecules* **1985**, 18, (6), 1241-4.
18. Dickey, M. D.; Burns, R. L.; Kim, E. K.; Johnson, S. C.; Stacey, N. A.; Willson, C. G., Study of the kinetics of Step and Flash imprint lithography photopolymerization. *AIChE Journal* **2005**, 51, (9), 2547-2555.
19. Jacobine, A. F., *Radiation Curing in Polymer Science and Technology III, Polymerization Mechanisms*. Elsevier Applied Science: London, 1993.
20. Cramer, N. B.; Davies, T.; O'Brien, A. K.; Bowman, C. N., Mechanism and Modeling of a Thiol-Ene Photopolymerization. *Macromolecules* **2003**, 36, (12), 4631-4636.
21. Cramer, N. B.; Scott, J. P.; Bowman, C. N., Photopolymerizations of Thiol-Ene Polymers without Photoinitiators. *Macromolecules* **2002**, 35, (14), 5361-5365.
22. Cramer, N. B.; Reddy, S. K.; Cole, M.; Hoyle, C.; Bowman, C. N., Initiation and kinetics of thiol-ene photopolymerizations without photoinitiators. *Journal of Polymer Science, Part A: Polymer Chemistry* **2004**, 42, (22), 5817-5826.
23. Leach, K. A.; Lin, Z.; Russell, T. P., Early Stages in the Growth of Electric Field-Induced Surface Fluctuations. *Macromolecules* **2005**, 38, (11), 4868-4873.
24. Verma, R.; Sharma, A.; Kargupta, K.; Bhaumik, J., Electric Field Induced Instability and Pattern Formation in Thin Liquid Films. *Langmuir* **2005**, 21, (8), 3710-3721.

25. Chou, S. Y.; Zhuang, L.; Guo, L., Lithographically induced self-construction of polymer microstructures for resistless patterning. *Applied Physics Letters* **1999**, 75, (7), 1004-1006.
26. Lin, Z.; Kerle, T.; Russell, T. P.; Schaeffer, E.; Steiner, U., Electric Field Induced Dewetting at Polymer/Polymer Interfaces. *Macromolecules* **2002**, 35, (16), 6255-6262.
27. Decker, C., The use of UV irradiation in polymerization. *Polymer International* **1998**, 45, (2), 133-141.
28. Morgan, C. R.; Magnotta, F.; Ketley, A. D., Thiol/ene photocurable polymers. *Journal of Polymer Science, Polymer Chemistry Edition* **1977**, 15, (3), 627-45.
29. Morgan, C. R.; Ketley, A. D., The effect of phosphines on thiol/ene curing systems. *Journal of Polymer Science, Polymer Letters Edition* **1978**, 16, (2), 75-9.
30. Morgan, C. R.; Ketley, A. D., The photopolymerization of allylic and acrylic monomers in the presence of polyfunctional thiols. *Journal of Radiation Curing* **1980**, 7, (2), 10-13.
31. Hoyle, C. E.; Lee, T. Y.; Roper, T., Thiol-enes: Chemistry of the past with promise for the future. *Journal of Polymer Science, Part A: Polymer Chemistry* **2004**, 42, (21), 5301-5338.

Chapter 7

Pillar Growth Mechanisms and Ordering

Linear stability analysis predicts that pillar arrays with predetermined diameter and characteristic spacing can be formed by controlling the surface tension and electrostatic forces acting at the film-air interface. The first part of this chapter discusses the applicability of linear stability analysis to low viscosity materials. Although pillars have a predictable characteristic spacing, they generally lack the long range order required for many practical applications. The second half of this chapter describes attempts at inducing long range order using (1) sinusoidal AC fields instead of the conventional DC bias, (2) ultrasonic piezo transducers to generate regular waves in the film prior to electric field amplification, and (3) patterned electrodes to guide the formation of the pillars. Initial results show that although both the AC fields and the ultrasonic piezo methods successfully produce pillar arrays, their ordering is short-ranged and does not extend throughout the entire sample area.

7.1 INTRODUCTION

Consistent with other instability driven phenomena, pillar arrays have a characteristic wavelength (defined as the center-to-center spacing of the pillars) but typically lack long range order. The characteristic wavelength is predicted by linear stability analysis in which the fastest growing mode is a function of the surface and electrostatic forces.¹⁻⁸ Linear stability analysis was derived in Chapter 4 and has been

verified in literature for polymeric systems.¹⁻⁹ The first part of this chapter will investigate the relevance of linear stability analysis for low viscosity systems. A Fast Fourier transform (FFT) method was developed to quantify the characteristic spacing and provide a qualitative measure of the long range order of the pillar arrays.

The natural spacing and order of the pillars can be modulated through the use of patterned electrodes containing protruding features such as posts. Pillars preferentially form under the protruding features presumably due to the locally enhanced electric field created by the narrowing of the capacitor gap. Although this technique was demonstrated, the use of a patterned electrode detracts from the elegance and simplicity of a non-patterned electrode system.

Two methods for improving long-range order using non-patterned electrodes were evaluated. First, the use of AC voltage at varying frequencies was investigated as a technique to improve order. Second, ultrasonic piezo transducers were used at various frequencies in the hope of inducing regular undulations in the film prior to pillar formation. The concept is similar to the Faraday waves that form when a liquid layer is placed on top of a vertically oscillating piston.

7.2 LINEAR STABILITY ANALYSIS OF LOW VISCOSITY FLUIDS

7.2.1 Background

Linear stability analysis predicts that the characteristic spacing between pillars is a function of the electrostatic and surface forces acting at the film-air interface. Linear stability analysis has been verified for polymeric systems,¹⁻⁹ but has not been studied for low viscosity systems. The theoretical characteristic spacing of a material should be independent of the viscosity and only dependent on factors that impact the strength of the

electrostatic force, such as the electrode gap, film height, and applied voltage. For example, altering the gap (while holding all other parameters constant) changes the strength of the electric field, resulting in an observable change in both the characteristic spacing and diameter of the pillars, as shown in Figure 7.1. Note that smaller electric fields that arise from larger electrode gaps, tends to leave residual material between the pillars (Figure 7.1a).

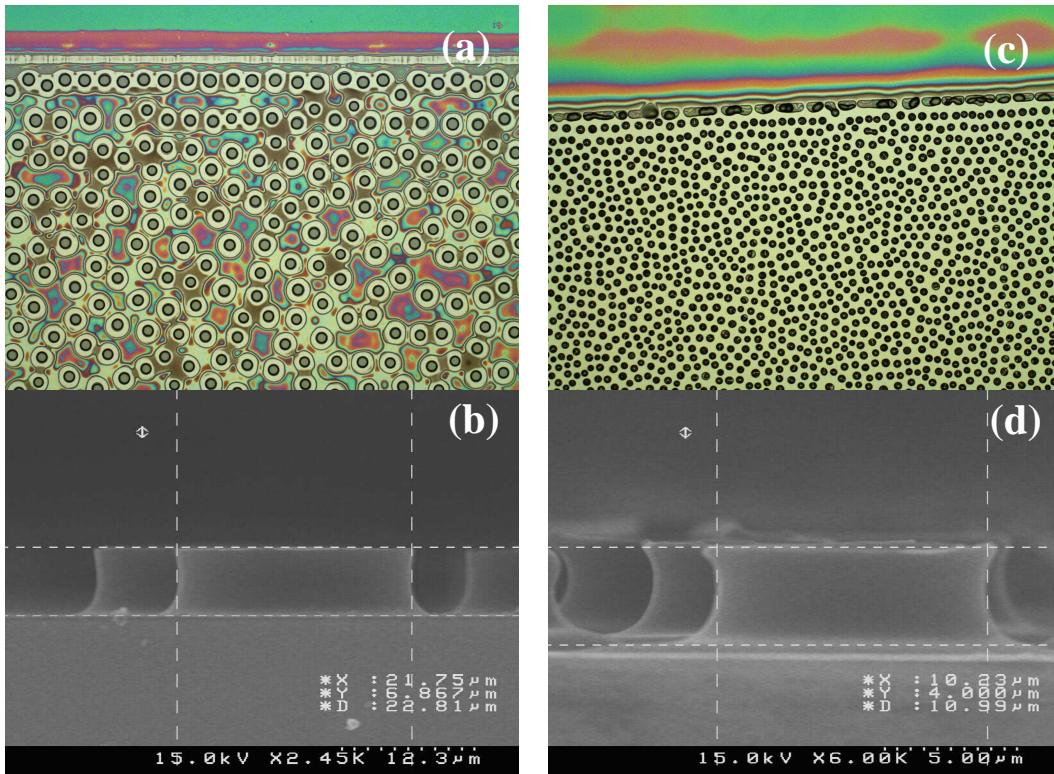


Figure 7.1: Example of the impact of changing the electrode gap on the pillars. Both samples started with 800 nm films and were exposed to 40 V. (a) Optical micrograph of pillars with a 6.9 μm electrode gap, as verified by SEM (b). (c) Optical micrograph of pillars with a 4.0 μm gap (d), resulting in a larger applied electric field and consequently shorter characteristic spacing.

The electrohydrodynamic behavior of low viscosity materials was systematically studied as a function of the adjustable processing parameters; film height, electrode spacing, and voltage.

7.2.2 Materials

Tris-(4-vinyloxybutyl)trimellitate (“ene”) and pentaerythritol tetrakis(3-mercaptopropionate) (“thiol”) were purchased from Aldrich and used as received. A solution consisting of a 1:1 (by weight) mixture of thiol-ene was spun cast onto doped silicon wafer substrates (functioning as the bottom electrode in the capacitor device) out of a PGMEA solvent. Three solutions of varying solvent concentration were formulated to produce 100, 800, and 1500 nm films. The film thickness was determined by ellipsometry.

7.2.3 Methodology

An experimental matrix was designed to study the effects of varying electrode spacing, applied voltage, and film thickness on the characteristic spacing of the pillars. A summary of the conditions studied is listed in Table 7.1. The film thickness, electrode gap, and applied voltage were chosen in combination to cover a wide range of theoretical pillar spacings, as predicted by Equation 7.1. The range of thicknesses (100-1500 nm) were chosen because of their relevance to the assumptions and bounds used to develop the linear stability analysis in Chapter 4 (i.e. films below 100 nm have significant van der Waals forces, while films above a few microns violate the thin film approximation). The gaps were chosen based on the limitations of the active gap tool described in Chapter 6. The voltages were chosen such that no values exceeded ~ 50 V/ μm , which approaches the experimentally observed dielectric breakdown for this system.

Conditions that produce an intermediate spacing (800 nm film, 3000 nm gap, 40 V) were replicated three times to evaluate measurement precision. These conditions produced an average spacing of $43 \pm 7 \mu\text{m}$, which demonstrates that there is appreciable variation from run to run even under identical conditions. Sources of variation are discussed in Section 7.2.4.

Table 7.1: Matrix of Experiments to Study Linear Stability Analysis

| Film Height (nm) | Gap (nm) | Voltage (V) | Theoretical Spacing (μm) |
|------------------|----------|-------------|---------------------------------------|
| 100 | 1000 | 80 | 7.4 |
| 100 | 1000 | 20 | 29.5 |
| 100 | 1500 | 200 | 5.7 |
| 100 | 1500 | 100 | 11.4 |
| 100 | 1500 | 40 | 28.4 |
| 100 | 3250 | 200 | 19.0 |
| 100 | 3250 | 100 | 38.1 |
| 100 | 3250 | 60 | 63.4 |
| 100 | 4000 | 180 | 29.1 |
| 800 | 1500 | 200 | 2.4 |
| 800 | 1500 | 100 | 4.8 |
| 800 | 1500 | 10 | 47.9 |
| 800 | 3250 | 200 | 13.7 |
| 800 | 3250 | 100 | 27.5 |
| 800 | 3250 | 20 | 137.3 |
| 800 | 5000 | 200 | 30.1 |
| 800 | 5000 | 45 | 133.8 |
| 800 | 5000 | 38 | 158.5 |
| 800 | 3000 | 40 | 58.8 |
| 1500 | 3250 | 100 | 18.1 |
| 1500 | 3250 | 50 | 36.2 |
| 1500 | 3250 | 20 | 90.5 |
| 1500 | 4000 | 20 | 148.2 |
| 1500 | 5000 | 200 | 23.9 |
| 1500 | 5000 | 200 | 23.9 |
| 1500 | 5000 | 100 | 47.7 |
| 1500 | 5000 | 60 | 79.5 |
| 1500 | 5000 | 40 | 119.3 |

The characteristic spacing was measured by two techniques. In most cases, the spacing was measured against calibration markings of known length via optical microscopy. Multiple measurements were taken (~5 per sample) and the data were averaged. For defect free samples whose optical micrograph exhibited high contrast, a two dimensional fast Fourier transform (FFT) analysis was performed on the image. The resulting spectra provided quantitative information on the spacing and qualitative information on the order of the pillars (e.g. compare the spectra in Figure 7.8). The characteristic spacing is inversely proportional to the distance from the center of the FFT spectrum to the first spectral ring. The FFT analysis was performed in Matlab after image processing using Scion[®] and Adobe Photoshop[®] software to increase the contrast. To verify the consistency of the two techniques, the characteristic spacing of a single sample was analyzed using both methods. The processed image and the resulting FFT spectrum for this sample are presented in Figure 7.2. Optical microscopy measurements result in an average spacing of 40.3 μm , whereas the FFT method results in a value of 43.4 μm , well within experimental error.

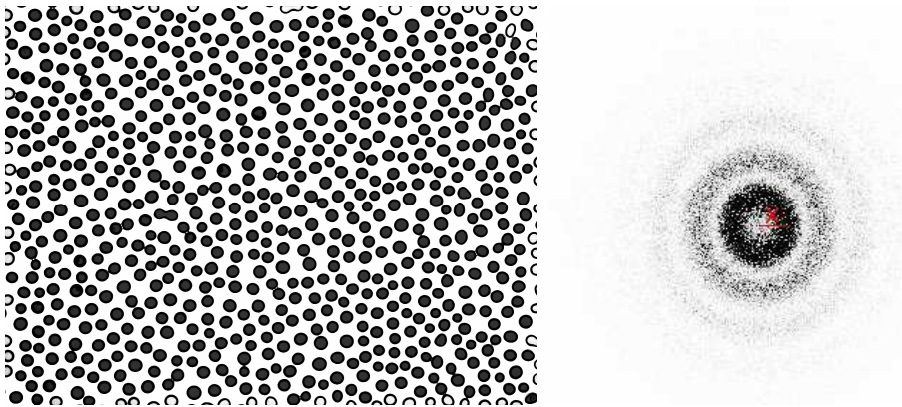


Figure 7.2: Representative optical micrograph (image width 1170 μm) with post-image processing to darken the pillars (left). The resulting FFT spectra (right). The red line indicates the measurement from the center of the spectrum to the first ring.

Image analysis of Figure 7.2 by Scion[®] software provides a reliable measure of the area of each pillar. The accuracy was verified by measuring pillar diameters using optical microscopy (<5% difference between the two techniques). The distribution of the diameters of the pillars (in this case, the pillars in Figure 7.2) can also be determined by Scion[®], as shown in Figure 7.3. Although there is a distribution of pillar sizes, the standard deviation is quite small on ideal samples (e.g. average diameter 18 +/- 3 μm). A large diameter distribution implies poor control over the characteristic spacing since material would not be evenly drawn into the pillars. The average pillar diameter is directly related to the characteristic spacing through use of a mass balance, and thus will not be discussed further.

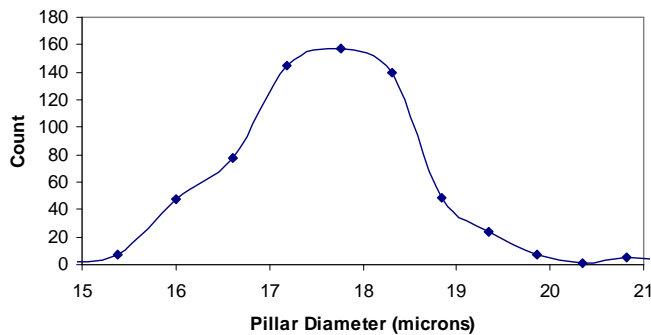


Figure 7.3: Pillar distribution of the array shown in Figure 7.2.

7.2.4 Experimental Limitations

Prior to viewing the data, a word of caution is warranted about the experimental limitations imposed by the pillar formation techniques currently available. Pillars were formed using two methods: (1) Using an electrode created from an etched glass slide as described in Chapter 4, or (2) using the active gap tool described in Chapters 6 and 8.

Both methods were used in this study, but both have experimental limitations that limit the precision of the data.

By necessity, the “glass slide” method (Figure 4.7) results in contact between the edge of the slide and the underlying film to provide a physical spacer between the film and the etched region of the slide. As a result, the film is disturbed prior to pillar formation (note: this problem is negligible for polymeric systems due to differences in the time scale of flow). This edge effect can be minimized by using a large electrode area. Large electrodes, however, tend to bow when the attractive electric field is applied. Thus, it is difficult to determine the true electrode gap at the time of pillar formation. Furthermore, controlling the initial electrode gap is challenging since dust and non-flat surfaces prevent intimate contact between the slide and the substrate. Even the highest quality glass slides have a flatness specification of $\sim 10\text{ }\mu\text{m/in}$.

In contrast, the active gap tool operates in non-contact mode and avoids many of the problems associated with the “glass slide” method. The gap can be non-invasively formed and measured prior to pillar formation using white light interferometry, providing an initial gap measurement. Nonetheless, under certain conditions the active gap tool suffers from problems similar to the “glass slide” method. Large electric fields pull the template towards the substrate, changing the operating conditions during pillar formation. In many cases, the template ultimately touches the substrate, thereby ruining the experiment and destroying the template. An improved design of the active gap tool is expected to overcome this problem. The current design of the active gap tool has several other limitations. The minimum achievable gap size is only $\sim 2\text{ }\mu\text{m}$ and in situ observation of pillar formation by optical microscopy is physically obstructed. Consequently, the substrate has to be removed to determine the spacing of the pillars. In some cases, a poor

surface treatment on the template results in a fraction of the pillars adhering to the template, thus introducing uncertainty into the spacing measurement.

As a result of the aforementioned sources of error, the characteristic spacing data presented in this section are noisy. Regardless, the trends are relevant and provide some insight into the process.

7.2.5 Results and Discussion

A plot of the characteristic spacing versus the theoretical spacing is shown in Figure 7.4. The theoretical spacing was calculated using Equation 7.1, which is simply a rearranged version of Equation 4.18 derived from linear stability analysis. The physical parameters used in the theoretical calculation were measured in Chapter 6.

$$\lambda = 2\pi \left[\frac{2\gamma \left(d + \frac{\epsilon_2 - \epsilon_1}{\epsilon_1} h_0 \right)^3}{\epsilon_2 (V_2 - V_1)^2} \left(\frac{\epsilon_1}{\epsilon_2 - \epsilon_1} \right)^2 \right]^{\frac{1}{2}} \quad (7.1)$$

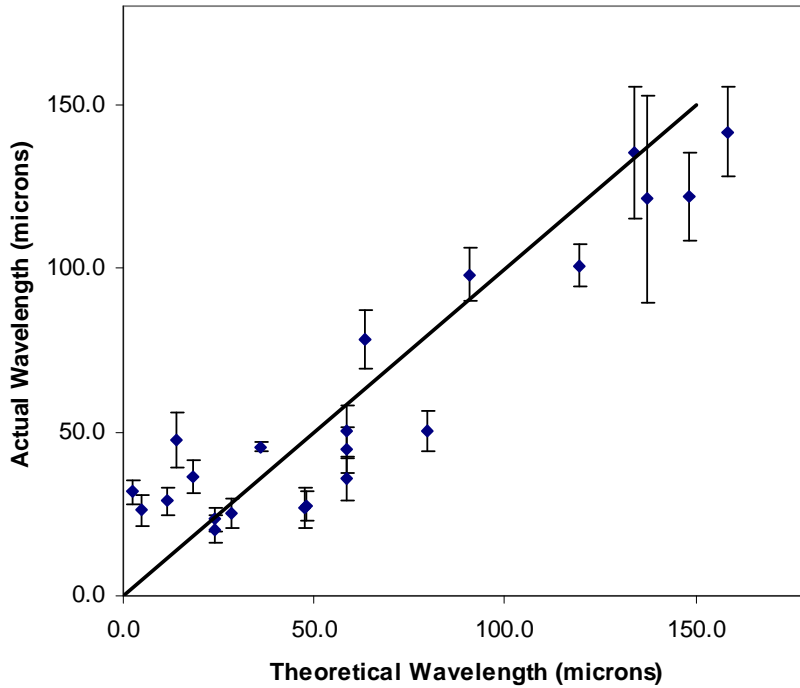


Figure 7.4: Comparison of the measured characteristic wavelength versus the theoretical wavelength for the thiol-ene system. The solid line is a plot of slope one and intercepts at zero to indicate the spacing predicted by theory.

The theoretical characteristic wavelength predicted by linear stability analysis captures the trend of the experimentally measured spacings above $\sim 30 \mu\text{m}$. Interestingly, at low theoretical wavelengths the data appear to plateau around $25\text{-}30 \mu\text{m}$, implying that smaller wavelengths may be impossible to obtain. This result may simply reflect the experimental challenges associated with the extreme conditions required to achieve small wavelengths (i.e. narrow gaps, large electric fields). In theory, positive deviations from linear stability theory can occur when lateral viscous forces become significant, which occurs at short wavelengths.⁴ However, the experiments performed here are not within the regime of theoretical deviation (d/λ must exceed unity).⁴

A common analytical approach used to study polymeric pillars is to plot a reduced electric field against a reduced wavelength.⁶ To do so, the electric field is defined in as (note: E_p is equivalent to “A” defined in Equation 4.1):

$$E_p = \frac{V}{\epsilon_1 d - (\epsilon_1 - 1)h} \quad (7.2)$$

The electric field can be normalized by E_0 ,

$$E_0 = \frac{V}{\lambda_0} \quad (7.3)$$

where λ_0 is,

$$\lambda_0 = \epsilon_0 \epsilon_1 \frac{V^2 (\epsilon_1 - 1)^2}{\gamma} \quad (7.4)$$

Figure 7.5 is a plot of reduced wavelength versus reduced electric field. The appeal of plotting the data in this manner is that the two dimensionless values are related via Equation 7.5.

$$\frac{\lambda}{\lambda_0} = 2\pi \left(\frac{E_p}{E_0} \right)^{-3/2} \quad (7.5)$$

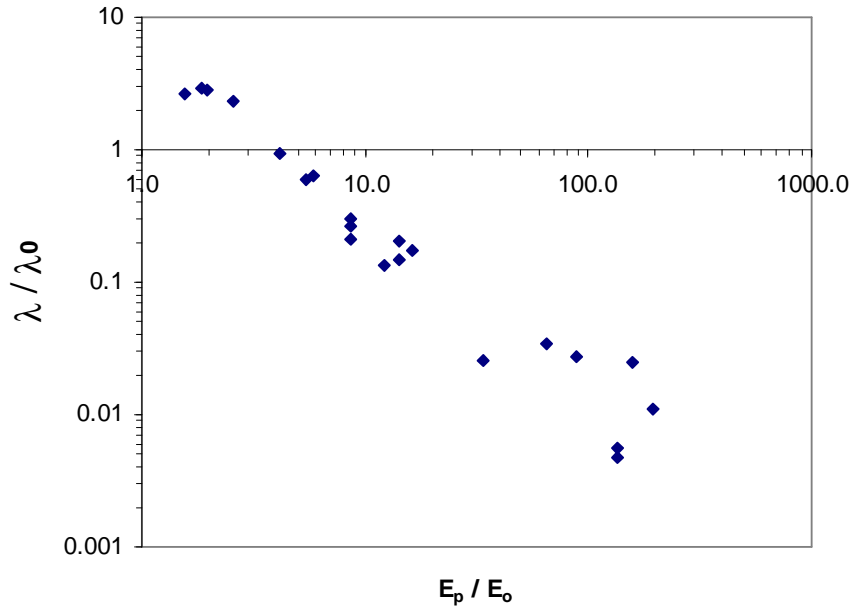


Figure 7.5: Variation of the characteristic wavelength with the electric field in the film in reduced coordinates.

A least squares analysis of the data in Figure 7.5 yields a slope of -1.33, deviating slightly from the theoretical value of -1.5 predicted by Equation 7.5. Analysis of this type found in the literature only plots E_p/E_0 to a value of ~ 20 .⁶ Interestingly, if E_p/E_0 values greater than 20 are removed from Figure 7.5, the slope becomes -1.5. E_p/E_0 values greater than ~ 20 correspond to the plateau observed at low wavelengths observed in Figure 7.4.

7.2.6 Theoretical Limitations

Creating pillars with the smallest characteristic wavelength is desirable for many patterning applications. For a given materials system, the characteristic spacing can be minimized by maximizing the electrostatic forces acting at the film-air interface. This force can be controlled by altering the film height, electrode spacing, and applied voltage.

Physically, the maximum voltage is dictated by the dielectric breakdown of the experimental configuration. This was found to be $\sim 80 \text{ V}/\mu\text{m}$, above which sparks cross the capacitor gap. If a maximum voltage of $50 \text{ V}/\mu\text{m}$ is assumed for a given gap, the effects of film height and spacing can be captured on one graph by plotting the fill factor, h/d (initial film height divided by the electrode spacing) for several gaps, d .

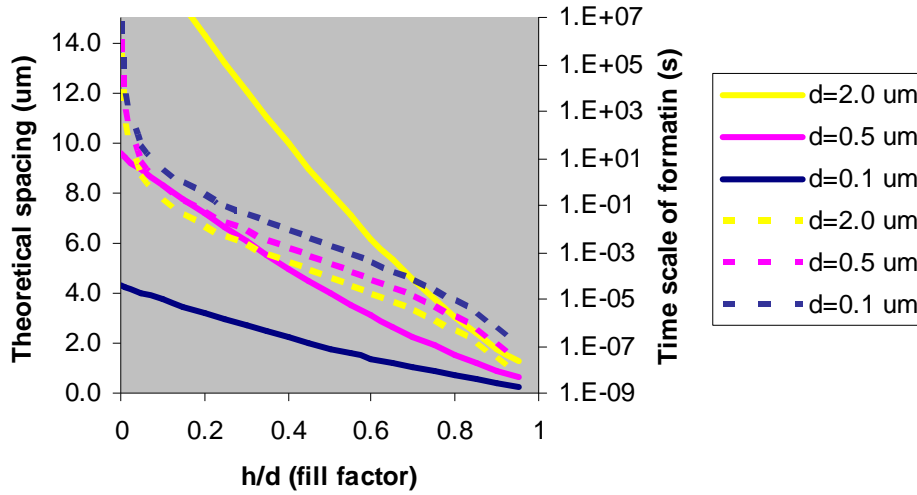


Figure 7.6: Theoretical characteristic spacing (solid lines) and time scale of formation versus fill factor, assuming a voltage applied at the dielectric breakdown of the capacitor. Each parameter is plotted for different gaps, d .

Figure 7.6 illustrates that for a given electrode gap, thicker films favor smaller characteristic spacing. It also shows that for a given fill factor, a narrower electrode gap favors a smaller characteristic spacing. Furthermore, both a narrower electrode gap and larger fill factor favor rapid pillar formation. This finding is physically intuitive since large electrostatic forces correspond to both smaller wavelengths and shorter time scales of formation. The caveat to Figure 7.6 is that larger fill factors favor the formation of pillars with larger diameters, thus increasing the likelihood of pillar coalescence. Three-dimensional fluid modeling by Verma et al. suggests that pillars are highly likely to

merge when the ratio of the air gap to initial film height is less than 3 (corresponding to fill factors >0.25).⁸ Another limiting subtlety of Figure 7.6 is that shorter wavelengths are accompanied by a greater tendency to form polydisperse pillars (i.e. pillars with a range of wavelengths and diameters).⁴ At large electric fields, numerous growth modes are favorable. Although the “theoretical characteristic wavelength” is defined as the mode that will grow the fastest, many modes grow at comparable rates in large electric fields. The range of favorable modes widens with larger electric fields, as is apparent in Figure 4.5 for increasing values of B .

In summary, the conditions that favor smaller pillars are experimentally challenging (i.e. small gaps, large electric fields, high fill factors) and result in an array of pillars with polydisperse wavelengths that tend to coalesce and merge. Without the use of a patterned electrode, the best case processing scenario will produce a pillar array with a characteristic wavelength on the order of 1-10 μm . This theoretical limitation is consistent with the experimental observations made with both polymers and low viscosity materials.⁴

7.3 GROWTH MECHANISMS

In situ observation of the pillar growth process by optical microscopy provides insight into the growth mechanisms that occur during pillar formation. In this section, the pillar growth mechanisms and their implication on pillar order are discussed.

Polymeric pillars are thought to form via two growth mechanisms: nucleation and stochastic growth.¹ The growth mechanisms of low viscosity materials (e.g. thiol-ene) appear to be similar.

Stochastic growth occurs when the film and electrode surfaces are both perfectly smooth. Under these ideal conditions, the initial electrostatic force across the film is

uniform. The relevance of linear stability analysis to the pillar formation process suggests that small undulations on the surface are amplified, implying that the spacing is determined very early in the growth process. The spacings are then projected to the upper electrode as the undulations are amplified. This has been verified experimentally using confocal microscopy to track the changes in the growing undulations with time.¹⁰ The theoretical growth rate during early stages of pillar formation is predicted to be exponential, as verified by Leach et al.¹⁰ These studies show that despite the development of undulation spacings very early in the growth process, slight differences in their initial heights result in pillars forming at different rates across the sample, which is magnified by the exponential growth rates. Thus, pillar growth appears to be stochastic despite having a characteristic wavelength. Figure 7.2 is an optical micrograph of a representative array of pillars formed by this stochastic mechanism.

Nucleated growth occurs when there is a protrusion (designed or inadvertent) on the upper electrode that results in a larger local electric field due to the smaller electrode gap. The locally enhanced field causes the directly underlying film to grow pillars faster than the surrounding film. Nucleated growth is accompanied by local ordering of the adjacent pillars up to several wavelengths from the nucleation source. This is shown in Figure 7.7 and has also been predicted by 3-D fluids modeling.⁸

The propagation of the nucleated growth is dependent on how the nucleation initially occurs. In the case of a nucleation point, concentric rings of pillars form around the initial nucleated pillar, as demonstrated in Figure 7.7. In the case of a nucleated line, rows of pillars grow sequentially away from the nucleation row. This often occurs at the electrode edge due to the sharp spatial gradients in the electric field that occur there. These fronts typically propagate away from the nucleation point until they impinge another growth region, with order degrading with distance. Local ordering is often

observed towards the electrode edge due to this edge nucleation effect, as shown in Figure 7.8a. This observation is in agreement with 3-D fluid modeling.⁸

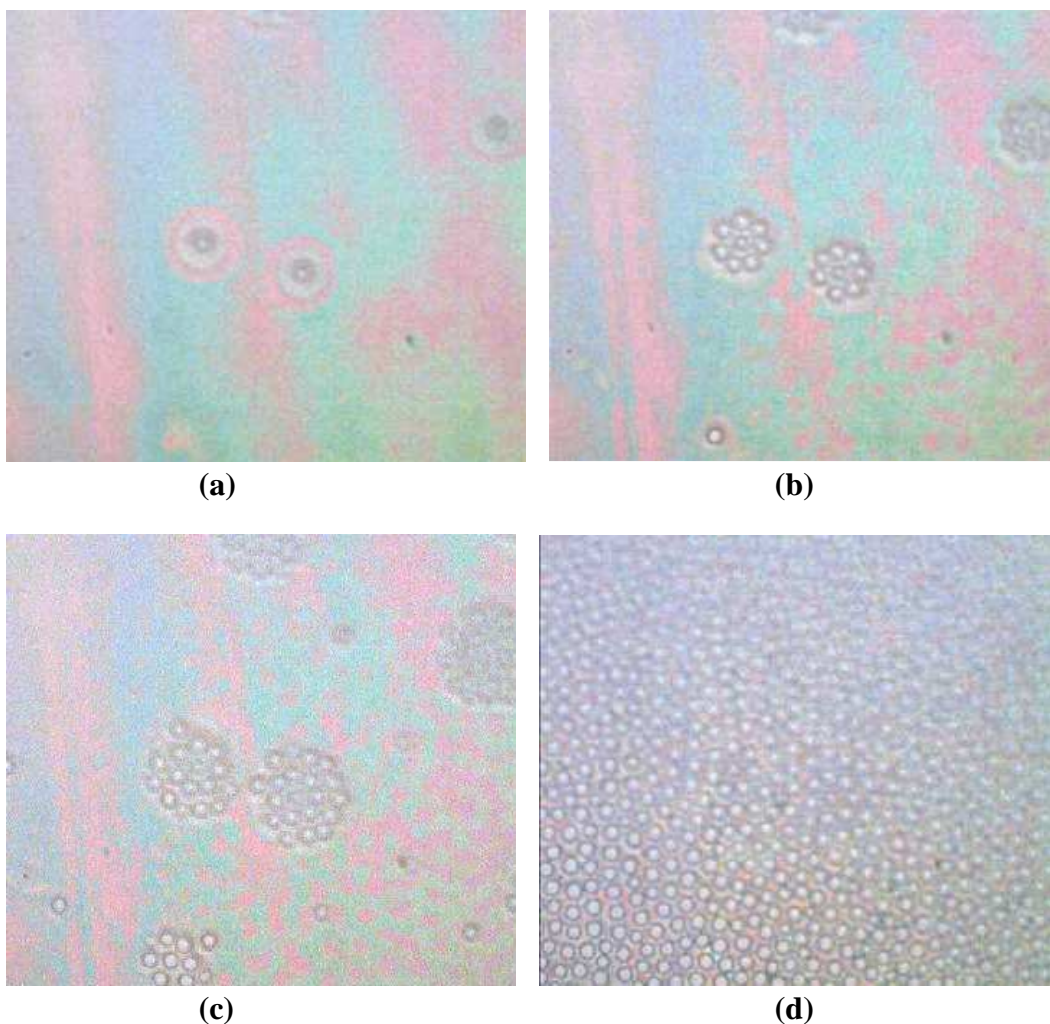


Figure 7.7: A temporal view of the nucleation growth process observed under 10X optical magnification (image width ~1 mm). (a) Individual pillars initially form in 3 nucleation sites. (b) The first layer of pillars forms around these nucleation sites. (c) Layers from different nucleation sites have grown enough to touch each other (d) Pillars have grown throughout, covering the sample surface. The whole process takes less than ten seconds to complete.

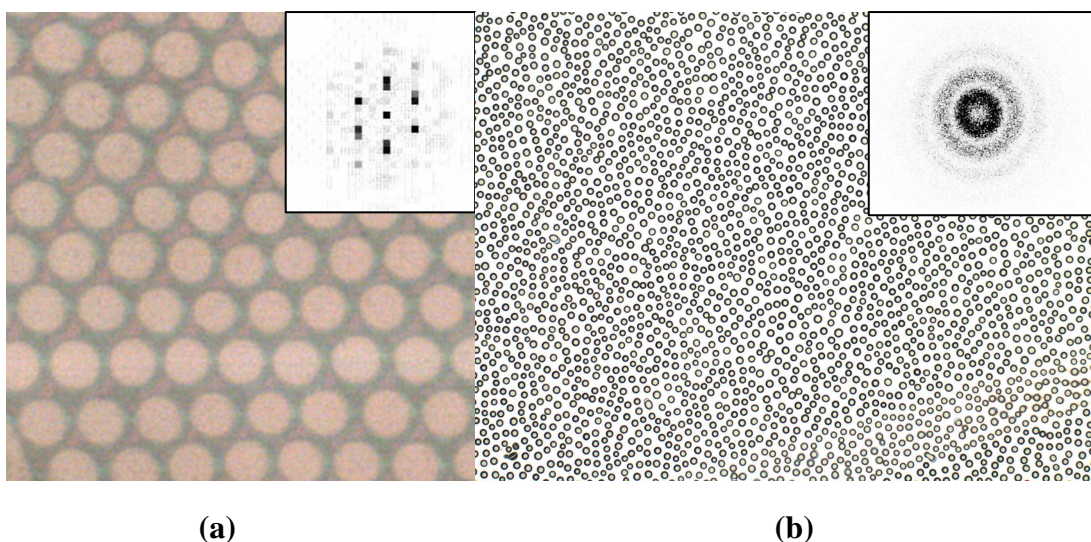


Figure 7.8: Example images of thiol-ene pillars with corresponding FFT spectra (inset). (a) Localized order can be obtained from nucleation effects, whereas most pillars are formed by stochastic growth and thus have a characteristic spacing, but no long range order (b).

In nucleated systems, local order is believed to occur due to the rings of depleted material surrounding each pillar and by the nature of the spinodal instability. As fluid is drawn into the nucleated pillar, it creates a depletion ring around the base of the structure. The film subsequently withdraws from the depleted region to minimize surface tension (in a manner similar to dewetting), creating an elevated rim of material. That rim is then closer to the upper electrode, resulting in a secondary nucleation effect.

The implication of nucleated growth is that regions with local close-packed order can form, but long range order does not occur spontaneously. The crisp FFT spectrum in the inset of Figure 7.8a indicates the formation of a hexagonally close packed array. In contrast, the stochastically formed array in Figure 7.8b produces a diffuse FFT spectrum in which the points are blurred into a ring. The lack of long range order in photocurable systems is consistent with published images of polymeric pillars.^{1,5,6,9-14} The remainder of this chapter focuses on methods to improve the long range order of the pillars.

7.4 PATTERNED ELECTRODES

7.4.1 Background

The most direct way to control both order and positioning of the pillars is to use an electrode with protruding features. The features provide numerous nucleation points across the electrode, resulting in generation of a replica of the features (Figure 7.9). The use of patterned electrodes was first demonstrated by Schaffer et al in which 140 nm lines were replicated in PMMA.¹ Subsequent modeling on patterned electrodes revealed that both the feature spacing and the fill factor (film height divided by electrode gap) determine the ability to faithfully replicate features.⁸

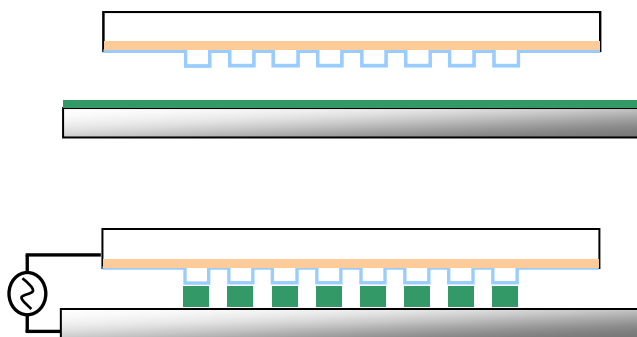


Figure 7.9: Illustration of the use of patterned electrodes to dictate the position of pillars.

Here, the ability to use patterned electrodes to create order is demonstrated as a proof of principle for feature replication in low viscosity material systems.

7.4.2 Methods

The thiol-ene formulation described in section 7.2.2 was used with the active gap tool described in both Chapters 6 and 8 to form the pillars.

Templates were formed by contact lithography using a custom designed chromium on quartz mask (Advanced Reproductions) featuring arrays of lines and shapes of various sizes and spacings. Feature sizes were limited to $>10\text{ }\mu\text{m}$, the approximate physical limitation for replicating features by contact lithography without the use of a contact aligner ($\frac{1}{4}$ " quartz templates do not fit into traditional contact aligners). E-beam lithography is the ideal patterning method for smaller features, but the JEOL tool at the University of Texas is only designed to process silicon wafer substrates.

Templates were created by dicing 5x5" fused silica mask blanks (Hoya, Schott, etc) into 65x65 mm pieces (American Precision Dicing). The chromium coated templates were then patterned using standard contact lithography methods to create a 1x1" mesa centered on the blank. The chromium serves as a mask to protect the mesa during buffered oxide etching, which was done to produce a 15-20 μm recess in the areas surrounding the mesa at a rate of $\sim 5.5\text{ }\mu\text{m/hr}$. This recess is referred to as the safety ledge because it prevents the template from contacting the substrate in the active gap tool in cases in which the template and substrate are not perfectly co-planar. The chromium coated mesa was patterned by contact lithography with a commercial photomask (Advanced Reproductions). The edges of the template were rounded by a belt sander to reduce the possibility of the conductive coating from wearing off. The resulting patterned template was coated with $\sim 100\text{ nm}$ of indium tin oxide (ITO) by e-beam evaporation followed by a 350°C anneal to make the ITO conductive. A wire was glued to the side of the template using conducting epoxy to connect the template to a power supply. The template was checked for conductivity by a hand held multimeter. In some cases, the ITO template was surface treated, as described in Chapter 9. A schematic along with a picture of an actual template are shown in Figure 7.9.

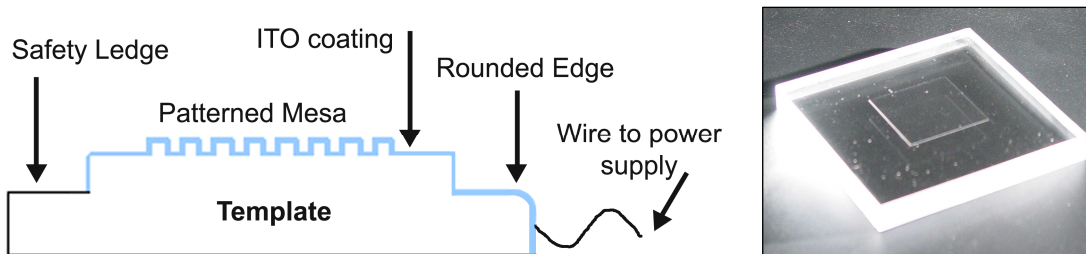


Figure 7.10: Illustration of the key features on a patterned template. Right, a photograph of a template with the mesa clearly visible at the center.

7.4.3 Results

Figure 7.11 provides evidence that patterned electrodes can effectively induce order in low-viscosity systems. An upper electrode with protruding $50\ \mu\text{m}$ diameter posts and $100\ \mu\text{m}$ pitch was used to direct the formation of pillars. Pillars preferentially form at the protruding features due to the locally higher electric field.

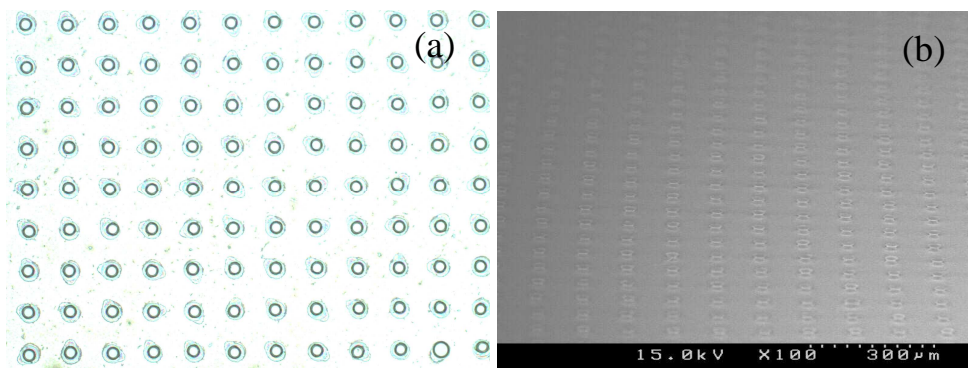


Figure 7.11: Thiol-vinyl ether pillar arrays formed using a patterned electrode. (a) Optical micrograph of pillar arrays (image width $1.1\ \text{mm}$). (b) Tilt-view SEM image of pillar array.

The ability to replicate arbitrary feature geometries was also demonstrated by creating a template with the familiar “Texas Longhorn” logo, as shown in Figure 7.12. Similarly, pentagons were replicated, as shown in Figure 7.13.

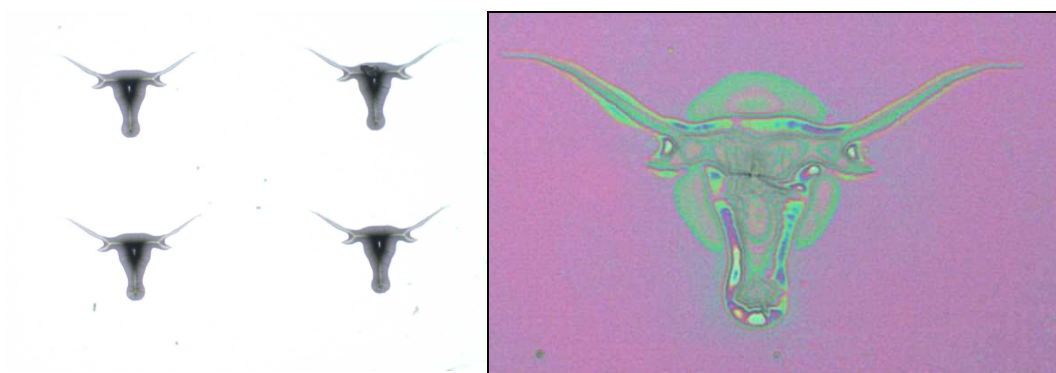


Figure 7.12: Demonstration of the use of a patterned electrode to create structures of arbitrary shape. Optical micrograph of the template patterns (left). Optical micrograph of the resulting structure formed in thiol-ene (right). The distance from horn to horn tip is $\sim 50\ \mu\text{m}$.

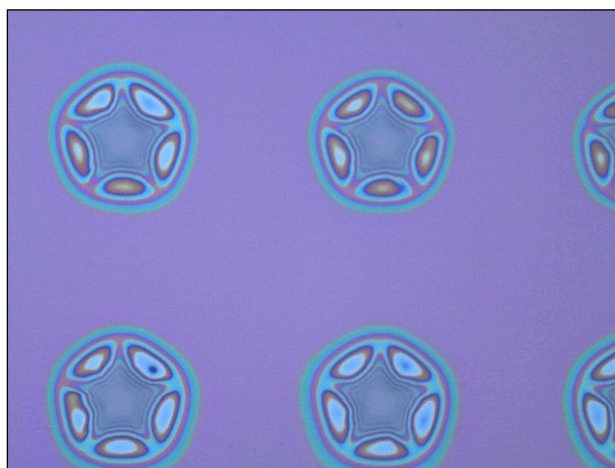


Figure 7.13: Optical micrograph of thiol-ene structures formed by electric field assisted assembly using a pentagon patterned electrode ($\sim 50\ \mu\text{m}$ diameter).

7.4.4 Summary

Patterned templates were used to improve the long range order of the pillars and form features with arbitrary geometry. This is the first demonstration of pattern replication with low viscosity fluids. Although patterned electrodes work well, the

challenges associated with fabricating the electrodes (discussed in Section 7.4.2) motivate the design of new techniques to improve order without the use of patterning.

7.5 PILLARS FORMED BY ALTERNATING FIELDS

7.5.1 Background

Pillar arrays are typically formed with a DC field. AC bias was investigated to (1) prove that it forms pillars and (2) study the effects on long range order. As the applied field alternates polarity, the induced molecular dipoles align in phase with the field, creating an attractive force between the surface of the film and the upper electrode (similar to the effects induced by DC fields). These forces are responsible for pillar formation. The hypothesis is that at high frequencies, the molecular dipole alignment would not be able to keep up with the rapidly alternating field, possibly impacting the growth mechanism. The concept is similar to that used in dielectric spectroscopy to study material properties.¹⁵ Another hypothesis is that at low frequencies the neutral field that occurs as the AC reverses polarity may allow the undulations to relax or reorganize, impacting the growth mechanism.

7.5.2 Methods

The glass slide method (Chapter 4) was used to apply the field to an 800 nm film of thiol-ene (Chapter 6). The AC signal was generated by either Labview or a commercial signal generator. A Labview program was written to generate signals from 1-100 Hz. BK Precision 4011A and HP 3314A signal generators were used for the 10 Hz to 5 M Hz range. The frequency signal was amplified by a Kepco Bipolar Operational Power Supply, Model BOP 1000M, for sub-1000 Hz signals. For larger frequencies, a EIN Model 240L RF power amplifier was utilized. The frequency and amplitude of the

signals were monitored by an oscilloscope (Tektronix 2235 or a Fluke multimeter for sub 100 Hz signals).

7.5.3 Results and Discussion

Pillars form under AC fields over a wide range of amplitudes (upper limit is dictated by the dielectric breakdown of air in the capacitor gap) and frequencies (varying by orders of magnitude). Varying the frequency of the applied AC voltage from 10 Hz to 5 MHz did not produce results that conclusively demonstrated an influence on the spacing or order of the formed pillars. Voltage amplitude and capacitor gap, however, were shown to modulate pillar spacing as predicted in Section 7.2. Figure 7.14 shows a typical pillar optical micrograph from an AC experimental run.

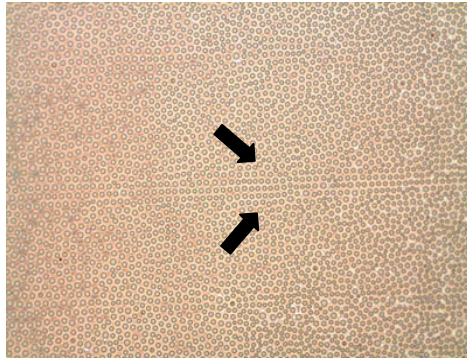


Figure 7.14: Micrograph of pillars formed by applying an AC voltage with $V = 200 \text{ V}_{\text{rms}}$ and $f = 100 \text{ Hz}$. Note the ordering of the pillars following a scratch across the upper electrode indicated by the arrows. Image width $1170 \mu\text{m}$.

Local ordering in several of the AC experiments occurred serendipitously. Figure 7.14 is a micrograph of an array of pillars formed with a nominally flat upper electrode that nonetheless displays distinctly ordered rows of pillars spanning the width of the sample. These ordered swatches are believed to result from microscopic scratches on the

upper glass electrode that are visible with an optical microscope and are believed to be due to the process used in the manufacturing of the glass slides.

The localized order was in the form of a hexagonal close-packed pattern that was analyzed using a 2-dimensional Fast Fourier Transform (FFT) method in Matlab.¹¹ Figure 7.15a is a micrograph of pillars formed with 40 Vrms and 2 MHz. An isolated portion of the sample surface (shown inside a rectangle) has pillars arranged in a hexagonal close-packing order. In this case, the average pillar diameter is 17.8 μm and the characteristic spacing was found to be $\sim 30 \mu\text{m}$. An ideal hexagonally ordered array will produce an FFT image of six dots (Figure 7.18c), whereas random ordering of pillars produces an FFT image that looks like multiple halos (for example, see Figure 7.8).

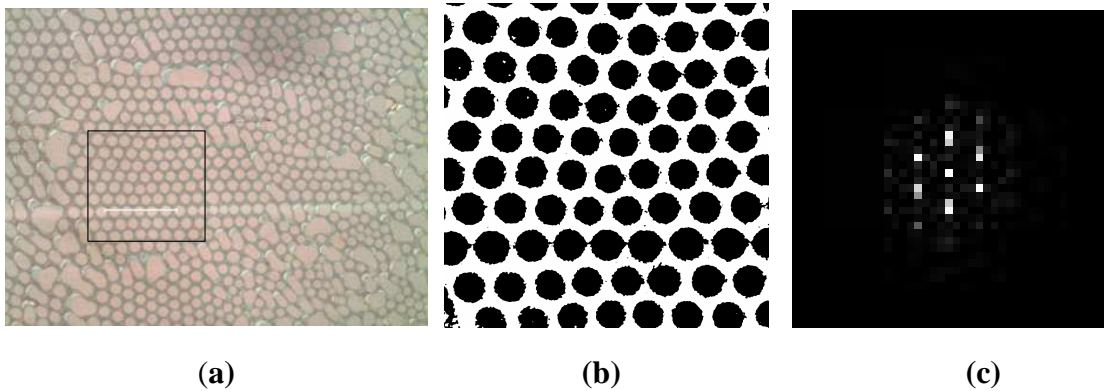


Figure 7.15: (a) Micrograph of pillars formed with AC voltage method, $V = 40 \text{ Vrms}$, $f = 2 \text{ MHz}$. White bar is $200 \mu\text{m}$. (b) Two-tone image crop of region exhibiting hexagonal close-packing order. (c) The FFT analysis of this image.

7.6 VIBRATION INDUCED WAVES

7.6.1 Background

It may be possible to tune the characteristic wavelength of the pillars by imposing vibrational waves on the film surface prior to the application of the electric field, which

would amplify the imposed undulations. This technique has the potential to improve long range order and has literature precedent.

In 1831, Michael Faraday first demonstrated the formation of parametrically pumped surface waves.¹⁶ “Faraday waves” are formed when a container of fluid is vibrated vertically at a given frequency and amplitude. Above an acceleration threshold, standing waves spontaneously appear at the surface of the fluid, vibrating at exactly half the driving frequency. These waves continue to be of interest to scientists today because the induced wave patterns can be controlled by varying the frequency, fluid properties, and sample geometry (e.g. fluid depth).^{17,18} An example of a Faraday wave pattern is shown in Figure 7.16.

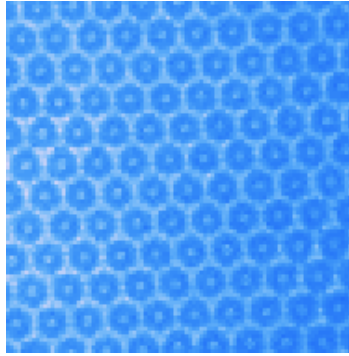


Figure 7.16: Example of Faraday waves on a liquid surface.¹⁹

Faraday waves are typically modeled using a damped Mathieu equation.²⁰ The boundary layer depth of the free surface is represented by δ . An order of magnitude estimate for this boundary layer is represented by $(\nu/\omega)^{0.5}$, where ν is the kinematic viscosity and ω is the forcing frequency.¹⁸ From this calculation, δ is estimated to be on the order of several microns. This is significant because the thickness of the film used to form pillars is only ~ 1 micron, implying that the viscous resistance to flow will be significant. The viscous effects can be estimated by the product $k\delta$, in which k is the

wavelength of the instability.¹⁸ Viscous effects are weak when $k\delta$ is $\ll 1$, whereas viscous effects are strong when $k\delta$ is ~ 1 . The value of $k\delta$ is greater than 1 under typical conditions for pillar formation, implying that viscous forces are significant. Therefore, it is theoretically unlikely that imposed vibrations will be strong enough to overcome the viscous resistance to flow required to form Faraday waves. In fact, the thinnest films studied in literature for Faraday wave experiments are on the order of 0.1-1 cm, two orders of magnitude thicker than the films we use to form pillars.^{17,18}

The viscous resistance to flow can be overcome by applying large accelerations to the film surface. For a given frequency, the acceleration increases with increasing vibrational amplitude. An infinite depth fluid with a viscosity comparable to thiol-ene requires an acceleration ~ 300 times that of gravity to produce Faraday surface waves with ~ 1 cm wavelengths.¹⁸ These waves are typically produced using a mechanical shaker operating at ~ 100 Hz.^{17,18} In contrast, pillars typically form at wavelengths on the micron scale, thus the operating frequency must be approximately four orders of magnitude larger (\sim MHz). Critical acceleration scales with frequency, thus the required acceleration for micron scale pillars would likely be at least 4 orders of magnitude larger than those used in typical Faraday experiments.²¹ Unfortunately, the piezo devices required to generate ~ 1 MHz waves have physical amplitude limitations dictated by the expansion and contraction of the piezo crystal. These physical changes to the crystal lattice produce tremendous amounts of heat that are capable of depoling the piezo, ultimately limiting the amplitude of the applied voltage to the piezo. Even if the piezos were capable of generating large accelerations, vibrational energy attenuates between the piezo and the sample due to viscous dissipation and poor acoustical matching between the materials.

Despite the aforementioned challenges, the fact that the electric field will amplify extremely small perturbations in a thin film and vibrational experiments are relatively

simple to perform justifies pursuing this concept as a proof of principle to induce long range order.

7.6.2 Methods

One micron films of thiol-ene (Chapter 6) were used in these studies. The glass slide method (Chapter 4) was used to apply the field to the film. 1 MHz and 2.25 MHz piezo transducers (Panametrics) were placed in contact with the substrate (coupled using vacuum oil) to produce ultrasonic waves in the thiol-ene film while simultaneously subjecting it to a 40 V DC potential across a $\sim 3 \mu\text{m}$ gap. Figure 7.17 is a photograph of the experimental set-up.

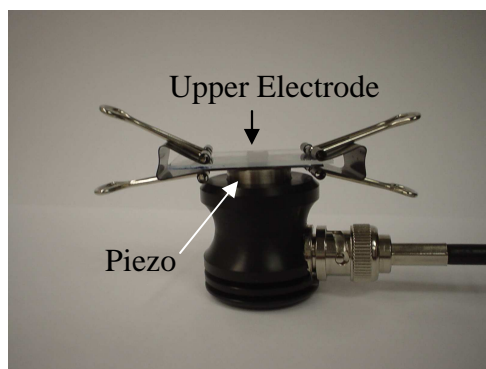


Figure 7.17: Photograph of piezo set up. A glass slide with a chromium coated recess (1 x 2.5 cm) is clipped to a film coated silicon substrate. The sample is placed on top of a 1/2" diameter piezo element, which is plugged into a power source. The electrodes used to apply the electric field are not shown.

The piezo transducers were operated in both continuous wave (voltage applied continuously) and in burst mode (voltage applied for only a fraction of each second). In order to prevent overheating and subsequent de-poling of the piezo ceramic, the amplitude of the AC voltage input to the piezo was limited to 8 V_{p-p} (peak to peak) in continuous wave mode. This limit was calculated using specifications provided by the

manufacturer. The voltage input could be increased further when operating in burst mode. The pillars were cured via exposure to a mercury light source. Optical microscopy was used for preliminary inspection of the ordering in the pillar arrays, followed by image analysis using a Fast Fourier Transform (FFT) method,¹¹ as described in Section 7.3.

7.6.3 Results and Discussion

Before forming the pillars, the substrate was placed in contact with an ultrasonic-wave-emitting piezo transducer. The hope was that the piezo vibrations would create regular undulations on the film surface that would be amplified by the electric field applied across the electrodes. When operated in continuous wave mode, no improvement in pillar ordering was observed. This may be a result of the low voltage input limitation, resulting in ultrasonic waves with insufficient amplitude to induce undulations in the thiol-ene film. Evidence of local ordering was observed when operating in voltage burst mode that allowed for higher applied peak-to-peak (V_{p-p}) voltage. Figure 7.18 shows typical results obtained using the ultrasonic piezo method. While long range order of the pillar arrays was not observed, Figures 7.18 b-e provide evidence of local order. It is unclear whether the piezos provide improved ordering compared to the control sample, Figure 7.18a, thus the results are inconclusive. Figures 7.18 c and e show evidence of merged pillars, a phenomena discussed in Chapter 6. The merging of pillars was particularly problematic for these experiments because the pillar formation and pillar photocuring occurred in different buildings, so there was a time delay that may have permitted pillars to merge prior to curing.

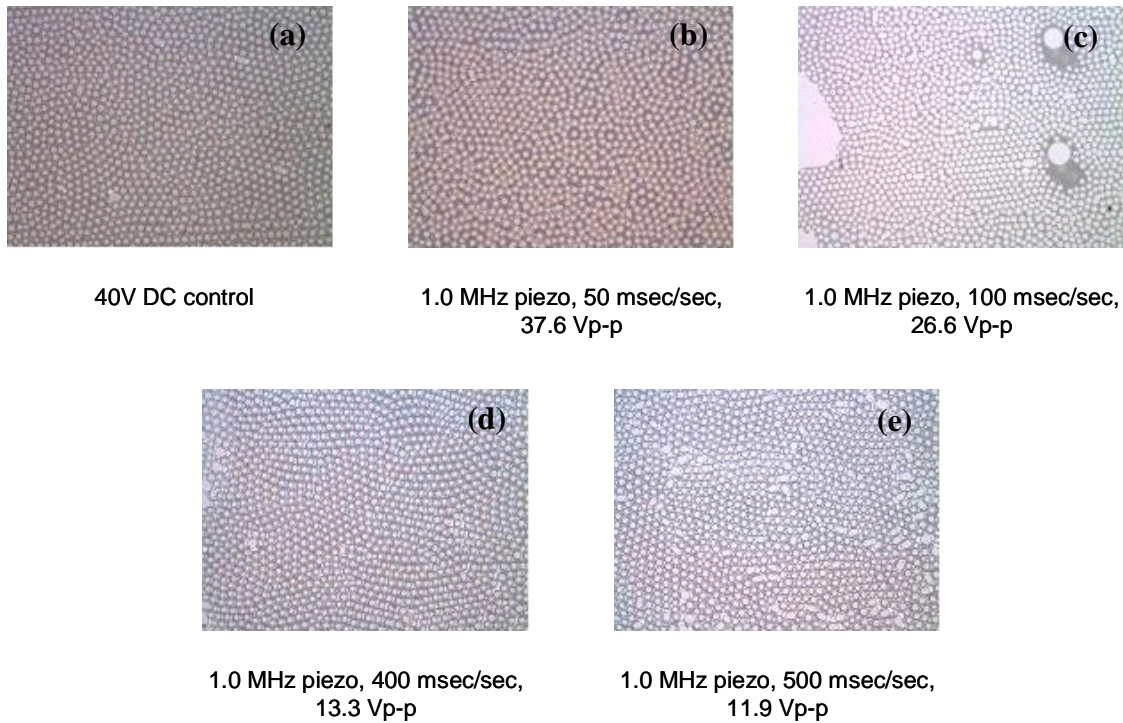


Figure 7.18: Micrographs of pillars formed by applying ultrasonic waves at different burst rates (voltage applied only for a fraction each second) and varying peak-to-peak (V_{p-p}) voltage. A 40V DC control sample is shown for comparison. The larger white areas in some of these micrographs represent pillars that have merged together. Each image is 1170 μm wide.

The initial results from this piezo study are promising, but inconclusive. Future work should consider methods to improve the delivery of high amplitude acoustical waves into the thin film. Piezos with larger power ranges exist, but must be submerged in water to dissipate heat rapidly. The method of delivery should also be optimized. With the current set up, acoustical waves may dissipate and reflect as they travel from the piezo through the coupling oil and substrate.

Rather than physically oscillating the substrate, as in Faraday waves, an alternative approach would be to harness the natural flexural modes of the silicon wafer. If the substrate has vibrational modes, then presumably the thin film would conform to

these vibrations, creating lateral variations of the field strength applied to the film. A simple Matlab model can determine the mode shapes for flexural waves on a silicon plate based on the assumption that the silicon acts like an elastic solid.^{22,23} In reality, silicon crystals are anisotropic, but thin plates (i.e. wafers) may behave like an isotropic solid. Assuming a 2 cm square silicon wafer with 400 μm thickness and the properties of 111 silicon, gives the modes shown in Figure 7.19 at 6.5 MHz. The antinodes occur approximately every 0.1 mm. Although these spacing are large, it would be an interesting demonstration, as it may induce nucleation points that could lead to improved ordering.

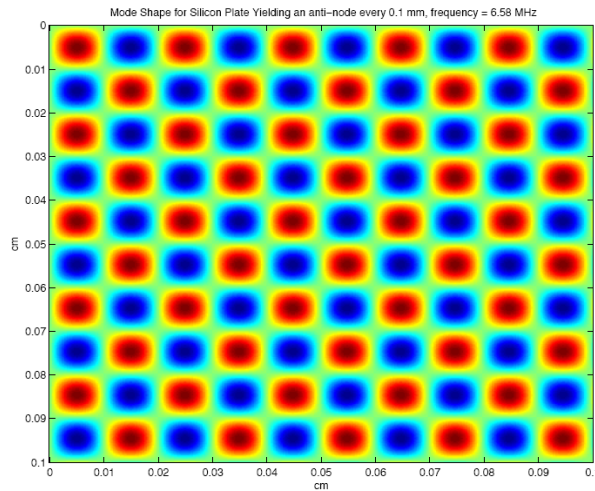


Figure 7.19: Flexural modes on a silicon plate at 6.58 MHz.

7.7 SUMMARY

Linear stability analysis was shown to capture the trends of the electric field assisted assembly of low viscosity pillars within experimental limitations. In situ monitoring of the pillar formation process showed that the pillars either form stochastically or through nucleated growth. Both processes result in pillars with a

predictable characteristic spacing, but nucleated growth provides the advantage of local ordering.

Attempts to improve the long range order of the pillars were unsuccessful. The formation of pillar arrays in the thiol-ene system via the use of AC voltages of varying amplitude and frequency was demonstrated. The spacing and ordering of the pillars appear to be insensitive to AC frequencies ranging from 10 Hz -5 MHz. In a separate set of experiments, pillar arrays were formed while applying ultrasonic waves to the substrate through the use of ultrasonic transducers. In both cases, instances of hexagonal closed-packing ordering of the pillars, as determined by image analysis using an FFT algorithm, were observed in localized portions of the sample surface. While it was not possible to extend this ordering throughout the sample surface in a spontaneous fashion, results show that ordering of the pillar arrays can be induced by the presence of patterned electrode surfaces.

7.8 REFERENCES

1. Schaffer, E.; Thurn-Albrecht, T.; Russell, T. P.; Steiner, U., Electrically induced structure formation and pattern transfer. *Nature* **2000**, 403, (6772), 874-877.
2. Herminghaus, S., Dynamical Instability of Thin Liquid Films Between Conducting Media. *Physical Review Letters* **1999**, 83, (12), 2359-2361.
3. Pease, L. F.; Russel, W. B., Electrostatically induced submicron patterning of thin perfect and leaky dielectric films: A generalized linear stability analysis. *Journal of Chemical Physics* **2003**, 118, (8), 3790-3803.
4. Pease, L. F., III; Russel, W. B., Limitations on Length Scales for Electrostatically Induced Submicrometer Pillars and Holes. *Langmuir* **2004**, 20, (3), 795-804.
5. Lin, Z.; Kerle, T.; Russell, T. P.; Schaeffer, E.; Steiner, U., Structure Formation at the Interface of Liquid/Liquid Bilayer in Electric Field. *Macromolecules* **2002**, 35, (10), 3971-3976.

6. Schaffer, E.; Thurn-Albrecht, T.; Russell, T. P.; Steiner, U., Electrohydrodynamic instabilities in polymer films. *Europhysics Letters* **2001**, 53, (4), 518-524.
7. Pease, L. F.; Russel, W. B., Linear stability analysis of thin leaky dielectric films subjected to electric fields. *Journal of Non-Newtonian Fluid Mechanics* **2002**, 102, (2), 233-250.
8. Verma, R.; Sharma, A.; Kargupta, K.; Bhaumik, J., Electric Field Induced Instability and Pattern Formation in Thin Liquid Films. *Langmuir* **2005**, 21, (8), 3710-3721.
9. Lin, Z.; Kerle, T.; Baker, S. M.; Hoagland, D. A.; Schaffer, E.; Steiner, U.; Russell, T. P., Electric field induced instabilities at liquid/liquid interfaces. *Journal of Chemical Physics* **2001**, 114, (5), 2377-2381.
10. Leach, K. A.; Lin, Z.; Russell, T. P., Early Stages in the Growth of Electric Field-Induced Surface Fluctuations. *Macromolecules* **2005**, 38, (11), 4868-4873.
11. Chou, S. Y.; Zhuang, L., Lithographically induced self-assembly of periodic polymer micropillar arrays. *Journal of Vacuum Science & Technology, B: Microelectronics and Nanometer Structures* **1999**, 17, (6), 3197-3202.
12. Chou, S. Y.; Zhuang, L.; Deshpande, P.; Chen, L.; Sun, X., Lithographically-induced self-assembly of periodic micro-pillar arrays in a single homopolymer film. *Polymer Preprints* (American Chemical Society, Division of Polymer Chemistry) **2000**, 41, (1), 78.
13. Chou, S. Y.; Zhuang, L.; Guo, L., Lithographically induced self-construction of polymer microstructures for resistless patterning. *Applied Physics Letters* **1999**, 75, (7), 1004-1006.
14. Lin, Z.; Kerle, T.; Russell, T. P.; Schaeffer, E.; Steiner, U., Electric Field Induced Dewetting at Polymer/Polymer Interfaces. *Macromolecules* **2002**, 35, (16), 6255-6262.
15. Runt, J. P.; Fitzgerald, J. J., Dielectric spectroscopy of polymeric materials: fundamentals and applications. American Chemical Society: Washington, DC, 1997; p xvi, 461.
16. Faraday, M., On a peculiar class of acoustical figures; and on certain forms assumed by groups of particles upon vibrating elastic surfaces. *Philosophical Transactions of the Royal Society London* **1831**, 52, 299.
17. Huepe, C.; Ding, Y.; Umbanhowar, P.; Silber, M., Forcing function control of Faraday wave instabilities in viscous shallow fluids. *Physical Review E*:

- Statistical, Nonlinear, and Soft Matter Physics* **2006**, 73, (1-2), 016310/1-016310/11.
18. Kumar, S., Mechanism for the Faraday instability in viscous liquids. *Physical Review E: Statistical Physics, Plasmas, Fluids, and Related Interdisciplinary Topics* **2000**, 62, (1-B), 1416-1419.
 19. Lifshitz, R. <http://haides.caltech.edu/~lifshitz/patterns.html>. (April 2006).
 20. Cerda, E. A.; Tirapegui, E. L., Faraday's instability in viscous fluid. *Journal of Fluid Mechanics* **1998**, 368, 195-228.
 21. Bechhoefer, J.; Ego, V.; Manneville, S.; Johnson, B., An experimental study of the onset of parametrically pumped surface waves in viscous fluids. *Journal of Fluid Mechanics* **1995**, 288, 325-50.
 22. Franca, D. R.; Blouin, A., All-optical measurement of in-plane and out-of-plane Young's modulus and Poisson's ratio in silicon wafers by means of vibration modes. *Measurement Science and Technology* **2004**, 15, (5), 859-868.
 23. Ma, C. C.; Lin, H. Y., Experimental measurements on transverse vibration characteristics of piezoceramic rectangular plates by optical methods. *Journal of Sound and Vibration* **2005**, 286, (3), 587-600.

Chapter 8

Pillar Aspect Ratio

8.1 BACKGROUND

Pillars formed by electric field assisted assembly have low aspect ratios, defined as the ratio of the height to the diameter of the pillar. A literature survey shows that experimentally generated polymeric pillar arrays typically have aspect ratios between 0.05-0.2, with 0.52 being the largest reported value.¹ Low viscosity pillar arrays also have small aspect ratios. Figure 8.1 is a tilt view scanning electron micrograph of typical thiol-ene pillars with aspect ratios of ~ 0.1 .

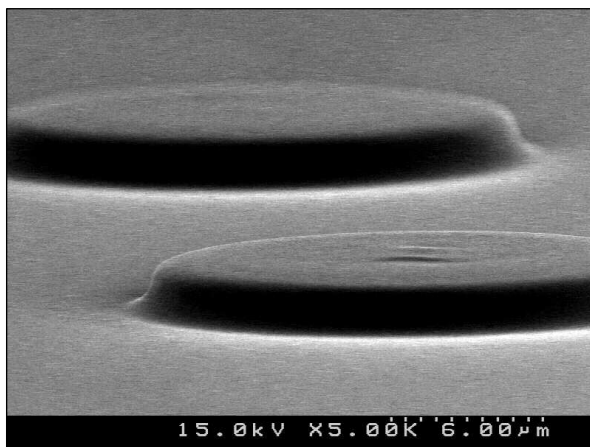


Figure 8.1: Tilt-view scanning electron micrograph of low viscosity thiol-ene pillars formed under reasonable conditions (40 V, 2.5 μm gap, 800 nm film). The pillars have low aspect ratios (~ 0.1), typical of the pillar formation process.

High aspect ratio features are ideal for patterning applications. Patterned “resist” features, which are typically sacrificial materials used to protect an underlying surface,

tend to degrade during the reactive ion etch (RIE) transfer processes. High aspect ratio features can accommodate the vertical degradation induced by RIE, a requirement to protect the underlying surface. High aspect ratio features are also appealing because of their potentially unique physical properties. Harvestable high aspect ratio pillar structures may have attractive properties when placed in solution or when used in composite materials. In this chapter, methods to overcome the inherently low aspect ratio of pillar arrays are developed.

8.2 THEORY

The theoretical aspect ratio can be derived by combining linear stability analysis with conservation of mass. Linear stability analysis was derived in Chapter 4 and its applicability has been verified experimentally.¹⁻⁹ Linear stability analysis predicts the theoretical center-to-center spacing of the pillars. If all of the initially undisturbed film is entrained into the pillars, a simple mass balance provides the aspect ratio, shown in Equation 8.1.

$$\frac{H}{D} = \left[\frac{\pi d^3}{4 \lambda^2 h} \right]^{1/2} \quad (8.1)$$

In Equation 8.1, H is the height of the pillar, which is equivalent to the electrode gap, d. D is the average diameter of the pillar, h is the undisturbed film height, and λ is the characteristic wavelength.

Based on Equation 8.1, for a given film height, the aspect ratio can be increased by either increasing the electrode gap, d, or by decreasing the characteristic spacing, λ . The characteristic wavelength can be decreased independently of d by increasing the

applied voltage (as predicted by Equation 7.1). The voltage can only be increased until the capacitor reaches the dielectric breakdown of the gap, which occurs between 50-80 V/ μm . Unfortunately, once the dielectric breakdown is reached, λ can only be lowered by reducing d , which results in a conflicting impact on the aspect ratio. To a first order approximation, any decrease in λ achieved by lowering d results in a negligible change in the aspect ratio since λ scales with $d^{3/2}$. These trends are captured in Figure 8.2, which assumes a 50 V/ μm applied field. Even under these extreme conditions (i.e. best case scenario), the aspect ratio is still below 1 in most cases. As discussed in Chapter 7, large fill factors (h/d) lead to pillar coalescence and small fill factors have exceedingly large time scales of pillar formation. Consequently, pillar formation usually occurs at intermediate fill factors, leading to low aspect ratios. The minimum theoretical aspect ratio for a given gap, d , occurs at a quarter of the ratio of the polymer dielectric constant to the balance of the polymer dielectric constant minus one ($h/d=0.28$ for the thiol-ene system). Typical operating conditions result in aspect ratios of ~ 0.1 (Figure 8.1).

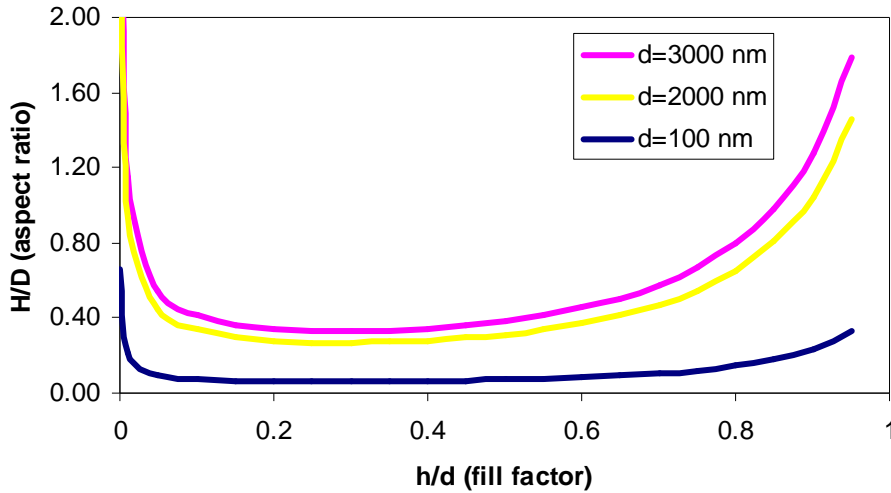


Figure 8.2: Theoretical aspect ratio versus fill factor for several electrode gaps. The plot assumes the largest physical electric field possible, which favors larger aspect ratios.

The aspect ratio can be increased through the use of patterned electrodes, which can be used to disrupt the natural spacing of the pillars. However, the natural spacing can only be reduced by a factor of ~ 0.5 since the electric field vectors begin to resemble those of a flat electrode as the protruding features are moved closer together.⁸ Consequently, one of the only ways to increase the aspect ratio is to physically stretch the pillars. This chapter focuses on the development and demonstration of an active gap tool designed to increase the aspect ratio of the pillars.

8.3 TOOL DESIGN

8.3.1 Mad City Labs Nanopositioner

Initially pillar stretching was attempted using a nanopositioner (Mad City Labs Nano-Align3). The nanopositioner, which uses piezo transducers to manipulate a stage, is designed for high resolution microscopy sample positioning. Figure 8.3 is a photograph of the nanopositioner mounted on a $\frac{3}{4}$ " thick aluminum frame elevated by laser table posts. The nanopositioner holds and positions the upper electrode, a metal coated microscope slide. The nanopositioner is elevated such that the lower electrode (i.e. the substrate) can be positioned beneath the upper electrode. The substrate is mounted on a custom designed stage that has clamps to both hold and ground the substrate. Once pillars form, the nanopositioner can increase the gap between the upper electrode and the grounded substrate to stretch the pillars.

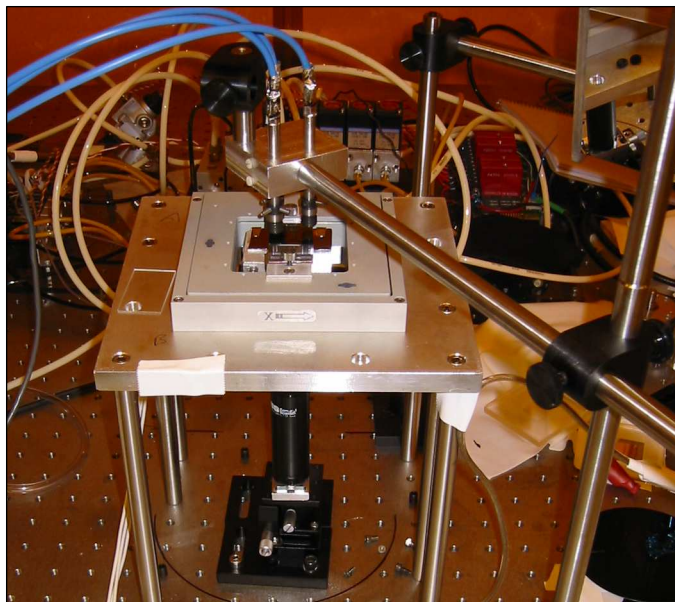


Figure 8.3: Photograph of a nanopositioner (Mad City Labs) mounted on an elevated aluminum frame.

The substrate positioning strategy is illustrated in Figure 8.4 and an additional photograph of the tool is shown in Figure 8.5. After mounting a silicon substrate (1 x 2 in), the stage was manually raised into proximity of the upper electrode by adjusting the coarse position of the post in the post-holder. The substrate stage was then brought into closer proximity of the upper electrode through use of micro-manipulators located on the vertical translation stage at the base of the post-holder. The interference fringe patterns between the upper electrode and substrate were visually monitored while simultaneously adjusting the tip-tilt controls on the tilt stage until the two electrodes were nearly parallel. A white light interferometer was used to measure the gap and pillars were formed by applying an electric field. The nanopositioner can be controlled externally by computer software provided with the tool.

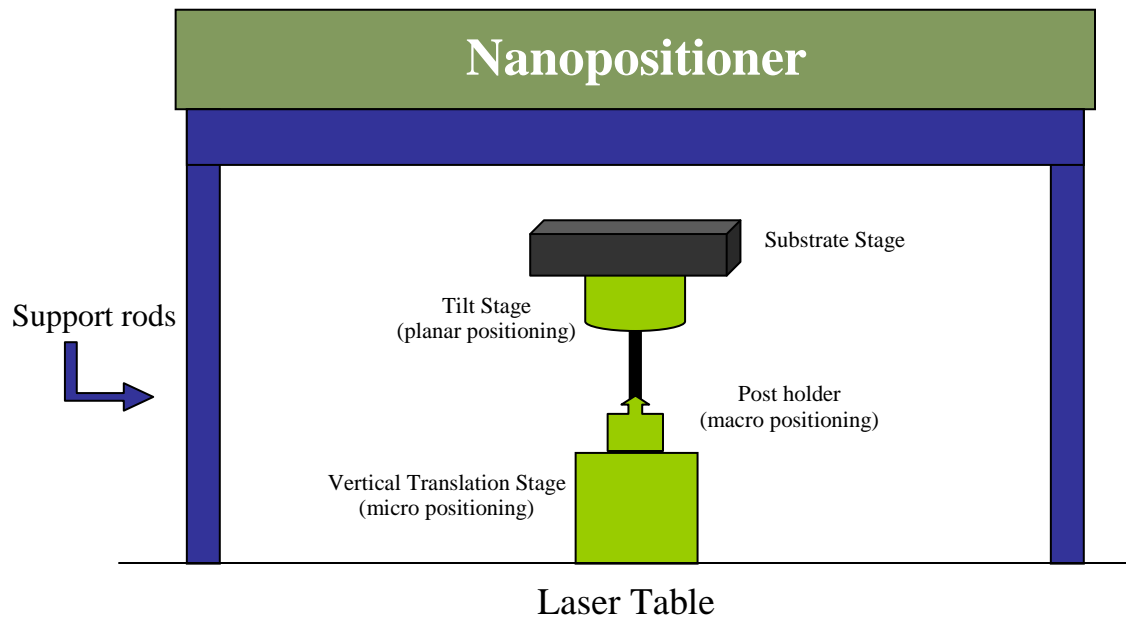


Figure 8.4: Schematic of substrate alignment scheme.

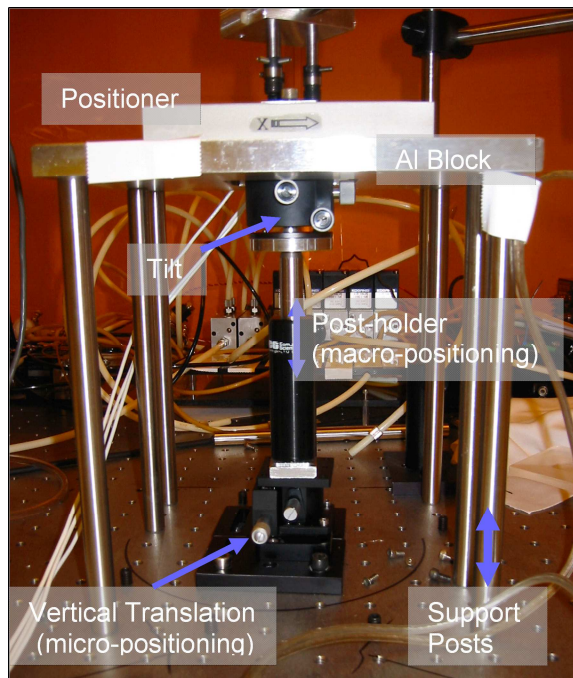


Figure 8.5: Side view of a labeled photograph of the substrate alignment scheme.

In principle, once pillars form, the nanopositioner can raise the upper electrode to stretch the pillars that span the electrodes. Figure 8.6 is a schematic of the nanopositioner and Figure 8.7 is a photograph of the nanopositioner experimental set-up.

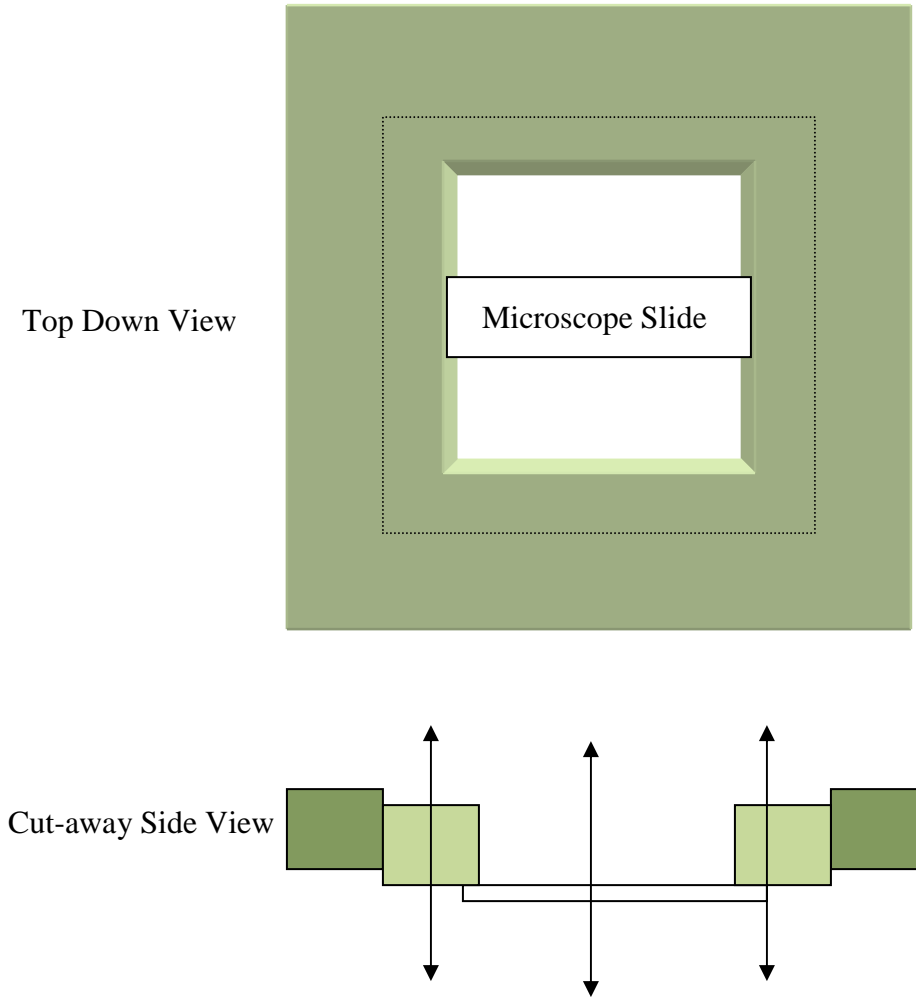


Figure 8.6: Schematic of the nanopositioner. A metal coated microscope slide, which served as the upper electrode, was mounted in the opening of the nanopositioner by L-brackets. Once mounted, the position of the inner portion of the nanopositioner was manipulated vertically, while the outer rim of the nanopositioner was mounted on a rigid aluminum block.

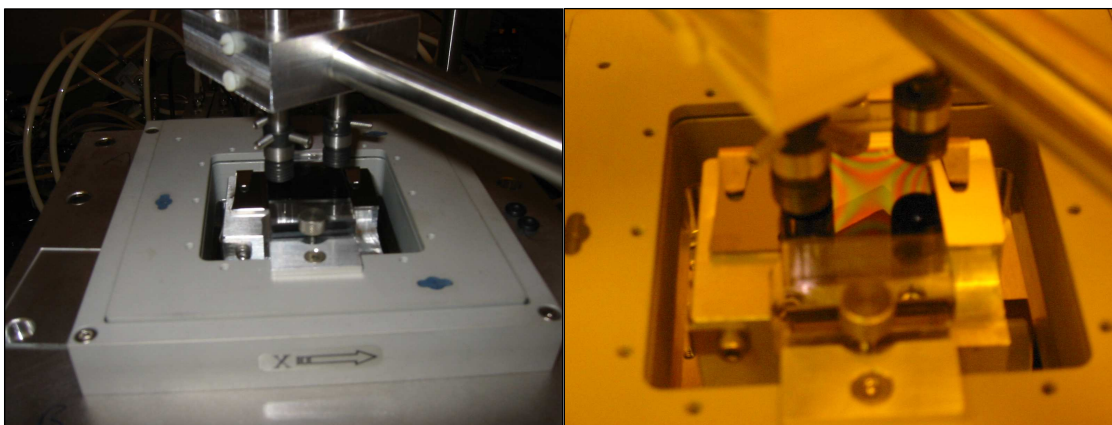


Figure 8.7: Tilt-view photographs of the nanopositioner during an experiment. In both images, three cylindrical optical spectroscopic sources are placed immediately above the sample. The long dimension of the substrate runs left to right, whereas the long dimension of the upper electrode (i.e. glass slide) runs top to bottom in both images. The fringe patterns between the upper electrode and substrate can be seen in the right image.

The nanopositioner had limited success in forming pillars. Figure 8.8 is a scanning electron micrograph of one of the few successful experiments that produced thiol-ene pillars.

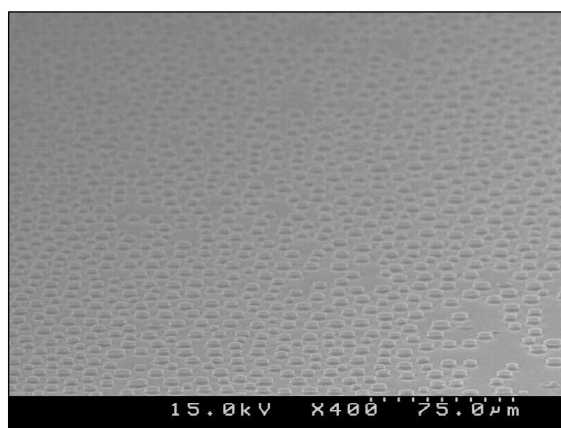


Figure 8.8: SEM image of thiol-ene pillars formed using the Mad City Labs nanopositioner.

The biggest obstacle to forming pillars consistently was the inability to reliably form a narrow electrode gap without the upper electrode touching the film on the substrate. Since the materials studied were low viscosity, the uniformity of the film rapidly degraded upon contact with the upper electrode, ultimately ruining the experiment. There were a number of specific problems which led to these experimental frustrations: (1) The substrate was not rigidly mounted and therefore was capable of moving, (2) The vertical translation movement was coarse (microns per fraction of a turn), (3) The tip-tilt controls were difficult to access because by necessity they were located in the cavity of the nanopositioner, and (4) The tip-tilt controls were coarse and were spring loaded, making them sensitive to the touch. In short, the controls utilized to manipulate the substrate were crude and very reliant on human intervention. The challenges associated with the nanopositioner led to the development of the active gap tool.

8.3.2 Active Gap Tool

The design of the active gap tool was a collaborative effort with Allen Raines and details of the tool can be found in his thesis (Department of Mechanical Engineering, University of Texas at Austin, 2006). The tool will be briefly discussed here to provide a context of understanding.

The active gap tool is illustrated in Figure 8.9. The tool is designed to accommodate 4 in. wafers, which are mounted rigidly using a ceramic vacuum chuck. The mounted substrate slightly overhangs the edge of the chuck, allowing the substrate to be grounded using an alligator clip. The upper electrode consists of a 65x65 mm quarter inch fused silica template, similar to those used in Step and Flash Imprint Lithography. The template must be both clear and conductive, typically accomplished by adding a

~100 nm coating of indium tin oxide (ITO). The details of the template fabrication process are provided in Chapter 9. The template was vacuum mounted on a flexure ring. The position of the flexure ring was manipulated by three computer controlled servo motors.

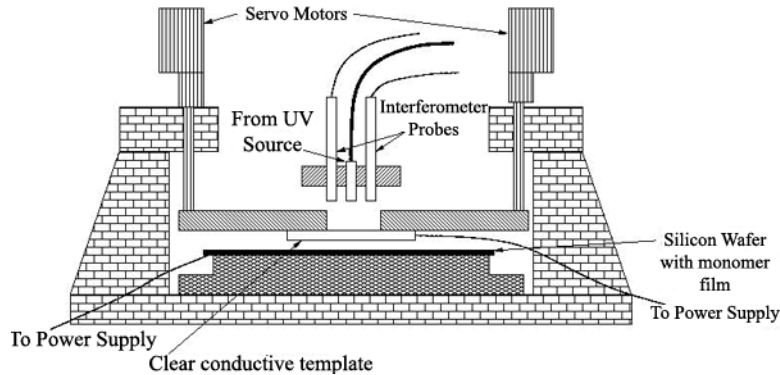


Figure 8.9: Labeled illustration of the active gap tool. Only 2 of the 3 servo motors and interferometer probes are shown in this cut-away depiction.

The gap between the template and the film coated substrate was monitored by 3 interferometric spectroscopy probes, which monitor the interference patterns generated by white light reflecting off the substrate. The concept of the gap monitoring scheme is illustrated in Figure 8.10.

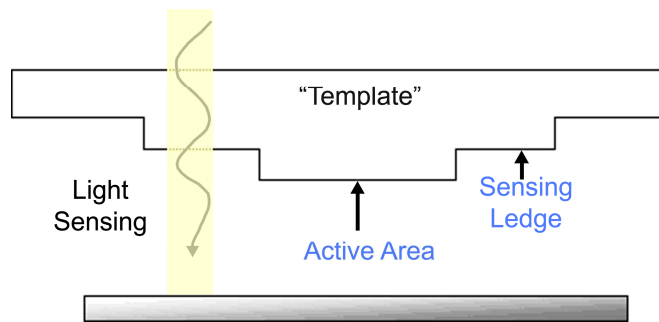


Figure 8.10: Side view schematic of the template and the gap monitoring scheme. Light passes through the template and reflects off the substrate. A spectrometer measures the reflected light spectrum to determine the gap thickness. The sensing ledge is typically 0-5 microns recessed from the active area mesa.

The active gap tool utilizes pneumatics to coarsely move the substrate / vacuum chuck assembly up and down. This is a requirement for loading and unloading samples. Once loaded, the substrate position was fixed while the template was manipulated with sub-micron resolution to achieve final positioning.

The first step to form pillars was to install a clean template. A bare wafer was also installed and the two electrode surfaces were aligned such that the surfaces were coplanar. This step was required to maximize the interferometer signals ultimately used for sample positioning. The template was then retracted by ~ 100 μm for safety considerations and the substrate was lowered several inches pneumatically. The wafer was removed and a film was spin coated on the substrate. The thin film coated wafer was mounted on the vacuum chuck and grounded. The chuck assembly was then rapidly raised pneumatically back to within ~ 100 μm of the template. The final fine positioning was done using the servo motors, which manipulate the position of the template within a few microns of the substrate. The entire alignment process was interfaced with Lab View computer controls. For gaps below ~ 3 microns, a protruding active area was utilized (Figure 8.10). If the protrusion depth was known, then the final gap was simply the measured gap minus the protrusion depth.

After forming pillars, the servo motors were utilized to raise the upper electrode an assigned distance. The final gap was measured by interferometry and the substrate was irradiated through the template to photocure the pillars. The substrate was lowered pneumatically and the resulting separation force was monitored by in-line piezo force sensors.

A photograph of the active gap tool is shown in Figure 8.11. Results of experiments using this tool are discussed in the following sections.

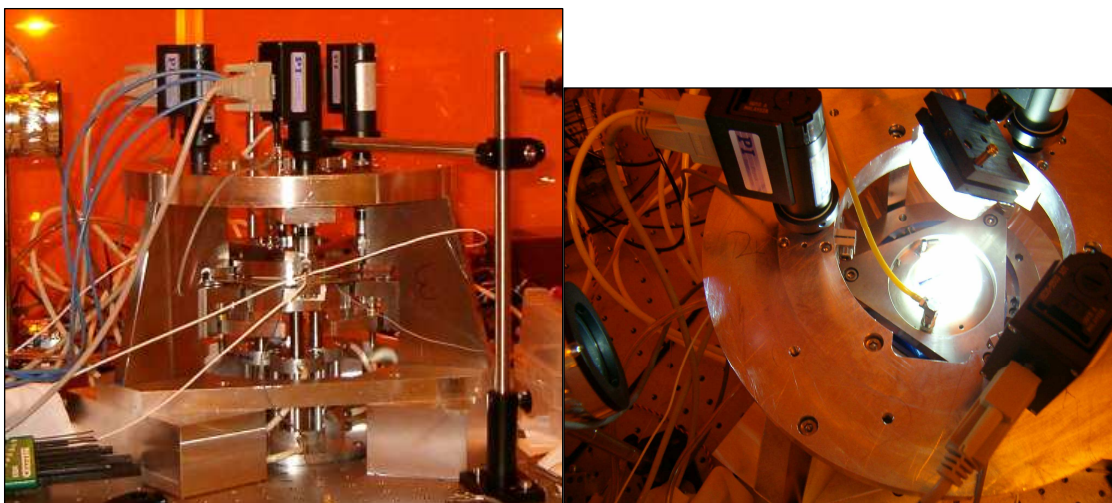


Figure 8.11: Photographs of the active gap tool. (Left) A side view of the tool. The interferometers are mounted on the boom arm, but cannot be seen from this view. The interferometers are identical to those seen in Figure 8.7. (Right) A top down view of a sample being irradiated. The triangular frame holds the template by vacuum and is mounted to the flexure ring that surrounds it. The three black servo motors can be seen in both images.

8.4 ACTIVE GAP TOOL STRETCHING RESULTS

8.4.1 Stretching Pillars

The active gap tool provides rigid substrate mounting and finer external control of the positioning of the electrodes than the tool described in Section 8.3.1. Consequently, the active gap tool was successful in both forming and stretching pillars.

Figure 8.12 is a photograph of an irradiated 4 in. wafer partially covered with pillars formed using the active gap tool. The irradiated light is apparent by the “halo” of light that surrounds the perimeter of the wafer. The pillars scatter the irradiated light, resulting in a glowing appearance in the center of the sample. Although the entire substrate is covered with film, the pillars only form under the 1x1” active area where the electric field is applied by the template. Additional control experiments showed that the film is stable until the electric field is applied and pillars only form under the mesa.

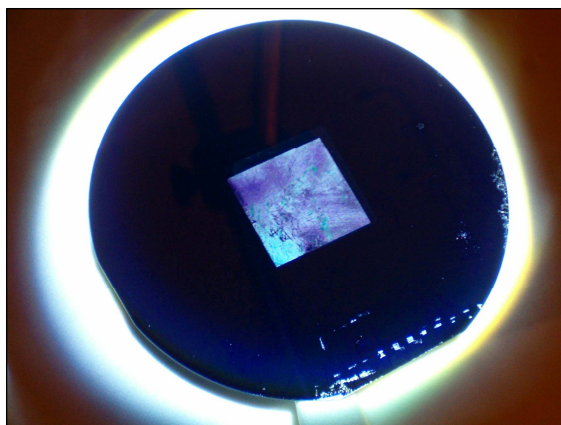


Figure 8.12: Photograph of a 4 inch wafer illuminated with light. The 1x1 inch square in the center is covered with pillars and consequently scatters the illuminated light. Tongs used to handle the wafer also leave marks at the wafer edge.

Figure 8.13 is a representative SEM image of an array of thiol-ene pillars formed using the active gap tool without stretching. In contrast, Figure 8.14 provides SEM images of a stretched pillar arrays formed using similar initial starting conditions as those used in Figure 8.13. A notable fraction of the structures in Figure 8.14a are puddles, indicative of pillars that broke as they reached their physical stability limit.

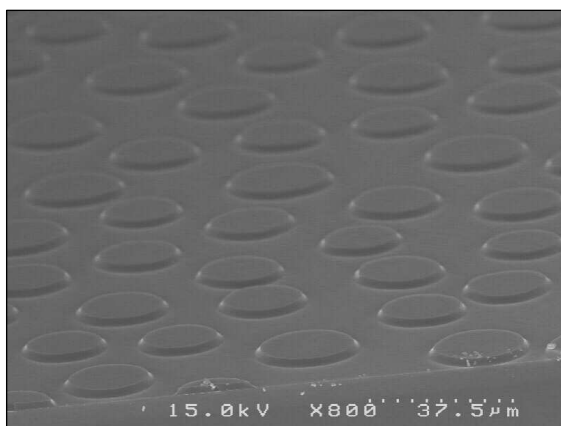


Figure 8.13: Tilt-view SEM of thiol-ene pillars formed using the active gap tool without stretching.

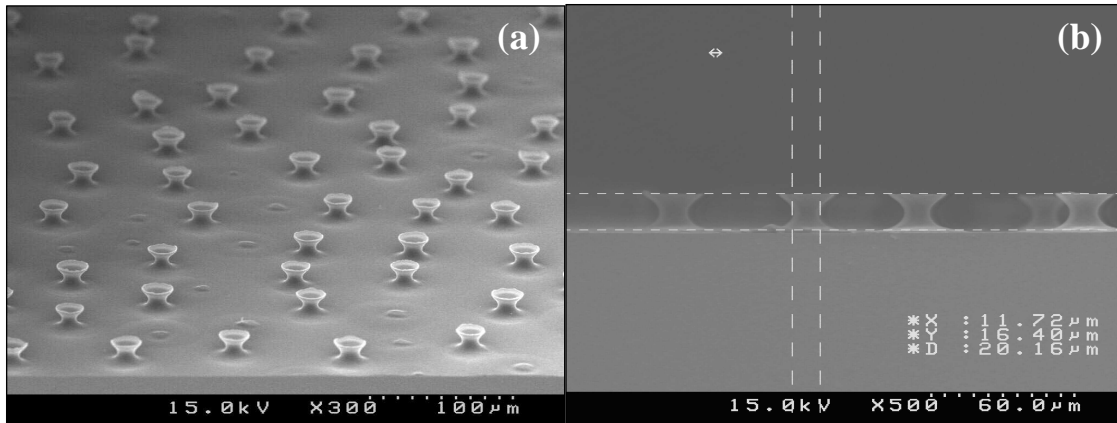


Figure 8.14: SEM images of stretched pillars. (a) Tilt-view SEM image shows that several of the pillars broke during stretching. (b) Side-view SEM shows that pillars were stretched to 16.4 microns in height.

8.4.2 Stretching Limits

At a certain point during stretching, the geometry of the pillar becomes unstable as surface forces conspire to minimize the overall surface energy of the structure. There is a large body of literature on the stability of “liquid bridges” because of their use in float zone melting. Liquid bridges are axisymmetric fluid structures held by surface tension between two disks. In essence, pillars are liquid bridges that span two surfaces and thus the analysis used for liquid bridges is applicable here.¹⁰

Plateau and Rayleigh were the first to study the stability of liquid cylinders.^{11,12} Their work suggests that the stability of a perfect cylinder occurs when the aspect ratio reaches π , which is called the Rayleigh-Plateau limit. Subsequent work has confirmed this value and analysis has been extended to non-cylindrical geometries.^{13,14} The equilibrium shape and stability of a liquid bridge is characterized by the aspect ratio (also called slenderness), Λ , and the relative volume, V . The relative volume is defined as the ratio of the volume of material in the liquid bridge, u , divided by the theoretical volume of a perfect cylinder defined by the diameter at the base of the column, D .

$$\Lambda = \frac{H}{D}$$

$$V = \frac{4u}{(\pi D^2 H)}$$

Liquid bridge stability is determined through analysis of two ordinary differential equations based on the capillary equation and conservation of mass.^{13,14} The boundary conditions are dictated by the contact angle.^{13,14} Structures are considered stable if they can withstand small perturbations. Figure 8.15 is the stability diagram for liquid bridges as a function of Λ and V .

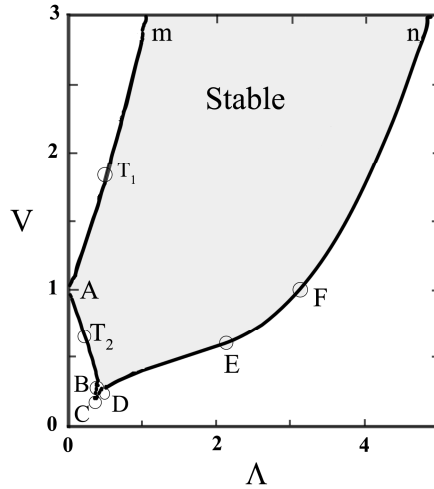


Figure 8.15: Liquid bridge stability diagram. The liquid bridge is stable in the region defined by points m-A-C-n (shaded grey).¹⁵

At the upper boundary in Figure 8.15, the liquid bridge loses its stability to non-axisymmetric perturbations, whereas the right portion of the lower boundary loses its stability to axisymmetric perturbations (i.e. it pinches off to form two hemispheres).¹⁶ This region is most relevant to the pillar stretching instabilities. The lower left portion of Figure 8.15 becomes unstable by detachment of the wetting line from the edges of the

disks.¹⁶ Essentially, this region is irrelevant to pillar instabilities since the pillar contact line is not pinned like the traditional liquid bridge structures.

Point F in Figure 8.15 corresponds to the conditions described by Plateau in which V is 1 (i.e. perfect cylinder) and the aspect ratio is π . When pillars initially form (Figure 8.13), they are located approximately near the letter “A” on the stability diagram ($V \sim 1$, $\Lambda \sim 0.1$). Upon stretching, the pillars have V values less than 1, as shown in Figure 8.16, with shapes that resemble a catenoid.

Technically, a catenoid is defined by the shape taken by a soap film suspended between two rings. Catenoids with aspect ratios above 0.47 are unstable. An unstable catenoid can be stabilized by filling in the theoretical volume with liquid such that the interior of the structure can have a pressure that differs from the surrounding medium. By adjusting the volume so the pressure is positive or negative, one gets the surfaces known as unduloids and nodoids, respectively.

Pillars are constant volume structures that typically have a relative volume less than one, implying that the stability limit will be less than π .¹⁰ Slobozhanin et al predict that for a liquid bridge with a contact angle of $\sim 35^\circ$ (estimated by contact angle measurements), the stability will have a maximum Λ between 0.5-0.7 for V values between 0.2-0.4.

Experimentally, the largest aspect ratio thiol-ene pillars obtained by stretching under typical formation conditions (~ 3.5 μm initial gap, 40 V, 800 nm initial film) were shown to be ~ 0.5 (Figure 8.16). The relative volume of the structure in Figure 8.16 is approximately 0.2 based on a 3-dimensional integral. Thus, the maximum aspect ratio for this volume fraction is nearly identical to that predicted by theory.

The stability limit was verified by in situ optical microscopy (Borescope), which was used to monitor the stretching process. Once $\sim 50\%$ of the pillars were broken,

stretching was halted and the remaining structures were photocured. Figures 8.14 and 8.15 are indicative of samples stretched to the stability limit. Figure 8.16 is a side view SEM image of a pillar with an aspect ratio of ~ 0.5 . Obviously the limit is even larger if the diameter is measured from the narrowest point (~ 1.5).

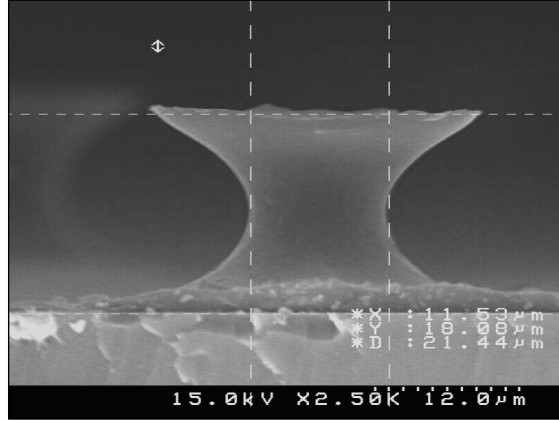


Figure 8.16: High aspect ratio pillar formed by stretching using the active gap tool.

Although the experimentally observed limit agrees closely with theory, there are several experimental limitations that may cause deviations from theory. First, the system is subject to both gravity and vibrations, non-idealities that are unaccounted for in the theory. The small length scale of the pillars should make gravity negligible compared to the surface forces (i.e. the Bond number is small). However, vibrations during stretching could prematurely induce an instability.

The stability diagram in Figure 8.15 does not account for the impact of the applied electric field, which has been previously studied for liquid bridges.¹⁷⁻¹⁹ Ramos et al showed that the theoretical electric field stabilization effects for liquid bridges with dimensions similar to those of pillars are negligible.¹⁷ Experimentally, there were no observable differences in the stability limit when stretching with or without electric fields. Properly modeling the effects of electric fields on the pillar geometry is non-

trivial since the fields can also change the contact angle through a process known as electrowetting,²⁰ a process described by the Lippmann equation.¹⁹ The contact angle of thiol-ene on ITO is similar to that observed during pillar formation ($\sim 30^\circ$), suggesting that the voltages are not large enough to induce significant changes.

Pillars can be stretched beyond the theoretical stability limit by retarding the instability through control of the material properties. This is akin to the methods used to draw fibers, in which the aspect ratio of the fibers can begin to approach infinity in continuous processes. Figure 8.17 shows high aspect ratio thiol-ene fibrils. These fibrils formed inadvertently and are believed to have partially cured during stretching due to “electrocuring” (see Chapter 6). Despite attempts to repeat these results in a controlled manner, this concept was not repeatable. Figure 8.17 simply illustrates that the stability limit can be exceeded to form high aspect ratio fibrils. Future work should focus on controlling the photocuring process to maximize the aspect ratio through control of the material properties.

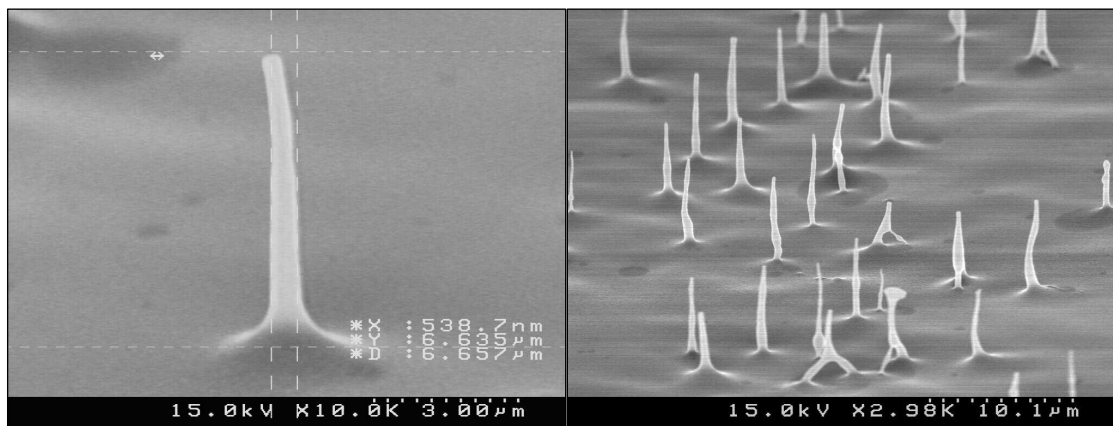


Figure 8.17: SEM images of high aspect ratio thiol-ene fibrils.

Liquid bridge instabilities also impact the ability to stretch features of arbitrary dimension. Chapter 7 discusses the use of patterned electrodes to generate features of arbitrary geometry. During stretching, these features resolve into single pillars as shown in Figure 8.18. The effects of “electrocuring” are evident as the original Longhorn pattern remains visible post-stretching.

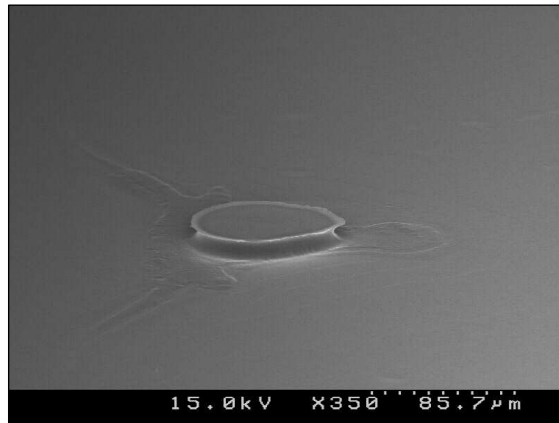


Figure 8.18: A longhorn formed via a patterned electrode resolves to a single pillar upon stretching.

8.4.3 Active Gap Tool Capabilities and Limits

The two most significant limitation of the active gap tool are (1) the inability to apply heat, which limits the types of materials that can be utilized and (2) the inability to apply large electric fields. Large electric fields generate forces that are significant enough to cause the upper electrode to “suck down” to the lower electrode. Suck down ruins experiments because the exact gap at the time of pillar formation is unknown. In many cases, template suck down destroys the expensive templates since the electrodes short upon contact.

The other limitation of the active gap tool is the minimum achievable gap. It is very difficult to achieve gaps below 2 microns without the use of a sensing ledge, shown

in Figure 8.10. The smallest gap to date that successfully formed pillars is ~560 nm, as shown in Figure 8.19.

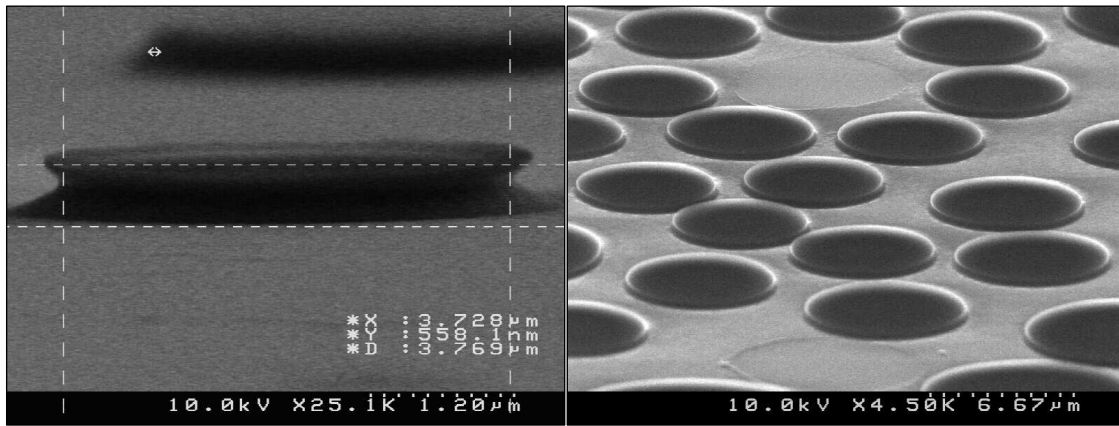


Figure 8.19: Small electrode gaps (~560 nm) formed using the active gap tool with a sensing ledge template.

Work is in progress by Allen Raines to increase the stiffness of the tool. Doing so would reduce the occurrence of suck down that is problematic with the current tool. Furthermore, the newer version of the active gap tool will use a modified positioning strategy that will allow for the formation of smaller gaps through the use of piezo electric motors.

8.5 HIGH ASPECT RATIO POLYMERIC PILLARS

8.5.1 Stretching polymeric pillars

The active gap tool is only designed to operate at ambient temperature; therefore it is not possible to process polymeric materials with T_g 's above room temperature. Polymeric pillars can be processed using the “glass slide” method described in Chapter 4 (Figure 4.7), but this method provides no controllable mechanism for stretching. Signs of stretching are occasionally observed when the upper electrode is separated from the pillar

array for polymers with low T_g . Stretching is only observed with non-treated templates in which adhesion is strong between the upper electrode and the pillars.

Polymers that “neck” under tensile stress may be ideal for forming high aspect ratio fibrils. Poly(caprolactone) (PCL, Dow Tone Polymer P-767) is an inexpensive polymer whose room temperature stress strain curve levels off at ~50% strain, indicative of a “necking” polymer.²¹ Figure 8.20 is a scanning electron micrograph of PCL pillars that formed high aspect ratio structures upon upper electrode removal. The pillars were initially formed by applying 150 V across a 6 μm gap to a 800 nm film (formed out of an 8 wt% toluene solution) at 60°C. The structures were cooled to room temperature prior to upper electrode removal. Several of the pillars released cleanly from the electrode without stretching, and serve as a basis for comparison.

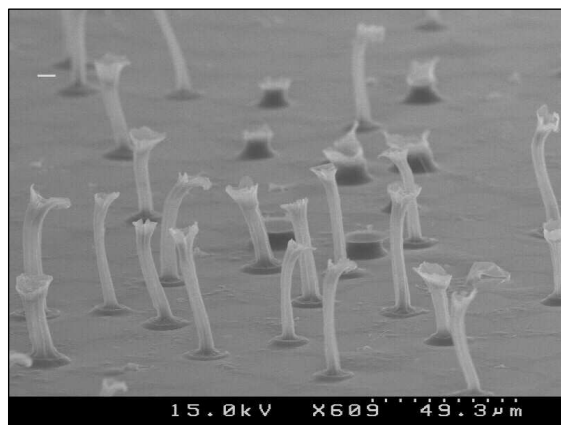


Figure 8.20: PCL pillars stretched during upper electrode removal.

The results in Figure 8.20 suggest that the ability to control the temperature on future active gap tool designs may be worth pursuing.

8.5.2 Viscoelastic polymers

Viscoelastic polymers naturally form high aspect ratio pillars without stretching. Figure 8.21a is a SEM image of polylactic acid (PLA) pillars. These pillars were formed by first spin casting a 900 nm film out of a 10 wt% PLA (Birmingham Polymers: D02038, $T_g \sim 60^\circ\text{C}$), 20 wt% acetonitrile, and 70% propylene glycol monomethyl ether acetate (PGMEA) solution. A 200 V potential was applied across a $\sim 5\ \mu\text{m}$ gap at 75°C until it was apparent pillars had formed ($\sim 15\ \text{min}$).

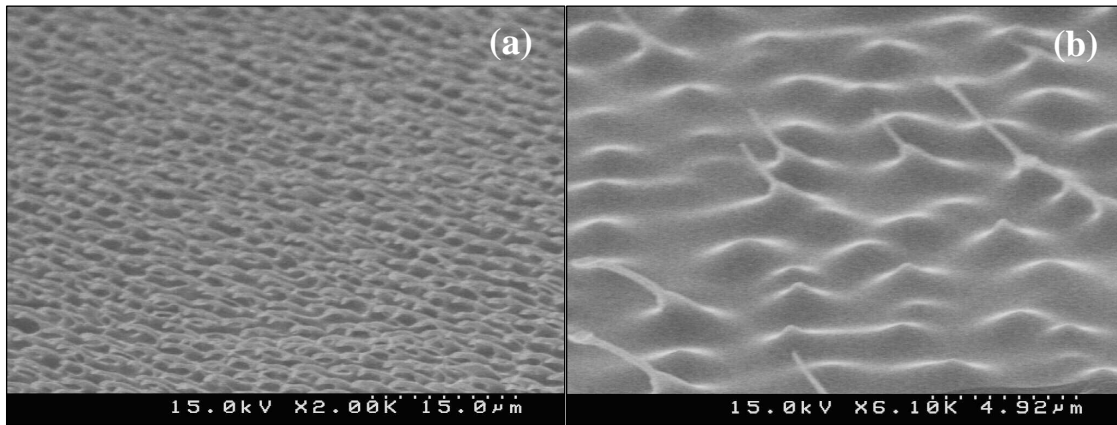


Figure 8.21: SEM images of PLA pillar arrays. (a) Overview. (b) Fibrils in the initial stages of growth.

The fibrils shown in Figure 8.21 are only a couple hundred nanometers in diameter and deviate significantly from the theoretical spacing and aspect ratio. For these operating conditions, linear stability analysis predicts the spacing to be $\sim 45\ \mu\text{m}$ (the dielectric constant of PLA is low,²² favoring larger wavelengths), corresponding to an aspect ratio of ~ 0.23 . The fibril wavelength in Figure 8.21 appears to be $2.5\text{--}3\ \mu\text{m}$, over an order of magnitude smaller than that predicted by theory. Similarly, the aspect ratio is well over 10:1, significantly higher than theoretical predictions.

The remarkable structures in Figures 8.21 are in stark contrast to “traditional pillars” formed with fluid films (e.g. low viscosity materials, such as thiol-ene, discussed in Chapter 6 or polymers heated significantly above T_g , such as PMMA, discussed in Chapter 5). PLA forms “traditional pillars” at elevated temperatures (~ 40 °C above T_g) suggesting that the viscoelastic properties of the polymer, which become more significant as the processing temperature approaches T_g , play a significant role in the formation of fibrils. Figure 8.22 is a scanning electron micrograph of PLA pillars formed at 100 °C. Under these processing conditions (200 V, 900 nm film, 2.5 μm gap), linear stability predicts a characteristic spacing of ~ 10 μm , consistent with the structures shown in Figure 8.22.

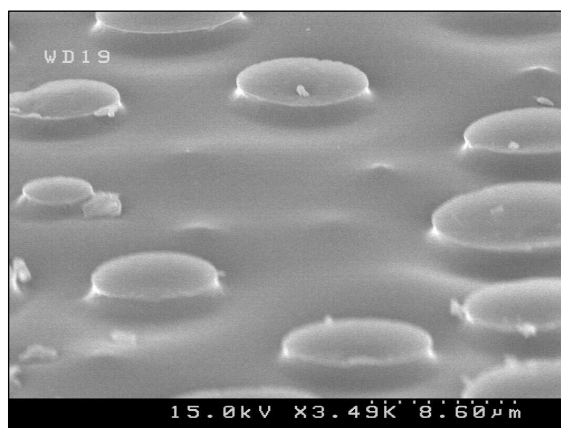


Figure 8.22: PLA pillars formed at 100 °C, 200 V, 2.5 μm gap.

The formation of fibrils is most pronounced with elastomeric materials such as PLA, poly(butadiene), and poly(isoprene). However, fibril formation has also been observed with PMMA, a common thermoplastic polymer used in numerous literature studies of pillars.^{1,23-25} PMMA forms “traditional pillars” at elevated temperatures (180-200 °C), as shown in the left image of Figure 8.24, with the wavelength predicted by linear stability analysis.² PMMA, however, forms fibrils at lower temperatures (~ 140

°C), as shown in the right image of Figure 8.24. This observation suggests that (1) the fibrils form in polymers with vastly different properties and (2) the polymer elasticity, which become prominent near T_g , must be playing a key role in the formation of these fibrils.

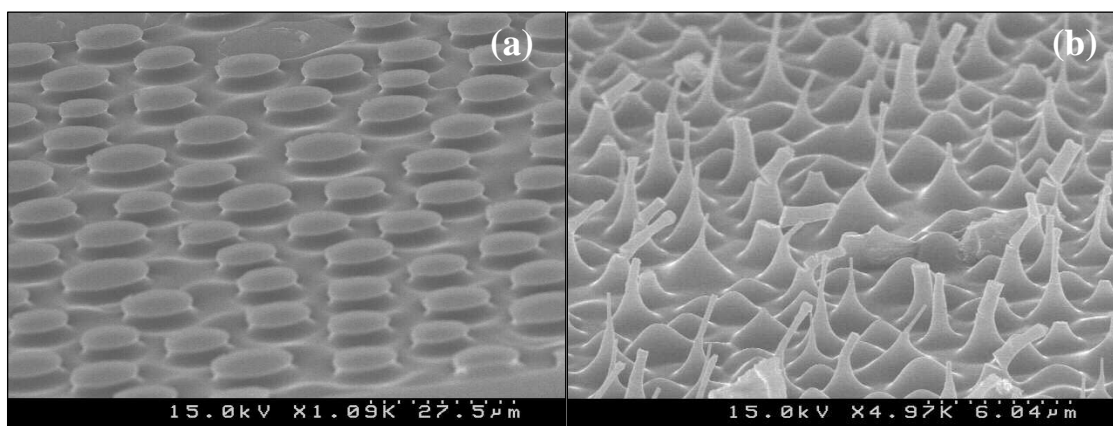


Figure 8.23: SEM images of PMMA pillars. (a) Pillars formed at 180 °C have “traditional” morphologies, with characteristic wavelength predicted by linear stability analysis. (b) Pillars formed at 140°C, closer to T_g , have wavelengths and aspect ratios that deviate significantly from theory.

Since multiple polymers form fibrils near their T_g , we hypothesize that the elastic properties of the films are responsible for the deviation from linear stability theory, which assumes a Newtonian fluid. To test this hypothesis, the rheological properties of PMMA and PLA were measured using a Rheometrics ARES. Figure 8.24 is a plot of the storage modulus (G'), the loss modulus (G''), and tan delta (G''/G') for PLA at 0.01 s^{-1} frequency. This frequency was chosen because it is representative of the time scale with which fibrils and pillars form. Similarly, Figure 8.25 is a plot of the same properties for PMMA plotted at 0.001 s^{-1} .

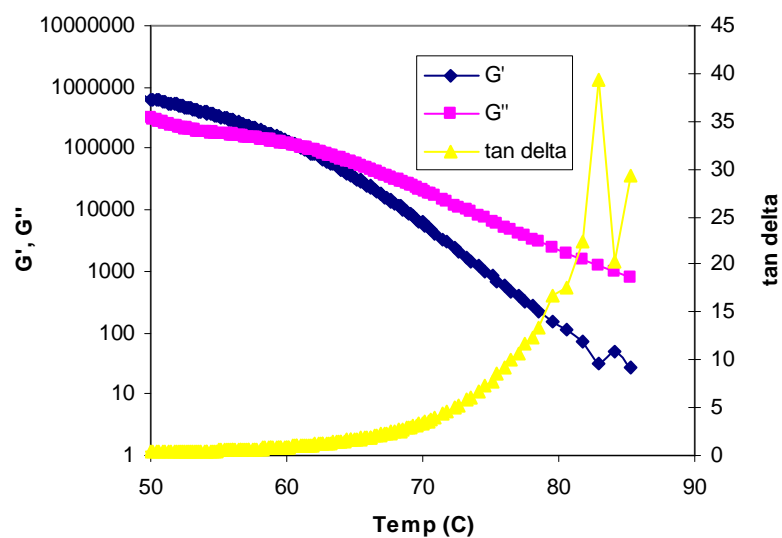


Figure 8.24: PLA rheological properties plotted at 0.01 s^{-1} frequency

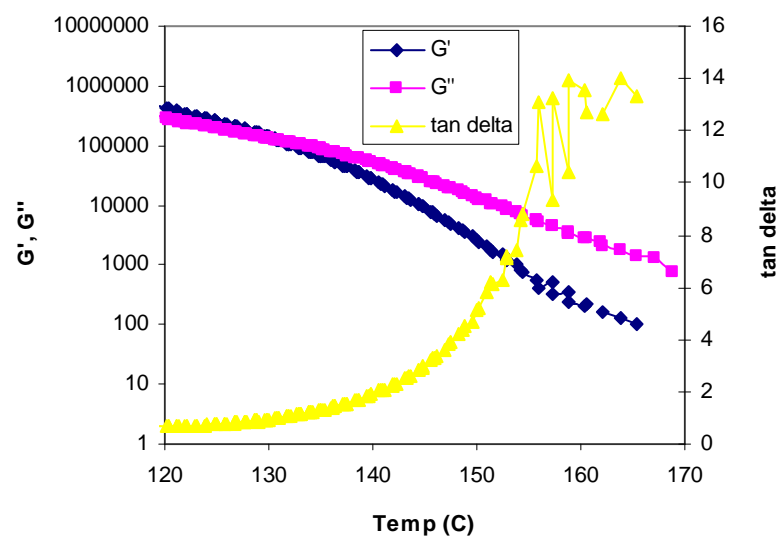


Figure 8.25: PMMA rheological properties plotted at 0.001 s^{-1} frequency

Rheological properties for both materials were measured over a wide range of frequencies at 6 different temperatures spanning a range of 60 degrees. The data in

Figures 8.24-8.25 were fit using the classical Williams-Landel-Ferry model with the parameters below.²⁶

| | | | |
|-------|--------------|--------------|--------------------------------------|
| PMMA: | $C_1=9.1079$ | $C_2=163.02$ | $T_{\text{ref}} = 170^\circ\text{C}$ |
| PLA: | $C_1=8.1606$ | $C_2=67.485$ | $T_{\text{ref}} = 70^\circ\text{C}$ |

The most striking aspect of Figures 8.24-25 is that tan delta spikes in the temperature region where “traditional pillars” form (i.e. $T > 160^\circ\text{C}$ for PMMA and $T > 90^\circ\text{C}$ for PLA). Similarly, tan delta plateaus in the temperature region where fibrils form (i.e. $T = 140^\circ\text{C}$ for PMMA and $T = 75^\circ\text{C}$ for PLA). These results are consistent with theory. When tan delta spikes, the viscous effects become dominant and linear stability is more likely to apply, resulting in “traditional pillars”. In the region in which tan delta levels out, elastic properties dominate and deviations from linear stability should be expected. Therefore, elasticity must be accounted for in the modeling to account for the fibrils.

The effect of viscoelasticity on pillars was modeled by Wu et al²⁵ in an attempt to understand why some processing conditions produce well organized structures. The film was assumed to be non-Newtonian and obey the Oldroyd-B constitutive equation.²⁷ The model shows that the elasticity and the electric field induced instability act in resonance when the Deborah number is large. The key finding from this work is that viscoelastic films form pillars with identical characteristic spacings as non-elastic films, but at a much faster rate (which they claim explains the improved order seen in certain experiments). Thus, this model does not predict the unique features seen in Figure 8.21, nor does it provide any experimental evidence for the claims made within the model.

We hypothesize that the smaller characteristic wavelength is better modeled using contact elastic instability theory.²⁸⁻³⁰ This theory predicts that the characteristic spacing scales like $\sim 3.5 h$, a function of film height only. The PLA fibrils (Figure 8.21) and the PMMA fibrils (Figure 8.23b) both have $\sim 3 \mu\text{m}$ wavelengths, which is in nearly perfect agreement with this theory considering both initial films were $\sim 900 \text{ nm}$. This is remarkable considering the differences in the rheological and dielectric properties of the polymers. Future work should investigate different thickness films to determine whether the spacing can be tuned with thickness.

The cause for the high aspect ratio fibrils is believed to be due to the strong electrostatic forces at the peak of the surface undulations. There is a significant resistance to flow since the material is close to the T_g , but the large electrostatic forces concentrated at the tip of the undulation (see right image in Figure 8.21) cause the material to elongate. This is reminiscent of a Taylor cone, in which a spout of water emerges in the form of a cone as large electric fields are applied normal to a film of water.^{31,32} Taylor cones have semi-angles of 49.3° . The undulations in Figure 8.22a and 8.25b appear to have similar cone semi-angles at the point of fibril emission.

Similar to Taylor cones, the fibril structures appear to begin as mounds that evolve into cones that eventually release a fibril at the tip, which experiences the largest electric fields. The initial stages of PMMA fibril formation are captured in Figure 8.26. This image is similar to the early stages of fibril formation in PLA, as captured in Figure 8.21 (right image).

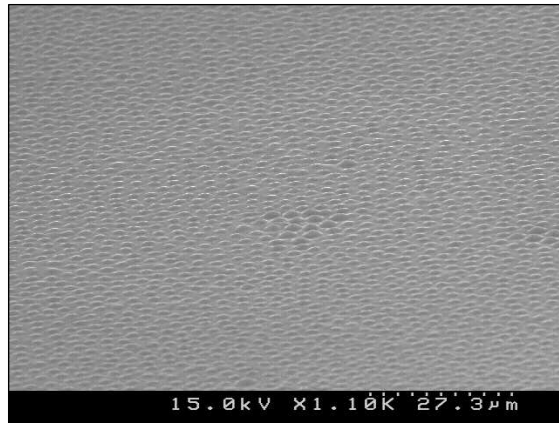


Figure 8.26: PMMA undulations formed at 140°C.

Once the fibrils span the electrodes, they are believed to coarsen over time. Figure 8.27 is a series of images taken from a sample with slightly wedged capacitor geometry, resulting in structures with different rates of growth.

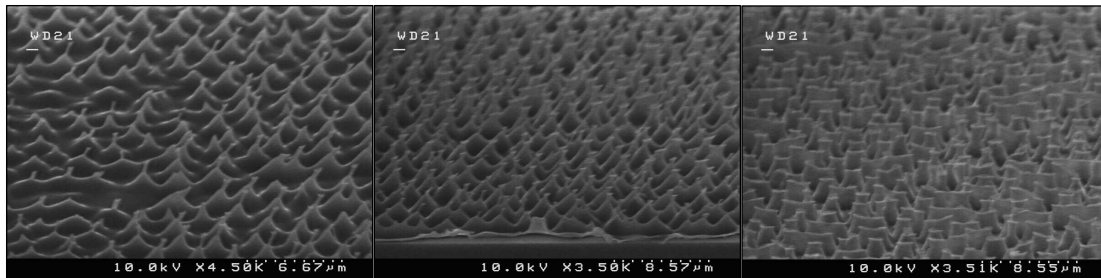


Figure 8.27: A series of SEM images of PLA pillars at different stages of growth. The fibrils thicken as material is entrained in the pillar, but the spacing stays approximately the same.

In summary, viscoelastic polymers form fibril structures when the elastic properties become dominate (i.e. near T_g). The fibrils have characteristic wavelengths much smaller than that predicted by linear stability analysis, which assumes a viscous fluid. Elastic contact theory appears to capture the initial data well, but more experiments are needed to confirm the validity of this theory for this process. As the electric field is

applied, the structures initially form mounds that evolve into Taylor cones. At the tip of the cone, a fibril is emitted due to the concentrated electric field. With time, this high aspect ratio fibril coarsens as more material is drawn into the structure. Viscoelastic polymers offer an elegant way to form pillar structures with aspect ratios and characteristic wavenumbers that exceed the limits observed with low viscosity films.

8.6 CONCLUSIONS

Low viscosity films (e.g. thiol-ene) form pillars with low aspect ratios, in a manner similar to thermoplastic polymers described in literature.¹ The aspect ratio can be predicted by combining linear stability analysis with a mass balance. Theory suggests that the only way to increase the aspect ratio is to stretch the structures post-formation. An active gap tool was built and successfully stretched the pillars. The aspect ratio was increased from ~0.1 to ~0.5, which is the theoretical limit for the pillar geometry, as predicted by liquid bridge stability analysis. The aspect ratio can be increased further by retarding the bridge instability via control of the material properties. High aspect ratio thiol-ene structures were formed by this route, but the results were not repeatable.

The active gap tool is not designed to operate above ambient conditions, thus polymeric materials were not explored. However, the “slide glass” method demonstrated that “necking” polymers can be stretched beyond the stability limit in a manner similar to drawing fibrils.

Viscoelastic polymers were shown to form high aspect ratio structures with small characteristic wavelengths that significantly deviate from theory. Multiple polymers showed this behavior when processed slightly above T_g , suggesting that the elastic properties may be playing a role in the phenomenon. Linear stability analysis, the classical model for pillars, assumes a viscous liquid, rendering it inappropriate for these

materials. Contact theory appears to accurately predict the characteristic spacing observed with these structures, but more experiments need to be performed to confirm this finding. The fibril structures initially grow as mounds that evolve into cones reminiscent of Taylor cones. These cones emit a fibril because of the enhanced electric field at the tip of the cone. The fibril coarsens with time as more material is drawn into the structure.

Stretching and viscoelastic polymers are two promising routes to forming high aspect ratio structures.

8.7 REFERENCES

1. Pease, L. F., III; Russel, W. B., Limitations on Length Scales for Electrostatically Induced Submicrometer Pillars and Holes. *Langmuir* **2004**, 20, (3), 795-804.
2. Schaffer, E.; Thurn-Albrecht, T.; Russell, T. P.; Steiner, U., Electrically induced structure formation and pattern transfer. *Nature* **2000**, 403, (6772), 874-877.
3. Herminghaus, S., Dynamical Instability of Thin Liquid Films Between Conducting Media. *Physical Review Letters* **1999**, 83, (12), 2359-2361.
4. Pease, L. F.; Russel, W. B., Electrostatically induced submicron patterning of thin perfect and leaky dielectric films: A generalized linear stability analysis. *Journal of Chemical Physics* **2003**, 118, (8), 3790-3803.
5. Lin, Z.; Kerle, T.; Russell, T. P.; Schaeffer, E.; Steiner, U., Structure Formation at the Interface of Liquid/Liquid Bilayer in Electric Field. *Macromolecules* **2002**, 35, (10), 3971-3976.
6. Schaffer, E.; Thurn-Albrecht, T.; Russell, T. P.; Steiner, U., Electrohydrodynamic instabilities in polymer films. *Europhysics Letters* **2001**, 53, (4), 518-524.
7. Pease, L. F.; Russel, W. B., Linear stability analysis of thin leaky dielectric films subjected to electric fields. *Journal of Non-Newtonian Fluid Mechanics* **2002**, 102, (2), 233-250.
8. Verma, R.; Sharma, A.; Kargupta, K.; Bhaumik, J., Electric Field Induced Instability and Pattern Formation in Thin Liquid Films. *Langmuir* **2005**, 21, (8), 3710-3721.

9. Lin, Z.; Kerle, T.; Baker, S. M.; Hoagland, D. A.; Schaffer, E.; Steiner, U.; Russell, T. P., Electric field induced instabilities at liquid/liquid interfaces. *Journal of Chemical Physics* **2001**, 114, (5), 2377-2381.
10. Erle, M. A.; Gillette, R. D.; Dyson, D. C., Stability of Interfaces of Revolution with Constant Surface Tension-The Case of the Catenoid. *The Chemical Engineering Journal* **1970**, 1, (1), 97-109.
11. Plateau, J., *Experimentale et Theoretique des Liquides*. 1873.
12. Rayleigh, L., On the capillary phenomena of jets. *Proceedings of the Royal Society of London* **1879**, 29, (71).
13. Myshkis, A. D., *Low-gravity fluid mechanics: mathematical theory of capillary phenomena*. Springer-Verlag: Berlin; New York, 1987; p xix, 583.
14. Slobozhanin, L. A.; Perales, J. M., Stability of liquid bridges between equal disks in an axial gravity field. *Physics of Fluids A: Fluid Dynamics* **1993**, 5, (6), 1305-14.
15. Slobozhanin, L. A.; Alexander, J. I. D.; Resnick, A. H., Bifurcation of the equilibrium states of a weightless liquid bridge. *Physics of Fluids* **1997**, 9, (7), 1893-1905.
16. Slobozhanin, L. A.; Alexander, J. I. D.; Patel, V. D., The stability margin for stable weightless liquid bridges. *Physics of Fluids* **2002**, 14, (1), 209-224.
17. Ramos, A.; Gonzalez, H.; Castellanos, A., Bifurcation diagrams of axisymmetric liquid bridges subjected to axial electric fields. *Physics of Fluids* **1994**, 6, (11), 3580-90.
18. Sankaran, S.; Saville, D. A., Experiments on the stability of a liquid bridge in an axial electric field. *Physics of Fluids A: Fluid Dynamics* **1993**, 5, (4), 1081-3.
19. Klingner, A.; Buehrle, J.; Mugele, F., Capillary Bridges in Electric Fields. *Langmuir* **2004**, 20, (16), 6770-6777.
20. Quilliet, C.; Berge, B., Electrowetting: a recent outbreak. *Current Opinion in Colloid & Interface Science* **2001**, 6, (1), 34-39.
21. Rosa, D. S.; Chiovatto Neto, I.; Calil, M. R.; Pedroso, A. G.; Fonseca, C. P.; Neves, S., Evaluation of the thermal and mechanical properties of poly(ϵ -caprolactone), low-density polyethylene, and their blends. *Journal of Applied Polymer Science* **2004**, 91, (6), 3909-3914.

22. Nakagawa, T.; Nakiri, T.; Hosoya, R.; Tajitsu, Y., Electrical properties of biodegradable polylactic acid film. *Proceedings of the International Conference on Properties and Applications of Dielectric Materials*, 7th, Nagoya, Japan, June 1-5, **2003**, 2, 499-502.
23. Chou, S. Y.; Zhuang, L., Lithographically induced self-assembly of periodic polymer micropillar arrays. *Journal of Vacuum Science & Technology, B: Microelectronics and Nanometer Structures* **1999**, 17, (6), 3197-3202.
24. Deshpande, P.; Sun, X.; Chou, S. Y., Observation of dynamic behavior of lithographically induced self-assembly of supramolecular periodic pillar arrays in a homopolymer film. *Applied Physics Letters* **2001**, 79, (11), 1688-1690.
25. Wu, L.; Chou, S. Y., Electrohydrodynamic instability of a thin film of viscoelastic polymer underneath a lithographically manufactured mask. *Journal of Non-Newtonian Fluid Mechanics* **2005**, 125, (2-3), 91-99.
26. Ferry, J. D., Viscoelastic properties of polymers. 3d ed.; Wiley: New York, 1980; p xxiv, 641.
27. Larson, R. G., The structure and rheology of complex fluids. Oxford University Press: New York, 1999; p xxi, 663.
28. Arun, N.; Sharma, A.; Shenoy, V. B.; Narayan, K. S., Electric-field-controlled surface instabilities in soft elastic films. *Advanced Materials* **2006**, 18, (5), 660-663.
29. Sarkar, J.; Sharma, A.; Shenoy, V., Adhesion and Debonding of Soft Elastic Films: Crack Patterns, Metastable Pathways, and Forces. *Langmuir* **2005**, 21, (4), 1457-1469.
30. Shenoy, V.; Sharma, A., Pattern formation in a thin solid film with interactions. *Physical Review Letters* **2000**, 86, (1), 119-122.
31. Taylor, G. I.; McEwan, A. D., The stability of a horizontal fluid interface in a vertical electric field. *Journal of Fluid Mechanics* **1965**, 22, (1), 1-15.
32. Oddershede, L.; Nagel, S. R., Singularity during the Onset of an Electrohydrodynamic Spout. *Physical Review Letters* **2000**, 85, (6), 1234-1237.

Chapter 9

Improved ITO Template Surface Treatment

Templates for the active gap tool are similar to those used for Step and Flash Imprint Lithography (SFIL) in dimension and composition. Pillar formation requires templates coated with a conductive film to form the upper electrode. Indium tin oxide (ITO) is commonly utilized because it is both transparent and conductive. ITO films on quartz are also ideal for producing SFIL templates. A new surface treatment method was developed to improve the release properties at the ITO electrode – pillar interface (or ITO – etch barrier interface in the case of SFIL) by binding a fluorosilane to the ITO surface. Conventional silylation techniques that are effective for modifying the surface of SiO_2 produce non-durable treatments when applied to ITO. The silane chemistry was optimized to produce a durably bonded functionality by pretreating the ITO surface with base. In comparison to the conventional method, the base pretreatment method results in a surface exhibiting a two-fold increase in the area concentration of fluorine and much improved durability against peel tests and sonication. Since the surface treatment is intended for multi-contact applications, the durability of the fluorinated ITO surface was characterized before and after mechanically and chemically stressing the surface.

9.1 INTRODUCTION

Indium tin oxide (ITO) films exhibit a remarkable combination of properties: high transmittance in the visible spectral region, high reflectance in the IR region, and nearly metallic conductivity - properties that make ITO a valuable functional film for a wide range of commercial applications such as solar cells, flat and touch panel displays, low emissivity windows, and electrochromic devices. A number of new applications for ITO have emerged that either require, or benefit considerably from, the ability to bound non-native atoms or molecules to the ITO surface. For example, ITO has been used as a substrate for various biological sensing technologies¹⁻⁶ and has been employed in optoelectronic devices such as organic light emitting diodes (OLEDs).⁷⁻⁹ ITO has also been used in templates for nanoimprint lithography,^{10,11} as introduced in Chapter 2. ITO is ideal for Step and Flash Imprint Lithography (SFIL) for several reasons: (1) The conductive nature of the ITO effectively dissipates electrons during the template e-beam writing process (Figure 2.3), (2) ITO serves as an effective etch stop during the template fabrication process (Figure 2.3), (3) The conductive ITO allows for the completed template to be inspected by scanning electron microscopy, a critical step for detecting defects. (4) ITO is transparent, a requirement to photocure the imprinted material.

ITO is also an ideal electrode material for electrohydrodynamic patterning.¹² The process used to fabricate the templates for the active gap tool is discussed in Chapter 8. The transparency of ITO is critical for the function of the white light interferometer used to measure the capacitor gap and for the transmission of UV light during the irradiation step used to cure the pillars. The conductivity is critical for applying the electric field that induces pillar formation. A thin layer of chromium also works as an electrode, but this severely reduces the transparency of the template, as shown in Figure 9.1.

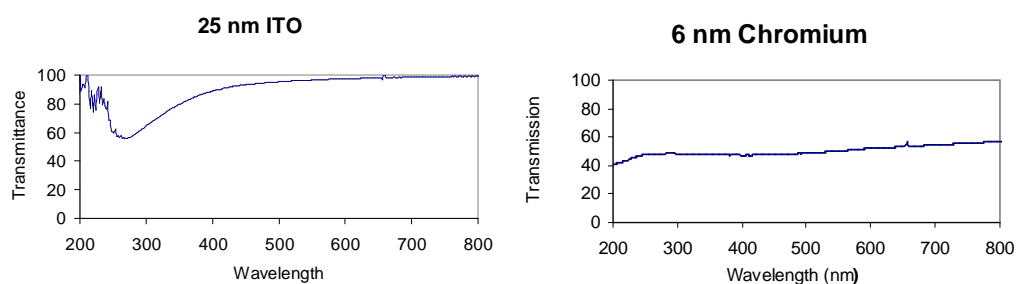


Figure 9.1: Comparison of the transparency of an ITO film compared to a thin chromium film. ITO is ideal for pillar formation because it is robust, highly conductive, and transparent.

Both SFIL and pillar formation are contact applications, in which the template comes into direct contact with a photocurable fluid. Ideally, upon completion of curing, the template should release cleanly from the cured polymer, as shown in Figure 9.2 (an analogous illustration for SFIL is shown in Figure 2.4). The clean release is facilitated by surface treating the template with a fluorinated mono-layer, which lowers the surface energy of the template. The longevity and functionality of the ITO depends on the stability of the treated surface. The primary aim of the work described in this chapter was to develop an ITO surface treatment method that produces a robust monolayer of covalently bound material based on optimized silylation chemistry.

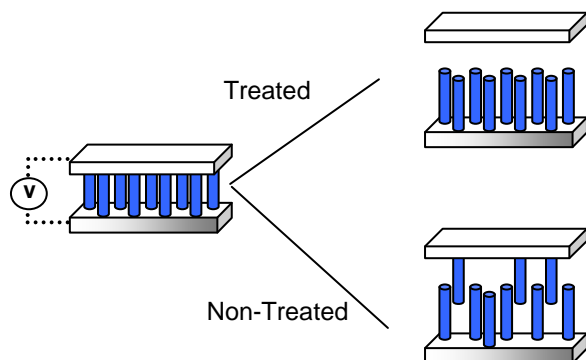


Figure 9.2: Treated templates (i.e. upper electrode) cleanly release upon separation. Pillars adhere to non-treated templates, resulting in defect formation.

Similar to SiO_2 , the ITO surface is covered with hydroxyl moieties. Consequently, many of the approaches described in the literature for surface treating ITO are identical to methods for treating SiO_2 .^{1-9,13,14} The conventional mechanism is depicted in Figure 9.3, in which the silylating reagent undergoes nucleophilic attack by a surface hydroxyl group. The reagent illustrated in Figure 9.3 has a fluorinated tail, identical to that used in this chapter to improve the release properties of the ITO surface. However, the approach in Figure 9.3 could be used to attach nearly any functionality to any hydroxyl covered surface. When using these silylating methods, special care must be taken to account for chemical differences between ITO and SiO_2 . For example, chlorosilanes must be run in dry conditions due to the HCl etch sensitivity of ITO.¹⁵

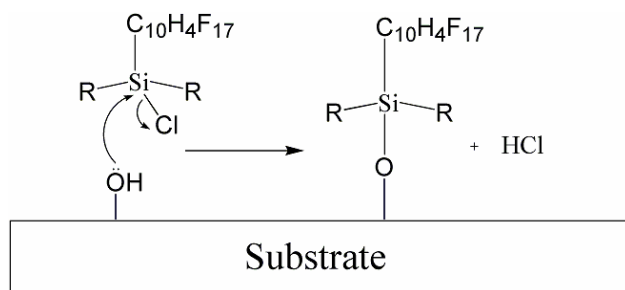


Figure 9.3: Conventional mechanism for surface silylation reaction.

Although silylation is commonly used to modify the surface of ITO, few studies have been performed to study the durability of the ITO treatment. A vapor phase silylation reaction was shown to produce a fluorinated self-assembled monolayer (FSAM) on an ITO SFIL template, which unfortunately suffered from catastrophic release failure during imprinting.¹⁶ This result is indicative of the limited durability of the FSAM on the ITO surface. FSAM was also formed on ITO by exposing it to an aqueous solution of tridecafluorooctyltriethoxysilane.¹⁷ X-ray photoelectron spectroscopy

(XPS) measurements showed that the fluorine level on these surfaces decreased dramatically after ultrasonic bathing in water, propanol, acetone and mechanical rubbing. This fluorine depletion is also indicative of weak bonding of the FSAM on the ITO surface.

Conventional SiO_2 based methods are sufficient for some ITO applications, but in general, none of the existing methods exhibit the durability necessary for repeated contact-type applications. The lack of durability implies that the silane is not covalently bound to the ITO. The ITO surface is less nucleophilic than that of SiO_2 ,¹⁸⁻²⁰ resulting in less substitution on the surface and reduced durability. This observation prompted an investigation into ways to improve the durability of silylation methods on ITO.

The approach discussed in this chapter involves enhancing the established $\text{S}_{\text{N}}2$ chemistry used in the surface modification of SiO_2 .²¹⁻²⁴ The reaction can be optimized by utilizing a good leaving group on the silane, increasing the nucleophilicity of the ITO hydroxyl groups, or both.²⁵ The simplest method is to increase ITO hydroxyl nucleophilicity via deprotonation. Thus, our method relies on a pretreatment of the ITO surface with base, not for the purpose of removing carbonaceous contamination²⁶ or catalyst formation,²¹ but for deprotonation.

In this chapter, base pretreatment is shown to be an effective, yet simple method for dramatically improving the durability of the ITO silylation process. A fluorinated silane was utilized in this study to lower the surface energy of the ITO. After treatment, the quality of the surface treatment was characterized both before and after stressing the surface as a means to quantify the durability of the fluorinated treatment. The durability of the base pretreatment method was compared to conventional silylation methods, in which base pretreatment was not used.

9.2 METHODS AND MATERIALS

9.2.1 Materials

All tests were done on 1×3 in ITO slides (Delta Technology, Stillwater, MN; Part No. CG-61IN-S115). Toluene and tetrahydrofuran (THF) were used separately as solvents for the silylation reactions. The primary base investigated was potassium tert-butoxide. A tri-chlorosilane, (heptadecafluoro-1,1,2,2-tetrahydrodecyl)trichlorosilane (Gelest SIH 5841.0), was used as the surface treatment agent. The tri-chlorosilane was chosen because of its ability to form a covalent network across the surface.²⁷

9.2.3 Silylation

The ITO samples were cleaned by sonicating for 30 minutes, first in acetone then in isopropyl alcohol (IPA). The samples were then placed in UV-ozone (UVO-Cleaner Model No. 42, Jelight Company, Inc.) to remove any residual organic contamination and to increase hydroxyl moiety concentration by surface oxidation.²⁸⁻³⁵ After cleaning, the samples were stored in an evacuated desiccator until use.

The silylation reaction environment must be dry to avoid polymerization of the silane in solution. Thus, dry solvent (less than 20 ppm water by Karl Fisher titration) was added to a flame-dried, nitrogen-purged, custom glass reaction vessel, designed such that the slides were oriented vertically. Base was added to give a ~0.003 M solution and allowed to react with the surface for 20 min before removal by cannulation. Fresh, dry solvent was added prior to injection of the trichlorosilane (0.2 wt. %) and the reaction was allowed to proceed for two hours, at which point a slightly cloudy solution persisted in the vessel. Finally, the samples were rinsed with solvent and annealed at 130° C for 24 hr.

As a basis for comparison, ITO slides were treated using an identical methodology but without base treatment. This non-base method is hereafter referred to as the “conventional method” because it is the standard technique used for treating SiO₂.^{1-9,13,14}

9.2.3 Characterization

The quality of the surface treatment was characterized by contact angle, X-ray photoelectron spectroscopy (XPS), and 90° peel force measurements. Characterization was done before and after several procedures designed to remove weakly bonded silylating agent as a measure of the durability of the surface. A summary of the implemented techniques and their purpose is shown in Table 9.1.

Table 9.1: Procedure Purposes

| Processing Step | Characterization |
|---|--------------------|
| 1. Post-Treatment (Mechanically Clean, Sonicate) | --- |
| 2. Pre-Stress Test | Contact Angle, XPS |
| 3. Stress Test (Peel Test, Sonicate) | Peel Force |
| 4. Post-Stress Test | Contact Angle, XPS |

After silylation, the slides were hazy because of oligomeric siloxanes adsorbed from the reaction solution, as shown in Figure 9.4. This physi-sorbed material was removed by passing the slides under a stationary cylindrical cleaning apparatus that applied a constant 10 N force to the surface. The cylinder had a 1.125 in radius and was sheathed in an acetone soaked clean room wipe (Vectra Alpha 10 Texwipe). This mechanical mechanism eliminated the possibility of human bias in the cleaning

procedure. The samples were then sonicated sequentially in acetone and IPA for 60 min to further clean the surface.

After cleaning, contact angle images were taken using a goniometer (Ramé-Hart 2000) and analyzed with FTA2000 software (First Ten Ångstroms). The chemical composition of the surfaces were analyzed by XPS (PHI 5700 spectrometer, Physical Electronics). Using monochromatic Al K_{α} X-rays, spectra were taken at a pass energy of 11.75 eV. XPS binding energies were calibrated using pure gold (Au4f), silver (Ag3d) and copper (Cu2p).



Figure 9.4: Photograph of the ITO slides before and after mechanically cleaning. The “post-treatment” sample is hazy with loosely bound material. After cleaning, the “post-clean” sample is transparent.

Peel tests based on ASTM D6862 were performed using an Instron 5848 Mircotester, which measures the force necessary to remove a film at a constant velocity normal to the substrate. In addition to removing weakly bonded species, this peel test also provides a qualitative measure of the work of adhesion. To perform the peel test, a pliable cleanroom wipe made of natural abaca fiber (Berkshire LabX123 Item #:LB123.090.60, ~40 μm thick) was photopolymerized to the surface using a 1:1 liquid mixture of thiol-ene, pentaerythritol tetrakis(3-mercaptopropionate) (Aldrich) and tris-(4-

vinylxybutyl)trimellitate (Aldrich). The cleanroom wipe was chosen for its large tensile strength, which maximized the 5 N load cell in tensile mode with no observable strain deformation of the wipe. During each peel test, an average force was measured in the region between 25 to 75% of total extension to eliminate end effects. In all cases, the thiol-ene released from the substrate such that the polymerized thiol-ene remained exclusively on the clean wipe during peeling. Five peel tests were performed on each slide. The peel test concept is illustrated in Figure 9.5.

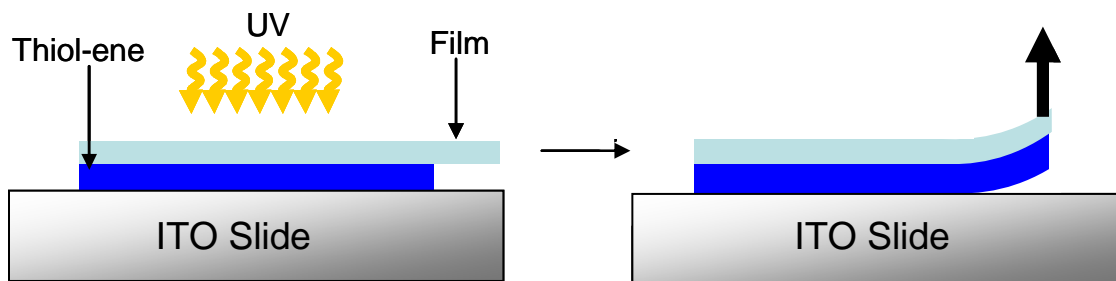


Figure 9.5: Peel test illustration. A photocurable liquid, thiol-ene, is photocured between the ITO and a pliable film. The adhered film is then peeled from the surface while measuring the force.

After completing the peel tests, the samples were cleaned by sonication in acetone and IPA for 60 min and characterized by contact angle and XPS measurements to quantify changes in the surface resulting from the various durability stress tests.

9.3 RESULTS

The key finding of this chapter is that conventional silylation methods used to treat SiO_2 create non-robust, heterogeneous treatments when applied to ITO. However, the quality of the surface treatment can be dramatically improved through the use of a base pretreatment. This simple method only differs from the conventional method in that

the ITO surface is exposed to potassium tert-butoxide prior to the addition of tri-chlorosilane. Table 9.2 provides a comparison of the treatment qualities both before and after durability stress tests (i.e. sonication and peel tests). The values reported in Table 9.2 are averages of over thirty measurements taken on five different samples for each treatment condition. The control sample was exposed to all of the processing equipment and steps as the other samples, but it was not silanized or exposed to base. The control has a larger contact angle than a freshly UV-ozoned sample. This phenomenon has been investigated throughout the literature.^{29,35}

Table 9.2: Summary of Results

| Substrate | Contact Angle (Pre-Peel) | | Contact Angle (Post-Peel) | | Peel Force (N) | |
|-------------------------|--------------------------|----------|---------------------------|----------|----------------|----------|
| | Avg | St. Dev. | Avg | St. Dev. | Avg | St. Dev. |
| Control | 59.1 | 5.6 | 55.5 | 4.3 | 0.368 | 0.047 |
| Conventional (THF) | 67.6 | 9.6 | 59.9 | 2.8 | 0.167 | 0.016 |
| Conventional (Toluene)* | 83.7 | 11.4 | 72.3 | 12.3 | 0.109 | 0.029 |
| Base Treatment (THF) | 112.6 | 2.4 | 108.0 | 2.8 | 0.058 | 0.007 |

* The SiO₂ side of the slide gave a contact angle well above 100°

The magnitude of the contact angle measurement is one indication of the quality of the surface treatment. Similarly, the standard deviation of the contact angle provides a measure of the heterogeneity of the surface. As seen in Table 9.2, the base pretreatment method produced larger contact angles with smaller standard deviations at every stage of measurement as compared to the conventional method. The conventional method contact angle dropped significantly after durability stressing to 72°, only slightly better than the

control. This drop implies that loosely bound silylating agent was removed during stressing, indicative of a physisorbed film. The large contact angle standard deviations of the conventional method are indicative of a non-uniform surface treatment.

In contrast to the conventional method, the use of a base pretreatment created a large initial contact angle that remained large ($\sim 110^\circ$) after durability stressing. The base pretreatment method had a significantly lower standard deviation for each set of measurements, indicative of a more homogenous treatment. Figure 9.6 is representative of the goniometer images taken after the potassium t-butoxide base treatment and silylation.

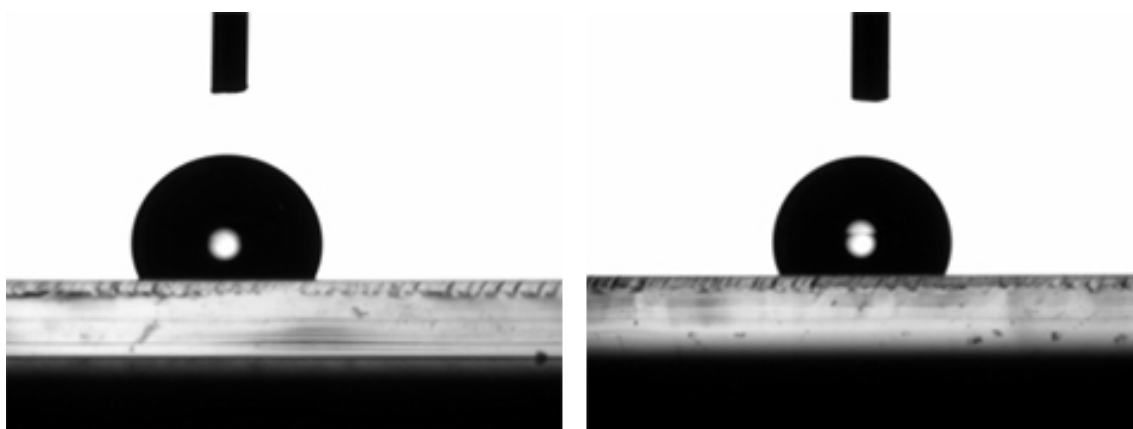


Figure 9.6: Water droplet on treated ITO surface using base method (a) pre-durability stress and (b) post-durability stress.

Peel tests provide a means to both stress and characterize the surface simultaneously. The measured peel force can not be directly converted to an established metric, such as work of adhesion, but it is indicative of the ease with which the peel releases at the surface. The general behavior of the conventional method compared with the base pretreatment method was consistent with the contact angle data. The average peel force of the conventional method was a factor of two larger than the base treated

method, and the force for the conventional method also had a larger standard deviation (both absolute and normalized). Again, this measurement was indicative of a heterogeneous, weakly bonded film.

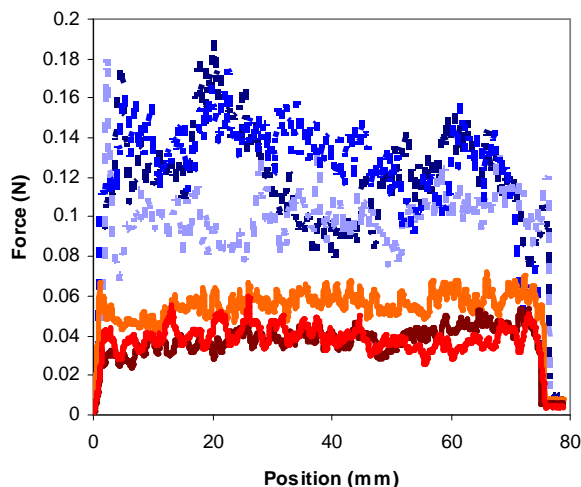


Figure 9.7: Typical peel force plot of the schematic in Figure 9.5. The force required to remove a photo-adhered film from the substrate is measured as a function of displacement. The dotted lines represent the conventional method and the solid lines represent the base pretreated method. The base pretreated method has reduced variability, indicative of a uniform treatment.

The notable improvement achieved by base pretreatment could be the result of several factors. Evidence points to base activating the SiO_2 surface hydroxyls, resulting in a more nucleophilic substrate.³⁶ However, the possibility exists that the base could be playing a catalytic role in the treatment, since amine bases have been used as SiO_2 surface treatment catalysts.²¹ None of the bases here were structurally equivalent to the catalysts used previously, due to the insolubility of the pentacoordinate silicon - tertiary amine salt intermediate of the particular silane used. Regardless, the possibility of base catalysis was investigated by a “half-slide” experiment performed such that an ITO slide was only half submersed in potassium tert-butoxide solution. After removing the base,

the reaction vessel was filled with chlorosilane solution such that the whole slide was submerged. The bottom, base pretreated half of the slide behaved much like the base pretreated results shown in Table 9.2, with an average contact angle of 104.3° and standard deviation of 1.5° . However, the top half of the slide, which was not directly exposed to base, did not treat as well, indicated by its relatively low contact angle of 82.0° and large standard deviation of 16.3° . This eliminated the possibility of trace amounts of residual base catalyzing the surface reaction. Also, the half of the slide unexposed to base had a much hazier film on the surface than the base treated counterpart, demarcated by a sharp line. This may be indicative of a greater propensity for physisorption of oligomers from solution onto a surface that has not been base treated. The conventional method slides were consistent with this observation, producing a much hazier film than the base pretreated samples.

System parameters were varied to determine the importance of factors such as solvent, base counter ion, and base strength. Solvent played a significant role in the conventional method, consistent with accepted theory.²¹ Compared to toluene, THF is a very poor solvent for the conventional method, as shown in Table 9.2. However, THF proved to be a slightly better solvent for the base pretreatment method ($\sim 15^\circ$ higher contact angle compared to toluene). A possible explanation for this behavior is that polar aprotic solvents are ideal for S_N2 reactions because they do not effectively solvate the anion, but do solvate the cation. In addition to varying the solvent, two different counter ions for tert-butoxide were investigated. As expected, there was no statistically significant difference between lithium tert-butoxide and potassium tert-butoxide.

The use of stronger bases such as LiHMDS ($pK_a = 40$) and nBuLi ($pK_a = 50$) did not enhance the performance of the surface treatment compared to tert-butoxide ($pK_a = 18$). In some cases, stronger bases actually performed worse than the tert-butoxide, albeit

much better than the conventional methods. For example, the LiHMDS gave values of 95° and 85°, before and after peeling. This behavior may be due to increased salt or polymer formation in solution, which could adsorb onto the surface and block reactive sites.

XPS studies complimented the contact angle and peel force measurements. Table 9.3 shows the relative fluorine area concentration compared to indium (i.e. the substrate). The base pretreatment method is clearly superior, both in its initial fluorine surface concentration and its ability to retain the fluorine after durability stressing. The relative fluorine intensity decreased 40% for the base treated samples, whereas the conventional method decreased 60%. Fluorine decreases in both samples might imply the existence of physi-sorbed polymer regardless of the method. After peeling, the base treated method had an area concentration ~2.5 times larger than the conventional method with a significantly smaller standard deviation, indicative of a more uniform treatment. The untreated ITO control has 0-6 % fluorine, so the conventional method post-peel signal is only slightly larger than the baseline.

Table 9.3: XPS Results

| Treatment Method | Pre-peel | | Post-peel | |
|--------------------------|------------|----------|------------|----------|
| | % Fluorine | St. Dev. | % Fluorine | St. Dev. |
| <i>Conventional</i> | 40 | 14 | 16 | 16 |
| <i>Base Pretreatment</i> | 70 | 1 | 42 | 4 |

9.4 DEMONSTRATIONS

The ultimate goal of this study was to reduce template contamination during pillar formation, as shown in Figure 9.2. Thiol-ene pillars were formed on an untreated ITO template. After one experiment, the template was grossly contaminated with thiol-ene residue, as evident by optical microscopy (Figure 9.8, left image). In contrast, a treated template remains residue free after nine experimental runs of pillar formation (Figure 9.8, right image). The template was treated using the technique described in Sections 9.2-9.3.

In addition to reducing adhesion of the thiol-ene to the template, the treated template also impacts the contact angle of the pillar at the upper electrode. Figure 9.9 is a scanning electron micrograph of a pillar array produced with a freshly treated template. In contrast, Figure 9.10 is a micrograph of a pillar array produced using an untreated template. The untreated template is wetting towards the thiol-ene, whereas the treated template produces a pillar with a larger contact angle. The contact angle is estimated to change from $\sim 60^\circ$ for the untreated template to $\sim 90^\circ$ for the treated template.

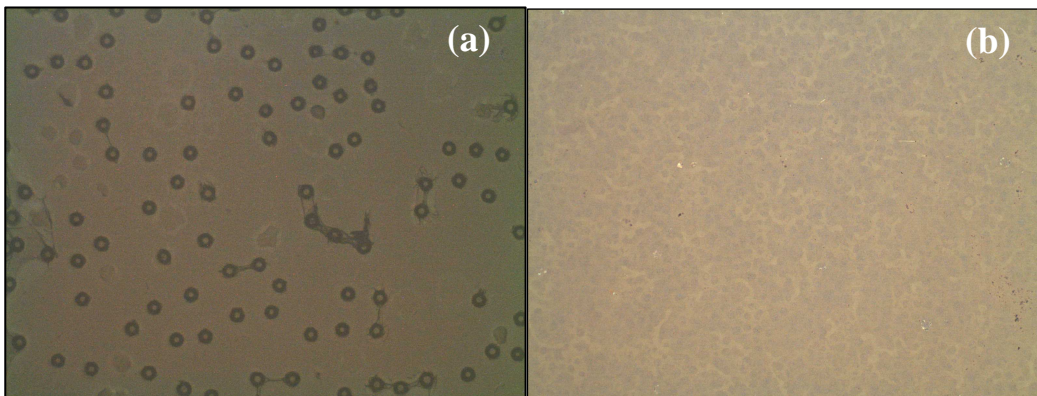


Figure 9.8: Optical micrographs of the ITO template surface at 10x magnification. (a) After one run, the untreated template is grossly contaminated with residue. (b) After nine experiments, the ITO surface remains residue free. Image widths 1170 μm .

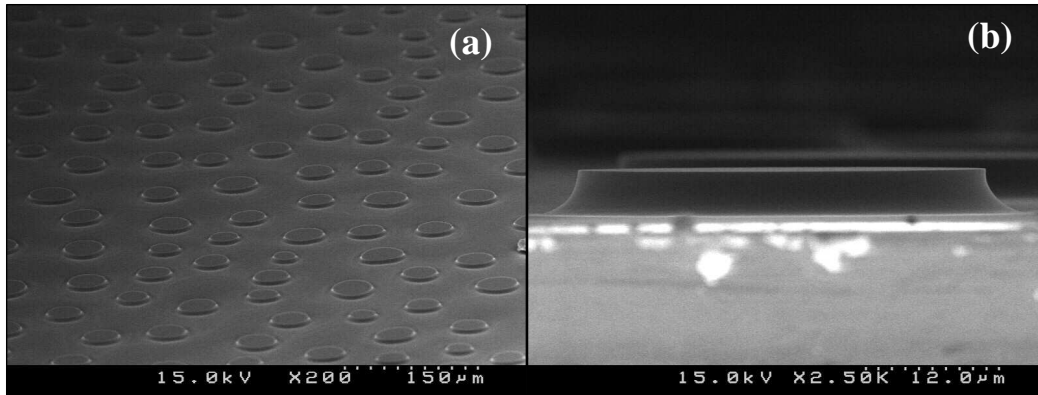


Figure 9.9: Electron micrographs of pillars formed using a surface treated template. (a) Overview (b) A cross section view of a pillar with a non-wetting upper contact angle.

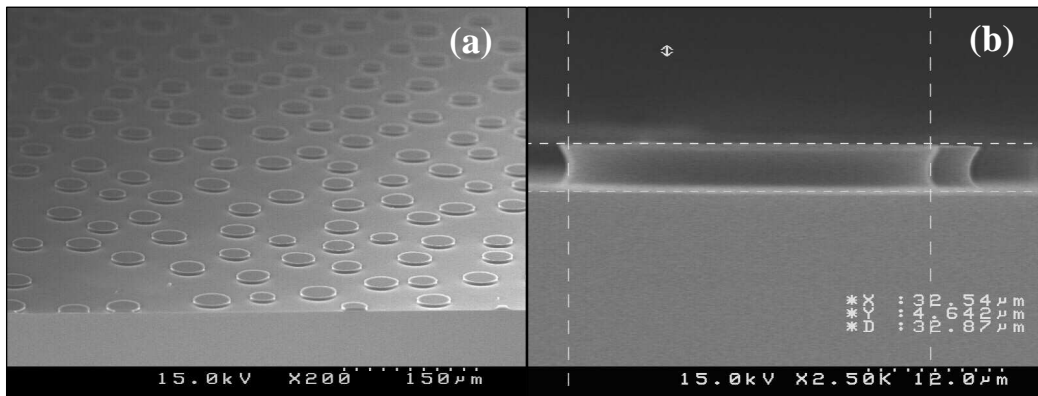


Figure 9.10: Electron micrographs of pillars formed using an untreated template. (a) Overview (b) A cross section view of a pillar with a non-wetting upper contact angle.

9.5 CONCLUSIONS

Base treatment was shown to give both better coverage and a more durable ITO surface treatment than conventional SiO_2 surface treatment methods. The contact angle of the base pretreated ITO was higher than the conventional method, indicative of a better surface treatment. The base pretreated ITO also had a lower contact angle standard

deviation than the conventional method, indicative of a more uniform surface coverage. XPS data corroborated these findings, showing more fluorine with a smaller standard deviation on the surface of the base treated slides compared to the conventional method. By all metrics utilized, the base pretreatment provided a more durable surface treatment after stressing the surface with controlled mechanical cleaning, sonication, and 90 degree peel tests. The base does not act as a catalyst; rather it appears to be deprotonating the ITO surface, making it more reactive towards the chlorosilane. This ultimately results in more covalent linkages to the substrate that are responsible for improved durability. An ITO treated template was shown to reduce pillar residue and improve the longevity of a template for processing.

9.6 REFERENCES

1. Asanov, A. N.; Wilson, W. W.; Oldham, P. B., Regenerable Biosensor Platform: A Total Internal Reflection Fluorescence Cell with Electrochemical Control. *Analytical Chemistry* **1998**, 70, (6), 1156-1163.
2. Hedges, D. H. P.; Richardson, D. J.; Russell, D. A., Electrochemical control of protein monolayers at indium tin oxide surfaces for the reagentless optical biosensing of nitric oxide. *Langmuir* **2004**, 20, (5), 1901-1908.
3. Fang, A.; Ng, H.; Su, X.; Li, S. F. Y., Soft-Lithography-Mediated Submicrometer Patterning of Self-Assembled Monolayer of Hemoglobin on ITO Surfaces. *Langmuir* **2000**, 16, (12), 5221-5226.
4. Ng, H. T.; Fang, A.; Huang, L.; Li, S. F. Y., Protein microarrays on ITO surfaces by a direct covalent attachment scheme. *Langmuir* **2002**, 18, (16), 6324-6329.
5. Willner, I.; Blonder, R., Patterning of surfaces by photoisomerizable antibody-antigen monolayers. *Thin Solid Films* **1995**, 266, (2), 254-7.
6. Hillebrandt, H.; Wiegand, G.; Tanaka, M.; Sackmann, E., High Electric Resistance Polymer/Lipid Composite Films on Indium-Tin-Oxide Electrodes. *Langmuir* **1999**, 15, (24), 8451-8459.

7. Hanson, E. L.; Guo, J.; Koch, N.; Schwartz, J.; Bernasek, S. L., Advanced Surface Modification of Indium Tin Oxide for Improved Charge Injection in Organic Devices. *Journal of the American Chemical Society* **2005**, 127, (28), 10058-10062.
8. Sfez, R.; Liu, D.-Z.; Turyan, I.; Mandler, D.; Yitzchaik, S., Polyaniline Monolayer Self-Assembled on Hydroxyl-Terminated Surfaces. *Langmuir* **2001**, 17, (9), 2556-2559.
9. Hatton, R. A.; Day, S. R.; Chesters, M. A.; Willis, M. R., Organic electroluminescent devices: enhanced carrier injection using an organosilane self assembled monolayer (SAM) derivatized ITO electrode. *Thin Solid Films* **2001**, 394, (1,2), 292-297.
10. Bailey, T.; Choi, B. J.; Colburn, M.; Meissl, M.; Shaya, S.; Ekerdt, J. G.; Sreenivasan, S. V.; Willson, C. G., Step and flash imprint lithography: Template surface treatment and defect analysis. *Journal of Vacuum Science & Technology, B: Microelectronics and Nanometer Structures* **2000**, 18, (6), 3572-3577.
11. Dauksher, W. J.; Nordquist, K. J.; Mancini, D. P.; Resnick, D. J.; Baker, J. H.; Hooper, A. E.; Talin, A. A.; Bailey, T. C.; Lemonds, A. M.; Sreenivasan, S. V.; Ekerdt, J. G.; Willson, C. G., Characterization of and imprint results using indium tin oxide-based step and flash imprint lithography templates. *Journal of Vacuum Science & Technology, B: Microelectronics and Nanometer Structures* **2002**, 20, (6), 2857-2861.
12. Dickey, M. D.; Collister, E.; Raines, A.; Tsiartas, P.; Holcombe, T.; Sreenivasan, S. V.; Bonnacaze, R. T.; Willson, C. G., Photocurable Pillar Arrays Formed via Electrohydrodynamic Instabilities. *Chemistry of Materials* **2006**, 18, (8), 2043-2049.
13. Hillebrandt, H.; Tanaka, M., Electrochemical Characterization of Self-Assembled Alkylsiloxane Monolayers on Indium-Tin Oxide (ITO) Semiconductor Electrodes. *Journal of Physical Chemistry B* **2001**, 105, (19), 4270-4276.
14. Markovich, I.; Mandler, D., Preparation and characterization of octadecylsilane monolayers on indium-tin oxide (ITO) surfaces. *Journal of Electroanalytical Chemistry* **2001**, 500, (1-2), 453-460.
15. Huang, C. J.; Su, Y. K.; Wu, S. L., The effect of solvent on the etching of ITO electrode. *Materials Chemistry and Physics* **2004**, 84, (1), 146-150.
16. Bailey, T. C. Imprint Template Advances and Surface Modification, and Defect Analysis for Step and Flash Imprint Lithography. University of Texas at Austin, Austin, **2003**.

17. Schondelmaier, D.; Cramm, S.; Klingeler, R.; Morenzin, J.; Zilkens, C.; Eberhardt, W., Orientation and Self-Assembly of Hydrophobic Fluoroalkylsilanes. *Langmuir* **2002**, 18, 6242-6245.
18. Appleyard, S. F. J.; Day, S. R.; Pickford, R. D.; Willis, M. R., Organic electroluminescent devices: enhanced carrier injection using SAM derivatized ITO electrodes. *Journal of Materials Chemistry* **2000**, 10, (1), 169-173.
19. Koide, Y.; Wang, Q.; Cui, J.; Benson, D. D.; Marks, T. J., Patterned luminescence of organic light-emitting diodes by hot microcontact printing (HmCP) of self-assembled monolayers. *Journal of the American Chemical Society* **2000**, 122, (45), 11266-11267.
20. Gardner, T. J.; Frisbie, C. D.; Wrighton, M. S., Systems for orthogonal self-assembly of electroactive monolayers on Au and ITO: an approach to molecular electronics. *Journal of the American Chemical Society* **1995**, 117, (26), 6927-6933.
21. Kinkel, J. N.; Unger, K. K., Role of solvent and base in the silanization reaction of silicas for reversed-phase high-performance liquid chromatography. *Journal of Chromatography* **1984**, 316, 193-200.
22. Haller, I., Covalently attached organic monolayers on semiconductor surfaces. *Journal of the American Chemical Society* **1978**, 100, (26), 8050-5.
23. Lork, K. D.; Unger, K. K.; Kinkel, J. N., Role of the functional group in n-octyldimethylsilanes in the synthesis of C8 reversed-phase silica packings for high-performance liquid chromatography. *Journal of Chromatography* **1986**, 352, 199-211.
24. Marzouk, S.; Rachdi, F.; Fourati, M.; Bouaziz, J., Synthesis and grafting of silica aerogels. *Colloids and Surfaces, A: Physicochemical and Engineering Aspects* **2004**, 234, (1-3), 109-116.
25. Tripp, C. P.; Hair, M. L., Chemical attachment of chlorosilanes to silica: a two-step amine-promoted reaction. *Journal of Physical Chemistry* **1993**, 97, (21), 5693-8.
26. Chaney, J. A.; Koh, S. E.; Dulcey, C. S.; Pehrsson, P. E., Surface chemistry of carbon removal from indium tin oxide by base and plasma treatment, with implications on hydroxyl termination. *Applied Surface Science* **2003**, 218, (1-4), 258-266.
27. Stevens, M. J., Thoughts on the Structure of Alkylsilane Monolayers. *Langmuir* **1999**, 15, (8), 2773-2778.

28. Kim, J. S.; Friend, R. H.; Cacialli, F., Surface wetting properties of treated indium tin oxide anodes for polymer light-emitting diodes. *Synthetic Metals* **2000**, 111-112, 369-372.
29. Kim, J. S.; Friend, R. H.; Cacialli, F., Surface energy and polarity of treated indium-tin-oxide anodes for polymer light-emitting diodes studied by contact-angle measurements. *Journal of Applied Physics* **1999**, 86, (5), 2774-2778.
30. Milliron, D. J.; Hill, I. G.; Shen, C.; Kahn, A.; Schwartz, J., Surface oxidation activates indium tin oxide for hole injection. *Journal of Applied Physics* **2000**, 87, (1), 572-576.
31. Ishii, M.; Mori, T.; Fujikawa, H.; Tokito, S.; Taga, Y., Improvement of organic electroluminescent device performance by in situ plasma treatment of indium-tin-oxide surface. *Journal of Luminescence* **2000**, 87-89, 1165-1167.
32. Djurisic, A. B.; Lau, T.; Kwong, C. Y.; Guo, W.; Bai, Y.; Li, E. H.; Chan, W. K., Surface treatments of indium tin oxide substrates: comprehensive investigation of mechanical, chemical, thermal, and plasma treatments. *Proceedings of SPIE-The International Society for Optical Engineering* **2002**, 4464, (Organic Light-Emitting Materials and Devices V), 273-280.
33. Donley, C.; Dunphy, D.; Paine, D.; Carter, C.; Nebesny, K.; Lee, P.; Alloway, D.; Armstrong, N. R., Characterization of Indium-Tin Oxide Interfaces Using x-ray Photoelectron Spectroscopy and Redox Processes of a Chemisorbed Probe Molecule: Effect of Surface Pretreatment Conditions. *Langmuir* **2002**, 18, (2), 450-457.
34. Song, W.; So, S. K.; Wang, D.; Qiu, Y.; Cao, L., Angle dependent X-ray photoemission study on UV-ozone treatments of indium tin oxide. *Applied Surface Science* **2001**, 177, (3), 158-164.
35. Kim, H.; Lee, J.; Park, C.; Park, Y., Surface characterization of O₂-plasma-treated indium-tin-oxide (ITO) anodes for organic light-emitting-device applications. *Journal of the Korean Physical Society* **2002**, 41, (3), 395-399.
36. Blitz, J. P.; Murthy, R. S. S.; Leyden, D. E., Ammonia-catalyzed silylation reactions of Cab-O-Sil with methoxymethylsilanes. *Journal of the American Chemical Society* **1987**, 109, (23), 7141-5.

Chapter 10

Conclusions and Future Work

This thesis focuses on the development of two emerging patterning strategies. The ability to pattern micro- and nano- structures rapidly and with great fidelity is critical to the development of a number of technologies including electronics, MEMS, biosensors, and microfluidic devices. Photolithography, introduced in Chapter 1, is an established patterning technology that has driven the exponential growth of the semiconductor industry. Unfortunately, photolithography is expensive and has limited resolution, which has motivated the search for patterning alternatives.

Two alternative patterning technologies are explored in this thesis that overcome at least one of the limitations of photolithography: (1) Imprint lithography is an inexpensive, yet high resolution contact patterning method that utilizes a topographically patterned template to physically transfer patterns, and (2) Electric field assisted assembly is a simple, inexpensive technique that spontaneously forms arrays of pillars across a narrow electrode gap by harnessing thin film instabilities.

10.1 NANOIMPRINT LITHOGRAPHY

Nanoimprint Lithography (NIL) is a high resolution, yet inexpensive patterning tool that achieves pattern transfer by pressing a topographically patterned template into a soft material. The template is fabricated by e-beam lithography, a slow, yet high resolution process. Thus, the advantage of NIL is that each imprint rapidly patterns large

areas of features with the resolution of e-beam lithography (<10 nm), but without the slow throughput that limits e-beam lithography.

As introduced in Chapter 2, there are two varieties of NIL: Thermal NIL and UV NIL. Thermal NIL is distinguished by the use of heat to modulate the properties of the imprinted material, typically a polymer. The polymer is softened by heating prior to imprinting and hardened by cooling prior to withdrawal of the template. Thermal NIL is slow because of this heating and cooling cycle. Furthermore, large pressures are required to displace the high viscosity polymer during imprinting. UV-NIL utilizes low viscosity materials that are rapidly imprinted at ambient conditions, providing a significant advantage compared to thermal NIL. The imprinted structures are hardened by exposure to UV light, which is irradiated through the template during the imprint process.

Acrylates are a popular UV-NIL material because they cure rapidly to form mechanically stable structures. Furthermore, acrylate monomers with all the requisite properties (low viscosity, ~12% silicon content) are commercially available. The drawback of acrylates is that the free radical polymerization mechanism is oxygen sensitive. Dissolved oxygen causes a polymerization inhibition period when the material is initially irradiated, lowering process throughput. Once all the oxygen is consumed, polymerization can proceed rapidly, except at the edge of the template, which is subject to oxygen diffusion from the surrounding ambient. A small rim of undercured material surrounds the template due to the effects of oxygen, which may contribute to defect propagation.

A semi-empirical model was presented in Chapter 3 that accounts for the effects of oxygen on the polymerization. The free radical rate coefficients were measured by real-time IR methods and the values were plugged into a set of differential equations that account for the concentration of the species in the reaction medium (i.e. oxygen, radicals,

monomer, and initiator). The model closely matches the experimental kinetic profiles. For typical irradiation conditions, the model shows approximately 2 seconds of inhibition time and $\sim 50\text{ }\mu\text{m}$ of inhibited perimeter, both of which are significant. These values can be reduced by increasing the rate of radical initiation. Ultimately, the only way to completely eliminate the deleterious oxygen effects is to use alternative materials or an inerting system.

10.2 ELECTRIC FIELD ASSISTED ASSEMBLY

Directed assembly processes are appealing because of their ability to harness natural phenomena to form useful structures. Recently, a technique has emerged that is capable of forming arrays of pillars across a capacitor gap through application of an electric field, as introduced in Chapter 4. Figure 10.1 is an optical micrograph of pillar arrays. Pillars form due to the force imbalance at the film-air interface. Electrostatic forces act to destabilize the film, whereas surface tension works to stabilize the film. Promising initial results obtained with polymeric films motivated further study of this phenomenon.³⁻⁷

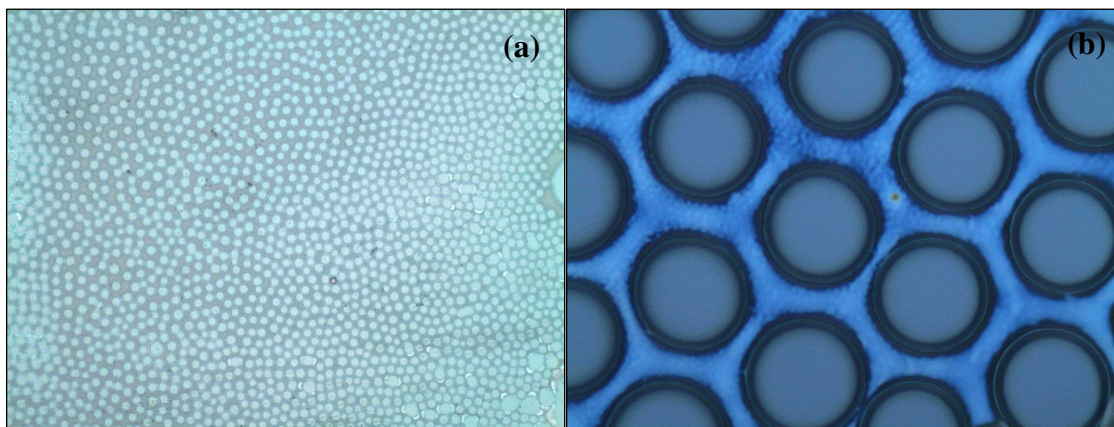


Figure 10.1: Optical micrographs of pillar arrays. (a) Thiol-ene pillars, image width $1170\text{ }\mu\text{m}$. (b) PMMA pillars, image width $100\text{ }\mu\text{m}$.

Initial work focused on the use of trilayer film stacks to form hierarchical structures that would be difficult to form by conventional patterning methods. The results of Chapter 5 illustrate the importance of the wetting properties of the electrodes in dictating the final structural geometry. Air-polystyrene (PS)-polymethylmethacrylate (PMMA) systems were studied under electrohydrodynamic conditions. An applied field generates electrostatic pressure at both the PS-air and PMMA-PS interfaces because of the dielectric contrast between the respective layers. PS pillars initially form on top of the PMMA underlayer because there is less viscous resistance to flow at the PS-air interface compared to the PMMA, which is sandwiched between PS and the substrate. The PMMA then grows up the sides of the PS pillars, in the form of tendrils. The tendrils can displace the PS at the upper electrode in cases in which the upper electrode is wetting, with the final structure resembling a cage.

Somewhat non-intuitively, reversing the polymer layers (air-PMMA-PS) does not simply reverse the phases of the structures obtained with the air-PS-PMMA system. Placing the PS on the bottom of the film stack changes the dynamics of the system by creating (1) a non-wetting interface at the PS-SiO₂ (i.e. native oxide) coated substrate and (2) a downward pressure at the PMMA-PS interface due to the larger dielectric constant of PMMA. The downward pressure at the PMMA-PS interface works in tandem with the dewetting properties of the PS-substrate interface to induce the break up the PS film into undulations that conform with the overlying PMMA layer. The PS gets entrained in the growing PMMA undulations, resulting in final structures with a PS core and a PMMA shell, reminiscent of the structures formed with the air-PS-PMMA configuration. This mechanism was elucidated by varying the wetting properties of the substrate to

demonstrate the impact of dewetting on the mechanism dynamics. For cases in which the substrate is wetting, the PMMA simply forms pillars on the underlying PS layer.

Although the aforementioned polymeric systems are capable of forming unique hierarchical structures, these systems are hampered by lengthy time scales of formation. The polymers must be heated to permit flow and the resulting melt viscosities are very high. Linear stability analysis, which is commonly used to model the pillar formation process, predicts that the time scale of formation is proportional to viscosity. Consequently, photocurable materials with low viscosity were rationally developed and characterized to decrease the time required to form pillars. In contrast to the polymeric materials, which take hours to form pillars, the photocurable materials form pillars nearly instantaneously at room temperature. The structures are locked into place by photopolymerization. Numerous photocurable systems were characterized (e.g. dielectric constant, surface energy, viscosity, pillar formation tendencies) and thiol-ene was identified as the best material for forming pillars in Chapter 6. It is commercially available, forms stable films via spin casting, and photocures quickly without any ambient inhibition. Most importantly, it forms pillars rapidly because of its relatively large dielectric constant and low viscosity.

In addition to measuring the relevant physical parameters, the thiol-ene material system was further characterized under electrohydrodynamic conditions. Linear stability analysis is an established method for predicting the characteristic spacing (center-to-center) for polymeric pillars. The applicability of linear stability analysis to the low viscosity thiol-ene system was verified in Chapter 7. Although the limitations of the experimental techniques resulted in noisy data, the theory captures the experimental trends. At low wavelengths, the experimental wavelengths level out around ~20 microns. This result could be due to experimental configuration limitations that are significant at

the extreme conditions required to form small wavelengths or could be due to vertical viscous effects that aren't accounted for in the linear stability analysis.

Although pillars have a characteristic wavelength, they often lack the long range order necessary for many applications. Short range order was observed to occur during nucleated growth (Chapter 7). Nucleated growth occurs when either a single pillar or row of pillars forms faster than the rest of the sample due to an enhanced local field (intentional or inadvertent). The mechanism of nucleated growth can be harnessed to improve long range order through the use of topographically patterned electrodes since the local electric field under the protruding features is enhanced. Pillars preferentially grow underneath these features. The use of patterned electrodes detracts from the elegance of the technique, and thus alternatives were explored to improve the long range order.

Both AC fields and piezo electric induced vibrations were studied as a means to improve long range order in Chapter 7. AC fields with a wide range of frequencies and amplitudes proved capable of forming pillars, but did not show any improved order or dependency on frequency. In a separate set of experiments, piezo electrics were used to vibrate the substrate in hopes of inducing undulations on the film surface, which would be amplified by the electric field. Although small regions of samples showed signs of local order, the piezos did not produce overwhelmingly conclusive evidence of improved order compared with control samples. The large viscous forces associated with the thin film combined with the inability to apply large voltages to the piezos may have limited the success of this technique.

Another limit of the pillar formation process is that the resulting structures have low aspect ratios (height divided by diameter), as predicted by linear stability analysis. The aspect ratios are typically between 0.05-0.2. Increasing the aspect ratio can be

accomplished by applying larger electric fields, but the electric field can not be raised past the dielectric breakdown of the capacitor (experimentally, this was found to be ~ 80 V/ μm). Therefore, the aspect ratio was increased by stretching the pillars using the active gap tool, as discussed in Chapter 8. The tool proved successful in stretching the pillars, and the maximum aspect ratio was ~ 0.5 , consistent with liquid bridge theory. The aspect ratio can be stretched past this theoretical limit by retarding the instability, although this has yet to be done reliably.

Viscoelastic polymers proved capable of forming high aspect ratios without stretching. The narrow fibrils that emit from the film undulations are reminiscent of the spouts that emit from classical Taylor cones. These fibrils coarsen with time as more material is drawn into the pillar. The most surprising aspect of these fibrils is that the characteristic spacing is a factor of 4-5 smaller than that predicted by linear stability theory. We speculate that literature models for the minimization of energy used to model contact elastic instabilities may be more appropriate.

Use of photocurable materials requires a transparent template for the irradiation step. Indium tin oxide (ITO) is an ideal material because it is both conductive and transparent. Ideally, pillars will preferentially adhere to the substrate and release cleanly when the upper electrode is removed. To meet this goal, the ITO surface chemistry must be modified to improve the release properties at the pillar-electrode interface. ITO is covered with hydroxyl groups, similar to SiO_2 , and consequently, a common approach to treat ITO is to use chlorosilane agents. We found that these methods result in a non-robust treatment that is insufficient for multi-contact applications. The lack of durability is believed to be due to the poorly nucleophilic ITO surface. The durability of the chlorosilane treatment is dramatically improved through the use of a base pretreatment, which activates the ITO surface towards silylation by increasing the nucleophilicity.

Specifically, ITO was pretreated with tert-butoxide base prior to exposing the surface to a fluorinated chloro-silane to lower the surface energy of the electrode, as discussed in Chapter 9. The improvement was characterized by water contact angle, XPS, and peel test measurements, which give a qualitative measure of the work of adhesion. By all measures, the base pretreated method resulted in a more durable treatment against durability tests that include mechanical abrasion, sonication, and peel tests.

In summary, the pillar formation process is a simple, inexpensive route to producing arrays of pillars. Polymeric systems are capable of forming some unique hierarchical structures because of their phase incompatibility and the ultimate geometry of these structures is dependent on the electrode wetting properties. Pillars benefit considerably through the use of low viscosity materials, which decrease the time scale of formation by orders of magnitude. Linear stability analysis accurately predicts the spacing of these structures, although the structures lack long range order. Use of patterned electrodes proved to be the only reliable route to producing long range order. Linear stability also predicts that pillars will have naturally low aspect ratios. The aspect ratio of the pillars was increased through use of a tool designed to stretch the pillars. Liquid bridge stability analysis correctly predicts the maximum aspect ratio that the structures can be stretched. In order for the pillars to release cleanly from the upper electrode upon separation, the electrode surface must be treated with a fluorinating agent. This was accomplished by pretreating an ITO electrode with base prior to silylation with a chlorosilane with a fluorinated tail to form a robust surface treatment that improved the release properties of the electrode from the pillars.

10.3 FUTURE WORK

There are several aspects of this work that would be worth pursuing further. The linear stability data is noisy due to experimental limitations. By building a stiffer active gap tool, the electrode gaps will be able to be controlled with greater fidelity. Furthermore, the ability to control smaller gaps may enable exploration of a wider variable space of the linear stability parameters.

Methods to improve the long range order should continue to be investigated. Order could be induced by having periodic nucleation points that would induce several wavelengths of adjacent order before having another nucleation point. Another option would be to optimize the piezo vibration experiments by either harnessing the flexure modes of silicon or by coupling larger piezo vibrations to the substrate more efficiently.

The formation of high aspect ratio, small characteristic spacing pillar arrays through the use of viscoelastic materials warrants further pursuit. Preliminary work suggests that the viscoelastic properties are responsible for the unique structures that are formed by electrohydrodynamics. Alternative models to linear stability analysis should be explored to explain the decrease in characteristic wavelength observed with these materials.

The “electrocuring” phenomenon observed with the thiol-ene material system may be worth further pursuit. The thiol-ene is believed to partially polymerize at the electrodes. Figure 10.2 shows a stretched thiol-ene pillar array in which the pillar basin is the same width as the pre-stretching basin, suggesting that the material partially cured prior to stretching.

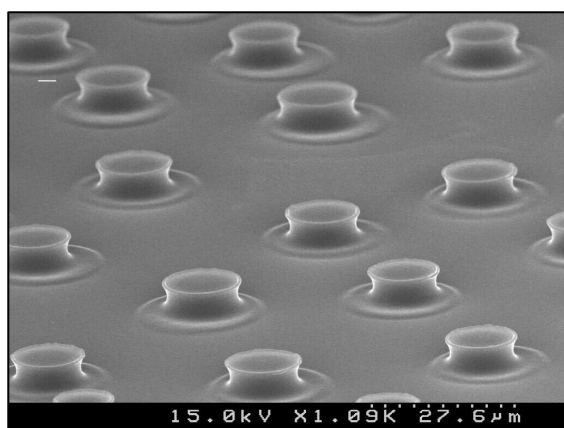


Figure 10.2: SEM image of stretched thiol-ene pillars with evidence of electrocuring.

Appendix A: Rotating Sector Method

Determining the rate coefficients k_p and k_t (polymerization and termination, respectively) are important for characterizing and modeling free radical polymerizations. Chapter 3 discusses the use of the dark polymerization method to determine k_p and k_t for the SFIL material system. Considerable effort was also expended using the rotating sector method, which is discussed in this Appendix.

Both the dark polymerization method and rotating sector method begin by determining the ratio of k_p and k_t . This ratio can be determined using real time IR methods combined with some simplifying assumptions, namely that the radical concentration within the reaction medium rapidly reaches a quasi-steady state upon irradiation. This assumption implies that the rate of radical generation is equal to the rate of termination. According to the model proposed in Chapter 3, this occurs very rapidly (<1 sec), as shown in Figure A.1.

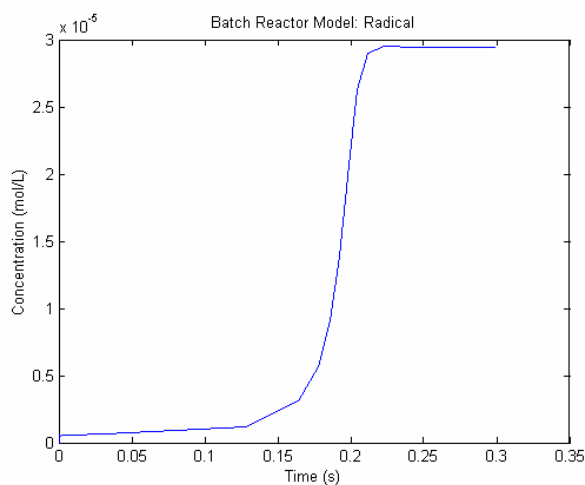


Figure A.1: Radical concentration as a function of time under typical (constant) irradiation.

The rotating sector method is a complementary technique used to measure the free radical polymerization rate coefficients k_p and k_t explicitly. The concept is to intermittently irradiate the monomer sample at known frequencies, which alters the temporal concentration of radicals in the reaction medium in a predictable way. The frequency and the duration of the irradiation are the controllable parameters in the rotating sector method. Figure A.2 shows a “rotating sector” (in black) that irradiates the sample $1/4^{\text{th}}$ of every rotation.

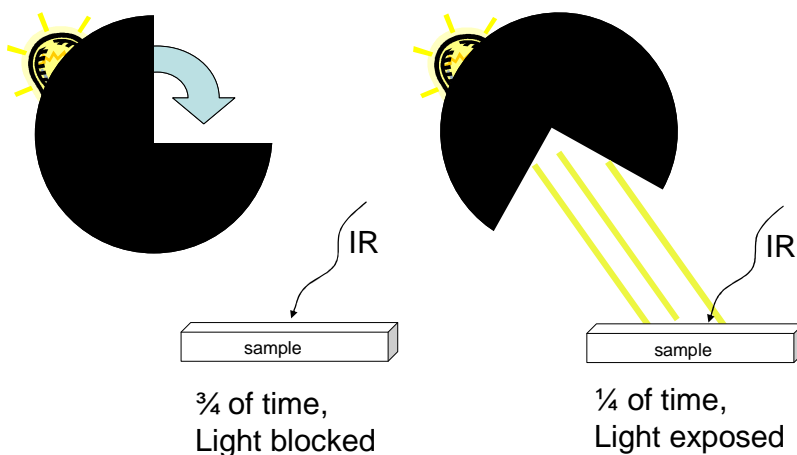


Figure A.2: Illustration of the rotating sector experimental approach.

As a consequence of this pulsed irradiation, the photogenerated radicals have time to recombine (i.e. terminate) during the dark period. For slow rotation rate (i.e. low frequencies), the radicals have enough time to terminate completely. Figure A.3 illustrates the difference in radical concentration between fast rotating and slow rotating speeds. The average radical concentration is higher at fast rotation speeds since the concentration never goes to zero. Thus, faster rotation speeds approach the polymerization rates of constant irradiation conditions, as shown in Figure A.4.

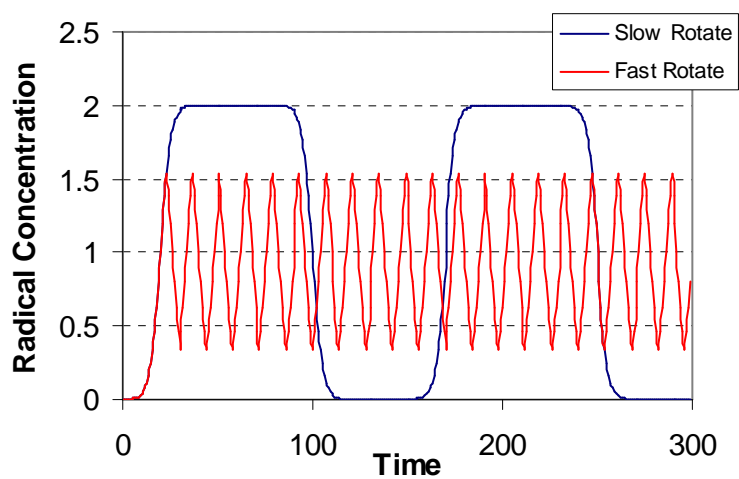


Figure A.3: Representative radical concentration as a function of time for various rotating sector frequencies.

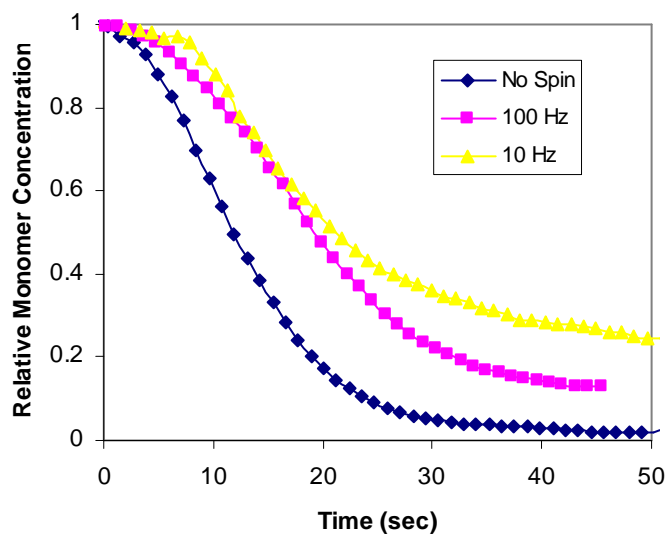


Figure A.4: Real time IR data of etch barrier polymerization at various rotating sector frequencies. The higher frequencies approach the rates obtained with constant irradiation (i.e. no spin).

In order to extract the rate coefficients from the rotating sector data, the rate of radical decay during the dark periods and the rate of radical generation during the light

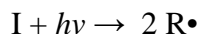
periods must be understood. The following derivation is modified from the text “Technique of Organic Chemistry Volume VIII, Rates and Mechanisms: Part II”.¹ The derivation is provided to (1) clarify several errors found within this text and (2) to fill in the missing links in the derivation of the equations found in this text as a resource for future students. The equation numbers listed in this Appendix correspond to the numbers listed in the book, for ease of cross referencing. Most of the symbols shown in this Appendix are defined in Chapter 3 and within the aforementioned text.

Unfortunately, in practice the rotating sector method proved to have several limitations. The rotating sector method has problems with unjustified assumptions, primarily due to the fact that the reaction environment is not necessarily constant from experiment to experiment. Regardless, the technique has been used by many investigators and the kinetic expressions for this technique are derived here.

A.1 DERIVATION

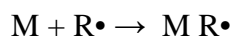
The three important steps in free radical kinetics are initiation, polymerization, and termination.

Initiation:



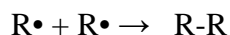
$$\text{Rate: } R_i = -2 k_I [I]$$

Polymerization:



$$\text{Rate: } R_p = -2 k_p [M][R\bullet] = d[M] / dt$$

Termination:



$$\text{Rate: } R_t = k_t [R\bullet][R\bullet]$$

Note that the rate of polymerization can be extracted from experimentally measured real time IR data. The rate of polymerization is proportional to radical concentration. Thus, the analytical strategy is to find an expression for the radical concentration during rotating sector conditions as a function of radical concentration during quasi-steady state conditions. The analysis starts with a radical balance, followed by an average radical concentration during the dark and light periods.

Radical Balance:

$$R_i - R_t = d[R\bullet]/dt$$

$$\text{Rate: } d[R]/dt = 2 f k_I [I] - 2 k_t [R\bullet][R\bullet]$$

At steady state,

$$\frac{d[R]}{dt} = 0$$

Therefore,

$$R_i = R_t \quad \text{and} \quad \left(\frac{R_i}{2k_t} \right)^{0.5} = [R]_s \quad (\text{Equation 10})$$

R_s is defined as the quasi-steady state radical concentration. Using this expression, a transient radical equation can be rewritten as,

$$\frac{d[R]}{dt} = 2k_t [R_s^2 - R^2]$$

Solving for the concentration of radicals, $[R]$, as a function of time:

$$\boxed{\frac{d[R]}{2k_t [R_s^2 - R^2]} = dt}$$

$$\frac{d[R]}{(R_s + R)(R_s - R)} = 2k_t dt$$

Rearrange by partial fractions

$$\frac{d[R]}{(2R_s)(R_s - R)} + \frac{d[R]}{(2R_s)(R_s + R)} = 2k_t dt$$

Integrate

$$\ln[R_s + R] - \ln[R_s - R] = 4R_s k_t t + c$$

Where t = time, and @ t=t₀, R=R_s

$$\ln \left(\frac{\left[1 + \frac{R}{R_s} \right]}{\left[1 - \frac{R}{R_s} \right]} \right) = 4R_s k_t (t - t_0)$$

Rearrange and solve for R,

$$\left(\frac{\left[1 + \frac{R}{R_s} \right]}{\left[1 - \frac{R}{R_s} \right]} \right) = e^{4R_s k_t (t - t_0)}$$

$$\left[1 + \frac{R}{R_s} \right] = \left[1 - \frac{R}{R_s} \right] e^{4R_s k_t (t - t_0)}$$

$$\left[1 + \frac{R}{R_s} \right] = \left[1 - \frac{R}{R_s} \right] e^{4R_s k_t (t - t_0)}$$

$$\frac{R}{R_s} \left[1 + e^{4R_s k_t (t - t_0)} \right] = e^{4R_s k_t (t - t_0)} - 1$$

$$\frac{R}{R_s} = \frac{\left(e^{4R_s k_t (t - t_0)} - 1 \right)}{\left(1 + e^{4R_s k_t (t - t_0)} \right)}$$

Multiply through by $e^{-2R_s k_t (t - t_0)}$

$$\frac{R}{R_s} = \frac{\left(e^{2R_s k_t (t - t_0)} - e^{-2R_s k_t (t - t_0)} \right)}{\left(e^{-2R_s k_t (t - t_0)} + e^{2R_s k_t (t - t_0)} \right)}$$

$$\tanh^{-1} \left(\frac{R}{R_s} \right) = 2R_s k_t (t - t_0)$$

Define $\tau_s = \frac{[R_s]}{(R_i)} = \frac{[R_s]}{(2k_t[R_s]^2)} = \frac{1}{(2k_t[R_s])}$ where R_t is rate of termination

Recall, at steady state $R_i = R_t$, so

$$2k_t[R_s]^2 = R_i \quad [R_s] = \left(\frac{R_i}{2k_t}\right)^{1/2} \quad \text{Plug in,}$$

$$\tau_s = \frac{1}{(2k_t R_i)^{0.5}} \quad \text{Therefore,}$$

$$\tanh^{-1}\left(\frac{R}{R_s}\right) = \frac{(t-t_0)}{\tau_s} \quad \tanh^{-1}\left(\frac{R}{R_s}\right) = (t-t_0)(2k_t R_i)^{0.5}$$

$$R = R_s \tanh\left[(t-t_0)(2k_t R_i)^{0.5}\right] \quad \text{(Equation 12)}$$

Light Period:

The next step is to determine the average radical concentration during the light and dark periods. Integrating Equation 12 over time lambda, λ , which is duration of light flash, gives average radical concentration during irradiation, R_λ :

$$\bar{R}_\lambda = \lambda^{-1} \int_0^\lambda [R] dt = \frac{1}{\lambda} R_s \int_0^\lambda \tanh\left[(2k_t R_i)^{0.5} t + c\right] dt$$

$$\bar{R}_\lambda = \frac{R_s}{\lambda(2k_t R_i)^{0.5}} \ln\left[\cosh\left((2k_t R_i)^{0.5} t + c\right)\right] \Big|_0^\lambda$$

$$\bar{R}_\lambda = \frac{\left(\frac{R_i}{2k_t}\right)^{1/2}}{\lambda(2k_t R_i)^{0.5}} \ln\left[\frac{\cosh\left((2k_t R_i)^{0.5} \lambda + c\right)}{\cosh\left((2k_t R_i)^{0.5} 0 + c\right)}\right]$$

$$\begin{aligned}
\bar{R}_\lambda &= \frac{1}{(2\lambda k_t)} \left[\ln[\cosh((2k_t R_i)^{0.5} \lambda + c)] - \ln[\cosh(c)] \right] \\
\bar{R}_\lambda &= \frac{1}{(4\lambda k_t)} \left[\ln[\cosh((2k_t R_i)^{0.5} \lambda + c)]^2 - \ln[\cosh(c)]^2 \right] \\
\bar{R}_\lambda &= \frac{1}{(4\lambda k_t)} \ln \left[\frac{\cosh((2k_t R_i)^{0.5} \lambda + c)}{\cosh(c)} \right]^2 \\
\bar{R}_\lambda &= \frac{1}{(4\lambda k_t)} \ln \left[\frac{\sec h^2(c)}{\sec h^2((2k_t R_i)^{0.5} \lambda + c)} \right] \\
\bar{R}_\lambda &= \frac{1}{(4\lambda k_t)} \ln \left[\frac{1 - \tanh^2(c)}{1 - \tanh^2((2k_t R_i)^{0.5} \lambda + c)} \right] \\
\bar{R}_\lambda &= \frac{1}{(4\lambda k_t)} \ln \left[\frac{R_s^2 - R_s^2 \tanh^2(c)}{R_s^2 - R_s^2 \tanh^2((2k_t R_i)^{0.5} \lambda + c)} \right] \\
\bar{R}_\lambda &= \frac{1}{(4\lambda k_t)} \ln \left[\frac{R_s^2 - R_1^2}{R_s^2 - R_2^2} \right] \\
\bar{R}_\lambda &= \frac{1}{(4\lambda k_t)} \ln \left[\frac{1 - \frac{R_1^2}{R_s^2}}{1 - \frac{R_2^2}{R_s^2}} \right]
\end{aligned}
\tag{Equation 13}$$

(R_λ is the average radical concentration during light exposure)

Dark Period:

The next step is to characterize the radical decay during the dark period when radicals are no longer being generated in order to find the average radical concentration during that period. Recall,

$$\frac{d[R]}{dt} = -2k_t[R]^2 \quad (\text{non-steady state radical decay}); \text{rearrange,}$$

$$\frac{d[R]}{[R]^2} = -2k_t dt \quad \text{integrate,}$$

$$\frac{-1}{[R]} = -2k_t t + c' \quad \text{subject to:} \quad @ \quad t = 0, R=R_2$$

$$t = r\lambda, R=R_1$$

(where r is ratio of light to dark)

$$\frac{1}{[R_1]} - \frac{1}{[R_2]} = 2rk_t\lambda \quad (\text{Equation 15})$$

The average radical concentration during the dark period, R_d , can be found by integrating over duration of the dark period, $r\lambda$.

$$\bar{R}_d = (r\lambda)^{-1} \int_0^{r\lambda} [R] dt = \frac{1}{r\lambda} \int_0^{r\lambda} \left[\frac{1}{2k_t t + c'} \right] dt$$

$$\bar{R}_d = \frac{1}{r\lambda(2k_t)} \ln(2k_t t + c') \Big|_0^{r\lambda}$$

$$\bar{R}_d = \frac{1}{2k_t r\lambda} [\ln(2k_t r\lambda + c') - \ln(c')]$$

$$\bar{R}_d = \frac{1}{2k_t r\lambda} \left[\ln\left(\frac{1}{[R_1]}\right) - \ln\left(\frac{1}{[R_2]}\right) \right]$$

$$\bar{R}_d = \frac{1}{2k_t r\lambda} \left[\ln\left(\frac{[R_2]}{[R_1]}\right) \right] \quad (\text{Equation 16})$$

(average radical concentration during dark period)

Overall Average Radical Concentration:

Average radical concentration overall is a combination of the dark and light periods weighed by the duration of those periods.

$$\begin{aligned}\bar{R}_0 &= \left(\frac{r}{r+1}\right)R_d + \left(\frac{1}{r+1}\right)R_\lambda \\ \bar{R}_0 &= \left(\frac{1}{r+1}\right)(rR_d + R_\lambda)\end{aligned}\quad \text{(Equation 17)}$$

Therefore, the average radical concentration for the rotating sector method is,

$$\bar{R}_0 = \left(\frac{1}{r+1}\right) \left(r \frac{1}{2k_i r \lambda} \left[\ln \left(\frac{[R_2]}{[R_1]} \right) \right] + \frac{1}{(4\lambda k_i)} \ln \left[\frac{1 - \frac{R_1^2}{R_s^2}}{1 - \frac{R_2^2}{R_s^2}} \right] \right) \quad \text{reduces to,}$$

$$\bar{R}_0 = \left(\frac{1}{r+1}\right) \left(\frac{1}{2k_i \lambda} \right) \left(\ln \left(\frac{[R_2]}{[R_1]} \right) + \frac{1}{2} \ln \left[\frac{1 - \frac{R_1^2}{R_s^2}}{1 - \frac{R_2^2}{R_s^2}} \right] \right) \quad \text{(Equation 18)}$$

Defining m:

Now define m, which is dimensionless, based on the rise in radical concentration during irradiation:

$$m = \tanh^{-1} \left(\frac{R_2}{R_s} \right) - \tanh^{-1} \left(\frac{R_1}{R_s} \right)$$

$$m = 2k_i \lambda R_s \quad \text{plug in equality from box}$$

$$m = (2k_i R_i)^{0.5} \lambda \quad \text{(Equation 19)}$$

From Equation 15 and Equation 19

$$\text{Rearrange Equation 15:} \quad \frac{1}{[R_1]} - \frac{1}{[R_2]} = 2rk_t \lambda$$

$$\frac{1}{[R_1]} = 2rk_t \lambda + \frac{1}{[R_2]}$$

$$[R_1] = \frac{1}{2rk_t \lambda + \frac{1}{[R_2]}} \quad \text{plug into m expression: } m = \tanh^{-1}\left(\frac{R_2}{R_s}\right) - \tanh^{-1}\left(\frac{R_1}{R_s}\right)$$

$$m = \tanh^{-1}\left(\frac{R_2}{R_s}\right) - \tanh^{-1}\left(\frac{R_2}{R_s(2rk_t \lambda R_2 + 1)}\right)$$

$$m = \tanh^{-1}\left(\frac{R_2}{R_s}\right) - \tanh^{-1}\left(\frac{R_2 / R_s}{(2rk_t \lambda R_2 + 1)}\right)$$

from Equation 19, plug in $m = 2k_t \lambda R_s$

$$m = \tanh^{-1}\left(\frac{R_2}{R_s}\right) - \tanh^{-1}\left(\frac{R_2 / R_s}{\left(\frac{R_2}{R_s} + 1\right)}\right) \quad (\text{Equation 21})$$

Now, convert Equation 19 to logarithmic form, as follows:

$$(\text{in general):} \quad x = \tanh(t) = \frac{e^t - e^{-t}}{e^t + e^{-t}} = \frac{e^{2t} - 1}{e^{2t} + 1}$$

$$xe^{2t} + x = e^{2t} - 1$$

$$e^{2t} = \frac{1+x}{1-x}$$

$$\tanh^{-1}(x) = t = \frac{1}{2} \ln \left(\frac{1+x}{1-x} \right)$$

Therefore, putting Equation 19 in logarithmic form:

$$m = \tanh^{-1} \left(\frac{R_2}{R_s} \right) - \tanh^{-1} \left(\frac{R_1}{R_s} \right)$$

$$m = \frac{1}{2} \ln \left(\frac{1 + \frac{R_2}{R_s}}{1 - \frac{R_2}{R_s}} \right) - \frac{1}{2} \ln \left(\frac{1 + \frac{R_1}{R_s}}{1 - \frac{R_1}{R_s}} \right) \quad \text{Rearrange:}$$

$$2m + \ln \left(1 + \frac{R_1}{R_s} \right) - \ln \left(1 + \frac{R_2}{R_s} \right) = \ln \left(1 + \frac{R_2}{R_s} \right) - \ln \left(1 + \frac{R_1}{R_s} \right) - \ln \left(1 - \frac{R_2}{R_s} \right) + \ln \left(1 - \frac{R_1}{R_s} \right) + \ln \left(1 + \frac{R_1}{R_s} \right) - \ln \left(1 + \frac{R_2}{R_s} \right)$$

$$2m + \ln \left(1 + \frac{R_1}{R_s} \right) - \ln \left(1 + \frac{R_2}{R_s} \right) = \ln \left(\frac{1 - \left(\frac{R_1}{R_s} \right)^2}{1 - \left(\frac{R_2}{R_s} \right)^2} \right) + \ln \left(1 + \frac{R_2}{R_s} \right) - \ln \left(1 + \frac{R_1}{R_s} \right)$$

$$2m + 2 \ln \left(1 + \frac{R_1}{R_s} \right) - 2 \ln \left(1 + \frac{R_2}{R_s} \right) = \ln \left(\frac{1 - \left(\frac{R_1}{R_s} \right)^2}{1 - \left(\frac{R_2}{R_s} \right)^2} \right)$$

Plug the right side of this equation into Equation 18

$$\bar{R}_0 = \left(\frac{1}{r+1} \right) \left(\frac{1}{2k_i \lambda} \right) \left(\ln \left(\frac{[R_2]}{[R_1]} \right) + \frac{1}{2} \ln \left[\frac{1 - \frac{R_1^2}{R_s^2}}{1 - \frac{R_2^2}{R_s^2}} \right] \right) \quad \text{(Equation 18)}$$

$$\bar{R}_0 = \left(\frac{1}{r+1}\right) \left(\frac{1}{2k_t \lambda}\right) \left(\ln \left(\frac{[R_2]}{[R_1]} \right) + m + \ln \left(1 + \frac{R_1}{R_s} \right) - \ln \left(1 + \frac{R_2}{R_s} \right) \right) \quad \text{Rearrange,}$$

$$\bar{R}_0 = \left(\frac{1}{r+1}\right) \left(\frac{1}{2k_t \lambda}\right) \left(\ln \left(\frac{[R_2]}{[R_1]} \right) + m + \ln \left(\frac{1 + \frac{R_1}{R_s}}{1 + \frac{R_2}{R_s}} \right) \right) \quad \text{Replace } R_1 \text{ with } R_2$$

We have shown,

$$[R_1] = \frac{1}{2rk_t \lambda + \frac{1}{[R_2]}} = \frac{R_2}{2rk_t \lambda R_2 + 1} = \frac{R_2}{rmR_2 / R_s + 1} \quad \text{Plug in}$$

$$\bar{R}_0 = \left(\frac{1}{r+1}\right) \left(\frac{1}{2k_t \lambda}\right) \left(\ln \left(\frac{rmR_2 / R_s + 1}{1 + \frac{R_2}{R_s}} \right) + m + \ln \left(\frac{1 + \frac{R_2}{R_s}}{1 + \frac{R_2}{R_s}} \right) \right)$$

$$\bar{R}_0 = \left(\frac{1}{r+1}\right) \left(\frac{1}{2k_t \lambda}\right) \left(m + \ln \left(\frac{1 + \frac{rmR_2}{R_s} + \frac{R_2}{R_s}}{1 + \frac{R_2}{R_s}} \right) \right)$$

Factor out m and multiply natural log term by Rs/R₂

$$\bar{R}_0 = \left(\frac{1}{r+1}\right) \left(\frac{m}{2k_t \lambda}\right) \left(1 + m^{-1} \ln \left(\frac{1 + rm + \frac{R_s}{R_2}}{1 + \frac{R_s}{R_2}} \right) \right) \quad \text{Rearrange,}$$

$$\bar{R}_0 = \left(\frac{1}{r+1} \right) \left(\frac{m}{2k_t \lambda} \right) \left(1 + m^{-1} \ln \left(1 + \frac{rm}{\left(1 + \frac{R_s}{R_2} \right)} \right) \right)$$

recall that R_s and m are:

$$m = (2k_t R_i)^{0.5} \lambda \quad [R_s] = \left(\frac{R_i}{2k_t} \right)^{1/2} \quad \text{therefore,}$$

$$\frac{\bar{R}_0}{R_s} = \left(\frac{1}{r+1} \right) \left(1 + m^{-1} \ln \left(1 + \frac{rm}{\left(1 + \frac{R_s}{R_2} \right)} \right) \right) \quad (\text{Equation 20})$$

Finally, to derive Equation 22, start with Equation 21

$$m = \tanh^{-1} \left(\frac{R_2}{R_s} \right) - \tanh^{-1} \left(\frac{R_2 / R_s}{\left(rm R_2 / R_s + 1 \right)} \right) \quad (\text{Equation 21})$$

Let $A = \left(\frac{R_2}{R_s} \right)$ and plug into Equation 21

$$m = \tanh^{-1}(A) - \tanh^{-1} \left(\frac{A}{(rmA + 1)} \right) \quad \text{Convert to logarithmic form,}$$

$$m = \frac{1}{2} \ln \left(\frac{1+A}{1-A} \right) - \frac{1}{2} \ln \left(\frac{1 + \frac{A}{(rmA+1)}}{1 - \frac{A}{(rmA+1)}} \right) \quad \text{rearrange,}$$

$$2m = \ln \left(\frac{1+A}{1-A} \right) - \ln \left(\frac{1+rmA+A}{1+rmA-A} \right) \quad \text{put in exponential form}$$

$$e^{2m} = \left(\frac{1+A}{1-A} \right) \left(\frac{1+rmA-A}{1+rmA+A} \right) \quad \text{Factor out:}$$

$$e^{2m} (1+rmA+A-A-rmA^2-A^2) = (1+rmA-A+A+rmA^2-A^2) \quad \text{cancel out A}$$

$$e^{2m} (1+rmA-rmA^2-A^2) = (1+rmA+rmA^2-A^2) \quad \text{rearrange}$$

$$e^{2m} - 1 = (rmA+rmA^2-A^2) - e^{2m} (rmA-rmA^2-A^2) \quad \text{separate } A^2, A$$

$$e^{2m} - 1 = e^{2m} (rmA^2 e^{-2m} - A^2 e^{-2m} + rmA^2 + A^2) + e^{2m} (-rmA + rmA e^{-2m})$$

$$e^{2m} - 1 = e^{2m} A^2 (rme^{-2m} - e^{-2m} + rm + 1) + e^{2m} A (-rm + rme^{-2m}) \quad \text{divide by } e^{2m}$$

$$1 - e^{-2m} = A^2 (rme^{-2m} - e^{-2m} + rm + 1) + A (-rm + rme^{-2m}) \quad \text{quadratic equation!}$$

$$A = \frac{(rm - rme^{-2m}) \pm \sqrt{\left((-rm + rme^{-2m})^2 - 4(1 + rm - e^{-2m} + rme^{-2m})(-1 + e^{-2m}) \right)}}{2(rme^{-2m} - e^{-2m} + rm + 1)}$$

Next, factor out rm from this expression,

$$A = \frac{rm(1 - e^{-2m}) \pm \sqrt{(r^2 m^2 (-1 + e^{-2m})^2 + 4(1 + rm - e^{-2m} + rme^{-2m})(1 - e^{-2m}))}}{2(rme^{-2m} - e^{-2m} + rm + 1)}$$

$$A = \frac{rm(1 - e^{-2m}) \pm \sqrt{(r^2 m^2 (1 - e^{-2m})^2 + 4(1 - e^{-2m} + rm(1 + e^{-2m}))(1 - e^{-2m}))}}{2(rm(1 + e^{-2m}) + 1 - e^{-2m})}$$

Multiply through

$$A = \frac{rm \frac{(1 - e^{-2m})}{(1 + e^{-2m})} \pm \sqrt{\left(r^2 m^2 \frac{(1 - e^{-2m})^2}{(1 + e^{-2m})^2} + 4 \left(\frac{(1 - e^{-2m})}{(1 + e^{-2m})} + rm \right) \frac{(1 - e^{-2m})}{(1 + e^{-2m})} \right)}}{2 \left(rm + \frac{(1 - e^{-2m})}{(1 + e^{-2m})} \right)}$$

Recall, that $\frac{(1 - e^{-2m})}{(1 + e^{-2m})} = \frac{(e^m - e^{-m})}{(e^m + e^{-m})} = \tanh(m)$ therefore,

$$A = \frac{rm \tanh(m) + \sqrt{(r^2 m^2 \tanh^2(m) + 4(\tanh(m) + rm)\tanh(m))}}{2(rm + \tanh(m))} \quad \text{plug in for A,}$$

$$\left(\frac{R_2}{R_s} \right) = \frac{rm \tanh(m) + \sqrt{(r^2 m^2 \tanh^2(m) + 4(\tanh(m) + rm)\tanh(m))}}{2(rm + \tanh(m))} \quad \text{(Equation 22)}$$

This derivation allows rotating sector data to be compared to quasi-steady state data to extract k_t . The rate of polymerization (i.e. the slop of monomer concentration versus time) is proportional to the radical concentration. Thus, comparing the slopes of rotating sector data and conventional data at a given monomer concentration provides an

experimental value for R_0/R_s in Equation 20. The value of m in Equation 20 is a function of k_t , which allows for the coefficient to be determined explicitly.

A.2 REFERENCES

1. Jonassen, H. B.; Weissberger, A., Technique of inorganic chemistry. In Interscience Publishers: New York, 1963; Vol. VIII, p v.

Appendix B

Automated Statistical Process Control Experiment

The experiment described in this appendix was designed for the “fundamentals of measurements and data analysis” junior level chemical engineering undergraduate laboratory at the University of Texas.¹ The work was motivated by feedback from recent graduates who indicate that familiarity with statistical process control (SPC) charts is one of the most valuable skills for newly hired process engineers. In the following experiment, students are introduced to the concept of SPC through a simple in-line mixing experiment. An aqueous stream with green food coloring is diluted with a stream of tap water and the dye concentration is monitored in-situ spectroscopically before and after an inline mixer. Students learn to create SPC control charts and, more importantly, to understand their function through some subtleties in the acquired data.

B.1 BACKGROUND

Dr. Walter A. Shewhart first introduced the concept of statistical process control (SPC) charts in the 1920's as a diagnostic tool that can be used to systematically reduce variability in production². SPC charts typically monitor important processing parameters (e.g.. temperature, product yield, etc.) associated with repetitive operations in industrial plants and scientific laboratories. The principal function of the control chart is to distinguish natural variability in a process from fluctuations attributable to an assignable cause (e.g. equipment failure, operator error, etc.).

Process control charts are generated by plotting a measurable process parameter as a function of time. The expectations for a stable, naturally fluctuating process are represented graphically on the control chart by three parallel horizontal lines: the centerline, the upper control limit (UCL), and lower control limit (LCL). Naturally occurring process variation causes the data to fluctuate about the centerline and the UCL and LCL lines provide statistically acceptable bounds for the data. The process control limits are typically set at $\pm 3\sigma$ from the centerline, where σ is the standard deviation of the measured parameter. For a stable system, ~99.7% of the measured parameter values should fall within the “three-sigma” control limits³.

An “out of control” process results when there is a statistically significant portion of the data outside the control limits (typically one or more points), or when there is systematic variability in the monitored parameter such as cyclic patterns, trends, and shifts that demonstrate non-random fluctuations resulting from assignable causes.

In this experiment, SPC charts will be created to evaluate an inline mixing process, where a solution stream with a high concentration of food coloring will be mixed with a pure water stream to create a diluted “product” stream. The dye concentration in the product stream will be monitored spectroscopically at points immediately before and after an inline mixing device. Charts created in this experiment illustrate some very important lessons in statistical process control. The most critical lesson is that effective use of control charts requires more than simple visual inspection. Knowledge of the process and a common sense approach to analysis are critical requirements for coming to the proper conclusions regarding SPC charts. Specifically, efforts to reduce variability in a process, such as adding an inline mixer, typically result in narrower control limits. Narrow control limits are more sensitive to minor non-random fluctuations and therefore

are more likely to produce “out of control” results. The key is for students to recognize this trade-off and make the proper recommendations for handling sensitive control limits.

B.2 EXPERIMENTAL PROCEDURE

A diagram of the experimental process is shown in Figure 1, where a feed stream of green dye solution is mixed with a pure water stream to create a “product” stream with a lower dye concentration. Green food coloring (Adam’s Extract) is used as the process dye and a pair of spectrometers are used for detection. Full details for the equipment and materials are given in the supplemental materials.

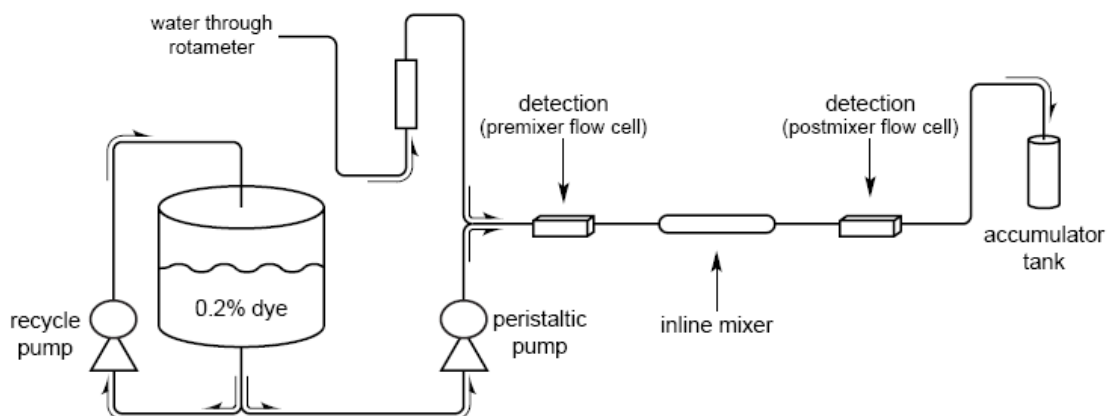


Figure B.1: Process diagram for the mixing system. A concentrated bulk green dye solution (0.2 wt%) is mixed with a pure water stream to create a “product” stream (0.1 wt%). The dye concentration is measured with spectrometers before and after an in-line mixer.

The students should be familiar with the basic concept of control charts from the lecture portion of the class. The students are required to perform several simple tasks during the experiment: mix the feedstock solution, calibrate the water flow meter prior to beginning the data acquisition, and make simple calculations using Beer’s law. The

spectrometer comes with user-friendly software, but may require a briefing by the instructor prior to operation.

At least 500 absorbance measurements are taken of just the feedstock stream, which is used for analysis of the variability of the detectors and to determine the concentration of the feedstock solution. Following these measurements, the pure water stream is set to the appropriate flow rate to dilute the feedstock stream to 0.1 wt%. A minimum of 1000 absorbance measurements are taken on this process stream (at a rate of about 1 per second). These experimental data are then used to generate SPC charts. The entire experiment can be performed in two hours.

B.3 HAZARDS

A safe, non-toxic food coloring should be used as the process dye. Some care should be taken to position electrical equipment (pumps, computer, spectrometer lamp) in dry areas away from any potential dripping/leaking piping.

B.4 RESULTS AND DISCUSSION

The primary pedagogical goal of this experiment is to teach students how to create and analyze SPC charts by evaluating the effects of the inline mixer on the dye mixing process. These charts can be quickly produced using a statistical software package (*e.g.* JMP, SAS Institute) or using a spreadsheet program such as Microsoft Excel. Students are required to provide sample hand calculations in the lab report to avoid an over-reliance on “black box” computer programs.

Some typical raw data from this experiment are shown Figure 2, where absorbance has been converted to dye concentration via Beer’s Law. It is readily

apparent that concentration fluctuations are much greater in the pre-mixer readings than in the post-mixer readings, which implies that the inline mixer is effectively reducing concentration variations.

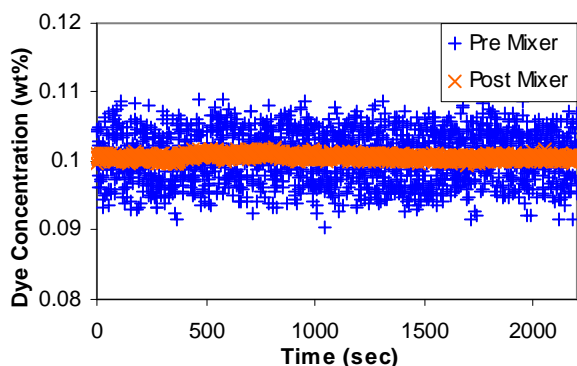


Figure B.2: Typical dye concentration data for the pre-mixer and post-mixer measured spectroscopically. The data demonstrates the dramatic decrease in variability achieved by the inline mixer and consequently, the improved process capability.

The students convert the raw data into control chart format, breaking down the data into subgroups of size $n=5$. Subgroups intervals are chosen such that the variation within each subgroup is attributable to only natural process variation. This is often accomplished by picking a time interval that is short relative to any possible systematic process variation. Figures 3 and 4 present the pre- and post-mixer data in the two control chart formats, X-bar chart and R (range) chart. X-bar charts plot the average value of each subgroup, while R charts plot the range of each subgroup, a measure of variability (see the Lab Documentation for details on the formation of control charts). As expected, the measured variability is lower after the stream passes through the inline mixer. Based on the R-bar values found on the R charts in Figures 3b and 4b, the mixer reduces concentration variance by a factor of 13. Students are asked to consider why decreased variance is important to the process by becoming familiar with the process capability

index (C_p). C_p is the ratio of product tolerance limits to the process control limits, which provides a useful heuristic for evaluating the ability of a process to meet given product specifications. The students will find that the pre-mixer and post-mixer capability values differ significantly. The pre-mixer process has a C_p value of about 0.2 versus a value of about 1.6 for the post-mixer (using specification limits of 0.100 ± 0.002 wt%). Generally, a C_p of at least 1.3 is desired to ensure that the product meets specification. Thus, the calculation of C_p clearly demonstrates the importance of the mixer in assuring the product is actually meeting specifications.

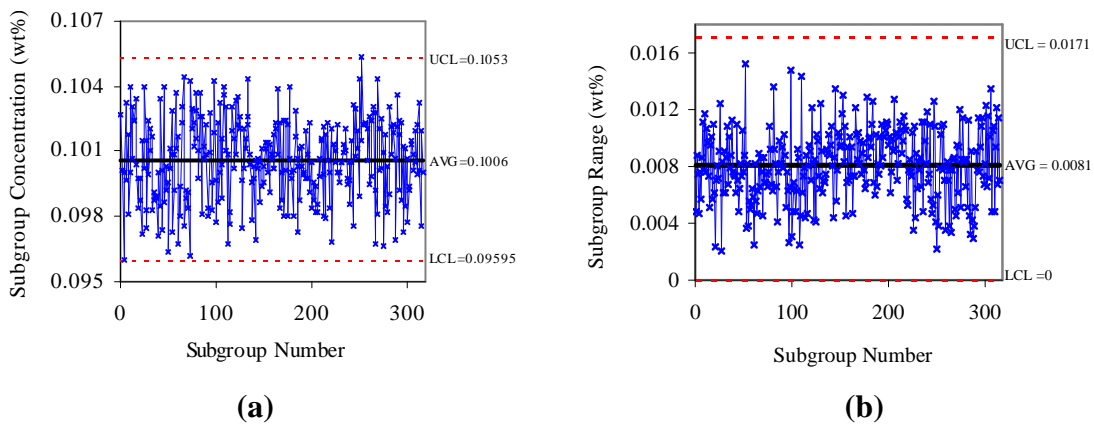


Figure B.3: Example SPC charts from the pre-mixer detector during mixing trial. (a) X-bar type chart, (b) R chart type.

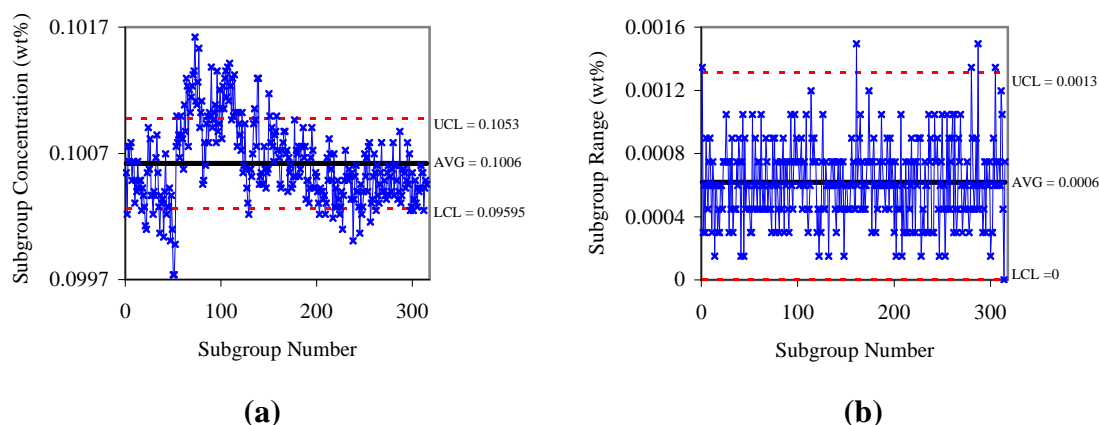


Figure B.4: Example SPC charts from the post-mixer detector during mixing trial. (a) X-bar type chart, (b) R chart type.

Intuition suggests to most students that having an inline mixer will provide an improvement in variance over not having a mixer in the process stream. This intuition is validated by the dramatic reduction in variability achieved by the inline mixer, as seen in Figure 2, and by the corresponding increase in C_p obtained through use of the mixer. Despite these improvements, a non-discerning examination of the SPC charts could lead to the incorrect conclusion that the inline mixer is detrimental to the process. The post-mixer X-bar chart (Figure 4a) shows that the process is “out of control” because there are numerous points outside the control limits, which is in contrast to the pre-mixer data. Based on this purely statistical analysis, the inline mixer has seemingly made things “worse” not “better”. This apparent contradiction between simplistic chart reading and common sense expectations provides a very powerful learning tool. The ability of the inline mixer to homogenize the solution reduces the post-mixer variability, which in turn results in narrower control limits for the post-mixer. Consequently, the post-mixer control charts are more sensitive to small processing fluctuations that are otherwise drowned out by the large variability in the pre-mixer data. Narrow control limits rapidly

alert the observer to small non-random fluctuations, but are also more likely to detect non-significant process variations. Therefore, it is critical that the student understands both the source and the impact of any assignable variations to determine whether the source should be addressed or neglected.

The primary reason the post-mixer data in Figure 4a is “out of control” is due to the presence of systematic trends in the data. The trends in the data are known as “autocorrelation,” where successive measurements are not independent. Although rigorous methods exist to quantify autocorrelation, a simple test is suggested in the lab handout to prove the data are non-random. The method involves randomizing the order of the data as a function of time, and recalculating the control charts. If the data is truly random, then the order of the data should have no impact on the control charts. After randomizing the data, the average range (\bar{R}) typically increases by a factor of 5-10 for the post mixer data. This simple analysis proves the fluctuations are non-random and implies that the data are correlated.

In the final step of the analysis, students must identify the source of the non-random trends. The most likely culprit is non-constant water flow rates due to changing water pressure in the building manifold. Careful observation of the rotameter on the water line would reveal slight fluctuations during the experiment. The sensitive control limits of the post-mixer charts are capable of detecting these small process fluctuations. The pre-mixer charts are incapable of detecting these fluctuations due to the magnitude of the variations caused by poor mixing.

Based on their analysis, students must make recommendations for a future course of action, such as eliminating the assignable causes of variation or re-evaluating the control limits in light of the processing requirements. Typically when a process is “out of control,” the source of non-random fluctuations must be removed. However, since all

of the data falls within the processing requirements, re-evaluation of the control limits would be the least expensive corrective action.

B.5 CONCLUSIONS

An experiment designed to teach students the power of SPC charts was presented. The students learn how to create and analyze control charts in an effort to evaluate the benefits of a mixer. The experimental configuration is useful for statistical analysis since the spectrometer detectors can rapidly acquire many data points. An important component of the pedagogical power of this experiment lies in the seemingly contradictory nature of the data obtained, which forces the students to develop a deeper understanding of control charts. The experimental results show that the mixer clearly reduces measured variability in dye concentration. However, the reduction in variability narrows the control limits, making the post-mixer control charts hypersensitive to minor process fluctuations. The consequence of this effect is that the post-mixer data are technically “out of control” whereas the pre-mixer data are “in control” despite having significantly greater process variance. The source of the “out of control” data can be logically narrowed down to a single assignable cause: variation water flow rate. Students are forced to justify a course of action based on the analysis of the control charts. Options include modifying the control limits or eliminating sources of non-natural variability.

B.5.1 Supplemental Material

An expanded version of the text and a detailed experimental procedure for the student and the instructor can be found on-line.¹ The techniques to create SPC charts are well established and can be found in most general statistics books.⁴⁻⁶

B.6 REFERENCES

1. Dickey, M. D.; Stewart, M. D.; Willson, C. G.; Dickey, D. A., An automated statistical process control study of in line mixing using spectrophotometric detection. *Journal of Chemical Education* **2006**, 83, (1), 110-113.
2. Shewhart, W. A., Economic control of quality of manufactured product. D. Van Nostrand Company Inc.: New York, 1931; p xiv, 501.
3. Wheeler, D. J.; Chambers, D. S., Understanding statistical process control. Statistical Process Controls: Knoxville, Tenn., 1986; p x, 340.
4. John, P. W. M., Statistical methods in engineering and quality assurance. Wiley: New York, 1990; p xvi, 373.
5. Walpole, R. E., Probability & statistics for engineers & scientists. 7th ed.; Prentice Hall: Upper Saddle River, NJ, 2002; p xvi, 730.
6. Miller, I.; Freund, J. E.; Johnson, R. A., Miller and Freund's Probability and statistics for engineers. Prentice Hall: Englewood Cliffs, N.J., 1994; p x, 630.

Appendix C: Supporting Data

This appendix contains miscellaneous data and supporting information that may aid in replicating the results presented in this thesis.

C.1 MATERIALS

The materials used in this thesis are listed in Table C.1 along with their full name and supplier.

Table C.1: Key Materials Used in Thesis

| Name in Thesis | Full Name | Supplier |
|-------------------------|--|-----------------------------|
| Thiol | Pentaerythritol tetrakis(3-mercaptopropionate) | Aldrich |
| Vinyl Ether (“Ene”) | Tris [4-(vinylloxy)butyl] trimellitate | Aldrich |
| Acrylate | Di(trimethylolpropane) tetraacrylate | Aldrich |
| Acrylate (DMS) | Acryloxy terminated polydimethylsiloxane | Gelest |
| Epoxy (“Epon Epoxy”) | Bisphenol A diglycidyl ether (Epon 828) | Polysciences |
| Epoxy (“CHO Epoxy”) | 3,4-Epoxy cyclohexylmethyl 3,4-epoxycyclohexanecarboxylate | Aldrich |
| PMMA | Poly(methyl methacrylate), 25k MW | Polysciences |
| PS | Polystyrene, 200k and 4k MW | Aldrich |
| PI | Polyisoprene (trans), catalog 182168 | Aldrich |
| PB | Polybutadiene (cis & trans), 420k MW | Aldrich |
| PCL | Poly(caprolactone) | Dow Tone Polymer P-767 |
| PLA | Poly (DL-lactide) | Birmingham Polymers: D02038 |

C.2 ELLIPSOMETRY

Ellipsometry was utilized to measure film thickness. To determine the thickness, the optical properties of the film must be known. The Cauchy equation, shown below, is a common model to capture the change in index as a function of wavelength.

$$n = A + \frac{B}{\lambda^2} + \frac{C}{\lambda^4}$$

Experimentally determined Cauchy coefficients (A, B, C) are listed in Table C.2.

Table C.2: Experimentally Determined Cauchy Coefficients

| Material | A | B | C |
|----------------|-------|-----------------------|-----------------------|
| Thiol-ene | 1.508 | 4.99×10^{-3} | 2.56×10^{-5} |
| Thiol-acrylate | 1.502 | 5.45×10^{-3} | 1.31×10^{-4} |
| Vinyl Ether | 1.518 | 5.16×10^{-3} | 4.32×10^{-4} |
| Epoxy | 1.516 | 5.66×10^{-3} | 3.15×10^{-4} |
| PMMA | 1.486 | 4.36×10^{-3} | 9.52×10^{-5} |
| PS | 1.57 | 7.33×10^{-3} | 4.81×10^{-4} |
| Polyisoprene | 1.58 | 1.11×10^{-2} | 1.74×10^{-4} |
| PLA | 1.447 | 3.96×10^{-3} | 1.16×10^{-6} |
| PGLA | 1.460 | 3.36×10^{-3} | 9.05×10^{-6} |
| DMS | 1.402 | 4.45×10^{-3} | 2.95×10^{-5} |

C.3 FILM THICKNESS

Thin films of various materials were studied under electrohydrodynamic conditions. Table C.3 lists various solution formulations and the spin speeds required to give the reported film thicknesses.

Table C.3: Solution Formulations and Spin Speeds

| Material | Component 1 | Component 2 | Solvent | Spin Speed (RPM) | Thickness (nm) |
|-------------------|-------------|-------------------------|------------|------------------|----------------|
| Thiol-Vinyl Ether | 20% Thiol | 20% VE | Toluene | 5000 | 1500 |
| Thiol-Vinyl Ether | 17.5% Thiol | 17.5% VE | PGMEA | 2500 | 800 |
| Thiol-Vinyl Ether | 10% Thiol | 10% VE | Toluene | 2500 | 800 |
| Thiol-Vinyl Ether | 10% Thiol | 10% VE | Chloroform | 2500 | 1934 |
| Thiol-Vinyl Ether | 5% Thiol | 5% VE | Chloroform | 2500 | 780 |
| Thiol-Vinyl Ether | 2.5% Thiol | 2.5% VE | Toluene | 3500 | 100 |
| Thiol-Vinyl Ether | 2.5% Thiol | 2.5% VE | Chloroform | 2500 | 70 |
| Vinyl Ether | 30% VE | 5% Cyacure | PGMEA | 2500 | 800 |
| Thiol-Acrylate | 17.5% Thiol | 17.5% Acrylate | PGMEA | 3300 | 800 |
| Acrylate (DMS) | 50% DMS | 5% Darocur | Toluene | 1000 | 4400 |
| Acrylate (DMS) | 50% DMS | 5% Darocur | Toluene | 3000 | 3370 |
| Acrylate (DMS) | 33% DMS | 5% Darocur | Toluene | 2300 | 1900 |
| Acrylate (DMS) | 33% DMS | 5% Darocur | Toluene | 3200 | 1200 |
| Acrylate (DMS) | 30% DMS | 5% Darocur | Toluene | 2500 | 1200 |
| Acrylate (DMS) | 25% DMS | 5% Darocur | Toluene | 2500 | 800 |
| Acrylate (DMS) | 17% DMS | 5% Darocur | Toluene | 1100 | 620 |
| Acrylate (DMS) | 17% DMS | 5% Darocur | Toluene | 2300 | 400 |
| Epoxy | 17.5% Epon | 17.5% CHO 5% Cyacure | PGMEA | 3500 | 800 |

Table C.3: (Continued) Solution Formulations and Spin Speeds

| Material | Component 1 | Component 2 | Solvent* | Spin Speed (RPM) | Thickness (nm) |
|--------------------|-------------|-------------|----------------------|------------------|----------------|
| PMMA | 20% PMMA | --- | Chlorobenzene | 1500 | 3000 |
| PMMA | 20% PMMA | --- | Chlorobenzene | 3100 | 2000 |
| PMMA | 14% PMMA | --- | Chlorobenzene | 3000 | 1200 |
| PMMA | 12.5% PMMA | --- | Chlorobenzene | 2500 | 1200 |
| PMMA | 10% PMMA | --- | Chlorobenzene | 2500 | 590 |
| PMMA | 8% PMMA | --- | Chloroform | 2500 | 1500 |
| PMMA | 6.5% PMMA | --- | Chloroform | 2500 | 930 |
| PMMA | 5% PMMA | --- | Chloroform | 3000 | 600 |
| PS | 12.5% PS | --- | Toluene | 3000 | 900 |
| Polyisoprene | 2% PI | --- | Chloroform | 2500 | 1500 |
| Polybutadiene | 5% PB | --- | Toluene | 2500 | 1100 |
| Poly(caprolactone) | 8% PCL | --- | Toluene | 2500 | 1000 |
| Poly(caprolactone) | 6% PCL | --- | Toluene | 2500 | 500 |
| PLA | 10% PLA | --- | 20% ACN 70% PGMEA | 2500 | 900 |
| PGLA | 7.5% PGLA | 22.5% ACN | PGMEA | 3000 | 460 |
| PGLA | 10% PGLA | 30% ACN | PGMEA | 3000 | 910 |
| SU-8 | 10% SU-8-10 | --- | CP | 3000 | 40 |
| SU-8 | 30% SU-8-10 | --- | CP | 3000 | 650 |
| SU-8 | 24% SU-8-10 | --- | CP | 3000 | 480 |
| SU-8 | 10% SU-8-10 | --- | CP | 3000 | 230 |

* PGMEA is propylene glycol monomethyl ether acetate, CP is cyclopentanone, ACN is acetonitrile.

Thiol-ene is the material used most frequently throughout this thesis. Figures C.1 and C.2 are spin curves of thiol-ene film thickness as a function of the inverse square root of spin speed for different formulation concentrations. The reported percentages in the legends are the weight percent of 1:1 thiol-ene in solvent (toluene and PGMEA, respectively). The data are fit with lines using the least squares method.

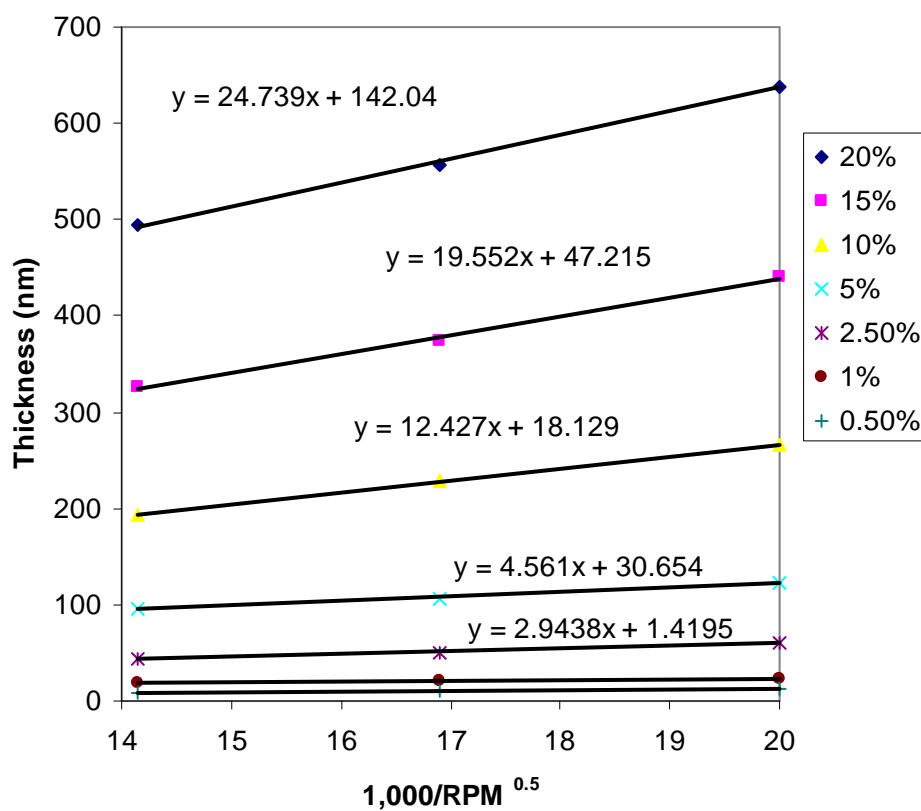


Figure C.1: Spin curves for thiol-ene (1:1 by weight) in toluene

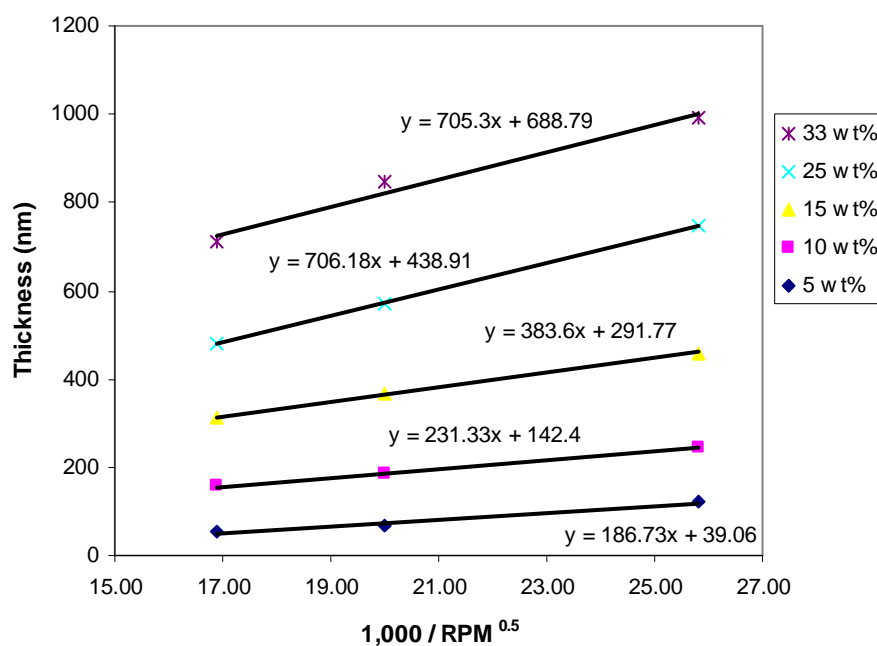


Figure C.2: Spin curves for thiol-ene (1:1 by weight) in PGMEA

C.4 ELECTRODE PROCESSING

The following helpful hints may facilitate future upper electrode processing. The electrodes in the “glass slide method” (Chapter 4) were fabricated from 1x3” glass slides. Corning 2947 Microslides are inexpensive and work well for forming the electrodes. The Fisherbrand (Cat 12-549) slides did not work well as they created physical streaks during etching. ArrayIt SuperClean Substrates (Microarray Technology, Cat ID: SMC) worked the best in terms of flatness and creating a clean etch, but these slides are quite expensive.

The electrode recesses in the slide were processed by first spray painting (Krylon “Fusion for Plastics”) the slides using a stencil mask. The stencil was a thin, 1 x 2.54 cm piece of metal. Each slide was patterned with two electrodes to improve efficiency. The slide was cut in half after processing to produce two upper electrodes.

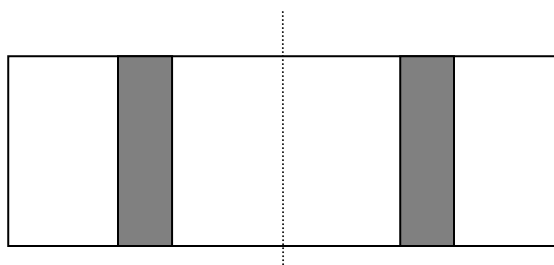


Figure C.3: Top down view of 1 x 3" microscope slide. The light regions of the slide are spray painted, and the gray areas of the slide are etched by a buffered oxide etch. The final step is to cut the slide in half, noted by the dotted line.

The slides are then submersed in a buffered oxide etch. The etch rate is ~ 0.6 $\mu\text{m/hr}$ for pure quartz (e.g. mask blanks used to form templates) and ~ 1 $\mu\text{m/min}$ for the float glass slides typically used in the "glass slide method". A custom designed Teflon holder was created to hold 8 slides at a time to maximize the throughput of the etching.

The recesses are coated with ~ 10 nm of chromium by thermal evaporation to create the upper electrode. The paint is removed by solvent (e.g. acetone) and the slide is cut in half to produce a pair of electrodes.

The templates used on the active gap tool are processed via photolithography, as described in Chapter 8. During the buffered oxide etch, used to create the template safety ledge, the back side of the templates can be protected through the use of tape (e.g. Kapton tape, CS Hyde or metallic tape, Ideal Tape Inc.) that has acrylic adhesive (i.e. not silicone based). Melted wax works well to seal the edge of the tape around the perimeter of the template.

The template surface can be protected by tape as the edge is rounded by a belt sander. The template is then cleaned by sonication in solvent, followed by oxygen plasma, prior to depositing ITO by e-beam evaporation.

C.5 ELECTROCURING

The thiol-ene material is believed to partially polymerize in the absence of light when placed between two charged electrodes. The ene does not polymerize by itself, implying that the thiol is responsible for the polymerization. Interestingly, the thiol-acrylate does not electrocure, only the thiol-vinyl ether (Chapter 6).

Cyclic voltammetry was performed to provide insights into the “electrocuring”. A 1 mm Pt electrode was utilized at a scan rate of 0.2 V/sec. The analyte concentration was set to 1mM and the solutions were degassed with argon. Tetrabutyl ammonium perchlorate was used as the electrolyte. The following cyclic voltammetry plots provide evidence of disulfide bond formation.

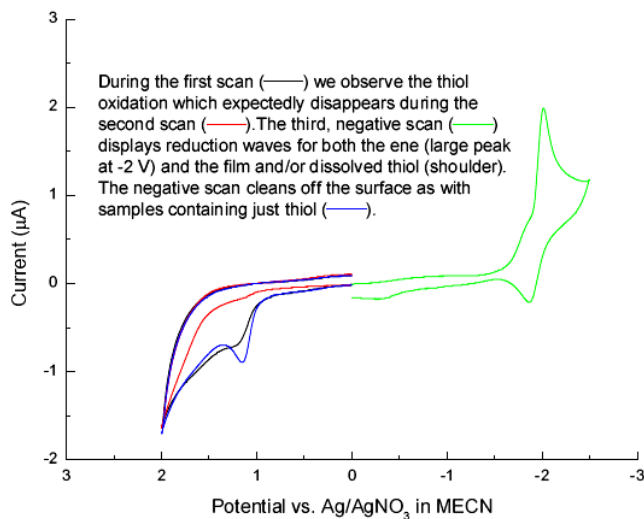


Figure C.4: Cyclic voltammogram of thiol-ene in MECN.

In Figure C.4, we believe sulfur oligomerizes on the probes such that the reverse of the first scan and the entire second scan have no “features” (i.e. humps) since the electrode probe is blocked by oligomer. The thiols undergo anodic oxidation to form

disulfide dimmers. Since the film is electroactive, the disulfide bonds can be reduced using a negative scan. This reversal is evident in Figure C.6.

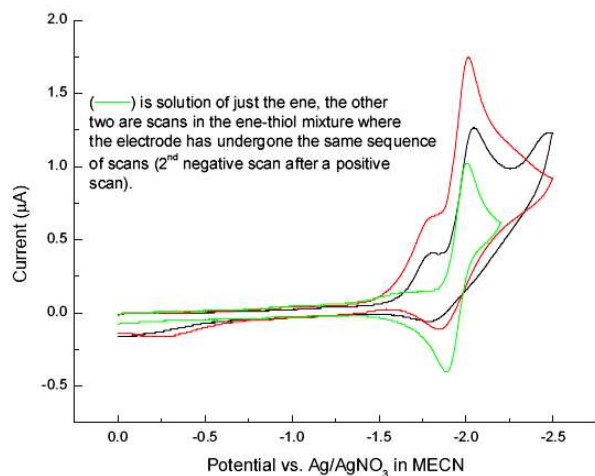


Figure C.5: Cyclic voltammogram of ene in MECN.

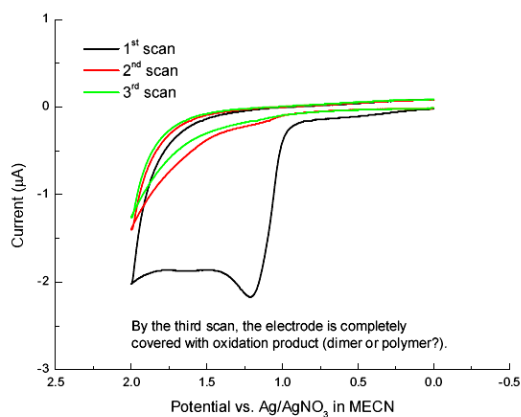


Figure C.6: Cyclic voltammograms of thiol in MECN.

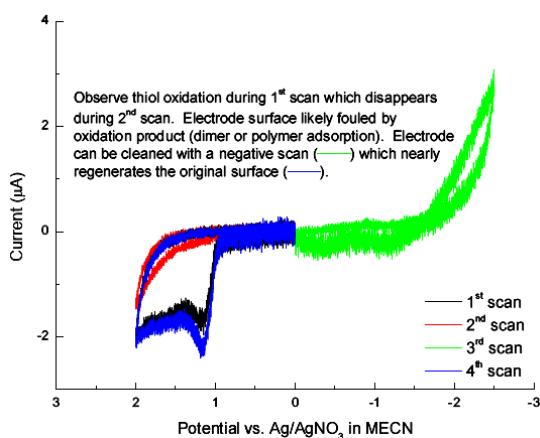


Figure C.7: Cyclic voltammogram of thiol in MECN.

The qualitative behavior of the scans was reproducible, but the quantitative nature of the scans was not reproducible. This is likely due to electrode contamination during the scans. Quantitative reproduction will require more rigorous conditions (dry MECN, oxygen free, better electrolyte). There were no obvious differences between pure thiol and thiol-ene, implying that the thiol is playing a major role in the electrocuring.

C.6 DSC MEASUREMENTS

Many of the polymers used in this thesis were characterized by differential scanning calorimetry (DSC). The DSC plots are shown in Figures C.8-C.10. The DSC measurements were made within the context of the elastomeric fibril study, Chapter 8.

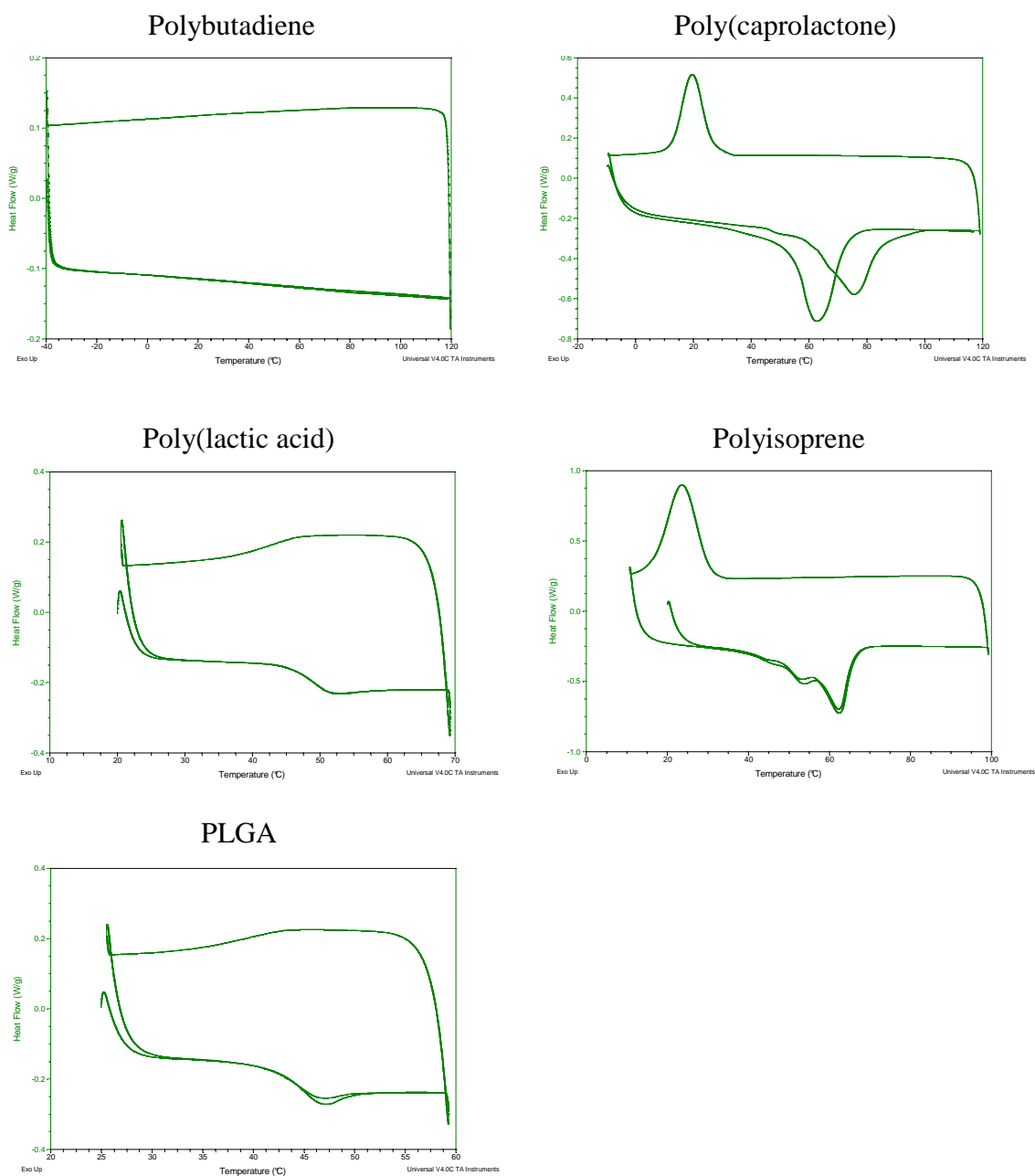


Figure C.8: DSC plots for the polymers utilized in this thesis.

C.7 SCION SOFTWARE AND FFT ANALYSIS

Scion[®] software can be used to count and characterize particles in a digital image. Scion[®] was used in this thesis to analyze optical micrographs of pillars to determine the diameter of the pillars. Matlab is capable of performing a fast Fourier Transform (FFT) of the image, which gives a measure of the characteristic spacing of the pillars. The following procedure was used to analyze images.

C.7.1 Scion Procedure

- I. Open the image you want to analyze by going to “File” and then “Open”. Find your image on the computer and click “Open”.
- II. Go to “Options” and then click on “Threshold”, your image should change slightly.
- III. Under the “Analyze” menu, select “Options”. Check the following boxes: “Area”, “Major Axis”, “Minor Axis”. If you need additional information just check the box that corresponds to the data you want.
- IV. Again under the “Analyze” select “Analyze Particles”. In the dialogue box that pops up, enter your minimum size as 100, and your maximum size as 800. Check the “Label Particles” and “Ignore particles touching edge” boxes. Now click “Ok”. At this point you should notice some of the shapes in your image start to disappear, most likely the ones touching the edges of the image.
- V. Once the analysis is complete, go to “Analyze” and select “Show Results”, a window with columns of data should pop up. Make sure that the box with the data in it is selected and then click “File” and then “Export”. Find where you wish to save the file and then save it. ** Make sure when naming your file

you attach the suffix “.txt”. This puts the data into a text file instead of a bitmap image.

- VI. Open the text file with your data in it, copy and paste the data into Microsoft Excel or a similar spreadsheet program. You should have at least three columns which represent the area (pixels squared), the major axis, and the minor axis. To determine the actual length, calibration markings on the microscope image must be converted to pixels.
- VII. Make a Histogram of the data by going to the “Tools” menu, selecting “Data Analysis”, and then clicking on “Histogram”. For your range, select the areas from your data. You can now plot the histogram in your favorite style.

C.7.2 FFT Analysis

The optical microscope images of pillars were analyzed by FFT to determine the characteristic spacing of the pillars. To extract meaningful information from the FTT, the original image must have pixel dimensions $2^n \times 2^n$. Prior to analysis, the contrast of the images must be increased and the file must be converted to a monochromic bitmap so that Matlab can extract the correct characteristic spacing. The following procedure was used to analyze the images by FFT.

- I. Open your image in Scion[®].
- II. Go to “Options’ and then select “Threshold”.
- III. Under the “Process” menu click “Binary” and then “Make Binary”.
- IV. Click “Analyze” and then “Options”, make sure that the maximum number of particles is set to 99999.

- V. Again under “Analyze” select “Analyze Particles”. In the menu that appears enter your minimum size as 100 and your maximum size as 600. The minimum limit eliminates noise and particles in the picture and the upper limits gets rid of merged pillars or artifacts of the picture. Uncheck the “Label particles” box and make sure the “Ignore particles touching edge box” is checked. Click “OK”.
- VI. Now go to “file” and “save as”. In the file type drop down menu select “Tagged Image Format(.tiff)” and save the file.
- VII. Open your saved image in Microsoft Photo Editor.
- VIII. Go to “file” and then “properties” and change the image to “Greyscale (8 bit)”. Click “OK”.
- IX. Click the button on the toolbar that looks like a sun. Go down to the gamma slider and move it all the way to the left, so its value is zero.
- X. Save the image.
- XI. Open the image you just saved in Microsoft Paint. Go to “file” and then “save as” and save the file as a monochromatic bitmap image. This is the only file type that will work with the MATLAB script file.
- XII. Open the MATLAB script file *logsfft1*. In red font should be two file names. The first is the name of the original image file. Change the text to the name of the saved bitmap image. Change the file name in red to the desired output FFT spectral image; make sure to include the file extension in the file name (i.e. .jpg, .bmp, etc.). Save the script file.
- XIII. Run MATLAB and make sure the directory is set to the folder that contains **BOTH** your monochromatic bitmap file and the *logsfft1* script file. The resulting FFT image will be placed in this same folder.

- XIV. Open the FFT image in Adobe Photoshop and find the pixel distance between the center of the image to the center of the first ring.

Alternatively, if you have access to Adobe Photoshop, steps 1 through 10 can be replaced with the following:

- I. Open the image you took with the microscope in Photoshop.
- II. Invert the image colors by pressing “Ctrl+I” or by go to the “image” menu select “adjustments” and then click on “invert”.
- III. Now, under the “Image” menu, select “Adjustments” and click on “Threshold...”. Adjust the slider bar at the bottom of the pop up window until most of the circles are filled in with black.
- IV. Again under the “Image” menu, select “Adjustments” and then “Brightness/Contrast...”. Adjust the sliders to get the image to desired quality.
- V. If you can not get a good quality image you may want to select the cropping tool by pressing ‘C’ and crop an area that looks good. After you have cropped the image, save it.
- VI. Save your image and then start with step 11 from above.

The FFT spectra are generated by a MATLAB script file that crops the bitmap image to 1024×1024 (or some power of 2) and then uses the `fft()` function to calculate the FFT. Zero-padding (i.e. adding zeros on to the original image) is a common strategy to make the image a $2^n \times 2^n$ square. This technique improves the resolution (since resolution is defined as the inverse of the sampling length, in this case the number of pixels), but corrupts the original image by adding false information. Thus, zero-padding is ideal for

systems with a single, narrow frequency. A unique characteristic of a zero padded FFT is the presence of a dashed cross in the center of the image as shown in Figure C.9.

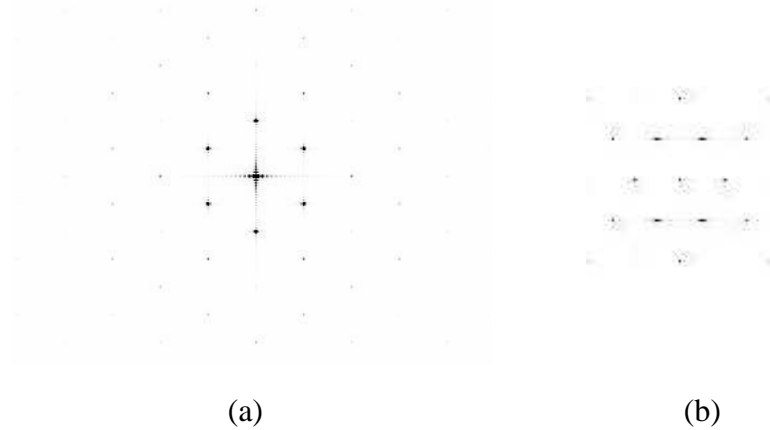


Figure C.9: FFT spectra for an ideally hexagonally closed-pack array of circles. (a) A zero padded image, distinguished by the artificial cross in the middle of the spectra. (b) A non-zero padded image.

Zero padding was not used in this analysis, rather the image was cropped to be the proper dimension (1024x1024 or 512x512).

The following Matlab code inputs the processed image and outputs the FFT spectra. The “%” symbol denotes comments that are added to provide clarity to the code.

```
clear all
i = imread('Image3.bmp');
% the bitmap image is imported
figure(1)
cmap = [[0:1/255:1]' [0:1/255:1]' [0:1/255:1]'];
colormap(cmap)
```

```

% the bitmap is converted to black and white

i = i(1:512,1:512);

image(i)

axis equal

% the image is cropped

I = fft2(i, 512, 512);

P = I .* conj(I);

% I is the output from the fft analysis

m = max(max(P));

P = (P ./ m) * 255*0.1;

P = fftshift(P);

% the spectrum is normalized and then amplified to increase contrast

figure(2)

image(P)

colormap(cmap)

imwrite(P, 'Image3.jpg', 'jpg');

% The image is plotted and the file is saved

```

The 2-D FFT output spectra can be used to determine the characteristic spacing of the original image in terms of “frequency”. FFT has a finite resolution defined by $1 / (\text{total sample length})$. Typically, sampling is done in terms of time. For example, sampling for 1 second, corresponds to a resolution of 1 Hz, 2 seconds equates to 0.5 Hz, etc. In this analysis, the image that is inputted for analysis is 1024x1024 pixels, thus the resolution is 1024^{-1} . The larger the original image (i.e. the more information it contains), the better the resolution of the resulting FFT (e.g. 2048 x 2048 image has a resolution of

2048⁻¹). Each point in the FFT is called a “frequency bin”. Based on this analysis, a distance X (in pixels) in the FFT output represents $X * 1024^{-1}$ characteristic frequency. As an aside, zero padding makes the frequency bins smaller by adding on artificial points to the original image. This technique works well for finding a simple frequency, but it corrupts the spectrum.

The output from this analysis gives a characteristic frequency in pixels that can be converted into a real (i.e. SI units) distance. This was accomplished by taking a microscope image of known pixel dimensions and using the calibration markers in the microscope software to draw a line of known length across one dimension. The result is a conversion factor from pixels to microns. The pixel distance between the center of the FFT spectrum to the nearest spectral ring can be converted to a physical distance using this conversion factor. The inverse of the product gives the characteristic spacing in microns, as shown in Equation C.1. The preceding analysis is summarized in Figure C.10.

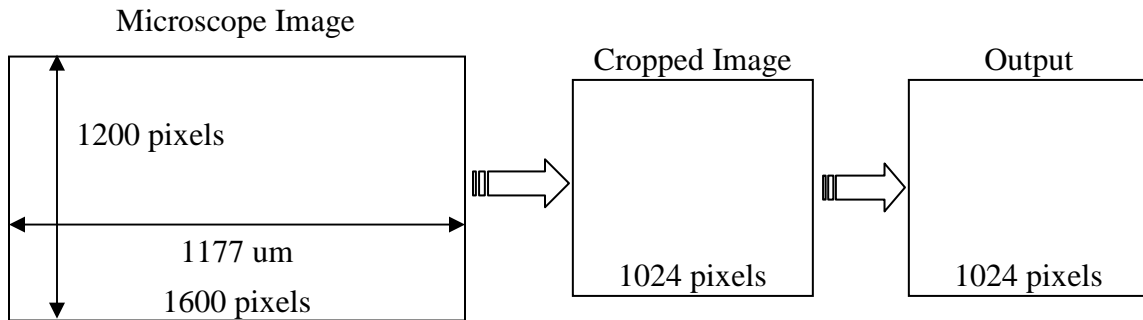


Figure C.10: FFT analysis strategy. A microscope image is cropped such that the dimensions are a power of 2. The FFT output is in the same dimensions as the input.

$$\bar{d}(\mu\text{m}) = \left[\left(\frac{x}{1024} \right) \left(\frac{1600}{1177} \right) \right]^{-1} \quad (\text{C.1})$$

In Equation C.1, “x” is the distance in pixels from the center of the fft output to the next closest feature. The ratio of 1600/1177 is a conversion factor, determined from the original microscope image as shown in Figure C.10.

A typical example of an FFT image is shown in Figure C.11.

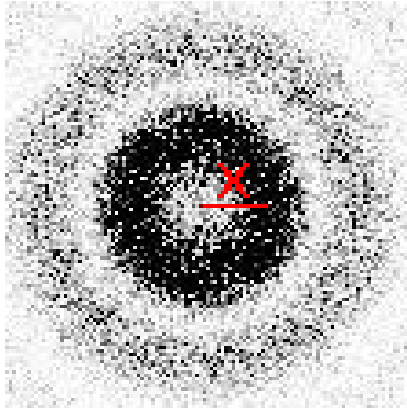


Figure C.11: Typical FFT image. The red “x” denotes the length in Equation C.1.

Appendix D: Academic Genealogy

C. Grant Willson
PhD U.C. Berkeley, 1973



Henry Rapoport
PhD MIT, 1943



Avery A. Morton
PhD MIT, 1924

James F. Norris
PhD Johns Hopkins, 1895

Ira Remsen
Göttingen, 1870



Wilhelm R. Fittig
PhD Göttingen, 1858



Heinrich Limpricht
PhD Göttingen, 1850



Friedrich Wohler
Heidelber, 1823



Friedrich was co-advised by:

Jons Jakob Berzelius

MD Uppsala, 1802



Leopold Gmelin

Göttingen, 1810



Johann Afzelius

MS Uppsala, Sweden 1776

Joseph Jacquin

MD Vienna, 1788

Tobern Olof Bergman

Uppsala, 1758



Nicolas Joseph Jacquin

Leiden, ~1752

Bengt Fermer

Uppsala ~1751

Laurent Theodor Gronovius II

MD Leiden ~1750

Samuel Klingenstierna

LLB Uppsala 1717



Johannes Fredrick Gronovius II

Leiden 1715

Anders Gabriel Duhre
LLB Uppsala ~1739

Petrus Elvius
MA Uppsala 1688

Petrus Hoffvenius
MD Leiden 1660

Johannes Antonides van der Linden
MD Franker 1630

Menelaus Winsemius
MD Leiden 1613

Petrus Pauw
MD Rostock 1587



Henricus Brucaeus
College Royal, Paris ~1550

Petrus Ramus
MA Paris 1536



References

- Abdo, A.; Schuetter, S.; Nellis, G.; Wei, A.; Engelstad, R.; Truskett, V., Predicting the fluid behavior during the dispensing process for step-and-flash imprint lithography. *Journal of Vacuum Science & Technology, B: Microelectronics and Nanometer Structures* **2004**, 22, (6), 3279-3282.
- Ajayan, P. M.; Schadler, L. S.; Braun, P. V., *Nanocomposite science and technology*. Wiley-VCH: Weinheim, 2003; p ix, 230.
- Ali, A. H.; Srinivasan, K. S. V., Photoresponsive functionalized vinyl cinnamate polymers: synthesis and characterization. *Polymer International* **1997**, 43, (4), 310-316.
- Andrzejewska, E., Photopolymerization kinetics of multifunctional monomers. *Progress in Polymer Science* **2001**, 26, (4), 605-665.
- Angelescu, D. E.; Waller, J. H.; Adamson, D. H.; Deshpande, P.; Chou, S. Y.; Register, R. A.; Chaikin, P. M., Macroscopic orientation of block copolymer cylinders in single-layer films by shearing. *Advanced Materials* **2004**, 16, (19), 1736-1740.
- Anseth, K. S.; Bowman, C. N.; Peppas, N. A., Polymerization kinetics and volume relaxation behavior of photopolymerized multifunctional monomers producing highly crosslinked networks. *Journal of Polymer Science, Part A: Polymer Chemistry* **1994**, 32, (1), 139-47.
- Anseth, K. S.; Wang, C. M.; Bowman, C. N., Kinetic evidence of reaction diffusion during the polymerization of multi(meth)acrylate monomers. *Macromolecules* **1994**, 27, (3), 650-5.
- Anseth, K. S.; Wang, C. M.; Bowman, C. N., Reaction behavior and kinetic constants for photopolymerizations of multi(meth)acrylate monomers. *Polymer* **1994**, 35, (15), 3243-50.
- Appleyard, S. F. J.; Day, S. R.; Pickford, R. D.; Willis, M. R., Organic electroluminescent devices: enhanced carrier injection using SAM derivatized ITO electrodes. *Journal of Materials Chemistry* **2000**, 10, (1), 169-173.
- Arakcheeva, E. M.; Tanklevskaya, E. M.; Nesterov, S. I.; Maksimov, M. V.; Gurevich, S. A.; Seekamp, J.; Sotomayor Torres, C. M., Fabrication of Semiconductor- and Polymer-Based Photonic Crystals Using Nanoimprint Lithography. *Technical Physics* **2005**, 50, (8), 1043-1047.
- Arun, N.; Sharma, A.; Shenoy, V. B.; Narayan, K. S., Electric-field-controlled surface instabilities in soft elastic films. *Advanced Materials* **2006**, 18, (5), 660-663.
- Asanov, A. N.; Wilson, W. W.; Oldham, P. B., Regenerable Biosensor Platform: A Total Internal Reflection Fluorescence Cell with Electrochemical Control. *Analytical Chemistry* **1998**, 70, (6), 1156-1163.

- Austin, M. D.; Chou, S. Y., Fabrication of 70 nm channel length polymer organic thin-film transistors using nanoimprint lithography. *Applied Physics Letters* **2002**, 81, (23), 4431-4433.
- Austin, M. D.; Ge, H.; Wu, W.; Li, M.; Yu, Z.; Wasserman, D.; Lyon, S. A.; Chou, S. Y., Fabrication of 5 nm linewidth and 14 nm pitch features by nanoimprint lithography. *Applied Physics Letters* **2004**, 84, (26), 5299-5301.
- Austin, M. D.; Zhang, W.; Ge, H.; Wasserman, D.; Lyon, S. A.; Chou, S. Y., 6 nm half-pitch lines and 0.04 mm² static random access memory patterns by nanoimprint lithography. *Nanotechnology* **2005**, 16, (8), 1058-1061.
- Bailey, T.; Choi, B. J.; Colburn, M.; Meissl, M.; Shaya, S.; Ekerdt, J. G.; Sreenivasan, S. V.; Willson, C. G., Step and flash imprint lithography: Template surface treatment and defect analysis. *Journal of Vacuum Science & Technology, B: Microelectronics and Nanometer Structures* **2000**, 18, (6), 3572-3577.
- Bailey, T.; Smith, B.; Choi, B. J.; Colburn, M.; Meissl, M.; Sreenivasan, S. V.; Ekerdt, J. G.; Willson, C. G., Step and flash imprint lithography: Defect analysis. *Journal of Vacuum Science & Technology, B: Microelectronics and Nanometer Structures* **2001**, 19, (6), 2806-2810.
- Bailey, T. C. Imprint Template Advances and Surface Modification, and Defect Analysis for Step and Flash Imprint Lithography. University of Texas at Austin, Austin, 2003.
- Bailey, T. C.; Johnson, S. C.; Sreenivasan, S. V.; Ekerdt, J. G.; Willson, C. G.; Resnick, D. J., Step and flash imprint lithography: an efficient nanoscale printing technology. *Journal of Photopolymer Science and Technology* **2002**, 15, (3), 481-486.
- Bailey, T. C.; Resnick, D. J.; Mancini, D.; Nordquist, K. J.; Dauksher, W. J.; Ainley, E.; Talin, A.; Gehoski, K.; Baker, J. H.; Choi, B. J.; Johnson, S.; Colburn, M.; Meissl, M.; Sreenivasan, S. V.; Ekerdt, J. G.; Willson, C. G., Template fabrication schemes for step and flash imprint lithography. *Microelectronic Engineering* **2002**, 61-62, 461-467.
- Bajdala, J.; Mueller, U.; Wartewig, S.; Winkler, K., Photoinitiated crosslinking of silicones. 10. Photoinitiated crosslinking of silicone acrylates as studied by Fourier transform infrared spectroscopy. *Makromolekulare Chemie* **1993**, 194, (11), 3093-105.
- Bakir, M. S.; Villalaz, R. A.; Ogunsola, O. O.; Gaylord, T. K.; Kohl, P. A.; Martin, K. P.; Meindl, J. D., Sea of polymer pillars: Dual-mode electrical-optical Input/Output interconnections. *Proceedings of the IEEE International Interconnect Technology Conference, 6th, San Francisco, CA, United States, June 2-4, 2003* **2003**, 77-79.
- Bard, A. J.; Faulkner, L. R., *Electrochemical methods: fundamentals and applications*. 2nd ed.; Wiley: New York, 2001; p xxi, 833.
- Bechhoefer, J.; Ego, V.; Manneville, S.; Johnson, B., An experimental study of the onset of parametrically pumped surface waves in viscous fluids. *Journal of Fluid Mechanics* **1995**, 288, 325-50.

- Beck, M.; Graczyk, M.; Maximov, I.; Sarwe, E. L.; Ling, T. G. I.; Keil, M.; Montelius, L., Improving stamps for 10 nm level wafer scale nanoimprint lithography. *Microelectronic Engineering* **2002**, 61-62, 441-448.
- Beck, M.; Persson, F.; Carlberg, P.; Graczyk, M.; Maximov, I.; Ling, T. G. I.; Montelius, L., Nanoelectrochemical transducers for (bio-) chemical sensor applications fabricated by nanoimprint lithography. *Microelectronic Engineering* **2004**, 73-74, 837-842.
- Berchtold, K. A.; Lovell, L. G.; Nie, J.; Hacıoglu, B.; Bowman, C. N., The significance of chain length dependent termination in cross-linking polymerizations. *Polymer* **2001**, 42, (11), 4925-4929.
- Beuermann, S.; Buback, M., Rate coefficients of free-radical polymerization deduced from pulsed laser experiments. *Progress in Polymer Science* **2002**, 27, (2), 191-254.
- Beuermann, S.; Paquet, D. A., Jr.; McMinn, J. H.; Hutchinson, R. A., Determination of free-radical propagation rate coefficients of butyl, 2-ethylhexyl, and dodecyl acrylates by pulsed-laser polymerization. *Macromolecules* **1996**, 29, (12), 4206-4215.
- Blitz, J. P.; Murthy, R. S. S.; Leyden, D. E., Ammonia-catalyzed silylation reactions of Cab-O-Sil with methoxymethylsilanes. *Journal of the American Chemical Society* **1987**, 109, (23), 7141-5.
- Bockris, J. O. M.; Reddy, A. K. N., *Modern electrochemistry; an introduction to an interdisciplinary area*. Plenum Press: New York, 1970; p v.
- Bonard, J.-M.; Dean Kenneth, A.; Coll Bernard, F.; Klinke, C., Field emission of individual carbon nanotubes in the scanning electron microscope. *Physical review letters* **2002**, 89, (19), 197602.
- Braun, E.; Eichen, Y.; Sivan, U.; Ben-Yoseph, G., DNA-templated assembly and electrode attachment of a conducting silver wire. *Nature* **1998**, 391, (6669), 775-778.
- Buback, M., Initiation and termination rates associated with free-radical polymerization in extended ranges of temperature and pressure. *ACS Symposium Series* **2000**, 768, (Controlled/Living Radical Polymerization), 39-56.
- Buback, M., Initiation, propagation and termination in fluid phase free-radical polymerization. *Macromolecular Symposia* **2001**, 174, (Polymerization Processes and Polymer Materials I), 213-227.
- Buback, M.; Degener, B., Rate coefficients for free-radical polymerization of butyl acrylate to high conversion. *Makromolekulare Chemie* **1993**, 194, (10), 2875-83.
- Buback, M.; Egorov, M.; Gilbert, R. G.; Kaminsky, V.; Olaj, O. F.; Russell, G. T.; Vana, P.; Zifferer, G., Critically evaluated termination rate coefficients for free-radical polymerization, 1: The current situation. *Macromolecular Chemistry and Physics* **2002**, 203, (18), 2570-2582.
- Buback, M.; Garcia-Rubio, L. H.; Gilbert, R. G.; Napper, D. H.; Guillot, J.; Hamielec, A. E.; Hill, D.; O'Driscoll, K. F.; Olaj, O. F.; et al., Consistent values of rate parameters in

free radical polymerization systems. *Journal of Polymer Science, Part C: Polymer Letters* **1988**, 26, (7), 293-7.

Buback, M.; Gilbert, R. G.; Russell, G. T.; Hill, D. J. T.; Moad, G.; O'Driscoll, K. F.; Shen, J.; Winnik, M. A., Consistent values of rate parameters in free radical polymerization systems. II. Outstanding dilemmas and recommendations. *Journal of Polymer Science, Part A: Polymer Chemistry* **1992**, 30, (5), 851-63.

Buback, M.; Huckestein, B.; Kuchta, F.-D.; Russell, G. T.; Schmid, E., Initiator efficiencies in 2,2'-azoisobutyronitrile-initiated free-radical polymerizations of styrene. *Macromolecular Chemistry and Physics* **1994**, 195, (6), 2117-40.

Buback, M.; Huckestein, B.; Russell, G. T., Modeling of termination in intermediate and high conversion free radical polymerizations. *Macromolecular Chemistry and Physics* **1994**, 195, (2), 539-54.

Cao, H.; Currie, E.; Tilley, M.; Jean, Y. C., Oxygen inhibition effect on surface properties of UV-curable acrylate coatings. *ACS Symposium Series* **2003**, 847, (Photoinitiated Polymerization), 152-164.

Cao, H.; Tegenfeldt, J. O.; Austin, R. H.; Chou, S. Y., Gradient nanostructures for interfacing microfluidics and nanofluidics. *Applied Physics Letters* **2002**, 81, (16), 3058-3060.

Cao, H.; Yu, Z.; Wang, J.; Tegenfeldt, J. O.; Austin, R. H.; Chen, E.; Wu, W.; Chou, S. Y., Fabrication of 10 nm enclosed nanofluidic channels. *Applied Physics Letters* **2002**, 81, (1), 174-176.

Cardinale, G. F.; Skinner, J. L.; Talin, A. A.; Brocato, R. W.; Palmer, D. W.; Mancini, D. P.; Dauksher, W. J.; Gehoski, K.; Le, N.; Nordquist, K. J.; Resnick, D. J., Fabrication of a surface acoustic wave-based correlator using step-and-flash imprint lithography. *Journal of Vacuum Science & Technology, B: Microelectronics and Nanometer Structures--Processing, Measurement, and Phenomena* **2004**, 22, (6), 3265-3270.

Cass, A. E. G., *Biosensors: a practical approach*. IRL Press at Oxford University Press: Oxford [England]; New York, 1990; p xv, 271.

Cerda, E. A.; Tirapegui, E. L., Faraday's instability in viscous fluid. *Journal of Fluid Mechanics* **1998**, 368, 195-228.

Chan-Park, M. B.; Yan, Y.; Neo, W. K.; Zhou, W.; Zhang, J.; Yue, C. Y., Fabrication of High Aspect Ratio Poly(ethylene glycol)-Containing Microstructures by UV Embossing. *Langmuir* **2003**, 19, (10), 4371-4380.

Chaney, J. A.; Koh, S. E.; Dulcey, C. S.; Pehrsson, P. E., Surface chemistry of carbon removal from indium tin oxide by base and plasma treatment, with implications on hydroxyl termination. *Applied Surface Science* **2003**, 218, (1-4), 258-266.

Chen, C.; Daniel, M.-C.; Quinkert, Z. T.; De, M.; Stein, B.; Bowman, V. D.; Chipman, P. R.; Rotello, V. M.; Kao, C. C.; Dragnea, B., Nanoparticle-Templated Assembly of Viral Protein Cages. *Nano Letters* **2006**, 6, (4), 611-615.

- Chen, X. Q.; Saito, T.; Yamada, H.; Matsushige, K., Aligning single-wall carbon nanotubes with an alternating-current electric field. *Applied Physics Letters* **2001**, 78, (23), 3714-3716.
- Chen, Z.; Hu, W.; Guo, J.; Saito, K., Fabrication of nanoelectrodes based on controlled placement of carbon nanotubes using alternating-current electric field. *Journal of Vacuum Science & Technology, B: Microelectronics and Nanometer Structures--Processing, Measurement, and Phenomena* **2004**, 22, (2), 776-780.
- Cheng, J. Y.; Mayes, A. M.; Ross, C. A., Nanostructure engineering by templated self-assembly of block copolymers. *Nature Materials* **2004**, 3, (11), 823-828.
- Cheng, X.; Chang, M.-H.; Guo, L. J., Combined nanoimprint- and- photolithography technique with a hybrid mold. *Proceedings of SPIE-The International Society for Optical Engineering* **2004**, 5374, 337-347.
- Cheng, X.; Guo, L. J., A combined-nanoimprint-and-photolithography patterning technique. *Microelectronic Engineering* **2004**, 71, (3-4), 277-282.
- Cheng, X.; Guo, L. J., One-step lithography for various size patterns with a hybrid mask-mold. *Microelectronic Engineering* **2004**, 71, (3-4), 288-293.
- Cheng, X.; Guo, L. J.; Fu, P.-F., Room-temperature, low-pressure nanoimprinting based on cationic photopolymerization of novel epoxysilicone monomers. *Advanced Materials* **2005**, 17, (11), 1419-1424.
- Cheng, X.; Hong, Y.; Kanicki, J.; Guo, L. J., High-resolution organic polymer light-emitting pixels fabricated by imprinting technique. *Journal of Vacuum Science & Technology, B: Microelectronics and Nanometer Structures* **2002**, 20, (6), 2877-2880.
- Choi, B. J.; Johnson, S. C.; Sreenivasan, S. V.; Colburn, M.; Bailey, T. C.; Willson, C. G. In *Partially Constrained Compliant Stages for High Resolution Imprint Lithography*, Proc. ASME DETC2000, 2000; 2000; p 861.
- Choi, D.-G.; Kim, S.; Jang, S.-G.; Yang, S.-M.; Jeong, J.-R.; Shin, S.-C., Nanopatterned Magnetic Metal via Colloidal Lithography with Reactive Ion Etching. *Chemistry of Materials* **2004**, 16, (22), 4208-4211.
- Choi, W. B.; Chung, D. S.; Kang, J. H.; Kim, H. Y.; Jin, Y. W.; Han, I. T.; Lee, Y. H.; Jung, J. E.; Lee, N. S.; Park, G. S.; Kim, J. M., Fully sealed, high-brightness carbon-nanotube field-emission display. *Applied Physics Letters* **1999**, 75, (20), 3129-3131.
- Chopra, N.; Xu, W.; De Long, L. E.; Hinds, B. J., Incident angle dependence of nanogap size in suspended carbon nanotube shadow lithography. *Nanotechnology* **2005**, 16, (1), 133-136.
- Chou, S. Y.; Keimel, C.; Gu, J., Ultrafast and direct imprint of nanostructures in silicon. *Nature* **2002**, 417, (6891), 835-837.
- Chou, S. Y.; Krauss, P. R., Imprint lithography with sub-10nm feature size and high throughput. *Microelectronic Engineering* **1997**, 35, (1-4, Micro- and Nano-Engineering 96), 237-240.

- Chou, S. Y.; Krauss, P. R.; Renstrom, P. J., Imprint lithography with 25-nanometer resolution. *Science* **1996**, 272, (5258), 85-7.
- Chou, S. Y.; Krauss, P. R.; Zhang, W.; Guo, L.; Zhuang, L., Sub-10 nm imprint lithography and applications. *Journal of Vacuum Science & Technology, B: Microelectronics and Nanometer Structures* **1997**, 15, (6), 2897-2904.
- Chou, S. Y.; Zhuang, L., Lithographically induced self-assembly of periodic polymer micropillar arrays. *Journal of Vacuum Science & Technology, B: Microelectronics and Nanometer Structures* **1999**, 17, (6), 3197-3202.
- Chou, S. Y.; Zhuang, L.; Deshpande, P.; Chen, L.; Sun, X., Lithographically-induced self-assembly of periodic micro-pillar arrays in a single homopolymer film. *Polymer Preprints (American Chemical Society, Division of Polymer Chemistry)* **2000**, 41, (1), 78.
- Chou, S. Y.; Zhuang, L.; Guo, L., Lithographically induced self-construction of polymer microstructures for resistless patterning. *Applied Physics Letters* **1999**, 75, (7), 1004-1006.
- Chung, J.; Lee, K.-H.; Lee, J.; Ruoff, R. S., Toward large-scale integration of carbon nanotubes. *Langmuir* **2004**, 20, (8), 3011-3017.
- Cobb, J. L.; Brainard, R. L.; O'Connell, D. J.; Dentinger, P. M., EUV lithography: patterning to the end of the road. *Materials Research Society Symposium Proceedings* **2002**, 705, (Nanopatterning: From Ultralarge-Scale Integration to Biotechnology), 91-100.
- Colburn, M.; Choi, B. J.; Sreenivasan, S. V.; Bonnacaze, R. T.; Willson, C. G., Ramifications of lubrication theory on imprint lithography. *Microelectronic Engineering* **2004**, 75, (3), 321-329.
- Colburn, M.; Grot, A.; Amistoso, M. N.; Choi, B. J.; Bailey, T. C.; Ekerdt, J. G.; Sreenivasan, S. V.; Hollenhorst, J.; Willson, C. G., Step and flash imprint lithography for sub-100-nm patterning. *Proceedings of SPIE-The International Society for Optical Engineering* **2000**, 3997, 453-457.
- Colburn, M.; Johnson, S.; Stewart, M.; Damle, S.; Bailey, T. C.; Choi, B.; Wedlake, M.; Michaelson, T.; Sreenivasan, S. V.; Ekerdt, J.; Willson, C. G., Step and flash imprint lithography: a new approach to high-resolution patterning. *Proceedings of SPIE-The International Society for Optical Engineering* **1999**, 3676, 379-389.
- Colburn, M.; Suez, I.; Choi, B. J.; Meissl, M.; Bailey, T.; Sreenivasan, S. V.; Ekerdt, J. G.; Willson, C. G., Characterization and modeling of volumetric and mechanical properties for step and flash imprint lithography photopolymers. *Journal of Vacuum Science & Technology, B: Microelectronics and Nanometer Structures* **2001**, 19, (6), 2685-2689.
- Cramer, N. B.; Davies, T.; O'Brien, A. K.; Bowman, C. N., Mechanism and Modeling of a Thiol-Ene Photopolymerization. *Macromolecules* **2003**, 36, (12), 4631-4636.

- Cramer, N. B.; Reddy, S. K.; Cole, M.; Hoyle, C.; Bowman, C. N., Initiation and kinetics of thiol-ene photopolymerizations without photoinitiators. *Journal of Polymer Science, Part A: Polymer Chemistry* **2004**, 42, (22), 5817-5826.
- Cramer, N. B.; Scott, J. P.; Bowman, C. N., Photopolymerizations of Thiol-Ene Polymers without Photoinitiators. *Macromolecules* **2002**, 35, (14), 5361-5365.
- Craster, R. V.; Matar, O. K., Electrically induced pattern formation in thin leaky dielectric films. *Physics of Fluids* **2005**, 17, (3), 032104/1-032104/17.
- Dammel, R. R.; Houlihan, F. M.; Sakamuri, R.; Rentkiewicz, D.; Romano, A., 193 nm immersion lithography - Taking the plunge. *Journal of Photopolymer Science and Technology* **2004**, 17, (4), 587-602.
- Dauksher, W. J.; Mancini, D.; Nordquist, K.; Resnick, D. J.; Hudek, P.; Beyer, D.; Groves, T.; Fortagne, O., Fabrication of step and flash imprint lithography templates using a variable shaped-beam exposure tool. *Microelectronic Engineering* **2004**, 75, (4), 345-351.
- Dauksher, W. J.; Mancini, D. P.; Nordquist, K. J.; Resnick, D. J.; Standfast, D. L.; Convey, D.; Wei, Y., Step and flash imprint lithography template characterization, from an etch perspective. *Journal of Vacuum Science & Technology, B: Microelectronics and Nanometer Structures--Processing, Measurement, and Phenomena* **2003**, 21, (6), 2771-2776.
- Dauksher, W. J.; Nordquist, K. J.; Le, N. V.; Gehoski, K. A.; Mancini, D. P.; Resnick, D. J.; Casoose, L.; Bozak, R.; White, R.; Csuy, J.; Lee, D., Repair of step and flash imprint lithography templates. *Journal of Vacuum Science & Technology, B: Microelectronics and Nanometer Structures--Processing, Measurement, and Phenomena* **2004**, 22, (6), 3306-3311.
- Dauksher, W. J.; Nordquist, K. J.; Mancini, D. P.; Resnick, D. J.; Baker, J. H.; Hooper, A. E.; Talin, A. A.; Bailey, T. C.; Lemonds, A. M.; Sreenivasan, S. V.; Ekerdt, J. G.; Willson, C. G., Characterization of and imprint results using indium tin oxide-based step and flash imprint lithography templates. *Journal of Vacuum Science & Technology, B: Microelectronics and Nanometer Structures* **2002**, 20, (6), 2857-2861.
- Decker, C., Kinetic study and new applications of UV radiation curing. *Macromolecular Rapid Communications* **2002**, 23, (18), 1067-1093.
- Decker, C., Laser-induced polymerization. *ACS Symposium Series* **1984**, 266, (Materials Microlithography), 207-23.
- Decker, C., Light-induced crosslinking polymerization. *Polymer International* **2002**, 51, (11), 1141-1150.
- Decker, C., Real-time monitoring of polymerization quantum yields. *Macromolecules* **1990**, 23, (25), 5217-20.
- Decker, C., The use of UV irradiation in polymerization. *Polymer International* **1998**, 45, (2), 133-141.

- Decker, C.; Elzaouk, B., Photopolymerization of functional monomers. VII. Evaluation of the rate constants of propagation and termination. *European Polymer Journal* **1995**, 31, (12), 1155-63.
- Decker, C.; Elzaouk, B.; Decker, D., Kinetic study of ultrafast photopolymerization reactions. *Journal of Macromolecular Science, Pure and Applied Chemistry* **1996**, A33, (2), 173-90.
- Decker, C.; Jenkins, A. D., Kinetic approach of oxygen inhibition in ultraviolet- and laser-induced polymerizations. *Macromolecules* **1985**, 18, (6), 1241-4.
- Decker, C.; Moussa, K., Kinetic investigation of photopolymerizations induced by laser beams. *Makromolekulare Chemie* **1990**, 191, (4), 963-79.
- Decker, C.; Moussa, K., Photopolymerization of polyfunctional monomers. III. Kinetic analysis by real-time IR spectroscopy. *European Polymer Journal* **1990**, 26, (4), 393-401.
- Decker, C.; Moussa, K., Radical trapping in photopolymerized acrylic networks. *Journal of Polymer Science, Part A: Polymer Chemistry* **1987**, 25, (2), 739-42.
- Denis, F. A.; Hanarp, P.; Sutherland, D. S.; Dufrene, Y. F., Nanoscale Chemical Patterns Fabricated by Using Colloidal Lithography and Self-Assembled Monolayers. *Langmuir* **2004**, 20, (21), 9335-9339.
- Deshpande, P.; Sun, X.; Chou, S. Y., Observation of dynamic behavior of lithographically induced self-assembly of supramolecular periodic pillar arrays in a homopolymer film. *Applied Physics Letters* **2001**, 79, (11), 1688-1690.
- Di Ventra, M.; Evoy, S.; Heflin, J. R., *Introduction to nanoscale science and technology*. Kluwer Academic Publishers: Boston, 2004; p xiii, 611.
- Dickey, M. D.; Burns, R. L.; Kim, E. K.; Johnson, S. C.; Stacey, N. A.; Willson, C. G., A Study of the Kinetics of Step and Flash Imprint Lithography Photopolymerization. *AIChE Journal* **In Press**.
- Dickey, M. D.; Burns, R. L.; Kim, E. K.; Johnson, S. C.; Stacey, N. A.; Willson, C. G., Study of the kinetics of Step and Flash imprint lithography photopolymerization. *AIChE Journal* **2005**, 51, (9), 2547-2555.
- Dickey, M. D.; Collister, E.; Kim, E. K.; Willson, C. G., Tailoring photopolymerization materials for nanotechnology. *Abstracts of Papers, 228th ACS National Meeting, Philadelphia, PA, United States, August 22-26, 2004* **2004**, POLY-337.
- Dickey, M. D.; Collister, E.; Raines, A.; Tsiartas, P.; Holcombe, T.; Sreenivasan, S. V.; Bonnacaze, R. T.; Willson, C. G., Photocurable Pillar Arrays Formed via Electrohydrodynamic Instabilities. *Chemistry of Materials* **2006**, 18, (8), 2043-2049.
- Dickey, M. D.; Gupta, S.; Leach, K. A.; Collister, E.; Willson, C. G.; Russell, T. P., Novel 3-D Structures in Polymer Films by Coupling External and Internal Fields. *Langmuir* **2006**, 22, (9), 4315-4318.
- Dickey, M. D.; Willson, C. G., Effects of oxygen on step and flash imprint lithography photopolymerization kinetics. *PMSE Preprints* **2004**, 90, 24-25.

- Dickey, M. D.; Willson, C. G., Kinetic parameters for step and flash imprint lithography photopolymerization. *AIChE Journal* **2006**, 52, (2), 777-784.
- Djurisic, A. B.; Lau, T.; Kwong, C. Y.; Guo, W.; Bai, Y.; Li, E. H.; Chan, W. K., Surface treatments of indium tin oxide substrates: comprehensive investigation of mechanical, chemical, thermal, and plasma treatments. *Proceedings of SPIE-The International Society for Optical Engineering* **2002**, 4464, 273-280.
- Donley, C.; Dunphy, D.; Paine, D.; Carter, C.; Nebesny, K.; Lee, P.; Alloway, D.; Armstrong, N. R., Characterization of Indium-Tin Oxide Interfaces Using x-ray Photoelectron Spectroscopy and Redox Processes of a Chemisorbed Probe Molecule: Effect of Surface Pretreatment Conditions. *Langmuir* **2002**, 18, (2), 450-457.
- Driskill-Smith, A. A. G.; Hasko, D. G.; Ahmed, H., The \"nanotriode\" A nanoscale field-emission tube. *Applied Physics Letters* **1999**, 75, (18), 2845-2847.
- Ebbesen, T. W.; Ajayan, P. M., Large-scale synthesis of carbon nanotubes. *Nature* **1992**, 358, (6383), 220-2.
- Eichler, J.; Herz, C. P.; Naito, I.; Schnabel, W., Laser flash photolysis investigation of primary processes in the sensitized polymerization of vinyl monomers. IV. Experiments with hydroxy alkylphenones. *Journal of Photochemistry* **1980**, 12, (3), 225-34.
- Elechiguerra, J. L.; Larios-Lopez, L.; Liu, C.; Garcia-Gutierrez, D.; Camacho-Bragado, A.; Yacaman, M. J., Corrosion at the Nanoscale: The Case of Silver Nanowires and Nanoparticles. *Chemistry of Materials* **2005**, 17, (24), 6042-6052.
- Englander, O.; Christensen, D.; Kim, J.; Lin, L.; Morris, S. J. S., Electric-field assisted growth and self-assembly of intrinsic silicon nanowires. *Nano Letters* **2005**, 5, (4), 705-708.
- Erle, M. A.; Gillette, R. D.; Dyson, D. C., Stability of Interfaces of Revolution with Constant Surface Tension-The Case of the Catenoid. *The Chemical Engineering Journal* **1970**, 1, (1), 97-109.
- Fan, D. L.; Zhu, F. Q.; Cammarata, R. C.; Chien, C. L., Manipulation of nanowires in suspension by ac electric fields. *Applied Physics Letters* **2004**, 85, (18), 4175-4177.
- Fang, A.; Ng, H.; Su, X.; Li, S. F. Y., Soft-Lithography-Mediated Submicrometer Patterning of Self-Assembled Monolayer of Hemoglobin on ITO Surfaces. *Langmuir* **2000**, 16, (12), 5221-5226.
- Faraday, M., On a peculiar class of acoustical figures; and on certain forms assumed by groups of particles upon vibrating elastic surfaces. *Philosophical Transactions of the Royal Society London* **1831**, 52, 299.
- Ferry, J. D., *Viscoelastic properties of polymers*. 3d ed.; Wiley: New York, 1980; p xxiv, 641.
- Fischer, J. P.; Schulz, G. V., Effect of solvent on the Arrhenius parameters of chain-growth and chain-breaking in the radical polymerization of methyl methacrylate. *Berichte der Bunsen-Gesellschaft* **1970**, 74, (10), 1077-82.

- Fouassier, J. P., Polymerization photoinitiators: excited state processes and kinetic aspects. *Progress in Organic Coatings* **1990**, 18, (3), 229-52.
- Fouassier, J. P.; Merlin, A., Laser investigation of Norrish type I photolysis in the photoinitiator Irgacure (2,2-dimethoxy-2-phenylacetophenone). *Journal of Photochemistry* **1980**, 12, (1), 17-23.
- Fox, T. G.; Flory, P. J., 2nd-Order Transition Temperatures and Related Properties of Polystyrene.1. Influence of Molecular Weight. *Journal of Applied Physics* **1950**, 21, (6), 581-591.
- Franca, D. R.; Blouin, A., All-optical measurement of in-plane and out-of-plane Young's modulus and Poisson's ratio in silicon wafers by means of vibration modes. *Measurement Science and Technology* **2004**, 15, (5), 859-868.
- Gao, J. X.; Chan-Park, M. B.; Xie, D. Z.; Yan, Y. H.; Zhou, W. X.; Ngoi, B. K. A.; Yue, C. Y., UV Embossing of Sub-micrometer Patterns on Biocompatible Polymeric Films Using a Focused Ion Beam Fabricated TiN Mold. *Chemistry of Materials* **2004**, 16, (6), 956-958.
- Gardner, J. W.; Varadan, V. K.; Awadelkarim, O. O., *Microsensors, MEMS, and smart devices*. J. Wiley: Chichester; New York, 2001; p xvi, 503.
- Gardner, T. J.; Frisbie, C. D.; Wrighton, M. S., Systems for orthogonal self-assembly of electroactive monolayers on Au and ITO: an approach to molecular electronics. *J. Am. Chem. Soc.* **1995**, 117, (26), 6927-6933.
- Gargini, P. A., Silicon nanoelectronics and beyond. *Journal of Nanoparticle Research* **2004**, 6, (1), 11-26.
- Gates, B. D.; Xu, Q.; Love, J. C.; Wolfe, D. B.; Whitesides, G. M., Unconventional nanofabrication. *Annual Review of Materials Research* **2004**, 34, 339-372.
- Gates, B. D.; Xu, Q.; Stewart, M.; Ryan, D.; Willson, C. G.; Whitesides, G. M., New Approaches to Nanofabrication: Molding, Printing, and Other Techniques. *Chemical Reviews* **2005**, 105, (4), 1171-1196.
- Gehoski, K. A.; Resnick, D. J.; Dauksher, W. J.; Nordquist, K. J.; Ainley, E.; McCord, M.; Raphaelian, M.; Hess, H., Indium tin oxide template development for step and flash imprint lithography. *Proceedings of SPIE-The International Society for Optical Engineering* **2005**, 5751, 986-993.
- Ghatak, A.; Chaudhury, M. K.; Shenoy, V.; Sharma, A., Meniscus Instability in a Thin Elastic Film. *Physical Review Letters* **2000**, 85, (20), 4329-4332.
- Giardi, M. T.; Piletska, E. V., *Biotechnological applications of photosynthetic proteins: biochips, biosensors, and biodevices*. Landes Bioscience/Eurekah.com; Springer Science+Business Media: Georgetown, Tex. New York, 2006.
- Goodner, M. D.; Bowman, C. N., Modeling primary radical termination and its effects on autoacceleration in photopolymerization kinetics. *Macromolecules* **1999**, 32, (20), 6552-6559.

- Groenenboom, C. J.; Hageman, H. J.; Overeem, T.; Weber, A. J. M., Photoinitiators and photoinitiation. 3. Comparison of the photodecompositions of α -methoxy- and α , α -dimethoxydeoxybenzoin in 1,1-diphenylethylene as model substrate. *Makromolekulare Chemie* **1982**, 183, (2), 281-92.
- Guo, L. J., Recent progress in nanoimprint technology and its applications. *Journal of Physics D: Applied Physics* **2004**, 37, (11), R123-R141.
- Gur, I.; Fromer, N. A.; Geier, M. L.; Alivisatos, A. P., Air-stable all-inorganic nanocrystal solar cells processed from solution. [Erratum to document cited in CA143:369944]. *Science* **2005**, 310, (5754), 1618.
- Hacioglu, B.; Berchtold, K. A.; Lovell, L. G.; Nie, J.; Bowman, C. N., Polymerization kinetics of HEMA/DEGDMA: using changes in initiation and chain transfer rates to explore the effects of chain-length-dependent termination. *Biomaterials* **2002**, 23, (20), 4057-4064.
- Haisma, J.; Verheijen, M.; van den Heuvel, K.; van den Berg, J., Mold-assisted nanolithography: A process for reliable pattern replication. *Journal of Vacuum Science & Technology, B: Microelectronics and Nanometer Structures* **1996**, 14, (6), 4124-4128.
- Haller, I., Covalently attached organic monolayers on semiconductor surfaces. *Journal of the American Chemical Society* **1978**, 100, (26), 8050-5.
- Hanrath, T. Germanium nanowires: Synthesis, characterization, and utilization. 2004.
- Hanrath, T.; Korgel Brian, A., Nucleation and growth of germanium nanowires seeded by organic monolayer-coated gold nanocrystals. *Journal of the American Chemical Society* **2002**, 124, (7), 1424-9.
- Hanson, E. L.; Guo, J.; Koch, N.; Schwartz, J.; Bernasek, S. L., Advanced Surface Modification of Indium Tin Oxide for Improved Charge Injection in Organic Devices. *Journal of the American Chemical Society* **2005**, 127, (28), 10058-10062.
- Harris, M.; Appel, G.; Ade, H., Surface morphology of annealed polystyrene and poly(methyl methacrylate) thin film blends and bilayers. *Macromolecules* **2003**, 36, (9), 3307-3314.
- Hatton, R. A.; Day, S. R.; Chesters, M. A.; Willis, M. R., Organic electroluminescent devices: enhanced carrier injection using an organosilane self assembled monolayer (SAM) derivatized ITO electrode. *Thin Solid Films* **2001**, 394, (1,2), 292-297.
- Hawryluk, A. M.; Ceglio, N. M.; Markle, D. A., EUV lithography. *Solid State Technology* **1997**, 40, (7), 151-152, 154, 156, 159.
- Hedges, D. H. P.; Richardson, D. J.; Russell, D. A., Electrochemical control of protein monolayers at indium tin oxide surfaces for the reagentless optical biosensing of nitric oxide. *Langmuir* **2004**, 20, (5), 1901-1908.
- Hermanson, K. O.; Lumsdon, S. O.; Williams, J. P.; Kater, E. W.; Velev, O. D., Dielectrophoretic assembly of electrically functional microwires from nanoparticle suspensions. *Science* **2001**, 294, (5544), 1082-1086.

- Herminghaus, S., Dynamical Instability of Thin Liquid Films Between Conducting Media. *Physical Review Letters* **1999**, 83, (12), 2359-2361.
- Hess, H. F.; Pettibone, D.; Adler, D.; Bertsche, K.; Nordquist, K. J.; Mancini, D. P.; Dauksher, W. J.; Resnick, D. J., Inspection of templates for imprint lithography. *Journal of Vacuum Science & Technology, B: Microelectronics and Nanometer Structures--Processing, Measurement, and Phenomena* **2004**, 22, (6), 3300-3305.
- Hillebrandt, H.; Tanaka, M., Electrochemical Characterization of Self-Assembled Alkylsiloxane Monolayers on Indium-Tin Oxide (ITO) Semiconductor Electrodes. *Journal of Physical Chemistry B* **2001**, 105, (19), 4270-4276.
- Hillebrandt, H.; Wiegand, G.; Tanaka, M.; Sackmann, E., High Electric Resistance Polymer/Lipid Composite Films on Indium-Tin-Oxide Electrodes. *Langmuir* **1999**, 15, (24), 8451-8459.
- Hirai, Y.; Harada, S.; Kikuta, H.; Tanaka, Y.; Okano, M.; Isaka, S.; Kobayasi, M., Imprint lithography for curved cross-sectional structure using replicated Ni mold. *Journal of Vacuum Science & Technology, B: Microelectronics and Nanometer Structures* **2002**, 20, (6), 2867-2871.
- Hoff, J. D.; Cheng, L.-J.; Meyhoefer, E.; Guo, L. J.; Hunt, A. J., Nanoscale Protein Patterning by Imprint Lithography. *Nano Letters* **2004**, 4, (5), 853-857.
- Holcombe, T. W., III; Dickey, M.; Willson, C. G., A New Method for Covalently Bonding Functionality to ITO Films. *Abstracts, 57th Southeast/61st Southwest Joint Regional Meeting of the American Chemical Society, Memphis, TN, United States, November 1-4* **2005**, NOV04-377.
- Hoyle, C. E.; Lee, T. Y.; Roper, T., Thiol-enes: Chemistry of the past with promise for the future. *Journal of Polymer Science, Part A: Polymer Chemistry* **2004**, 42, (21), 5301-5338.
- Hsu, H. Y.; Sharma, N.; Ruoff, R. S.; Patankar, N. A., Electro-orientation in particle light valves. *Nanotechnology* **2005**, 16, (2), 312-319.
- Hu, S.; Popielarz, R.; Neckers, D. C., Fluorescence Probe Techniques (FPT) for Measuring the Relative Efficiencies of Free-Radical Photoinitiators. *Macromolecules* **1998**, 31, (13), 4107-4113.
- Hua, F.; Sun, Y.; Gaur, A.; Meitl, M. A.; Bilhaut, L.; Rotkina, L.; Wang, J.; Geil, P.; Shim, M.; Rogers, J. A.; Shim, A., Polymer Imprint Lithography with Molecular-Scale Resolution. *Nano Letters* **2004**, 4, (12), 2467-2471.
- Huang, C. J.; Su, Y. K.; Wu, S. L., The effect of solvent on the etching of ITO electrode. *Materials Chemistry and Physics* **2004**, 84, (1), 146-150.
- Huang, Y.; Paloczi, G. T.; Poon, J. K. S.; Yariv, A., Bottom-up soft-lithographic fabrication of three-dimensional multilayer polymer integrated optical microdevices. *Applied Physics Letters* **2004**, 85, (15), 3005-3007.

- Huepe, C.; Ding, Y.; Umbanhowar, P.; Silber, M., Forcing function control of Faraday wave instabilities in viscous shallow fluids. *Physical Review E: Statistical, Nonlinear, and Soft Matter Physics* **2006**, 73, (1-2), 016310/1-016310/11.
- Huff, H. R.; Zeitzoff, P. M., An analytical look at vertical transistor structures. *Solid State Technology* **2004**, 47, (8), 59-60, 62, 64, 66, 72.
- Hughes, M. P., *Nanoelectromechanics in engineering and biology*. CRC Press: Boca Raton, 2003; p 322.
- Hui, C. Y.; Jagota, A.; Lin, Y. Y.; Kramer, E. J., Constraints on Microcontact Printing Imposed by Stamp Deformation. *Langmuir* **2002**, 18, (4), 1394-1407.
- Hutchinson, R. A.; Aronson, M. T.; Richards, J. R., Analysis of pulsed-laser-generated molecular weight distributions for the determination of propagation rate coefficients. *Macromolecules* **1993**, 26, (24), 6410-15.
- Huynh, W. U.; Dittmer, J. J.; Alivisatos, A. P., Hybrid nanorod-polymer solar cells. *Science* **2002**, 295, (5564), 2425-2427.
- Iijima, S., Helical microtubules of graphitic carbon. *Nature* **1991**, 354, (6348), 56-8.
- Ishii, M.; Mori, T.; Fujikawa, H.; Tokito, S.; Taga, Y., Improvement of organic electroluminescent device performance by in situ plasma treatment of indium-tin-oxide surface. *Journal of Luminescence* **2000**, 87-89, 1165-1167.
- Jacobine, A. F., *Radiation Curing in Polymer Science and Technology III, Polymerization Mechanisms*. Elsevier Applied Science: London, 1993.
- Jaszewski, R. W.; Schiff, H.; Schnyder, B.; Schneuwly, A.; Groning, P., The deposition of anti-adhesive ultra-thin Teflon-like films and their interaction with polymers during hot embossing. *Applied Surface Science* **1999**, 143, (1-4), 301-308.
- Johnson, S.; Burns, R.; Kim, E. K.; Dickey, M.; Schmid, G.; Meiring, J.; Burns, S.; Willson, C. G.; Convey, D.; Wei, Y.; Fejes, P.; Gehoski, K.; Mancini, D.; Nordquist, K.; Dauksher, W. J.; Resnick, D. J., Effects of etch barrier densification on step and flash imprint lithography. *Journal of Vacuum Science & Technology, B: Microelectronics and Nanometer Structures--Processing, Measurement, and Phenomena* **2005**, 23, (6), 2553-2556.
- Johnson, S. C.; Bailey, T. C.; Dickey, M. D.; Smith, B. J.; Kim, E. K.; Jamieson, A. T.; Stacey, N. A.; Ekerdt, J. G.; Willson, C. G.; Mancini, D. P.; Dauksher, W. J.; Nordquist, K. J.; Resnick, D. J., Advances in Step and Flash imprint lithography. *Proceedings of SPIE-The International Society for Optical Engineering* **2003**, 5037, 197-202.
- Jones, T. B., *Electromechanics of particles*. Cambridge University Press: Cambridge; New York, 2005; p xxii, 265.
- Kam, A. P.; Seekamp, J.; Solovyev, V.; Cedeno, C. C.; Goldschmidt, A.; Torres, C. M. S., Nanoimprinted organic field-effect transistors: fabrication, transfer mechanism and solvent effects on device characteristics. *Microelectronic Engineering* **2004**, 73-74, 809-813.

- Kargupta, K.; Sharma, A., Templating of Thin Films Induced by Dewetting on Patterned Surfaces. *Physical Review Letters* **2001**, 86, (20), 4536-4539.
- Kee, C.-S.; Han, S.-P.; Yoon, K. B.; Choi, C.-G.; Sung, H. K.; Oh, S. S.; Park, H. Y.; Park, S.; Schiff, H., Photonic band gaps and defect modes of polymer photonic crystal slabs. *Applied Physics Letters* **2005**, 86, (5), 051101/1-051101/3.
- Kee, C.-S.; Yoon, K. B.; Choi, C.-G.; Kim, J.-T.; Han, S. P.; Park, S.; Schiff, H., Nanopatterned Polymer Thin Films. *Journal of Nonlinear Optical Physics & Materials* **2005**, 14, (3), 299-303.
- Khudyakov, I. V.; Purvis, M. B.; Turro, N. J., Kinetics of photopolymerization of acrylate coatings. *ACS Symposium Series* **2003**, 847, (Photoinitiated Polymerization), 113-126.
- Kim, E. K.; Ekerdt, J. G.; Willson, C. G., Importance of evaporation in the design of materials for step and flash imprint lithography. *Journal of Vacuum Science & Technology, B: Microelectronics and Nanometer Structures--Processing, Measurement, and Phenomena* **2005**, 23, (4), 1515-1520.
- Kim, E. K.; Stacey, N. A.; Smith, B. J.; Dickey, M. D.; Johnson, S. C.; Trinque, B. C.; Willson, C. G., Vinyl ethers in ultraviolet curable formulations for step and flash imprint lithography. *Journal of Vacuum Science & Technology, B: Microelectronics and Nanometer Structures--Processing, Measurement, and Phenomena* **2004**, 22, (1), 131-135.
- Kim, E. K.; Stewart, M. D.; Wu, K.; Palmieri, F. L.; Dickey, M. D.; Ekerdt, J. G.; Willson, C. G., Vinyl ether formulations for step and flash imprint lithography. *Journal of Vacuum Science & Technology, B: Microelectronics and Nanometer Structures--Processing, Measurement, and Phenomena* **2005**, 23, (6), 2967-2971.
- Kim, H.; Lee, J.; Park, C.; Park, Y., Surface characterization of O₂-plasma-treated indium-tin-oxide (ITO) anodes for organic light-emitting-device applications. *Journal of the Korean Physical Society* **2002**, 41, (3), 395-399.
- Kim, J. S.; Friend, R. H.; Cacialli, F., Surface energy and polarity of treated indium-tin-oxide anodes for polymer light-emitting diodes studied by contact-angle measurements. *Journal of Applied Physics* **1999**, 86, (5), 2774-2778.
- Kim, J. S.; Friend, R. H.; Cacialli, F., Surface wetting properties of treated indium tin oxide anodes for polymer light-emitting diodes. *Synthetic Metals* **2000**, 111-112, 369-372.
- Kim Sang, O.; Solak Harun, H.; Stoykovich Mark, P.; Ferrier Nicola, J.; De Pablo Juan, J.; Nealey Paul, F., Epitaxial self-assembly of block copolymers on lithographically defined nanopatterned substrates. *Nature* **2003**, 424, (6947), 411-4.
- King, W. P.; Rowland, H. D., Understanding polymer flow during micro- and nano-embossing. *PMSE Preprints* **2006**, 94, 732.

Kinkel, J. N.; Unger, K. K., Role of solvent and base in the silanization reaction of silicas for reversed-phase high-performance liquid chromatography. *Journal of Chromatography* **1984**, 316, 193-200.

Kinoshita, H.; Watanabe, T., Current status of EUV lithography. *Journal of Photopolymer Science and Technology* **2000**, 13, (3), 379-384.

Kinoshita, H.; Watanabe, T., Present status and future prospects of EUV lithography. *Journal of Photopolymer Science and Technology* **1997**, 10, (3), 369-376.

Klingner, A.; Buehrle, J.; Mugele, F., Capillary Bridges in Electric Fields. *Langmuir* **2004**, 20, (16), 6770-6777.

Kloosterboer, J. G.; Van de Hei, G. M. M.; Gossink, R. G.; Dortant, G. C. M., The effects of volume relaxation and thermal mobilization of trapped radicals on the final conversion of photopolymerized diacrylates. *Polymer Communications* **1984**, 25, (11), 322-5.

Koide, Y.; Wang, Q.; Cui, J.; Benson, D. D.; Marks, T. J., Patterned luminescence of organic light-emitting diodes by hot microcontact printing (HmCP) of self-assembled monolayers. *Journal of the American Chemical Society* **2000**, 122, (45), 11266-11267.

Kovtyukhova, N. I.; Mallouk, T. E., Nanowire p-n heterojunction diodes made by templated assembly of multilayer carbon-nanotube/polymer/semiconductor-particle shells around metal nanowires. *Advanced Materials* **2005**, 17, (2), 187-192.

Krongauz, V. V.; Chawla, C. P., Oxygen and radical photopolymerization in films. *Abstracts of Papers, 222nd ACS National Meeting, Chicago, IL, United States, August 26-30, 2001* **2001**, POLY-376.

Krongauz, V. V.; Chawla, C. P.; Dupre, J., Oxygen and radical photopolymerization in films. *ACS Symposium Series* **2003**, 847, (Photoinitiated Polymerization), 165-175.

Krongauz, V. V.; Schmelzer, E. R.; Yohannan, R. M., Kinetics of anisotropic photopolymerization in polymer matrix. *Polymer* **1991**, 32, (9), 1654-62.

Kumar, S., Mechanism for the Faraday instability in viscous liquids. *Physical Review E: Statistical Physics, Plasmas, Fluids, and Related Interdisciplinary Topics* **2000**, 62, (1-B), 1416-1419.

Kurdikar, D. L.; Peppas, N. A., Investigation of diffusion-controlled homopolymerization of bifunctional monomers. *Vysokomolekulyarnye Soedineniya, Seriya A i Seriya B* **1994**, 36, (11), 1852-61.

Kurdikar, D. L.; Peppas, N. A., Kinetics of photopolymerizations of multifunctional monomers. *Polymeric Materials Science and Engineering* **1993**, 69, 174-5.

Landau, L. D.; Lifshits, E. M., *Electrodynamics of continuous media*. Pergamon Press: Oxford, New York, 1960; p 417.

Larson, R. G., *The structure and rheology of complex fluids*. Oxford University Press: New York, 1999; p xxi, 663.

Le, N. V.; Dauksher, W. J.; Gehoski, K. A.; Resnick, D. J.; Hooper, A. E.; Johnson, S.; Willson, G., Selective dry etch process for step and flash imprint lithography. *Microelectronic Engineering* **2005**, 78-79, 464-473.

Le, N. V.; Gehoski, K. A.; Dauksher, W. J.; Baker, J. H.; Resnick, D. J.; Dues, L., Development of an etch-definable lift-off process for use with step and flash imprint lithography. *Proceedings of SPIE-The International Society for Optical Engineering* **2005**, 5751, 219-226.

Leach, K. A.; Gupta, S.; Dickey, M. D.; Willson, C. G.; Russell, T. P., Electric field and dewetting induced hierarchical structure formation in polymer/polymer/air trilayers. *Chaos* **2005**, 15, (4), 047506/1-047506/5.

Leach, K. A.; Lin, Z.; Russell, T. P., Early Stages in the Growth of Electric Field-Induced Surface Fluctuations. *Macromolecules* **2005**, 38, (11), 4868-4873.

Lee, J. N.; Park, C.; Whitesides, G. M., Solvent Compatibility of Poly(dimethylsiloxane)-Based Microfluidic Devices. *Analytical Chemistry* **2003**, 75, (23), 6544-6554.

Lendlein, A.; Jiang, H.; Juenger, O.; Langer, R., Light-induced shape-memory polymers. *Nature* **2005**, 434, (7035), 879-882.

Lewis, F. D.; Magyar, J. G., Photoreduction and α cleavage of aryl alkyl ketones. *Journal of Organic Chemistry* **1972**, 37, (13), 2102-7.

Lieber, C. M., The incredible shrinking circuit. *Scientific American* **2001**, 285, (3), 58-64.

Lifshitz, R. <http://haides.caltech.edu/~lifshitz/patterns.html>. (April 2006).

Lin, B. J., Immersion lithography and its impact on semiconductor manufacturing. *Journal of Microlithography, Microfabrication, and Microsystems* **2004**, 3, (3), 377-395.

Lin, Z.; Kerle, T.; Baker, S. M.; Hoagland, D. A.; Schaffer, E.; Steiner, U.; Russell, T. P., Electric field induced instabilities at liquid/liquid interfaces. *Journal of Chemical Physics* **2001**, 114, (5), 2377-2381.

Lin, Z.; Kerle, T.; Russell, T. P.; Schaeffer, E.; Steiner, U., Electric Field Induced Dewetting at Polymer/Polymer Interfaces. *Macromolecules* **2002**, 35, (16), 6255-6262.

Lin, Z.; Kerle, T.; Russell, T. P.; Schaeffer, E.; Steiner, U., Structure Formation at the Interface of Liquid/Liquid Bilayer in Electric Field. *Macromolecules* **2002**, 35, (10), 3971-3976.

Lin, Z. Q.; Kerle, T.; Baker, S. M.; Hoagland, D. A.; Schaffer, E.; Steiner, U.; Russell, T. P., Electric field induced instabilities at liquid/liquid interfaces. *Journal of Chemical Physics* **2001**, 114, (5), 2377-2381.

Lin, Z. Q.; Kerle, T.; Russell, T. P.; Schaffer, E.; Steiner, U., Electric field induced dewetting at polymer/polymer interfaces. *Macromolecules* **2002**, 35, (16), 6255-6262.

Lin, Z. Q.; Kerle, T.; Russell, T. P.; Schaffer, E.; Steiner, U., Structure formation at the interface of liquid liquid bilayer in electric field. *Macromolecules* **2002**, 35, (10), 3971-3976.

- Loos, J., The art of SPM: Scanning probe microscopy in materials science. *Advanced Materials* **2005**, 17, (15), 1821-1833.
- Lork, K. D.; Unger, K. K.; Kinkel, J. N., Role of the functional group in n-octyldimethylsilanes in the synthesis of C8 reversed-phase silica packings for high-performance liquid chromatography. *Journal of Chromatography* **1986**, 352, 199-211.
- Lumsdon, S. O.; Kaler, E. W.; Williams, J. P.; Velez, O. D., Dielectrophoretic assembly of oriented and switchable two-dimensional photonic crystals. *Applied Physics Letters* **2003**, 82, (6), 949-951.
- Lyons, R. A.; Hutovic, J.; Piton, M. C.; Christie, D. I.; Clay, P. A.; Manders, B. G.; Kable, S. H.; Gilbert, R. G., Pulsed-Laser Polymerization Measurements of the Propagation Rate Coefficient for Butyl Acrylate. *Macromolecules* **1996**, 29, (6), 1918-27.
- Ma, C. C.; Lin, H. Y., Experimental measurements on transverse vibration characteristics of piezoceramic rectangular plates by optical methods. *Journal of Sound and Vibration* **2005**, 286, (3), 587-600.
- MacDonald, S.; Hughes, G.; Stewart, M.; Palmieri, F.; Willson, C. G., Design and fabrication of highly complex topographic nano-imprint template for dual Damascene full 3-D imprinting. *Proceedings of SPIE-The International Society for Optical Engineering* **2005**, 5992, 786-794.
- Mack, C. A., Absorption and exposure in positive photoresist. *Applied Optics* **1988**, 27, (23), 4913-19.
- Mack, C. A., *Field guide to optical lithography*. SPIE Press: Bellingham, Wash., 2006.
- Mack, C. A.; Stevenson, T.; European Optical Society., *Lithography for semiconductor manufacturing: 19-21 May 1999, Edinburgh, Scotland*. SPIE: Bellingham, Wash., USA, 1999; p vii, 262.
- Mack, C. A.; Stevenson, T.; Society of Photo-optical Instrumentation Engineers.; Scottish Enterprise.; European Optical Society.; Institution of Electrical Engineers., *Lithography for semiconductor manufacturing II: 30 May-1 June, 2001, Edinburgh, UK*. SPIE: Bellingham, Wash., 2001; p vii, 422.
- Mancini, D. P.; Gehoski, K. A.; Dauksher, W. J.; Nordquist, K. J.; Resnick, D. J.; Schumaker, P.; McMackin, I., Template fabrication for sub-80-nm contact hole patterning using step and flash imprint lithography. *Proceedings of SPIE-The International Society for Optical Engineering* **2003**, 5256, 122-131.
- Mancini, D. P.; Resnick, D. J.; Sreenivasan, S. V.; Watts, M. P. C., S-FIL for sub-80 nm contact hole patterning. *Solid State Technology* **2004**, 47, (2), 55-56, 58.
- Markovich, I.; Mandler, D., Preparation and characterization of octadecylsilane monolayers on indium-tin oxide (ITO) surfaces. *Journal of Electroanalytical Chemistry* **2001**, 500, (1-2), 453-460.
- Markvart, T.; Castañer, L., *Practical handbook of photovoltaics: fundamentals and applications*. Elsevier Advanced Technology: New York, 2003; p xiv, 984.

- Marrian, C. R. K.; Tennant, D. M., Nanofabrication. *Journal of Vacuum Science & Technology, A: Vacuum, Surfaces, and Films* **2003**, 21, (5, Suppl.), S207-S215.
- Marty, J. D.; Marty, J. D., *Microolithography/molecular imprinting*. 1st ed.; Springer: New York, NY, 2005.
- Marzouk, S.; Rachdi, F.; Fourati, M.; Bouaziz, J., Synthesis and grafting of silica aerogels. *Colloids and Surfaces, A: Physicochemical and Engineering Aspects* **2004**, 234, (1-3), 109-116.
- Mateo, J. L.; Serrano, J.; Bosch, P., Photopolymerization of Di- and Tetrafunctional Methacrylic Monomers in a Polymeric Medium: Kinetics and Evidence of Reaction Diffusion during an All Photopolymerization Reaction. *Macromolecules* **1997**, 30, (5), 1285-1288.
- McAlpine, M. C.; Friedman, R. S.; Lieber, C. M., Nanoimprint Lithography for Hybrid Plastic Electronics. *Nano Letters* **2003**, 3, (4), 443-445.
- McClelland, G. M.; Hart, M. W.; Rettner, C. T.; Best, M. E.; Carter, K. R.; Terris, B. D., Nanoscale patterning of magnetic islands by imprint lithography using a flexible mold. *Applied Physics Letters* **2002**, 81, (8), 1483-1485.
- McMackin, I.; Choi, J.; Schumaker, P.; Nguyen, V.; Xu, F.; Thompson, E.; Babbs, D.; Sreenivasan, S. V.; Watts, M.; Schumaker, N., Step and Repeat UV nanoimprint lithography tools and processes. *Proceedings of SPIE-The International Society for Optical Engineering* **2004**, 5374, 222-231.
- McMackin, I.; Schumaker, P.; Babbs, D.; Choi, J.; Collison, W.; Sreenivasan, S. V.; Schumaker, N. E.; Watts, M. P. C.; Voisin, R. D., Design and performance of a step and repeat imprinting machine. *Proceedings of SPIE-The International Society for Optical Engineering* **2003**, 5037, 178-186.
- Meindl, J. D.; Chen, Q.; Davis, J. A., Limits on silicon nanoelectronics for terascale integration. *Science* **2001**, 293, (5537), 2044-9.
- Melcher, J. R., *Field-coupled surface waves, a comparative study of surface-coupled electrohydrodynamic and magnetohydrodynamic systems*. M.I.T. Press: Cambridge, Mass., 1963; p xiv, 190.
- Meng, G.; Jung, Y. J.; Cao, A.; Vajtai, R.; Ajayan, P. M., Controlled fabrication of hierarchically branched nanopores, nanotubes, and nanowires. *Proceedings of the National Academy of Sciences of the United States of America* **2005**, 102, (20), 7074-7078.
- Miller, C. W.; Hoyle, C. E.; Jonsson, S.; Nason, C.; Lee, T. Y.; Kuang, W. F.; Viswanathan, K., N-vinylamides and reduction of oxygen inhibition in photopolymerization of simple acrylate formulations. *ACS Symposium Series* **2003**, 847, (Photoinitiated Polymerization), 2-14.
- Miller, M.; Doyle, G.; Stacey, N.; Xu, F.; Sreenivasan, S. V.; Watts, M.; LaBrake, D. L., Fabrication of nanometer sized features on non-flat substrates using a nano-imprint

lithography process. *Proceedings of SPIE-The International Society for Optical Engineering* **2005**, 5751, 994-1002.

Milliron, D. J.; Hill, I. G.; Shen, C.; Kahn, A.; Schwartz, J., Surface oxidation activates indium tin oxide for hole injection. *Journal of Applied Physics* **2000**, 87, (1), 572-576.

Milliron, D. J.; Hughes, S. M.; Cui, Y.; Manna, L.; Li, J.; Wang, L.-W.; Alivisatos, A. P., Colloidal nanocrystal heterostructures with linear and branched topology. *Nature* **2004**, 430, (6996), 190-195.

Mills, C. A.; Escarre, J.; Engel, E.; Martinez, E.; Errachid, A.; Bertomeu, J.; Andreu, J.; Planell, J. A.; Samitier, J., Micro- and nanostructuring of poly(ethylene-2,6-naphthalate) surfaces, for biomedical applications, using polymer replication techniques. *Nanotechnology* **2005**, 16, (4), 369-375.

Mills, C. A.; Martinez, E.; Bessueille, F.; Villanueva, G.; Bausells, J.; Samitier, J.; Errachid, A., Production of structures for microfluidics using polymer imprint techniques. *Microelectronic Engineering* **2005**, 78-79, 695-700.

Minteer, S. D., *Microfluidic techniques: reviews and protocols*. Humana Press: Totowa, N.J., 2006.

Modi, A.; Koratkar, N.; Lass, E.; Wei, B.; Ajayan, P. M., Miniaturized gas ionization sensors using carbon nanotubes. *Nature* **2003**, 424, (6945), 171-174.

Monch, W.; Herminghaus, S., Elastic instability of rubber films between solid bodies. *Europhysics Letters* **2001**, 53, (4), 525-531.

Moon, E. E.; Mondol, M. K.; Everett, P. N.; Smith, H. I., Dynamic alignment control for fluid-immersion lithographies using interferometric-spatial-phase imaging. *Journal of Vacuum Science & Technology, B: Microelectronics and Nanometer Structures--Processing, Measurement, and Phenomena* **2005**, 23, (6), 2607-2610.

Moore, G. E., Cramming more components onto integrated circuits. *Electronics* **1965**, 38, (8).

Morariu, M. D.; Voicu, N. E.; Schaeffer, E.; Lin, Z.; Russell, T. P.; Steiner, U., Hierarchical structure formation and pattern replication induced by an electric field. *Nature Materials* **2003**, 2, (1), 48-52.

Morgan, C. R.; Ketley, A. D., The effect of phosphines on thiol/ene curing systems. *Journal of Polymer Science, Polymer Letters Edition* **1978**, 16, (2), 75-9.

Morgan, C. R.; Ketley, A. D., The photopolymerization of allylic and acrylic monomers in the presence of polyfunctional thiols. *Journal of Radiation Curing* **1980**, 7, (2), 10-13.

Morgan, C. R.; Magnotta, F.; Ketley, A. D., Thiol/ene photocurable polymers. *Journal of Polymer Science, Polymer Chemistry Edition* **1977**, 15, (3), 627-45.

Morkved, T. L.; Lu, M.; Urbas, A. M.; Ehrichs, E. E.; Jaeger, H. M.; Mansky, P.; Russell, T. P., Local control of microdomain orientation in diblock copolymer thin films with electric fields. *Science* **1996**, 273, (5277), 931-933.

- Mrozek, R. A.; Taton, T. A., Alignment of Liquid-Crystalline Polymers by Field-Oriented, Carbon Nanotube Directors. *Chemistry of Materials* **2005**, 17, (13), 3384-3388.
- Myron, L. J.; Gershtein, L.; Gottlieb, G.; Burkhardt, B.; Griffiths, A.; Mellenthin, D.; Rentzsch, K.; MacDonald, S.; Hughes, G., Advanced mask metrology enabling characterization of imprint lithography templates. *Proceedings of SPIE-The International Society for Optical Engineering* **2005**, 5752, 384-391.
- Myshkis, A. D., *Low-gravity fluid mechanics: mathematical theory of capillary phenomena*. Springer-Verlag: Berlin; New York, 1987; p xix, 583.
- Nagle, L.; Ryan, D.; Cobbe, S.; Fitzmaurice, D., Templated Nanoparticle Assembly on the Surface of a Patterned Nanosphere. *Nano Letters* **2003**, 3, (1), 51-53.
- Nakagawa, T.; Nakiri, T.; Hosoya, R.; Tajitsu, Y., Electrical properties of biodegradable polylactic acid film. *Proceedings of the International Conference on Properties and Applications of Dielectric Materials, 7th, Nagoya, Japan, June 1-5, 2003* **2003**, 2, 499-502.
- Narasimhan, B.; Peppas, N. A., The physics of polymer dissolution: modeling approaches and experimental behavior. *Advances in Polymer Science* **1997**, 128, 157-207.
- Neta, P.; Huie, R. E.; Ross, A. B., Rate constants for reactions of peroxy radicals in fluid solutions. *Journal of Physical and Chemical Reference Data* **1990**, 19, (2), 413-513.
- Ng, H. T.; Fang, A.; Huang, L.; Li, S. F. Y., Protein microarrays on ITO surfaces by a direct covalent attachment scheme. *Langmuir* **2002**, 18, (16), 6324-6329.
- Nguyen, N.-T.; Wereley, S. T., *Fundamentals and applications of microfluidics*. Artech House: Boston, MA, 2002; p xiii, 471.
- Nilsson, L.; Groening, O.; Emmenegger, C.; Kuettel, O.; Schaller, E.; Schlapbach, L.; Kind, H.; Bonard, J. M.; Kern, K., Scanning field emission from patterned carbon nanotube films. *Applied Physics Letters* **2000**, 76, (15), 2071-2073.
- Nishiyama, I., EUV lithography. *Optronics* **2003**, 256, 122-127.
- Nordquist, K. J.; Ainley, E. S.; Mancini, D. P.; Dauksher, W. J.; Gehoski, K. A.; Baker, J.; Resnick, D. J.; Masnyj, Z.; Mangat, P. J. S., Image placement issues for ITO-based step and flash imprint lithography templates. *Journal of Vacuum Science & Technology, B: Microelectronics and Nanometer Structures--Processing, Measurement, and Phenomena* **2004**, 22, (2), 695-701.
- O'Brien, A. K.; Bowman, C. N., Impact of Oxygen on Photopolymerization Kinetics and Polymer Structure. *Macromolecules* **2006**, 39, (7), 2501-2506.
- O'Brien, A. K.; Bowman, C. N., Modeling the effect of oxygen on photopolymerization kinetics. *Macromolecular Theory and Simulations* **2006**, 15, (2), 176-182.
- Oddershede, L.; Nagel, S. R., Singularity during the Onset of an Electrohydrodynamic Spout. *Physical Review Letters* **2000**, 85, (6), 1234-1237.

- Oddy, M. H.; Santiago, J. G.; Mikkelsen, J. C., Electrokinetic instability micromixing. *Analytical Chemistry* **2001**, 73, (24), 5822-5832.
- Odian, G. G., *Principles of polymerization*. 3rd ed.; Wiley: New York, 1991; p xxii, 768.
- Odom, T. W.; Love, J. C.; Wolfe, D. B.; Paul, K. E.; Whitesides, G. M., Improved pattern transfer in soft lithography using composite stamps. *Langmuir* **2002**, 18, (13), 5314-5320.
- Okamura, S.; Manabe, T., Radiation polymerization in solution. III. Effect of primary radicals in the termination reaction. *Polymer* **1961**, 2, 83-94.
- Okazaki, S., Current status and issues of EUV lithography research. *Optronics* **1999**, 205, 104-110.
- Okazaki, S., Recent development activities and future plans for EUV lithography in Japan. *Proceedings of SPIE-The International Society for Optical Engineering* **2005**, 5592, 27-37.
- Ongaro, A.; Griffin, F.; Beecher, P.; Nagle, L.; Iacopino, D.; Quinn, A.; Redmond, G.; Fitzmaurice, D., DNA-templated assembly of conducting gold nanowires between gold electrodes on a silicon oxide substrate. *Chemistry of Materials* **2005**, 17, (8), 1959-1964.
- Ongaro, A.; Griffin, F.; Nagle, L.; Iacopino, D.; Eritja, R.; Fitzmaurice, D., DNA-Templated assembly of a protein-functionalized nanogap electrode. *Advanced Materials* **2004**, 16, (20), 1799-1803.
- Oron, A., Nonlinear dynamics of three-dimensional long-wave Marangoni instability in thin liquid films. *Physics of Fluids* **2000**, 12, (7), 1633-1645.
- Pang, S. W.; Tamamura, T.; Nakao, M.; Ozawa, A.; Masuda, H., Direct nano-printing on Al substrate using a SiC mold. *Journal of Vacuum Science & Technology, B: Microelectronics and Nanometer Structures* **1998**, 16, (3), 1145-1149.
- Parikh, A. N.; Allara, D. L.; Azouz, I. B.; Rondelez, F., An Intrinsic Relationship between Molecular Structure in Self-Assembled n-Alkylsiloxane Monolayers and Deposition Temperature. *Journal of Physical Chemistry* **1994**, 98, (31), 7577-90.
- Park, M.; Harrison, C.; Chaikin, P. M.; Register, R. A.; Adamson, D. H., Block copolymer lithography: periodic arrays of ~1011 holes in 1 square centimeter. *Science* **1997**, 276, (5317), 1401-1404.
- Pease, L. F., III; Russel, W. B., Limitations on Length Scales for Electrostatically Induced Submicrometer Pillars and Holes. *Langmuir* **2004**, 20, (3), 795-804.
- Pease, L. F.; Russel, W. B., Electrostatically induced submicron patterning of thin perfect and leaky dielectric films: A generalized linear stability analysis. *Journal of Chemical Physics* **2003**, 118, (8), 3790-3803.
- Pease, L. F.; Russel, W. B., Linear stability analysis of thin leaky dielectric films subjected to electric fields. *Journal of Non-Newtonian Fluid Mechanics* **2002**, 102, (2), 233-250.

- Peppas, N. A.; Wu, J. C.; von Meerwall, E. D., Mathematical Modeling and Experimental Characterization of Polymer Dissolution. *Macromolecules* **1994**, 27, (20), 5626-38.
- Pettibone, D.; Stokowski, S., Optical inspection of next generation lithography masks. *Journal of Vacuum Science & Technology, B: Microelectronics and Nanometer Structures--Processing, Measurement, and Phenomena* **2004**, 22, (6), 3366-3372.
- Plateau, J., Experimentale et Theoretique des Liquides. **1873**.
- Poa, C. H.; Silva, S. R. P.; Watts, P. C. P.; Hsu, W. K.; Kroto, H. W.; Walton, D. R. M., Field emission from nonaligned carbon nanotubes embedded in a polystyrene matrix. *Applied Physics Letters* **2002**, 80, (17), 3189-3191.
- Poa, C. H. P.; Henley, S. J.; Chen, G. Y.; Adikaari, A. A. D. T.; Giusca, C. E.; Silva, S. R. P., Growth and field emission properties of vertically aligned carbon nanofibers. *Journal of Applied Physics* **2005**, 97, (11), 114308/1-114308/6.
- Poa, C. H. P.; Smith, R. C.; Silva, S. R. P.; Watts, P. C. P.; Hsu, W. K.; Kroto, H. W.; Walton, D. R. M., Field emission from nonaligned carbon nanotube-polymer matrix cathodes. *Journal of Vacuum Science & Technology, B: Microelectronics and Nanometer Structures--Processing, Measurement, and Phenomena* **2003**, 21, (4), 1715-1719.
- Qu, S.; Clarke, C. J.; Liu, Y.; Rafailovich, M. H.; Sokolov, J.; Phelan, K. C.; Krausch, G., Dewetting dynamics at a polymer-polymer interface. *Macromolecules* **1997**, 30, (12), 3640-3645.
- Quilliet, C.; Berge, B., Electrowetting: a recent outbreak. *Current Opinion in Colloid & Interface Science* **2001**, 6, (1), 34-39.
- Ramos, A.; Gonzalez, H.; Castellanos, A., Bifurcation diagrams of axisymmetric liquid bridges subjected to axial electric fields. *Physics of Fluids* **1994**, 6, (11), 3580-90.
- Rayleigh, L., On the capillary phenomena of jets. *Proceedings of the Royal Society of London* **1879**, 29, (71).
- Reddy, S.; Bonnecaze, R. T., Simulation of fluid flow in the step and flash imprint lithography process. *Microelectronic Engineering* **2005**, 82, (1), 60-70.
- Reisner, W.; Morton, K. J.; Riehn, R.; Wang, Y. M.; Yu, Z.; Rosen, M.; Sturm, J. C.; Chou, S. Y.; Frey, E.; Austin, R. H., Statics and Dynamics of Single DNA Molecules Confined in Nanochannels. *Physical Review Letters* **2005**, 94, (19), 196101/1-196101/4.
- Reiter, G., Dewetting of Thin Polymer-Films. *Physical Review Letters* **1992**, 68, (1), 75-78.
- Ren, Z. F.; Huang, Z. P.; Xu, J. W.; Wang, J. H.; Bush, P.; Siegel, M. P.; Provencio, P. N., Synthesis of large arrays of well-aligned carbon nanotubes on glass. *Science* **1998**, 282, (5391), 1105-1107.
- Report, S., Technology Review. In MIT: 2003; Vol. 106, p 36.
- Resnick, D. J.; Bailey, T. C.; Mancini, D.; Nordquist, K. J.; Dauksher, W. J.; Ainley, E.; Talin, A.; Gehoski, K.; Baker, J. H.; Choi, B. J.; Johnson, S.; Colburn, M.; Meissl, M.;

- Sreenivasan, S. V.; Ekerdt, J. G.; Willson, C. G., New methods for fabricating step and flash imprint lithography templates. *Proceedings of SPIE-The International Society for Optical Engineering* **2002**, 4608, 176-181.
- Resnick, D. J.; Dauksher, W. J.; Mancini, D.; Nordquist, K. J.; Ainley, E.; Gehoski, K.; Baker, J. H.; Bailey, T. C.; Choi, B. J.; Johnson, S.; Sreenivasan, S. V.; Ekerdt, J. G.; Willson, C. G., High resolution templates for step and flash imprint lithography. *Journal of Microlithography, Microfabrication, and Microsystems* **2002**, 1, (3), 284-289.
- Resnick, D. J.; Dauksher, W. J.; Mancini, D.; Nordquist, K. J.; Bailey, T. C.; Johnson, S.; Stacey, N.; Ekerdt, J. G.; Willson, C. G.; Sreenivasan, S. V.; Schumaker, N., Imprint lithography for integrated circuit fabrication. *Journal of Vacuum Science & Technology, B: Microelectronics and Nanometer Structures--Processing, Measurement, and Phenomena* **2003**, 21, (6), 2624-2631.
- Resnick, D. J.; Dauksher, W. J.; Mancini, D. P.; Nordquist, K. J.; Ainley, E. S.; Gehoski, K. A.; Baker, J. H.; Bailey, T. C.; Choi, B. J.; Johnson, S.; Sreenivasan, S. V.; Ekerdt, J. G.; Willson, C. G., High-resolution templates for step and flash imprint lithography. *Proceedings of SPIE-The International Society for Optical Engineering* **2002**, 4688, 205-213.
- Resnick, D. J.; Mancini, D. P.; Sreenivasan, S. V.; Willson, G., Release layers for contact and imprint lithography. *Semiconductor International* **2002**, 25, (6), 71-72,74,76,78,80.
- Ristenpart, W. D.; Aksay, I. A.; Saville, D. A., Assembly of colloidal aggregates by electrohydrodynamic flow: kinetic experiments and scaling analysis. *Physical Review E: Statistical, Nonlinear, and Soft Matter Physics* **2004**, 69, (2-1), 021405/1-021405/8.
- Rockford, L.; Liu, Y.; Mansky, P.; Russell, T. P.; Yoon, M.; Mochrie, S. G. J., Polymers on Nanoperiodic, Heterogeneous Surfaces. *Physical Review Letters* **1999**, 82, (12), 2602-2605.
- Rolland, J.; Hagberg, E. C.; Dension, G. M.; Carter, K. R.; De Simone, J. M., Lithography: High-resolution soft lithography: Enabling materials for nanotechnologies. *Angewandte Chemie, International Edition* **2004**, 43, (43), 5796-5799.
- Rolland, J. P.; Maynor, B. W.; Euliss, L. E.; Exner, A. E.; Denison, G. M.; DeSimone, J. M., Direct fabrication and harvesting of monodisperse, shape-specific nanobiomaterials. *Journal of the American Chemical Society* **2005**, 127, (28), 10096-10100.
- Rosa, D. S.; Chiovatto Neto, I.; Calil, M. R.; Pedroso, A. G.; Fonseca, C. P.; Neves, S., Evaluation of the thermal and mechanical properties of poly(e-caprolactone), low-density polyethylene, and their blends. *Journal of Applied Polymer Science* **2004**, 91, (6), 3909-3914.
- Rothmund, P. W. K., Folding DNA to create nanoscale shapes and patterns. *Nature* **2006**, 440, (7082), 297-302.
- Rothschild, M.; Bloomstein, T. M.; Kunz, R. R.; Liberman, V.; Switkes, M.; Palmacci, S. T.; Sedlacek, J. H. C.; Hardy, D.; Grenville, A., Liquid immersion lithography: Why, how, and when? *Journal of Vacuum Science & Technology, B: Microelectronics and*

Nanometer Structures--Processing, Measurement, and Phenomena **2004**, 22, (6), 2877-2881.

Rowland, H. D.; King, W. P.; Sun, A. C.; Schunk, P. R., Simulations of nonuniform embossing: The effect of asymmetric neighbor cavities on polymer flow during nanoimprint lithography. *Journal of Vacuum Science & Technology, B: Microelectronics and Nanometer Structures--Processing, Measurement, and Phenomena* **2005**, 23, (6), 2958-2962.

Rowland, H. D.; Sun, A. C.; Schunk, P. R.; King, W. P., Impact of polymer film thickness and cavity size on polymer flow during embossing: Toward process design rules for nanoimprint lithography. *Journal of Micromechanics and Microengineering* **2005**, 15, (12), 2414-2425.

Ruckenstein, E.; Jain, R. K., Spontaneous rupture of thin liquid films. *Journal of the Chemical Society, Faraday Transactions 2: Molecular and Chemical Physics* **1974**, 70, (1), 132-47.

Runt, J. P.; Fitzgerald, J. J., *Dielectric spectroscopy of polymeric materials: fundamentals and applications*. American Chemical Society: Washington, DC, 1997; p xvi, 461.

Sainsbury, T.; Fitzmaurice, D., Templated Assembly of Semiconductor and Insulator Nanoparticles at the Surface of Covalently Modified Multiwalled Carbon Nanotubes. *Chemistry of Materials* **2004**, 16, (19), 3780-3790.

Saito, Y.; Hamaguchi, K.; Uemura, S.; Uchida, K.; Tasaka, Y.; Ikazaki, F.; Yumura, M.; Kasuya, A.; Nishina, Y., Field emission from multi-walled carbon nanotubes and their application to electron tubes. *Applied Physics A: Materials Science & Processing* **1998**, 67, (1), 95-100.

Sankaran, S.; Saville, D. A., Experiments on the stability of a liquid bridge in an axial electric field. *Physics of Fluids A: Fluid Dynamics* **1993**, 5, (4), 1081-3.

Sarkar, J.; Sharma, A.; Shenoy, V., Adhesion and Debonding of Soft Elastic Films: Crack Patterns, Metastable Pathways, and Forces. *Langmuir* **2005**, 21, (4), 1457-1469.

Saville, D. A., Electrohydrodynamics: the Taylor-Melcher leaky-dielectric model. *Annual Review of Fluid Mechanics* **1997**, 29, (27).

Schaffer, E.; Harkema, S.; Blossey, R.; Steiner, U., Temperature-gradient-induced instability in polymer films. *Europhysics Letters* **2002**, 60, (2), 255-261.

Schaffer, E.; Harkema, S.; Roerdink, M.; Blossey, R.; Steiner, U., Thermomechanical lithography: pattern replication using a temperature gradient driven instability. *Advanced Materials* **2003**, 15, (6), 514-517.

Schaffer, E.; Thurn-Albrecht, T.; Russell, T. P.; Steiner, U., Electrically induced structure formation and pattern transfer. *Nature* **2000**, 403, (6772), 874-877.

Schaffer, E.; Thurn-Albrecht, T.; Russell, T. P.; Steiner, U., Electrohydrodynamic instabilities in polymer films. *Europhysics Letters* **2001**, 53, (4), 518-524.

- Scherzer, T.; Decker, U., Kinetic investigations on UV-induced photopolymerization reactions by real-time FTIR-ATR spectroscopy: the efficiency of photoinitiators at 313 and 222 nm. *Nuclear Instruments & Methods in Physics Research, Section B: Beam Interactions with Materials and Atoms* **1999**, 151, (1-4), 306-312.
- Schondelmaier, D.; Cramm, S.; Klingeler, R.; Morenzin, J.; Zilkens, C.; Eberhardt, W., Orientation and Self-Assembly of Hydrophobic Fluoroalkylsilanes. *Langmuir* **2002**, 18, 6242-6245.
- Schulz, G. V., Polymerization kinetics in highly concentrated systems. Kinetics of the Trommsdorf effect on methyl methacrylate. *Zeitschrift fuer Physikalische Chemie* **1956**, 8, 290-317.
- Schulz, H.; Scheer, H. C.; Hoffmann, T.; Sotomayor Torres, C. M.; Pfeiffer, K.; Bleidiessel, G.; Grutzner, G.; Cardinaud, C.; Gaboriau, F.; Peignon, M. C.; Ahopelto, J.; Heidari, B., New polymer materials for nanoimprinting. *Journal of Vacuum Science & Technology, B: Microelectronics and Nanometer Structures* **2000**, 18, (4), 1861-1865.
- Seekamp, J.; Zankovych, S.; Helfer, A. H.; Maury, P.; Sotomayor Torres, C. M.; Boettger, G.; Liguda, C.; Eich, M.; Heidari, B.; Montelius, L.; Ahopelto, J., Nanoimprinted passive optical devices. *Nanotechnology* **2002**, 13, (5), 581-586.
- Segalman, R. A.; Yokoyama, H.; Kramer, E. J., Graphoepitaxy of spherical domain block copolymer films. *Advanced Materials* **2001**, 13, (15), 1152-1155.
- Sfez, R.; Liu, D.-Z.; Turyan, I.; Mandler, D.; Yitzchaik, S., Polyaniline Monolayer Self-Assembled on Hydroxyl-Terminated Surfaces. *Langmuir* **2001**, 17, (9), 2556-2559.
- Sharma, A.; Ruckenstein, E., An analytical nonlinear theory of thin film rupture and its application to wetting films. *Journal of Colloid and Interface Science* **1986**, 113, (2), 456-79.
- Shenoy, V.; Sharma, A., Pattern formation in a thin solid film with interactions. *Physical Review Letters* **2000**, 86, (1), 119-122.
- Slobozhanin, L. A.; Alexander, J. I. D.; Patel, V. D., The stability margin for stable weightless liquid bridges. *Physics of Fluids* **2002**, 14, (1), 209-224.
- Slobozhanin, L. A.; Alexander, J. I. D.; Resnick, A. H., Bifurcation of the equilibrium states of a weightless liquid bridge. *Physics of Fluids* **1997**, 9, (7), 1893-1905.
- Slobozhanin, L. A.; Perales, J. M., Stability of liquid bridges between equal disks in an axial gravity field. *Physics of Fluids A: Fluid Dynamics* **1993**, 5, (6), 1305-14.
- Smith, B. J.; Stacey, N. A.; Donnelly, J. P.; Onsongo, D. M.; Bailey, T. C.; Mackay, C. J.; Resnick, D. J.; Dauksher, W. J.; Mancini, D. P.; Nordquist, K. J.; Sreenivasan, S. V.; Banerjee, S. K.; Ekerdt, J. G.; Willson, G. C., Employing Step-and-Flash imprint lithography for gate-level patterning of a MOSFET device. *Proceedings of SPIE-The International Society for Optical Engineering* **2003**, 5037, 1029-1034.

- Smith, P. A.; Nordquist, C. D.; Jackson, T. N.; Mayer, T. S.; Martin, B. R.; Mbindyo, J.; Mallouk, T. E., Electric-field assisted assembly and alignment of metallic nanowires. *Applied Physics Letters* **2000**, 77, (9), 1399-1401.
- Smith, R. C.; Carey, J. D.; Poa, C. H. P.; Cox, D. C.; Silva, S. R. P., Electron field emission from room temperature grown carbon nanofibers. *Journal of Applied Physics* **2004**, 95, (6), 3153-3157.
- Song, W.; So, S. K.; Wang, D.; Qiu, Y.; Cao, L., Angle dependent X-ray photoemission study on UV-ozone treatments of indium tin oxide. *Applied Surface Science* **2001**, 177, (3), 158-164.
- Sotomayor Torres, C. M., *Alternative lithography: unleashing the potentials of nanotechnology*. Kluwer Academic/Plenum: New York, 2003; p xx, 333.
- Stamm, U.; Kleinschmidt, J.; Gaebel, K.; Birner, H.; Ahmad, I.; Bolshukhin, D.; Brudermann, J.; Chinh, T. D.; Flohrer, F.; Goetze, S.; Hergenhan, G.; Kloepfel, D.; Korobochko, V.; Mader, B.; Mueller, R.; Ringling, J.; Schriever, G.; Ziener, C., EUV source power and lifetime: the most critical issues for EUV lithography. *Proceedings of SPIE-The International Society for Optical Engineering* **2004**, 5374, 133-144.
- Stamm, U.; Kleinschmidt, J.; Gaebel, K. M.; Birner, H.; Ahmad, I.; Bolshukhin, D.; Brudermann, J.; Chinh, T. D.; Flohrer, F.; Goetze, S.; Hergenhan, G.; Kloepfel, D.; Korobochko, V.; Mader, B.; Mueller, R.; Ringling, J.; Schriever, G.; Ziener, C., High-power sources for EUV lithography: state of the art. *Proceedings of SPIE-The International Society for Optical Engineering* **2004**, 5448, 722-736.
- Stanca, S. E.; Eritja, R.; Fitzmaurice, D., DNA-templated assembly of nanoscale architectures for next-generation electronic devices. *Faraday Discussions* **2006**, 131, 155-165.
- Stevens, M. J., Thoughts on the Structure of Alkylsilane Monolayers. *Langmuir* **1999**, 15, (8), 2773-2778.
- Stewart, M. D.; Wetzel, J. T.; Schmid, G. M.; Palmieri, F.; Thompson, E.; Kim, E. K.; Wang, D.; Sotodeh, K.; Jen, K.; Johnson, S. C.; Hao, J.; Dickey, M. D.; Nishimura, Y.; Laine, R. M.; Resnick, D. J.; Willson, C. G., Direct imprinting of dielectric materials for dual damascene processing. *Proceedings of SPIE-The International Society for Optical Engineering* **2005**, 5751, 210-218.
- Stewart, M. D.; Willson, C. G., Imprint materials for nanoscale devices. *MRS Bulletin* **2005**, 30, (12), 947-952.
- Stoykovich, M. P.; Mueller, M.; Kim, S. O.; Solak, H. H.; Edwards, E. W.; de Pablo, J. J.; Nealey, P. F., Directed assembly of block copolymer blends into nonregular device-oriented structures. *Science* **2005**, 308, (5727), 1442-1446.
- Studer, K.; Decker, C.; Beck, E.; Schwalm, R., Overcoming oxygen inhibition in UV-curing of acrylate coatings by carbon dioxide inerting, Part I. *Progress in Organic Coatings* **2003**, 48, (1), 92-100.

- Studer, K.; Decker, C.; Beck, E.; Schwalm, R., Overcoming oxygen inhibition in UV-curing of acrylate coatings by carbon dioxide inerting: Part II. *Progress in Organic Coatings* **2003**, 48, (1), 101-111.
- Sun, X.; Zhuang, L.; Zhang, W.; Chou, S. Y., Multilayer resist methods for nanoimprint lithography on nonflat surfaces. *Journal of Vacuum Science & Technology, B: Microelectronics and Nanometer Structures* **1998**, 16, (6), 3922-3925.
- Sundrani, D.; Darling, S. B.; Sibener, S. J., Guiding Polymers to Perfection: Macroscopic Alignment of Nanoscale Domains. *Nano Letters* **2004**, 4, (2), 273-276.
- Tabeling, P., *Introduction to microfluidics*. Oxford University Press: New York, 2005.
- Tan, H.; Gilbertson, A.; Chou, S. Y., Roller nanoimprint lithography. *Journal of Vacuum Science & Technology, B: Microelectronics and Nanometer Structures* **1998**, 16, (6), 3926-3928.
- Tang, J.; Gao, B.; Geng, H.; Velez, O. D.; Qin, L.-C.; Zhou, O., Assembly of 1D nanostructures into sub-micrometer diameter fibrils with controlled and variable length by dielectrophoresis. *Advanced Materials* **2003**, 15, (16), 1352-1355.
- Taniguchi, J.; Tokano, Y.; Miyamoto, I.; Komuro, M.; Hiroshima, H., Diamond nanoimprint lithography. *Nanotechnology* **2002**, 13, (5), 592-596.
- Taniguchi, J.; Tokano, Y.; Miyamoto, I.; Komuro, M.; Hiroshima, H.; Kobayashi, K.; Miyazaki, T.; Ohya, H., Preparation of diamond mold using electron beam lithography for application to nano-imprint lithography. *Japanese Journal of Applied Physics, Part 1: Regular Papers, Short Notes & Review Papers* **2000**, 39, (12B), 7070-7074.
- Taylor, G. I.; McEwan, A. D., The stability of a horizontal fluid interface in a vertical electric field. *Journal of Fluid Mechanics* **1965**, 22, (1), 1-15.
- Terrones, M.; Grobert, N.; Olivares, J.; Zhang, J. P.; Terrones, H.; Kordatos, K.; Hsu, W. K.; Hare, J. P.; Townsend, P. D.; Prassides, K.; Cheetham, A. K.; Kroto, H. W.; Walton, D. R. M., Controlled production of aligned-nanotube bundles. *Nature* **1997**, 388, (6637), 52-55.
- Thompson, E.; Rhyms, P. D.; Voisin, R. D.; Sreenivasan, S. V.; Martin, P. M., Fabrication of Step and Flash imprint lithography templates using commercial mask processes. *Proceedings of SPIE-The International Society for Optical Engineering* **2003**, 5037, 1019-1028.
- Thompson, L. F.; Willson, C. G.; Bowden, M. J., *Introduction to microlithography*. 2nd ed.; American Chemical Society: Washington, DC, 1994; p xiv, 527.
- Thurn-Albrecht, T.; Schotter, J.; Kastle, G. A.; Emley, N.; Shibauchi, T.; Krusin-Elbaum, L.; Guarini, K.; Black, C. T.; Tuominen, M. T.; Russell, T. P., Ultrahigh-density nanowire arrays grown in self-assembled diblock copolymer templates. *Science* **2000**, 290, (5499), 2126-2129.
- Tripp, C. P.; Hair, M. L., Chemical attachment of chlorosilanes to silica: a two-step amine-promoted reaction. *Journal of Physical Chemistry* **1993**, 97, (21), 5693-8.

- Troian, S. M.; Herbolzheimer, E.; Safran, S. A.; Joanny, J. F., Fingering Instabilities of Driven Spreading Films. *Europhysics Letters* **1989**, 10, (1), 25-30.
- Tryson, G. R.; Shultz, A. R., A calorimetric study of acrylate photopolymerization. *Journal of Polymer Science, Polymer Physics Edition* **1979**, 17, (12), 2059-75.
- Tsai, J. T. H.; Ko, H. C., Plasma illumination devices enhanced by carbon nanotubes. *Applied Physics Letters* **2006**, 88, (1), 013104/1-013104/2.
- Tseng, G. Y.; Ellenbogen, J. C., Nanotechnology. Toward nanocomputers. *Science* **2001**, 294, (5545), 1293-1294.
- Ulman, A., *An introduction to ultrathin organic films: from Langmuir-Blodgett to self-assembly*. Academic Press: Boston, 1991; p xxiii, 442.
- Ural, A.; Li, Y.; Dai, H., Electric-field-aligned growth of single-walled carbon nanotubes on surfaces. *Applied Physics Letters* **2002**, 81, (18), 3464-3466.
- Van der Zande, B. M. I.; Koper, G. J. M.; Lekkerkerker, H. N. W., Alignment of Rod-Shaped Gold Particles by Electric Fields. *Journal of Physical Chemistry B* **1999**, 103, (28), 5754-5760.
- Van Herk, A. M., Pulsed initiation polymerization as a means of obtaining propagation rate coefficients in free-radical polymerizations. II Review up to 2000. *Macromolecular Theory and Simulations* **2000**, 9, (8), 433-441.
- Velev, O. D.; Prevo, B. G.; Bhatt, K. H., On-chip manipulation of free droplets. *Nature* **2003**, 426, (6966), 515-516.
- Verma, R.; Sharma, A.; Kargupta, K.; Bhaumik, J., Electric Field Induced Instability and Pattern Formation in Thin Liquid Films. *Langmuir* **2005**, 21, (8), 3710-3721.
- Wallraff, G. M.; Hinsberg, W. D., Lithographic Imaging Techniques for the Formation of Nanoscopic Features. *Chemical Reviews* **1999**, 99, (7), 1801-1821.
- Wang, J.; Schablitsky, S.; Yu, Z.; Wu, W.; Chou, S. Y., Fabrication of a new broadband waveguide polarizer with a double-layer 190 nm period metal-gratings using nanoimprint lithography. *Journal of Vacuum Science & Technology, B: Microelectronics and Nanometer Structures* **1999**, 17, (6), 2957-2960.
- Warner, M. R. E.; Craster, R. V.; Matar, O. K., Pattern formation in thin liquid films with charged surfactants. *Journal of Colloid and Interface Science* **2003**, 268, (2), 448-463.
- Weisbrod, E. J.; Dauksher, W. J.; Zhang, D.; Rauf, S.; Mangat, P. J. S.; Ventzek, P. L. G.; Smith, K. H.; Clemens, S. B.; Martin, C. J.; Engelstad, R. L., Thermal modeling of extreme ultraviolet and step and flash imprint lithography substrates during dry etch. *Journal of Vacuum Science & Technology, B: Microelectronics and Nanometer Structures* **2002**, 20, (6), 3047-3052.
- Whidden, T. K.; Ferry, D. K.; Kozicki, M. N.; Kim, E.; Kumar, A.; Wilbur, J.; Whitesides, G. M., Pattern transfer to silicon by microcontact printing and RIE. *Nanotechnology* **1996**, 7, (4), 447-451.

- Whitesides, G. M.; Grzybowski, B., Self-assembly at all scales. *Science* **2002**, 295, (5564), 2418-2421.
- Wight, F. R., Oxygen inhibition of acrylic photopolymerization. *Journal of Polymer Science, Polymer Letters Edition* **1978**, 16, (3), 121-7.
- Wiley, B.; Sun, Y.; Mayers, B.; Xia, Y., Shape-controlled synthesis of metal nanostructures: The case of silver. *Chemistry--A European Journal* **2005**, 11, (2), 454-463.
- Williams, R. M.; Khudyakov, I. V.; Purvis, M. B.; Overton, B. J.; Turro, N. J., Direct and sensitized photolysis of phosphine oxide polymerization photoinitiators in the presence and absence of a model acrylate Monomer: A time resolved EPR, cure monitor, and photoDSC study. *Journal of Physical Chemistry B* **2000**, 104, (44), 10437-10443.
- Willner, I.; Blonder, R., Patterning of surfaces by photoisomerizable antibody-antigen monolayers. *Thin Solid Films* **1995**, 266, (2), 254-7.
- Winkleman, A.; Gates, B. D.; McCarty, L. S.; Whitesides, G. M., Directed self-assembly of spherical particles on patterned electrodes by an applied electric field. *Advanced Materials* **2005**, 17, (12), 1507-1511.
- Winters, J. O., *Nanostructures for Cellular Engineering*. Wiley VHC: 2006; Vol. 8.
- Wu, K.; Kim, E. K.; Ekerdt, J. G.; Willson, C. G., Effect of interfacial surfactants on template release in imprint lithography. *Abstracts of Papers, 229th ACS National Meeting, San Diego, CA, United States, March 13-17, 2005* **2005**, COLL-573.
- Wu, L.; Chou, S. Y., Electrohydrodynamic instability of a thin film of viscoelastic polymer underneath a lithographically manufactured mask. *Journal of Non-Newtonian Fluid Mechanics* **2005**, 125, (2-3), 91-99.
- Wu, W.; Cui, B.; Sun, X.-y.; Zhang, W.; Zhuang, L.; Kong, L.; Chou, S. Y., Large area high density quantized magnetic disks fabricated using nanoimprint lithography. *Journal of Vacuum Science & Technology, B: Microelectronics and Nanometer Structures* **1998**, 16, (6), 3825-3829.
- Wyart, F. B.; Martin, P.; Redon, C., Liquid-Liquid Dewetting. *Langmuir* **1993**, 9, (12), 3682-3690.
- Xia, Y.; Gates, B.; Li, Z.-Y., Self-assembly approaches to three-dimensional photonic crystals. *Advanced Materials* **2001**, 13, (6), 409-413.
- Xia, Y.; Whitesides, G. M., Soft lithography. *Angewandte Chemie, International Edition* **1998**, 37, (5), 550-575.
- Xia, Y.; Whitesides, G. M., Soft lithography. *Annual Review of Materials Science* **1998**, 28, 153-184.
- Xiang, H.; Lin, Y.; Russell, T. P., Electrically Induced Patterning in Block Copolymer Films. *Macromolecules* **2004**, 37, (14), 5358-5363.

- Xu, F.; Stacey, N. A.; Watts, M.; Truskett, V.; McMackin, I.; Choi, J.; Schumaker, P.; Thompson, E.; Babbs, D.; Sreenivasan, S. V.; Willson, C. G.; Schumaker, N., Development of imprint materials for the Step and Flash Imprint Lithography process. *Proceedings of SPIE-The International Society for Optical Engineering* **2004**, 5374, 232-241.
- Yamamoto, K.; Akita, S.; Nakayama, Y., Orientation and purification of carbon nanotubes using ac electrophoresis. *Journal of Physics D: Applied Physics* **1998**, 31, (8), L34-L36.
- Yamamoto, K.; Akita, S.; Nakayama, Y., Orientation of carbon nanotubes using electrophoresis. *Japanese Journal of Applied Physics, Part 2: Letters* **1996**, 35, (7B), L917-L918.
- Yan, X.; Liu, G.; Dickey, M.; Willson, C. G., Preparation of porous polymer membranes using nano- or micro-pillar arrays as templates. *Polymer* **2004**, 45, (25), 8469-8474.
- Yang, M.-C.; Shieh, J.; Hsu, C.-C.; Cheng, T.-C., Well-Aligned Silicon Nanograss Fabricated by Hydrogen Plasma Dry Etching. *Electrochemical and Solid-State Letters* **2005**, 8, (10), C131-C133.
- Yang, S.-M.; Jang, S. G.; Choi, D.-G.; Kim, S.; Yu, H. K., Nanomachining by colloidal lithography. *Small* **2006**, 2, (4), 458-475.
- Yang, X. M.; Peters, R. D.; Nealey, P. F.; Solak, H. H.; Cerrina, F., Guided Self-Assembly of Symmetric Diblock Copolymer Films on Chemically Nanopatterned Substrates. *Macromolecules* **2000**, 33, (26), 9575-9582.
- Yoo, P. J.; Choi, S.-J.; Kim, J. H.; Suh, D.; Baek, S. J.; Kim, T. W.; Lee, H. H., Unconventional Patterning with A Modulus-Tunable Mold: From Imprinting to Microcontact Printing. *Chemistry of Materials* **2004**, 16, (24), 5000-5005.
- Young, S. R.; Daulsher, W. J. Repair of imprint lithography templates prior to relief etching. 2005.
- Yue, G. Z.; Qiu, Q.; Gao, B.; Cheng, Y.; Zhang, J.; Shimoda, H.; Chang, S.; Lu, J. P.; Zhou, O., Generation of continuous and pulsed diagnostic imaging x-ray radiation using a carbon-nanotube-based field-emission cathode. *Applied Physics Letters* **2002**, 81, (2), 355-357.
- Zhang, W.; Chou, S. Y., Fabrication of 60-nm transistors on 4-in. wafer using nanoimprint at all lithography levels. *Applied Physics Letters* **2003**, 83, (8), 1632-1634.
- Zhang, W.; Chou, S. Y., Multilevel nano-imprint lithography with submicron alignment over 4 in. Si wafers. *Applied Physics Letters* **2001**, 79, (6), 845-847.
- Zhang, W. W.; Lister, J. R., Similarity solutions for van der waals rupture of a thin film on a solid substrate. *Physics of Fluids* **1999**, 11, (9), 2454-2462.
- Zhu, W.; Bower, C.; Zhou, O.; Kochanski, G.; Jin, S., Large current density from carbon nanotube field emitters. *Applied Physics Letters* **1999**, 75, (6), 873-875.

Zope, M.; Kargupta, K.; Sharma, A., Self-organized structures in thin liquid films on chemically heterogeneous substrates: Effect of antagonistic short and long range interactions. *Journal of Chemical Physics* **2001**, 114, (16), 7211-7221.

Vita

Michael David Dickey was born on October 18, 1976 in Raleigh, NC; home of the N.C. State Wolfpack. He is the son of David and Barbara Dickey. Michael graduated from Enloe High School in 1995. Michael attended Georgia Institute of Technology from 1995-99, earning a B.S. in Chemical Engineering. While at Georgia Tech, he worked as co-op engineer at Kimberly Clark in the Non-Wovens Division in Roswell, GA and also did undergraduate research with Professor Dennis Hess. Upon graduation, Michael worked for two years at Merck in Rahway, NJ developing pharmaceutical processes within the Chemical R&D Department. While at Merck, Michael met Kimberly Felmet, whom he married in 2005 in Austin, TX. In fall 2001, Michael enrolled in the Ph.D. program at the University of Texas under the supervision of Professor Grant Willson. Michael earned his Masters degree in 2003 in Chemical Engineering while pursuing a doctorate degree. Michael has accepted a two year post-doc position at Harvard under the guidance of Professor George Whitesides, followed by a professorship in the Department of Chemical Engineering at NC State in Raleigh, NC in the fall of 2008.

Permanent address: 6805 Woodmere Dr., Raleigh, NC 27612

This dissertation was typed by the author.

